Detection of Engineered Nanoparticles and Characterization of their Fate and Transformations in Aquatic Environments

Sarayu Rao

Department of Civil Engineering and Applied Mechanics

McGill University, Montreal, Canada

March 2020

A thesis submitted to McGill University in partial fulfillment of the requirements of the degree of Doctor of Philosophy

I

Table of Contents

List of Figures

List of Supplementary Figures

List of Tables

List of Supplementary Tables

Abstract

Engineered nanoparticles (ENPs) have become an important component of many nanotechnology-enabled consumer products. The increasing use of ENPs and their consequential release into the aquatic environment such as natural surface waters generates a need to characterize their fate and behavior at environmental concentrations to thoroughly understand the risks they may pose to the environment and biota. ENPs undergo a variety of transformation processes upon entering the aquatic environment, which influence their ultimate fate and bioavailability. The overall objective of this thesis is to characterize different fate processes of silver nanoparticles (nAg), an ENP widely used for its antimicrobial properties, in the aquatic environment. In order to achieve this, improved emerging detection techniques such as Asymmetric Flow Field Flow Fractionation (AF4) and Single Particle Inductively Coupled Plasma Mass Spectrometer (spICP-MS) were developed to enable ENP analysis in complex matrices.

The first objective of this thesis was to characterize and quantify different fate processes of nAg at an environmentally relevant concentration (6 µg/L) in natural lake water (LW), in the absence and presence of natural colloids, using filtered LW or FLW and unfiltered LW or UFLW. The re-precipitation process of nAg (r-nAg, ~26 nm) from pristine nAg ($nAg_{pristine}$) was detected in all systems and characterized using spICP-MS. The environmental fate of $nAg_{pristine}$ and r-nAg was evaluated under both quiescent and mixed conditions. In FLW systems, homoagglomeration dominated the fate of r-nAg, whereas heteroagglormation-induced sedimentation was found to be the dominant fate process in UFLW. The smaller r-nAg particles were persistent in UFLW over long exposure periods (44 days).

Sulfidation of nAg is another important transformation process as it can reduce or eliminate dissolution of nAg, therefore supressing any toxicity posed by Ag^+. The persistence of the toxic

potential of nAg due to incomplete sulfidation raises the need to understand the extent of sulfidation nAg particles undergo at any given S/Ag dose. The second objective of this thesis was to determine the role of polydisperse nAg sizes on extents of sulfidation ([S/Ag]$_{particle}$) within a particle size distribution, using AF4-ICP-MS. The amount of sulfur associated with each size fraction within the nAg particle population was found to be independent of particle size or specific surface area. Instead, it was dependent on both nAg mass as well as the total nAg surface area available in any given size bin.

The third objective of this thesis was to improve the detection of ENPs using spICP-MS. Improved particle sizing and counting efficiencies were observed for detection in the lower size range (20 - 40 nm), by employing smaller reference nAu for transport efficiency or nAu$_{TE}$ (30 nm instead of the conventional 55 - 60 nm). The results from this study indicate that the size of nAu$_{TE}$ directly influences the calculated size (diameter $\propto \sqrt[3]{transport\ efficiency}$) and particle concentration recoveries. The fourth objective was to improve detection of polydisperse ENPs in complex matrices by coupling AF4 with spICP-MS to analyse separated size fractions for concentrations and particle size. AF4 fractionation prior to spICP-MS analysis improved particle sizing of the released nTiO$_2$ in the lower range (45 – 90 nm) and higher size range (> 90 nm) compared to samples which were not fractionated using AF4.

Overall, the research characterized different fate processes of nAg in complex aquatic systems under environmentally relevant conditions. Analytical techniques were developed to overcome existing challenges with ENP measurement at environmentally relevant concentrations in complex matrices. These newly developed methods can be used for more detailed investigations of the environmental fate of ENPs in natural aquatic systems.

Résumé

Les nanoparticules artificielles (NPAs) sont devenues des composants importants des produits de consommation basés sur les nanotechnologies. L'augmentation de l'utilisation des NPAs ainsi que, par conséquent, leur rejet dans des environnements aquatiques tels que dans les eaux de surface naturelles, engendre le besoin de caractériser leur devenir et leur comportement en milieu naturel pour rigoureusement comprendre les risques qu'elles posent pour l'environnement et la biote. Après être émises dans l'environnement aquatique, les NPAs subissent plusieurs transformations, ce qui influence leur devenir et leur biodisponibilité. L'objectif principal de cette thèse est de caractériser les différents processus de transformation des nanoparticules d'argent (nAg, qui sont connues pour leurs propriétés antimicrobiennes) dans l'environnement aquatique. Pour cela, nous avons amélioré des techniques émergentes de détection des NPAs, telles que le fractionnement de flux asymétrique par couplage flux-force (AF4) et la spectrométrie de masse par plasma à couplage inductif à une seule particule (spICP-MS), qui permettent l'analyse des NPAs dans des matrices complexes.

Le premier objectif de cette thèse est d'identifier et de caractériser les différents processus de transformation subis par les nAg dans les eux de lacs naturels (LN), en présence ou non de colloïdes naturels filtrés (LNF) et infiltrés (LNNF). Le processus de re-précipitation des particules nAg issues de la dissolution des particules de nAg intactes nAg$_{pristine}$ (processus créant des particules notées r-nAg) a été systématiquement détecté dans tous les systèmes et caractérisé par la spICP-MS. Le devenir environnemental des particules nAg$_{pristine}$ et r-nAg a été évalué dans des conditions au repos et agitées. Nous avons noté que dans les systèmes LNF, l'homo-agglomération domine le devenir des r-nAg, alors que dans les LNNF, la sédimentation induite par hétéro-

agglomération est prédominante. Les plus petites particules r-nAg demeurent dans les LNNF pendant de longues périodes (44 jours).

La sulfuration des particules nAg est un autre procédé de transformation important, puisqu'elle peut réduire ou éliminer la dissolution des nAg, ce qui entraine la suppression de la toxicité apportée par Ag^+. La persistance du potentiel toxique de nAg dû à une sulfuration incomplète nécessite une compréhension approfondie de la sulfuration de nAg à différentes doses S/Ag. Le second objectif de cette thèse est de déterminer le rôle de la distribution par taille des particules de nAg sur la sulfuration ($[S/Ag]_{particle}$) en utilisant AF4-ICP-MS. Nous avons observé que la quantité de sulfure associée à chaque groupe de tailles au sein de la population de particules nAg est indépendante de la taille et de l'aire surfacique spécifique. Au contraire, elle dépend de la masse de nAg et de l'aire surfacique totale de nAg disponible dans chaque groupe de tailles.

Le troisième objectif de cette thèse est d'améliorer la détection des NPAs en utilisant la spICP-MS. Nous avons observé une amélioration de l'efficacité de la caractérisation de la taille des particules de 20-40 nm et de leur nombre en utilisant une plus petite référence nAu pour transport efficace ou nAu_{TE} (taille de 30 nm au lieu de 55 - 60 nm qui est conventionnellement utilisée). Les résultats de cette étude indiquent que la taille de nAu_{TE} influence directement la taille calculée (diamètre proportionnel à $\sqrt[3]{(transport\ efficacité)}$), ainsi que la récupération des concentrations de particules. Le quatrième objectif de cette thèse est d'améliorer la détection des NPAs polydispersées dans des matrices complexes en couplant AF4 avec spICP-MS pour analyser séparément par groupe de taille les concentrations et la taille des particules. Nous avons observé que le fractionnement AF4 avant l'analyse spICP-MS améliore la différentiation par taille des $nTiO_2$ de petite taille (45 – 90 nm) et de grande taille (> 90nm), comparé à des échantillons non-fractionnés avec AF4.

La recherche conduite dans cette thèse caractérise les différents processus de transformation des nAg en système aquatique complexe et en conditions environnementales pertinentes. Nous avons développé de nouvelles techniques analytiques pour outrepasser les défis posés par les mesures de de concentrations environnementales de NPAs en matrices complexes. Ces nouvelles méthodes peuvent être utilisées pour des études plus précises sur le devenir environnemental des NPAs en milieu aquatique naturel.

Acknowledgements

As this five-year long journey approaches the end, I am reflecting back on all the people that have supported, encouraged and walked with me to the finish line. This would not have been possible without the help and support of several people, who I would like to thank.

I will begin expressing my gratitude towards my supervisor, Dr. Subhasis Ghoshal, who gave me an opportunity, not once, but twice to realize my passion for science and research. His guidance and encouragement, while giving me the freedom to explore my own ideas has made me a confident researcher today. I have always appreciated our meetings and discussions where he has challenged me to think deeper and bigger, which has helped me hone my thinking as a researcher. Finally, I would like to thank him for encouraging me to do activities outside of my PhD, which have led to me being the person I am today.

Research experiences are enhanced when you have an opportunity to work with and learn from other researchers. I would like to thank all the people I have collaborated with or had an opportunity to discuss different aspects of my research with over the last five years. I would like to thank Dr. Thilo Hoffman and Dr. Frank von der Kammer from University of Vienna, who gave me an opportunity to work in their lab, which not only led to me gaining a lot of research experience, but also led to many sessions of meaningful discussions. Brainstorming and discussing research with your peers often leads to new ideas and solutions. I want to thank Aude Bechu (Department of Chemistry, McGill University) and Dr. Xiaoyu Gao for their enthusiasm with helping me address some key research knowledge gaps. This research would not have been possible without the help of David Liu (FEMR, McGill University) and Andrew Golsztajn (Chemical Engineering, McGill University) who patiently analysed all my TEM and TOC samples. I would also like to thank Jorge Sayat, Dr. William Cook, John Bartczak, William

Dumais, Daina Brumelis and Dr. Pinar Ozcer who have supported and helped me in times of experimental and instrumental breakdowns. I would also like to thank the administrative staff (Sun Chee Wong and Sandra Shewchuk-Boyd) who have been extremely helpful. I would also like to acknowledge the financial support I received from McGill Engineering Doctoral Award (MEDA), NSERC CREATE in Green Chemistry and the Graduate Mobility Award.

The people you work with and encounter on a daily basis often govern the experiences during a PhD. I would like to thank Dr. Ali Akbari, Dr. Mehrnoosh Azodi, Dr. Yanyan Zhang, Arshath Abdul Rahim and Mariana Umpiérrez for making this journey so much more meaningful by helping me grow as a researcher and support me during difficult times. I would like to thank Laura Minet and Sarah el Outayek for translating my abstract to French and Mamdouh Jaber for his help with the formatting. It has been delightful working with all the previous and present lab members and friends of the Benedek Laboratories, Claire, Sampriti, Julie, Chenxiao, Anirban, Aleksandra, Bing and Vini. I would also like to thank Dr. Sanaz Alizadeh (École Polytechnique, Montreal) for her kind words and support and all my other friends that have embarked this PhD journey with me.

Finally, this would not have been possible with the support of family, my parents, my sister, Suman and my partner, Akhil, who have stood by me through every low point and have constantly encouraged me to keep going forward and do my best. They have been my strength through this journey and I could never have achieved this without them. I would like to end this with a stanza from "The Road Not Taken" by Robert Frost, which I would often read to motivate me.

"Two roads diverged in a wood, and I—
I took the one less traveled by,
And that has made all the difference."

Preface and Contributions to Knowledge

Preface

In accordance with the "*Guidelines for Thesis Preparation",* this thesis is presented in a manuscript-based format. Chapters 1 and 2 include the introduction and literature review. Chapters 3 to 6 present experimental methods, results of the experimental work and discussions. Chapter 7 presents the summary and conclusion of this thesis and the potential for future work. The results presented in Chapters 3 to 6 have been or are in preparation to be submitted to different peer-reviewed journals. In all the publications stated above, the author of the manuscript is the primary author of this thesis. A detailed description of the efforts and contributions to new knowledge of all authors is presented below.

Contributions to knowledge

The specific contributions to new knowledge are listed below.

1. **The persistence of re-precipitated nAg from primary nAg is enhanced in the presence of natural organic matter in lake waters.** Recently, several studies have reported the re-precipitation of nAg from spiked Ag^+ in natural waters. This research reported the fate of pristine nAg and nAg re-precipitated (r-nAg) from the release of Ag^+ from pristine nAg ($nAg_{pristine}$) particles in natural lake water microcosms at environmentally relevant concentrations (ng/L to low µg/L) using single particle ICP-MS and transmission electron microscopy (TEM). A significant fraction of re-precipitated nAg remains in suspension over long exposure periods (~45 days) due to the stabilizing effect of natural organic matter.

2. **A significant fraction of nAg (re-precipitated and pristine nAg) heteroagglomerate with natural colloids and eventually settle down.** Previous literature has defined

heteroagglomeration of ENPs and colloids as an important environmental fate endpoint. In this study, the extent of heteroagglomeration of r-nAg and $nAg_{pristine}$ was determined by sonicating samples at different time points and calculated the difference to determine the release. Heteroagglomeration between nAg and natural colloids was confirmed with TEM and energy dispersive X-ray spectroscopy (EDS). All the fate process of nAg in lake water (homoagglomeration, heteroagglomeration, sedimentation, dissolution and re-precipitation) were quantified.

3. **Particle size of nAg does not influence the overall extent of sulfidation within a given polydisperse size distribution.** Previous studies have established an inverse correlation between nAg size and completeness of sulfidation for different sets of nAg size distributions on a whole population basis. Using a size separation technique such as asymmetric flow field flow fractionation (AF4) with triple quadrupole inductively coupled plasma mass spectrometer (ICP-MS) enables determining size related aspects of complex transformation processes such as sulfidation. Overall invariance of extent of sulfidation in a given size distribution occurs as larger nAg particles (present fewer in number) can provide a source of Ag ions for the heterogeneous sulfidation reaction due to its larger particle surface area leading to higher concentrations of S associated with larger nAg particles. Further, smaller particles present in higher number concentrations within a given size bin, can continuously undergo sulfidation in the presence of lower concentrations of S. The sulfidation reaction of nAg continues until one of the reactants of the heterogeneous reaction (Ag surface for Ag ions or bisulfides in solution) is exhausted. This finding is of environmental significance as nAg found in environmental systems is seldom monodisperse.

4. **Incomplete sulfidation of nAg has undesirable environmental implications such as dissolution and re-precipitation.** By determining the actual extent of sulfidation occurring in an aquatic system at any given dose of sulfides, the completeness of sulfidation can be determined. An S/Ag dose 10 times higher (S/Ag = 5) than the stoichiometric dose (S/Ag = 0.5) was required to achieve full sulfidation. Incomplete sulfidation was observed at the stoichiometric S/Ag dose of 0.5. Incomplete sulfidation can preserve the toxic potential of nAg by releasing of Ag^+ over long-term exposure times. In the presence of organic sulfide sources such as thiols or natural organic matter, Ag^+ can re-precipitate into smaller nAg particles, which are more bioavailable owing to their smaller sizes.

5. **Improvement in nanoparticle sizing and counting efficiencies on single particle ICP-MS.** Current practices of spICP-MS method optimization and development mostly use 50 - 60 nm gold nanoparticles (nAu) for transport efficiency (TE) estimations. These conditions are not fully representative of the sample, if the samples contain nanoparticles in the lower size range (20 - 40 nm). The accuracy and sensitivity of spICP-MS was enhanced by exploring the effect of nAu reference size on transport efficiency; consequently, its effects on nanoparticle characterization. Particle counting and sizing efficiencies of smaller size NPs (< 30 nm) are influenced by nAu_{TE} used for transport efficiency calculations. Improving the resolution and overall data quality obtained from spICP-MS increases the range of applicability of this technique.

6. **Asymmetric flow field flow fractionation (AF4) hyphenated with ICP-MS and spICP-MS can overcome existing detection challenges for environmental ENP samples.** Recent studies have extensively used AF4 for pristine ENP characterization. AF4 is a promising method for environmental ENP detection and characterization, if combined with suitable detection techniques. Optimized AF4 methods were developed to fractionate and

characterize pristine and transformed ENPs in commercial paint matrices using a downstream multi-angle light scattering detector (MALS). Further, a method was developed to improve sizing and concentration for lower size fraction data obtained by spICP-MS by pre-fractionating $nTiO_2$ with AF4.

Publications

(1). Findings from Chapter 3 are in preparation for submission to the following journal: Environmental Science and Technology.

Rao S., Xiaoyu Gao., Ghoshal S., (2020) Characterization of the fate of primary and re-precipitated silver nanoparticles in lake water microcosms.

- Rao S., Designed and conducted experiments, analysed data and wrote the manuscript.
- Xiaoyu Gao., Discussion of experimental results, revision of manuscript.
- Ghoshal S., Experimental design, research supervision, discussion of experimental results, revision of manuscript.

(2). Findings from Chapter 4 are in preparation for submission to the following journal: Environmental Pollution.

Rao S., Hofmann T., Kammer F., Ghoshal S., (2020) Extent of silver nanoparticle sulfidation in a polydisperse population is independent of particle size.

- Rao S., Designed and conducted experiments, analysed data and wrote the manuscript.
- Hofmann T., Discussion of experimental results, revision of manuscript.
- Kammer F., Discussions on conception of study and revision of manuscript.
- Ghoshal S., Experimental design, research supervision, discussion of experimental results and revision of manuscript.

(3). Findings from Chapter 5 are in preparation for submission to the following journal: Environmental Science: Nano.

Rao S., Rahim A., Bechu A., Ghoshal S. (2020), Reference nanoparticle size used for transport efficiency estimation influences particle counting and sizing in single particle ICP-MS.

- Rao S., Designed and conducted experiments, analysed data and wrote the manuscript.
- Rahim A., Assisted with spICP-MS experiments, discussion of experimental results.
- Bechu A., Performed calculations required to prove experimental results.
- Ghoshal S., Experimental design, research supervision, discussion of experimental results and revision of manuscript.

(4). Findings from Chapter 6 are written in the form of a chapter.

Rao S., Ghoshal S., (2019) Improving Detection and Characterization of Engineered Nanoparticles using AF4-MALS and spICP-MS in complex matrices.

- Rao S., Designed and conducted experiments, analysed data and wrote the manuscript.
- Ghoshal S., Experimental design, research supervision, discussion of experimental results and revision of chapter.

List of Abbreviations

AAS: Atomic absorption spectroscopy

AF4: Asymmetric flow field flow fractionation

DI: De-ionized

DLS: Dynamic light scattering

DOC: Dissolved organic carbon

DOM: Dissolved organic matter

dRI: Differential refractive index

EDS: Energy dispersive X-ray spectroscopy

ENP: Engineered Nanoparticles

EXFAS: Extended X-ray absorption fine structure spectroscopy

FA: Fulvic acid

FFF: Field flow fractionation

FLW: Filtered lake water

HA: Humic acid

HR-ICP-MS: High resolution inductively coupled plasma mass spectrometer

ICP-MS: Inductively coupled plasma mass spectrometer

ICP-OES: Inductively coupled plasma optical emission spectrometry

IHSS: International humic substances society

LOD: Limit of detection

LW: Lake water

MALS: Multi angle light scattering

nAg: Silver nanoparticles

nAu: Gold nanoparticles

$nTiO_2$: Titanium dioxide nanoparticles

NOM: Natural organic matter

NP: Nanoparticle

NTA: Nanoparticle tracking analysis

PES: Polyethersulfone

PVP: Polyvinylpyrrolidone

QLES: Quasi-elastic light scattering

RC: Regenerated cellulose

RMS: Root mean square

SEM: Scanning electron microscopy

spICP-MS: Single Particle Inductively Coupled Plasma Mass Spectrometer

SRFA: Suwannee river fulvic acid

SRHA: Suwannee river humic acid

SRNOM: Suwannee river natural organic matter

SA: Surface area

SSA: Specific surface area

TE: Transport efficiency

TEM: Transmission electron microscopy

UFLW: Unfiltered lake water

UV-Vis: Ultraviolet-visible

WWTP: Wastewater treatment plants

Chapter 1 . Introduction

The "nano-effect" was first observed in the 4th century with the Roman Lycurgus cup (Leonhardt 2007). Light scattered by silver and gold nanoparticles (nAg and nAu) embedded in the glass, made it appear in different colors depending on the direction of illuminated light, due to surface plasmon resonance effect of the nanoparticles (NPs). Nanoparticles are defined as materials which have at least one dimension in the range of 1 to 100 nm (Moore 2006). At a talk titled "There is plenty of room at the bottom" (Feynman 1959) by Richard Feynman in the year 1959, the concept of "nanomaterials" was first theorized; *"I would like to describe a field, in which little has been done, but in which an enormous amount can be done in principle. What I want to talk about is the problem of manipulating and controlling things on a small scale"*.

In the recent years, engineered nanoparticles (ENPs) have been used in many commercial products (Boxall et al. 2007, Gottschalk et al. 2009, Keller et al. 2014) to enhance particular functions. Due to their unique size-related physical and chemical properties, they enable functions (e.g., luminescence, antimicrobial) that are not achievable with their bulk counterparts. The Nano2 WTEC report (Bonnell et al. 2010) predicted that the global market for nanotechnology for societal needs will reach 3 trillion dollars by 2020. Currently, ENPs such as titanium oxide ($nTiO_2$) are used in a variety of consumer products such as, sunscreen, paints and coatings due to their photo-catalytic properties. Silver nanoparticles (nAg) are used in socks, paints, bandages, textiles and food containers for their antimicrobial properties (Benn and Westerhoff 2008, Al-Kattan et al. 2014). Nanoparticles of zinc oxide, iron oxide, fullerenes, gold are used in cosmetics products (Boxall et al. 2007). Nanotechnology has the potential to provide efficient, cost effective solutions for potable water, food safety and even sustainable habitats. Nanoscale manufacturing will provide the means for sustainable development: less materials, less water, less energy, and less

manufacturing waste, and new methods to convert energy (Helland and Kastenholz 2008, Vaseashta 2009). As important as all these applications are for a more sustainable future, there is a strong need to study their impact on the environment. As many benefits as ENPs may posses due to their properties, studies have shown toxic effects of ENPs on organisms (Warheit et al. 2006, Warheit et al. 2007, Sotiriou and Pratsinis 2010, Miller et al. 2012, Giese et al. 2018). Studies have shown that metal nanoparticles (e.g. Ag, TiO_2, ZnO, and Fe_2O_3) can enter human cells and exhibit cytotoxicity, and cause cell membrane leakage and inflammatory response (Zhang et al. 2008).
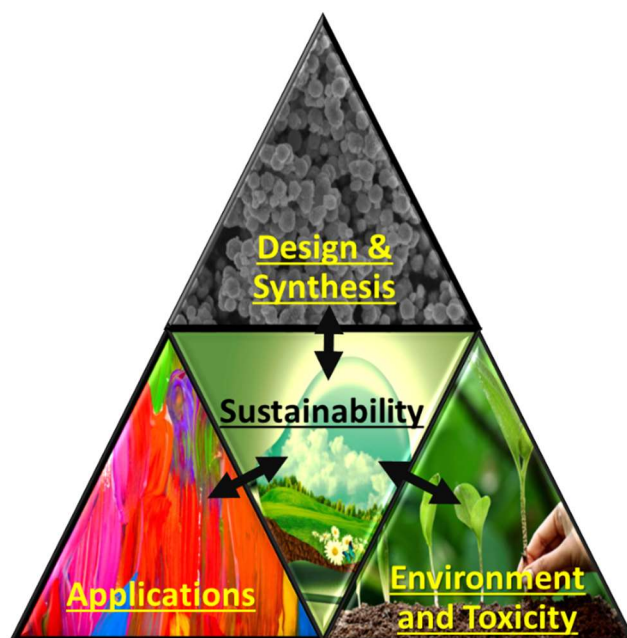
Figure 1.1: Facets of nanotechnology for a sustainable future

Potential risks to ecosystems and human beings depend on transformations and mobility of ENPs upon release to the environment. One of the main sources of release of ENPs used in consumer products into the environment is via wastewater treatment plants (WWTP). A survey estimate of nanoparticles released from personal care products to the environment carried out by Keller *et al*. showed that 93% of ENPs enter into municipal wastewater treatment plants, which are then

released with the effluent into surface water bodies or with waste biomass into landfills or agricultural lands. Approximately 4.5% of the ENPs are also directly released into water bodies, e.g., as ENPs released from outdoor paints and coatings into precipitation runoff (Keller et al. 2014). Nanoparticles may leach into groundwater from treated sludge applied to agricultural land or from nano-enhanced products such as electronic devices disposed in landfills (Choi et al. 2008, Fabrega et al. 2009, Brar et al. 2010, Fabrega et al. 2011). Additionally, risks depend on concentrations, state of ENPs upon release (aggregated or non-aggregated) and prevailing environmental conditions. Assessing production, consumption and release patterns of ENPs is the first step towards estimating probable ENP concentrations in the environment. Recently, estimates have been provided from model predictions based on approximate worldwide production volumes, and materials flow analyses from the products to different environmental compartments (Mueller and Nowack 2008). However, experimental data is necessary to characterize the behavior of ENPs in the environment, as model predictions only track the total mass through a system and do not distinguish between the specific state of the ENP (single/free, aggregated, transformed) (Nowack et al. 2015).

1.1 Behavior of ENPs in aquatic systems

In aquatic environments, the nature of particle surfaces is related to aquatic chemistry (pH, ionic strength, presence of organic matter) and their behavior is strongly dependent on the aqueous chemistry. Therefore, characterizing ENPs in their potential environmental matrix is a very important step in determining their ultimate fate and behavior in the environment.

ENPs may undergo a variety of processes upon entering the aquatic environment, e.g., agglomeration (Kaegi et al. 2013, Markus et al. 2015), dissolution (Liu and Hurt 2010) and surface chemical transformation such as reaction with sulfides (Kim et al. 2010, Levard et al. 2011, Levard

3

et al. 2013). Many studies have shown that the fate and toxicity of ENPs in aquatic environments is directly related to their high affinity to other surfaces or with each other (Wiesner and Bottero 2007, Wilkinson and Lead 2007, Praetorius et al. 2012, Praetorius et al. 2014). The fate of ENPs in aquatic systems are made particularly complex due to the presence of large amounts of natural colloids (e.g. clays, mineral oxides, silica as well as biocolloids) and natural organic matter. These materials interact directly with ENPs and determine their colloidal stability, propensity for removal from the water column, toxicity and bioavailability (Thill et al. 2006, Wiesner and Bottero 2007, Wilkinson and Lead 2007).
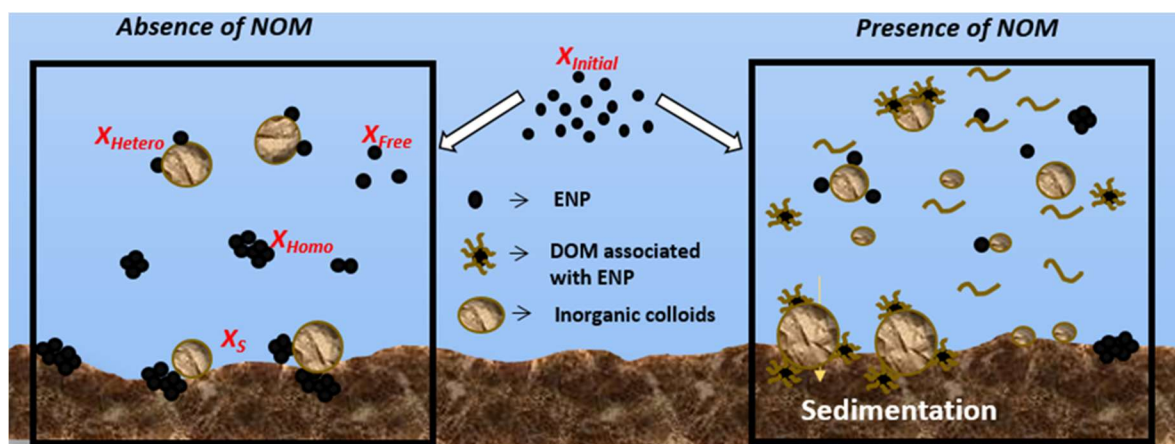
Figure 1.2: Depiction of interactions of colloids, ENPs and natural organic matter (DOM). Fraction of ENPs that are heteroaggregated is X_{hetero}, homoaggregated is X_{homo} and sedimentated is Xs.

Important processes that control the fate and transport of ENPs in aquatic systems can be defined using mathematical equations such as Stokes law for settling, Smoluchowski equation for size dependence on Brownian motion and for describing aggregation (Wiesner and Bottero 2007). These fate processes (Figure 1.2) can be combined into a quantitative description of colloidal transport in water, which takes into account the aggregation (leading to the formation of larger

aggregates) and sedimentation which was first described by Farley and Morel (Farley and Morel 1986). The detailed equations are stated in the literature review (Chapter 2).

The ultimate fate of the ENPs (primary and re-precipitated) can be dominated by the presence of natural colloids in natural aquatic systems (Quik et al. 2012). Agglomeration of two dissimilar particles is termed as heteroagglomeration (e.g., colloid and ENP), while agglomeration of similar particles is homoagglomeration (e.g., ENP-ENP). An important factor that determines agglomeration is the attachment efficiency between two particles, which is defined as the probability of two particles sticking to each other upon collision. Particle interactions in the aquatic environment are usually described using the classical Derjaguin-Landau-Verwey-Overbeek (DLVO) theory; the total interaction energy between two surfaces as a sum of attractive van der Waals forces and repulsive electrostatic forces possessed by the two particles (Wiesner and Bottero 2007). Some other non- DLVO forces such as acid-base, Born repulsion and steric interactions are also important parameters in controlling the interaction energy between particles in the aquatic environment.

Processes that have not been included in the fate and transport equations nonetheless occur in aquatic systems, which are discussed herein. Dissolution of metallic ENPs leads to a release in metal ions (Barriada et al. 2007, Li et al. 2010, Azodi et al. 2016) and is described as a first order reaction (Kittler et al. 2010). Released and free metallic ions can undergo re-precipitation to form new nanoparticles under suitable aquatic chemistries (Akaighe et al. 2011, Adegboyega et al. 2013).

Insufficient data is currently available on the concentrations and state of ENPs upon release into the environment due to limitations posed by existing analytical techniques (Gottschalk et al. 2009).

The fate of ENPs in natural waters can be fully assessed only if they are characterized for size, concentrations and any transformations they may undergo upon release into the environment.

1.2 Detection and characterization of ENPs

The natural aquatic environment is quite complex, the presence of colloids and natural organic matter makes detection of ENPs more challenging. Microscopy techniques like scanning electron microscopy (SEM), transmission electron microscopy (TEM) require extensive sample preparation and do not provide reliable quantitative information about the concentration given the small sample size analysed (Hassellöv et al. 1999, Tiede et al. 2008). Simple and fast particle sizing techniques such as dynamic light scattering (DLS) has limitations for analysis in complex media due to its inability to distinguish metal or other ENPs from background colloids. The scattering intensity is proportional to the sixth power of particle size, even the presence of a small amount of larger background natural colloids will lead to biased higher estimates of ENP size (Baalousha et al. 2011, Mitrano et al. 2012). Single particle inductively coupled plasma mass spectrometry (spICP-MS) is a powerful technique for measuring metal ENP sizes and concentrations in complex environmental samples, but is limited in terms of detecting ENP sizes smaller than 20 nm (Mitrano et al. 2012). Asymmetric flow field flow fractionation (AF4) is a hydrodynamic elution technique that allows separation of particles according to their sizes. The separation of macromolecules and colloids of different sizes in a flowing aqueous medium, and channelling of these size fractions at different retention times to online detectors enables elemental composition and size measurements of different size fractions. Connecting AF4 with multi angle light scattering (MALS) and dynamic light scattering (DLS), ultraviolet-visible (UV-vis), differential refractive index (dRI), and ICP-MS detectors will likely overcome challenges faced by these detectors when used separately. This configuration also provides information about shape,

particle size distribution and concentration. Figure 1.3 shows different analytical techniques used for ENP characterization.
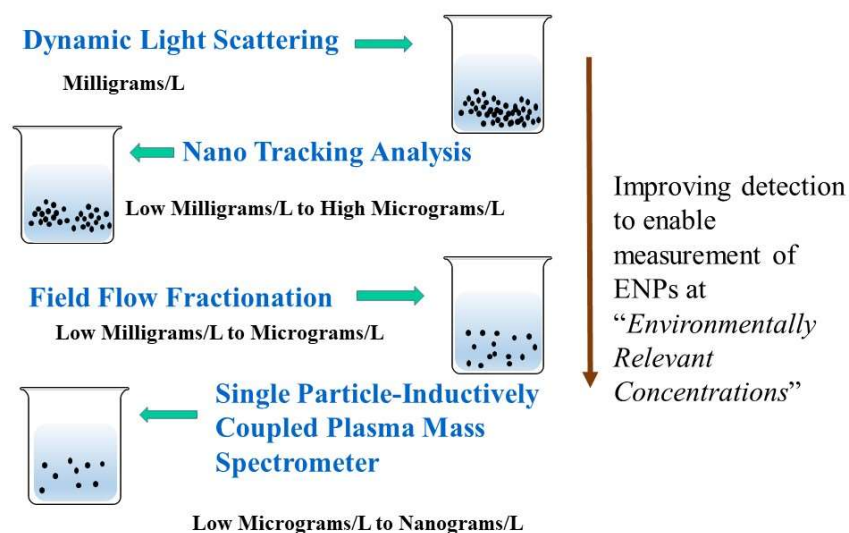
Figure 1.3: Various analytical techniques used for ENP measurement and their limit of detection

1.3 Knowledge Gaps

Increasing use of ENPs in consumer products leads to an inevitable release into the environment. However, their implications in the aquatic environment is still not fully understand. Current material flow models are mostly based on the life cycle of products containing ENPs and provide estimates of the mass of ENPs that may be discharged into various environmental compartments (Giese et al. 2018). These models do not distinguish between single ENPs, agglomerated ENPs, dissolved fractions, they only account for the total mass (Nowack et al. 2015). ENP fate and transport models account for various transport mechanisms as well physical and chemical transformations of ENPs and provide more detailed predictions of ENP and aggregate sizes and any transformation products in various compartments, in temporal and spatial dimensions.

However, there is a dearth of knowledge of various agglomeration, dissolution kinetic coefficients that are essential for accurate predictions by the fate models (Praetorius et al. 2012, Meesters et al. 2014, Garner et al. 2017). As well, there is a lack of robust measurements of ENP concentrations in various compartments, due to the lack of appropriate analytical techniques.

Development of analytical techniques to measure transformed ENPs at their predicted environmental concentrations is an important aspect from the environmental risk assessment standpoint. For example, an important fate process, which is overlooked by material flow models, is re-precipitation of small silver nanoparticles from dissolved Ag generated from primary nAg over time in natural waters. Over the last few years, re-precipitation of nAg from Ag^+ in aquatic environments has been reported (Akaighe et al. 2011, Yin et al. 2012, Adegboyega et al. 2013, Wimmer et al. 2018). However, there is a lack of information on the persistence and fate of re-precipitated nAg in surface waters.

Another example of a common transformation process is the sulfidation of nAg in wastewater treatment plants. Sulfidation of nAg reduces the bioavailability of nAg due to the formation of insoluble Ag_2S, inhibiting the release of Ag^+. However, recent studies have shown that sulfidated nAg may still be toxic due to incomplete sulfidation (Starnes et al. 2016, Kraas et al. 2017).Therefore, detection and characterization of sulfidated nAg is crucial in determining extent of transformation, the sulfidation mechanism and examining the factors that lead to incomplete sulfidation.

The overall objective of this thesis is to investigate and characterize different fate processes of nAg, a commonly used ENP in consumer products in aquatic systems at environmentally relevant

concentrations. An imperative step in achieving this was to develop and optimize novel detection techniques to achieve detection closer to predicted environmental concentrations.

1.4 Research Objectives

The specific objectives of this research is as follows:

1) Characterize the fate (aggregation, dissolution) and persistence of re-precipitated and pristine nAg in natural surface waters such as lake water.

2) To characterize the effect of stoichiometrically exact S/Ag dose (0.5) as well as excess doses on extent of sulfidation (S/Ag$_{particle}$) for various particle sizes in a polydisperse size distribution of silver nanoparticles.

3) Evaluate the effect of gold nanoparticle size used for transport efficiency calculations in single particle inductively coupled plasma mass spectrometer (spICP-MS) on size and concentration estimations.

4) Optimize conditions of asymmetric flow field flow fractionation (AF4) for the analysis of pristine and transformed ENPs. Develop methods to improve detection of ENPs in complex matrices using AF4 and spICP-MS.

1.5 Thesis Organization

- **Chapter 1** is the introduction to research subject, objectives of thesis and the thesis structure.

- **Chapter 2** provides a detailed literature review on use and release patterns of ENPs, toxicity posed by nTiO$_2$ and nAg, which are the focus ENPs in this study, potential fate of nAg in the aquatic environment (aggregation, dissolution, re-precipitation) and importance of studying sulfidation of nAg as an environmental transformation process. Different ENP analytical models have been discussed to determine fate processes such as homo and hetero

aggregation, sedimentation. Further, literature on ENP detection techniques such AF4 and spICP-MS are discussed.

- **Chapter 3** investigates the fate of 80 nm PVP-nAg and re-precipitated nAg in lake water microcosms under favorable (quiescent) and unfavorable settling conditions (mixed). Experiments revealed an important fate process occurring in all systems; re-precipitation of nAg (~20 nm of r-nAg) from primary nAg. In the absence of colloids (filtered lake water), homoagglomeration between primary and r-nAg was found to be a dominant process. In the presence of colloids, heteroagglomeration followed by settling was the dominant process. Inducing mixing increased rates of heteroagglomeration whereas reduced homoagglomeration.

- **Chapter 4** investigates the effect of different particle sizes in a polydisperse particle size distribution on sulfide loading on nAg particles and the effect of stoichiometrically exact and excess sulfide doses on the extents of sulfidation. These processes were investigated by hyphenating AF4 with ICP-MS. The mechanism of sulfidation of nAg in the presence of stoichiometrically sufficient and excess sulfides is discussed.

- **Chapter 5** discusses the effect of nAu size used for transport efficiency estimation using spICP-MS on ENP size and concentration detection. We found that detection of smaller size NPs (< 30 nm) is influenced by nAu reference size used for transport efficiency calculations. Particle counting efficiencies are affected by nAu reference size.

- **Chapter 6** entails method development of AF4 for detection and characterization nanoparticles. Calibration curve to convert retention time to hydrodynamic diameter is the first method developed. Characterization of different types of $nTiO_2$ and ENPs (Ag, TiO_2, ZnO, and magnetite) used in paints (pristine and transformed) using AF4-UV/vis-MALS.

Lastly, a method developed using AF4 has a sample clean up technique to improve detection of nTiO$_2$ using spICP-MS.

- **Chapter 7** summarizes all the major findings of this research and highlights the important conclusions and describes the potential for future work.

1.6 References

1) Adegboyega, N. F., et al. (2013). "Interactions of Aqueous Ag+ with Fulvic Acids: Mechanisms of Silver Nanoparticle Formation and Investigation of Stability." Environmental Science & Technology **47**(2): 757-764.

2) Akaighe, N., et al. (2011). "Humic Acid-Induced Silver Nanoparticle Formation Under Environmentally Relevant Conditions." Environmental Science & Technology **45**(9): 3895-3901.

3) Al-Kattan, A., et al. (2014). "Behavior of TiO2 Released from Nano-TiO2-Containing Paint and Comparison to Pristine Nano-TiO2." Environmental science & technology **48**(12): 6710-6718.

4) Azodi, M., et al. (2016). "Dissolution Behavior of Silver Nanoparticles and Formation of Secondary Silver Nanoparticles in Municipal Wastewater by Single-Particle ICP-MS." Environmental Science & Technology **50**(24): 13318-13327.

5) Baalousha, M., et al. (2011). "Flow field-flow fractionation for the analysis and characterization of natural colloids and manufactured nanoparticles in environmental systems: a critical review." Journal of Chromatography A **1218**(27): 4078-4103.

6) Barriada, J. L., et al. (2007). "Dissolved silver measurements in seawater." TrAC Trends in Analytical Chemistry **26**(8): 809-817.

7) Benn, T. M. and P. Westerhoff (2008). "Nanoparticle Silver Released into Water from Commercially Available Sock Fabrics." Environmental science & technology **42**(11): 4133-4139.

8) Bonnell, D., et al. (2010). Nanotechnology Research Directions for Societal Needs in 2020. M. C. Roco, C. A. Mirkin and M. C. Hersam. http://www.wtec.org/nano2, WORLD TECHNOLOGY EVALUATION CENTER, INC. (WTEC).

9) Boxall, A. B., et al. (2007). "Current and future predicted environmental exposure to engineered nanoparticles." Central Science Laboratory, Department of the Environment and Rural Affairs, London, UK: 89.

10) Brar, S. K., et al. (2010). "Engineered nanoparticles in wastewater and wastewater sludge – Evidence and impacts." Waste Management **30**(3): 504-520.

11) Choi, O., et al. (2008). "The inhibitory effects of silver nanoparticles, silver ions, and silver chloride colloids on microbial growth." Water Research **42**(12): 3066-3074.

12) Fabrega, J., et al. (2011). "Silver nanoparticles: behaviour and effects in the aquatic environment." Environment international **37**(2): 517-531.

13) Fabrega, J., et al. (2009). "Interactions of silver nanoparticles with Pseudomonas putida biofilms." Environmental science & technology **43**(23): 9004-9009.

14) Farley, K. J. and F. M. M. Morel (1986). "Role of coagulation in the kinetics of sedimentation." Environmental Science & Technology **20**(2): 187-195.

15) Feynman, R. P. (1959). Plenty of Room at the Bottom. A. P. Society. Pasadena

16) Garner, K. L., et al. (2017). "Assessing the Risk of Engineered Nanomaterials in the Environment: Development and Application of the nanoFate Model." Environmental Science & Technology **51**(10): 5541-5551.

17) Giese, B., et al. (2018). "Risks, release and concentrations of engineered nanomaterial in the environment." Scientific Reports **8**(1): 1565.

18) Gottschalk, F., et al. (2009). "Modeled environmental concentrations of engineered nanomaterials (TiO2, ZnO, Ag, CNT, fullerenes) for different regions." Environmental Science & Technology **43**(24): 9216-9222.

19) Hassellöv, M., et al. (1999). "Determination of continuous size and trace element distribution of colloidal material in natural water by on-line coupling of flow field-flow fractionation with ICPMS." Analytical Chemistry **71**(16): 3497-3502.

20) Helland, A. and H. Kastenholz (2008). Development of nanotechnology in light of sustainability, Elsevier.

21) Kaegi, R., et al. (2013). "Fate and transformation of silver nanoparticles in urban wastewater systems." Water Research **47**(12): 3866-3877.

22) Keller, A. A., et al. (2014). "Release of engineered nanomaterials from personal care products throughout their life cycle." Journal of Nanoparticle Research **16**(7): 1-10.

23) Kim, B., et al. (2010). "Discovery and Characterization of Silver Sulfide Nanoparticles in Final Sewage Sludge Products." Environmental Science & Technology **44**(19): 7509-7514.

24) Kittler, S., et al. (2010). "Toxicity of Silver Nanoparticles Increases during Storage Because of Slow Dissolution under Release of Silver Ions." Chemistry of Materials **22**(16): 4548-4554.

25) Kraas, M., et al. (2017). "Long-term effects of sulfidized silver nanoparticles in sewage sludge on soil microflora." Environmental Toxicology and Chemistry **36**(12): 3305-3313.

26) Leonhardt, U. (2007). "Invisibility cup." Nature Photonics **1**(4): 207-208. Cloaking devices for visible light come a step closer to reality by combining the modern form of a Roman technology with ideas from ancient Greece.

27) Levard, C., et al. (2013). "Sulfidation of Silver Nanoparticles: Natural Antidote to Their Toxicity." Environmental Science & Technology **47**(23): 13440-13448.

28) Levard, C., et al. (2011). "Sulfidation Processes of PVP-Coated Silver Nanoparticles in Aqueous Solution: Impact on Dissolution Rate." Environmental Science & Technology **45**(12): 5260-5266.

29) Li, X., et al. (2010). "Dissolution-Accompanied Aggregation Kinetics of Silver Nanoparticles." Langmuir **26**(22): 16690-16698.

30) Liu, J. and R. H. Hurt (2010). "Ion Release Kinetics and Particle Persistence in Aqueous Nano-Silver Colloids." Environmental Science & Technology **44**(6): 2169-2175.

31) Markus, A., et al. (2015). "Modeling aggregation and sedimentation of nanoparticles in the aquatic environment." Science of the Total Environment **506**: 323-329.

32) Meesters, J. A. J., et al. (2014). "Multimedia Modeling of Engineered Nanoparticles with SimpleBox4nano: Model Definition and Evaluation." Environmental Science & Technology **48**(10): 5726-5736.

33) Miller, R. J., et al. (2012). "TiO2 Nanoparticles Are Phototoxic to Marine Phytoplankton." PLOS ONE **7**(1): e30321.

34) Mitrano, D., et al. (2012). "Field-flow-fractionation coupled with ICP-MS for the analysis of engineered nanoparticles in environmental samples."

35) Moore, M. N. (2006). "Do nanoparticles present ecotoxicological risks for the health of the aquatic environment?" Environment International **32**(8): 967-976.

36) Mueller, N. C. and B. Nowack (2008). "Exposure modeling of engineered nanoparticles in the environment." Environmental Science & Technology **42**(12): 4447-4453.

37) Nowack, B., et al. (2015). "Progress towards the validation of modeled environmental concentrations of engineered nanomaterials by analytical measurements." Environmental Science: Nano **2**(5): 421-428.

38) Praetorius, A., et al. (2014). "Heteroaggregation of titanium dioxide nanoparticles with model natural colloids under environmentally relevant conditions." Environmental science & technology **48**(18): 10690-10698.

39) Praetorius, A., et al. (2012). "Development of Environmental Fate Models for Engineered Nanoparticles—A Case Study of TiO2 Nanoparticles in the Rhine River." Environmental Science & Technology **46**(12): 6705-6713.

40) Praetorius, A., et al. (2012). "Development of Environmental Fate Models for Engineered Nanoparticles・A Case Study of TiO2 Nanoparticles in the Rhine River." Environmental science & technology **46**(12): 6705-6713.

41) Quik, J. T. K., et al. (2012). "Natural colloids are the dominant factor in the sedimentation of nanoparticles." Environmental Toxicology and Chemistry **31**(5): 1019-1022.

42) Sotiriou, G. A. and S. E. Pratsinis (2010). "Antibacterial Activity of Nanosilver Ions and Particles." Environmental Science & Technology **44**(14): 5649-5654.

43) Starnes, D. L., et al. (2016). "Distinct transcriptomic responses of Caenorhabditis elegans to pristine and sulfidized silver nanoparticles." Environmental Pollution **213**: 314-321.

44) Thill, A., et al. (2006). "Cytotoxicity of CeO2 nanoparticles for Escherichia coli. Physico-chemical insight of the cytotoxicity mechanism." Environmental science & technology **40**(19): 6151-6156.

45) Tiede, K., et al. (2008). "Detection and characterization of engineered nanoparticles in food and the environment." Food Additives and Contaminants **25**(7): 795-821.

46) Vaseashta, A. (2009). Nanomaterials nexus in environmental, human health, and sustainability. Silicon versus carbon, Springer**:** 105-118.

47) Warheit, D. B., et al. (2007). "Pulmonary toxicity study in rats with three forms of ultrafine-TiO2 particles: Differential responses related to surface properties." <u>Toxicology</u> **230**(1): 90-104.

48) Warheit, D. B., et al. (2006). "Pulmonary Instillation Studies with Nanoscale TiO2 Rods and Dots in Rats: Toxicity Is not Dependent upon Particle Size and Surface Area." <u>Toxicological Sciences</u> **91**(1): 227-236.

49) Wiesner, M. and J.-Y. Bottero (2007). <u>Environmental nanotechnology</u>, McGraw-Hill Professional Publishing New York.

50) Wiesner, M. R. and J.-Y. Bottero (2007). "Environmental nanotechnology." <u>Applications and Impacts of Nanomaterials</u>: 395-517.

51) Wilkinson, K. J. and J. R. Lead (2007). <u>Environmental colloids and particles: behaviour, separation and characterisation</u>, John Wiley & Sons.

52) Wimmer, A., et al. (2018). "New insights into the formation of silver-based nanoparticles under natural and semi-natural conditions." <u>Water Research</u> **141**: 227-234.

53) Yin, Y., et al. (2012). "Sunlight-induced reduction of ionic Ag and Au to metallic nanoparticles by dissolved organic matter." <u>ACS nano</u> **6**(9): 7910-7919.

54) Zhang, Y., et al. (2008). "Stability of commercial metal oxide nanoparticles in water." <u>Water Research</u> **42**(8–9): 2204-2212.

Chapter 2 . Literature Review

2.1 Use and Release of ENPs in the Aquatic Environment

The growth of engineered nanoparticles (ENP) applications in consumer products has exponentially increased in the past few decades owing to the unique properties they pose due to their small size (D'Mello et al. 2017, Sun et al. 2017). Forecasts predict a constant growth in ENP production (Giese et al. 2018). According to the Future Markets study in 2010, nAg and nTiO$_2$ had production rates between 360 - 450 and 83,500 - 88,000 metric tons per year, respectively (Keller and Lazareva 2013). nTiO$_2$ is one of the most widely used in ENP in industries and consumer care products (Chowdhury et al. 2013). They are used in coatings and paints (Mueller and Nowack 2008), cosmetics such as, sunscreen, soap, skin pigment, lipsticks (Rezaei and Mosaddeghi 2006), photocatalyst for decomposing organic waste and sterilizing bacteria and viruses in water and air treatment processes (Gupta and Tripathi 2011); and lastly, as charge collectors in dye-sensitized solar cell (Li et al. 2009). They are also used as photo-catalyst for electrolysis of water for the purpose of hydrogen fuel production (Gupta et al. 2016). Silver nanoparticles are used for their anti-microbial properties in consumer products. They are also used in cosmetics, paints and coatings, textiles, dietary supplements (Gottschalk et al. 2009).

The implications of ENP release into different environmental compartments is still not fully understood (Moore 2006). Several studies have progressed in assessing the exposure of ENPs using modeling tools by predicting environmental concentrations (Mueller and Nowack 2008, Gottschalk et al. 2009, Keller et al. 2013, Sun et al. 2017, Giese et al. 2018) . Most of these models follow the top down approaches (Nowack et al. 2015). The production of a certain mass of an ENP is first determined, followed by identifying its use in different types of products. Their release into environment during production, use and disposal is calculated and finally the mass that flows into

different environmental compartments is identified (Nowack et al. 2015). However, there are many fate processes that occur in the environment which are not captured by the models: aggregation, dissolution, re-precipitation, surface transformation. In the recent years, a few studies have developed process specific fate models (Wiesner and Bottero 2007, Praetorius et al. 2012, Barton et al. 2014, Meesters et al. 2014, Quik et al. 2014, Velzeboer et al. 2014, Markus et al. 2015, Garner et al. 2017, Ellis et al. 2018). Nevertheless, these models have to be validated using analytical data to ensure the model is capturing all possible aspects of the environmental system (Nowack et al. 2015).

One of the main sources of release of ENPs into the environment is via wastewater treatment plants (WWTP). An estimate of ENPs released from personal care products carried out by Keller et al showed that 93% of nanoparticles go into the wastewater treatment unit, 2.5% into landfills and 4.5% into direct water bodies (Keller et al. 2014). ENPs enter the wastewater plant due to the anthropogenic use and disposal of ENP containing products like cosmetics, fragrances, electronic products, clothing, and pharmaceuticals (Kaegi et al. 2011, Kaegi et al. 2013, Keller et al. 2014). ENPs may leach into groundwater or subsurface water from the treated sludge applied to agricultural land or from the discharged effluent (Choi et al. 2008, Fabrega et al. 2009, Brar et al. 2010, Fabrega et al. 2011).

2.2 Toxicity of ENPs

2.2.1 Toxicity of Silver Nanoparticles

Silver nanoparticles are most commonly used for their antimicrobial properties (Sharma et al. 2014). Toxicity of nAg in bacteria is caused by cell membrane damage due to the inactivation of important enzymes and oxidative stress caused due to the formation of reactive oxygen species (Durán et al. 2016). Navarro *et al*. demonstrated that Ag^+ from nAg was the main cause of toxicity

towards *Chlamydomonas reinhardtii* (Navarro et al. 2008). Similarly, a study by Kittler *et al*. also showed that Ag^+ released from nAg was the cause for an increase in toxicity, and release rates also depended on functionalization and temperature the nAg suspensions (Kittler et al. 2010). However, several mechanisms of nAg toxicity due to the particulate form has also been proposed previously (Li et al. 2008, Durán et al. 2016); (i) adhesion of nAg to the cell membrane altering membrane properties. (ii) nAg penetrating inside cells resulting in DNA damage (Li et al. 2008). The effect of nAg size on toxicity has been explored by Sotiriou *et al*. , their experiments revealed smaller nAg < 10 nm release more Ag^+ and as particle diameters increased , the release of Ag^+ decreased (Sotiriou and Pratsinis 2010). In a study determining the effect of nAg particles on *Pseudomonas putida* in biofilms, in the absence of Suwannee river fulvic acid (SRFA) an increased sloughing of the biofilm bacteria was observed (Fabrega et al. 2009). Effect of nAg on biofilm in moving bed biofilm reactors indicated adverse structural and functional response of biofilms based on exposure time and influent nAg concentration (Alizadeh et al. 2019). It is clear from literature that nAg can enter cells and pose toxicity in the particulate form and also generate a toxic potential by the release of Ag^+ ions (Durán et al. 2016).

2.2.2 Toxicity of Titanium Dioxide Nanoparticles

Oxidative stress exhibited by photoactive $nTiO_2$ is the probable cause of toxicity in microorganisms (Miller et al. 2012). $nTiO_2$ caused phototoxicity in marine phytoplankton due to an increase in oxidative stress under the influence of UV light (Miller et al. 2012). In a toxicity study done in rats and mice, inhalation of ultrafine TiO_2 caused pulmonary inflammation in rats; however, the effects are strongly dependent on the crystal structure and the composition of $nTiO_2$ (Warheit et al. 2007). Size of the nanoparticles did not have an impact on the acute lung toxicity (Warheit et al. 2006). Oxidative DNA damage was observed in human bronchial epithelial cell

line caused due to 10 and 20 nm nTiO$_2$ (Gurr et al. 2005). In a chronic exposure (21 days) study to *Daphnia magna*, 21 nm sized (mean diameter) nTiO$_2$ indicated mortality, growth retardation and reproductive defects. The toxicity effect was concentration dependent; at concentrations as 0.1 mg/L affected reproduction. At 0.5 mg/L, both growth and reproduction were inhibited (Zhu et al. 2010).

2.3 Fate of nAg in aquatic environments

Upon entering the aquatic environment, ENPs may undergo a variety of processes such as; aggregation (agglomeration) (Kaegi et al. 2013, Markus et al. 2015), dissolution (Brar et al. 2010, Kaegi et al. 2013) and surface chemical transformation. Agglomerated nanoparticles are usually held together by weaker van der Waals forces and aggregates are held together by hard bonds due to sintering (Jiang et al. 2009). However, in the current chapter, the term aggregation in this chapter broadly encompasses both agglomeration as well as aggregation. Recent studies have shown that dissolved organic matter (DOM), ionic strength, type of electrolyte, aggregation state, pH can impact the colloidal stability of nanoparticles in aqueous solutions (Benn and Westerhoff 2008, Jiang et al. 2009, Badawy et al. 2010). For example, studies have shown that DOM has a stabilizing effect on ENPs in aqueous media mainly through steric stabilization (Chen et al. 2006, Diegoli et al. 2008, Domingos et al. 2009, Zhou and Keller 2010, Bian et al. 2011). Decreased rates of dissolution and aggregation of ENPs in the presence of DOM have also been established previously (Pelley and Tufenkji 2008, Fabrega et al. 2009, Li et al. 2010, Fabrega et al. 2011) .
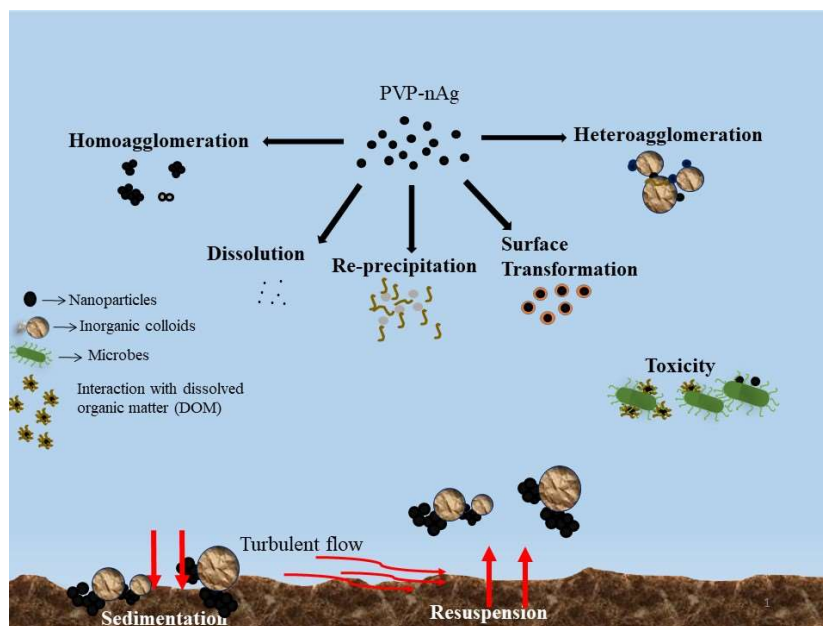
Figure 2.1: *Different fate processes of nAg in natural surface waters*

The enormous dilution ENPs undergo in aquatic environments leads to the presence of ENPs at significantly lower concentrations compared to suspended particulate matter (SPM) or colloidal particles, which increases the probability of nanoparticles colliding with these colloidal particles. Since aggregation is one of the primary controls on both transport and toxicity of ENPs in the aquatic environment, it is very important to study how naturally occurring colloids can interact with engineered nanoparticles and influence their aggregation state. Understanding the aggregation and removal of commercial nanoparticles in aquatic environments is crucial in assessing their fate in the environment and their potential risks to humans (Zhang et al. 2008).

Recently, a few studies have determined the fate of nAg (aggregation, sedimentation, dissolution) in aquatic environments by studying the effect of seasonal variations, sunlight and organic coatings. Total silver concentrations were measured by inductively coupled plasma optical emission spectrometer (ICP-OES) (Li and Lenhart 2012), high resolution – inductively coupled plasma mass spectrometer (HR-ICPMS) (Ilona et al. 2014, Quik et al. 2014) and flame AAS (Ellis

et al. 2018) . A study by Li *et al.* investigated aggregation and dissolution of bare and coated nAg (Tween 80 and citrate) in natural lake water at an initial concentration of 1.5 mg/L. Experiments were performed in the presence and absence of sunlight on an orbital shaker at 30 rpm. Total and dissolved silver concentrations were measured using ICP-OES and sizes were measured using DLS. Their results indicated that sunlight did not have any particular influence on the release of dissolved silver. However, Tween coated nAg released most of the silver particulate mass within six hours and therefore started decreasing in diameter due to dissolution. However, there was no aggregation in tween systems. Other studies have also studied the effect of organic coatings such as polyvinylpyrrolidone (PVP) and citrate on nAg colloidal stability (Liu and Hurt 2010, Huynh and Chen 2011, Ma et al. 2012). PVP-nAg was determined to be more stable than citrate-nAg in aquatic samples (Huynh and Chen 2011, Ellis et al. 2018). Furtado *et al*. determined dissolution, aggregation, surface modification of nAg in lake water mesocosms and used multiple techniques to determine the fate of nAg. They suggested that all the dissolved silver complexed with organic matter (thiol containing ligands), which made them less bioavailable. Ellis *et al*. used column experiments to model the behavior of nAg at different depths under seasonal changes. PVP-nAg remained colloidally stable whereas citrate nAg showed to rapid aggregation, sedimentation, dissolution and re-precipitation; their transport in the water column was attributed to both diffusion and sedimentation. In winter with citrate nAg, they found higher concentrations at lower depths compared to higher depths, indicating aggregation and sedimentation. They also observed re-precipitation of nAg in their systems, however it was not quantified.

2.3.1 Dissolution and Re-precipitation of nAg in Surface Waters

In the recent years, there has been increased research devoted to physical and chemical transformations of nAg in the aquatic environment (Li et al. 2010, Akaighe et al. 2011, Delay et

al. 2011, Levard et al. 2011, Li and Lenhart 2012, Adegboyega et al. 2013, Dobias and Bernier-Latmani 2013). Dissolution and natural formation or re-precipitation of nAg are important transformation process of nAg in the aquatic environment. Dissolution of nAg in the presence of oxygen has already been widely studied (Li et al. 2010, Liu and Hurt 2010, Azodi et al. 2016). Dissolved silver ions (Ag^+) found in natural waters is either due to dissolution of particulate nAg (Dobias and Bernier-Latmani 2013) or release from industrial effluents (Eckelman and Graedel 2007). Ion release from nAg is said to occur in the presence of protons and dissolved oxygen. In the absence of any other reductants and oxidants, the reaction is predicted to proceed in the following manner (equation (2.1)) (Liu and Hurt 2010).

$$2Ag_{(s)} + \frac{1}{2}O_{2(aq)} + 2H^+_{(aq)} \leftrightarrow 2Ag^+_{(aq)} + H_2O_{(l)} \tag{2.1}$$
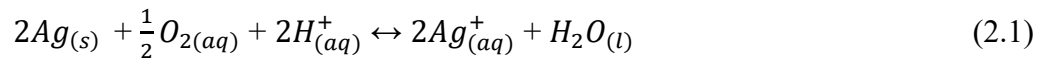
Dissolution rate of nAg increases with decrease in size (Dobias and Bernier-Latmani 2013) and increase in temperature (Liu and Hurt 2010) and the kinetics of Ag^+ release from nAg follows first order kinetics (Sharma et al. 2014). However, in the presence of dissolved organic carbon at 20 mg/L, dissolution of nAg (citrate, PVP and Tannic acid) was negligible within 24 hours (Mitrano et al. 2014). In heterogeneous natural waters, nAg dissolution does not often reach completion due to other processes like aggregation, reduction of Ag^+ to Ag^0 in the presence of natural organic matter (Li and Lenhart 2012).

Natural formation of nAg from Ag^+ in natural waters is associated with the reduction of Ag^+ to nAg by different fractions of natural organic matter (Akaighe et al. 2011, Adegboyega et al. 2013). Initial studies, which investigated the re-precipitation of nAg from dissolved Ag, used humic acid and fulvic acid as natural organic matter sources. For example, Akaighe *et al.* demonstrated that at ambient room temperatures, nAg particles were formed from silver nitrate (10 µM to 1 mM) in

the presence of Suwannee River HA and sediment HA's (Akaighe et al. 2011). In another study, re-precipitation of nAg from silver nitrate was observed in the presence of Suwannee River FA (Adegboyega et al. 2013). It is important to note that both these studies were done under irradiation of UV light. A study by Hou *et al*. demonstrated that nAg formation requires both light and natural organic matter (NOM) (Hou et al. 2013). However, more recent studies have shown that re-precipitation of nAg is independent of sunlight irradiation. At a dissolved Ag concentration at 50 ng/L, light irradiation was not necessary to form nAg (Wimmer et al. 2018) and they attributed re-precipitation to low molecular weight quinones which are usually present in natural organic matter . An interesting observation is that in the studies where light irradiation was deemed necessary for re-precipitation, initial Ag^+ concentrations were considerably higher (mg/L range). Therefore, light is not an important factor for nAg formation at environmentally relevant concentrations. A previous study done in our lab also showed re-precipitation of nAg from dissolved Ag in wastewater effluent both in the absence and presence of light (Azodi et al. 2016).

2.4 Mathematical description of Environmental Fate Processes

Determining fate and behavior of ENPs at environmentally relevant concentrations is extremely important in natural water systems to determine their bioavailability and toxicity. As seen in the previous section, ENPs can undergo a variety of processes upon entering the aquatic environment. While exposure models provide us with predicted environmental concentrations, transformation processes of ENPs that ultimately affect their fate in the aquatic environment are not captured. Each of the environmental process shown in Figure 2.1 will have an effect on the fate of ENPs in the aquatic environment. Different studies have developed equations to quantify each of these processes, which are discussed more in detail.

2.4.1 Sedimentation

There have been many suggested equations to calculate sedimentation in aquatic systems. The first one is the classic Stokes settling velocity:

$$U = \frac{g*(\rho_p - \rho_f)*d^2}{18*\mu} \tag{2.2}$$

Where g is acceleration due to gravity (9.81 m/s^2), ρ_p = density of particles, ρ_f = density of medium/fluid, d = diameter of particles, µ = viscosity of medium (kg.m^{-1}.s^{-1})

Using this equation, sedimentation velocity can be calculated for colloids as well as nanoparticles suspended in aquatic systems. Equation (2.2) in many studies to calculate the settling velocity (Quik et al. 2014, Ellis et al. 2018). The second method for estimating sedimentation is by measuring the decrease in concentration of NP's over time, where sedimentation a first order process.

$$\frac{dc}{dt} = -\frac{Vs}{h}*C \tag{2.3}$$

C = concentration of non-settled NPs, v_s = first order rate constant of sedimentation (m/day), h = height of the sedimentation column. Equation (2.3) is integrated with integration limits C_0 at t = 0 and C_t at t to obtain the following:

$$c_t = c_0 * e^{-\frac{Vs}{h}t} \tag{2.4}$$

Plotting experimental data to equation (2.4) and fitting the data using non-linear regression will provide a value for V_s. Several studies have used the above equation to determine sedimentation rates by measuring a change in concentration of NP over time (Keller et al. 2010, Brunelli et al.

2013, Markus et al. 2015). A variation of the above equation was derived by Quik *et al.*, 2012 (Quik et al. 2012) to fit their experimental sedimentation date in the form of semi-empirical equation which accounted for the non-settling concentration at the end of their experiment (14 days).

$$C_t = (C_0 - C_{ns}) * e^{\left(-\frac{Vs}{h}t\right)} + C_{ns} \tag{2.5}$$

Lastly, a dissolution term was included in equation (2.3) by Quik et al, 2014 to account for any loss in mass concentration due to dissolution (Quik et al. 2014).

$$\frac{dc}{dt} = -\left(\frac{Vs}{h} + k_{diss}\right) * c \tag{2.6}$$

Classical Smoluchowski equation

Equation (2.7) is the classical kinetic Smoluchowski equation to describe aggregation (Wiesner and Bottero 2007).

$$\frac{dn_k}{dt} = \frac{1}{2}\alpha \sum_{i+j \to k} \beta(i,j)n_i n_j - \alpha n_k \sum_i \beta(i,k)n_i \tag{2.7}$$

Here, n_k is the number concentration of particles/aggregates size class k, α is attachment efficiency, $\beta(i,j)$ is collision frequency between particles or aggregates of classes i and j/ i and k and n_i/n_j is number concentration of particles/aggregate size class i or j. The first positive term represent the formation of aggregates/particles of size class k and the second negative term represents the loss of aggregates/particles of size class k. Collision frequencies can be described by three collision mechanisms: Brownian diffusion, fluid motion and differential settling. Collision frequency varies as a function of the diameters of nano- and background particles, mixing conditions, temperature, fluid viscosity, and particle densities (Barton et al. 2014).

In a coagulation study by Farley and Morel, 1986, the Smoluchowski equation was used with a sedimentation term incorporated which also causes a decrease in concentration of size class k and is described equation (2.8).

$$\frac{dn_k}{dt} = \frac{1}{2}\alpha \sum_{i+j \to k} \beta(i,j)n_i\, n_j\ -\ \alpha n_k \sum_i \beta(i,k)n_i - n_k \frac{Vs,k}{h} \qquad (2.8)$$

2.4.2 Homoaggregation

Homoaggregation under different aquatic chemistries has been widely studied (Petosa et al. 2010, Chowdhury et al. 2013, Zhou et al. 2013, Zhu et al. 2014). The perikinetic aggregation rate constant or Brownian diffusion dominated aggregation for spherical nanoparticles is given by (Petosa et al. 2010):

$$k_{ij} = \frac{2k_bT(a_i+a_j)^2}{3\mu a_i a_j}\ (\text{m}^3/\text{s}) \qquad (2.9)$$

Where k_b is Boltzmann constant = 1.3805×10^{-23} J/K, T = absolute temperature (K), a_i and a_j = particle sizes (nm), μ = viscosity of fluid (kg.m^{-1}.s^{-1}). Equation (2.9) is a very general description of aggregation rate under standard conditions. Under real environmental conditions, aquatic chemistries play a very important role in determining aggregation rates.

Under favorable aggregation conditions, in the absence of repulsive energy barriers, aggregation of nanoparticles is said to diffusion limited. In order to experimentally determine aggregation constants, attachment efficiency is calculated (Chen and Elimelech 2006). Essentially, is defined as the ratio of the coagulation rate in the presence of an energy barrier to that in the absence of an energy barrier (Zhu et al. 2014).

$$\alpha = \frac{k}{k_{fast}} = \frac{\frac{d_{rh}}{dt}_{t \to 0}}{\frac{d_{rh}}{dt}_{t \to 0,fast}} \qquad (2.10)$$

Aggregation studies that used equation (2.10) to determine aggregation rates with attachment efficiencies, tracked change in diameter over time. One of the drawbacks of this method is to use high initial concentrations of NPs to measure using dynamic light scattering. For example, homoaggregation studies done with $nTiO_2$ have used initial concentrations such as 10 mg/L (Praetorius et al. 2014), 20 mg/L (Zhu et al. 2014), 10-100 mg/L (Adam et al. 2016), nAg used mg/L range as well (Badawy et al. 2010, Liu et al. 2015, Wang et al. 2015). Such high mg/L concentrations are not very representative of environmentally relevant conditions.

Based on the study by Farley and Morel, 1986, a few important assumptions have been stated to simplify the Smoluchowski equation to determine aggregation. For any given system, one coagulation mechanism is dominant for a particle size (Brownian: smallest sizes, shear force: intermediate sizes and differential settling: largest sizes). This implies that in a monodisperse system, collision between single sizes are very important. In an extreme case, aggregation is considered as a rate-limiting step for sedimentation. When we are looking at the change in concentration of one type (size) of NP, then the first term of equation (2.8) which represents growth of that size of NP can be removed. The second term of the homoaggregation equation represents the loss of size class of NP, integrating and converting the equation in the form of concentrations; the loss of NPs due to homoaggregation is represented as:

$$\frac{dC}{dt} = -\alpha \beta C^n \tag{2.11}$$

Depending on the number of interactions (doublet, triplet etc) and the kinetics of homoaggregation, the value of n changes. Quik *et al.*, 2014 suggested that equation (2.11) can be described as a pseudo first order reaction when kinetics of collision occur between large aggregates and primary particles (Quik et al. 2014).

2.4.3 Heteroaggregation

In natural water systems, the presence of colloids play a very important role in fate of NPs. The collision occurring between natural colloids and NPs leading to formation of aggregates is defined as heteroaggregation. This phenomenon is another process that contributes to a decrease in un-aggregated NP over time. Heteroaggregation can be represented by the following equation:

$$\frac{dN_{NP}}{dt} = -\alpha\beta N_{NP}N_{NC} \tag{2.12}$$

Where, α is attachment efficiency, β is collision frequency, N_{NP} is the ENP number concentration and N_{NC} is the natural colloid concentration (NP/mL). In most studies, mass concentrations are used as a parameter to estimate aggregation. However, according to Dale *et al.*, 2015, error can arise while converting between number concentrations and mass concentrations as sizes are changing over time (Dale et al. 2015). Major drawbacks in mass balance-based models in the inability to track or describe size-related processes such as change in particle size distribution or effect of dissolution (if at all, any).

A mass based version of equation (2.13) is given by:

$$\frac{dC_{NP}}{dt} = -k_{he}\ C_{NP}C_{NC} \tag{2.13}$$

Quik *et al.* (2014) showed that the number concentration balance model for aggregation and sedimentation could be reliably replaced with a mass balance equivalent that follows a first-order loss rate to a non-aggregated fraction. Further, the model by Quik *et al.* (2014) was derived mainly from Smoluchowski equation based on a series of assumptions similar to Farley and Morel, the above equation is simplified.

$$\frac{dn_k}{dt} = \frac{1}{2}\alpha \sum_{i+j \to k}\beta(i,j)n_i\ n_j\ - \alpha n_k \sum_i \beta(i,k)n_i - \ \alpha_{NC,k}\ \beta_{NC,k}\ N_{NC}\ n_k - \frac{V_{s,k}}{h}n_k \tag{2.14}$$

Where, α is attachment efficiency, β is collision frequency, n_k is the ENP number concentration and N_{NC} is the natural colloid concentration (NP/mL), v_s = first order rate constant of sedimentation (m/day), h = height of the sedimentation column. Aggregation is the rate-limiting step for removal of NPs from aquatic microcosms as NP's aggregated have to be large enough to settle down. With these assumptions, the settling term in the above equation can be removed. Summation terms in the above equation can be simplified by replacing them with apparent critical collision behavior for sedimentation. The collisions occurring will not yet lead to homo or hetero-aggregates large enough to settle as represented by the above equation. However, at a certain time, collisions will lead to critical limit after which they start to settle. Now at this point, the system is very polydisperse, hence all the single terms are represented as apparent parameters reflecting the average properties at the onset of settling. NP concentration changing in overlying water is determined by aggregation due to settling only and not due to progressively growing to larger aggregates.

$$C_{NP,crit}\ (t) =\ C_{0,crit}\ e^{-At+B(e^{-D}\ -1)} \tag{2.15}$$

$$A = -k_{homo} \quad B = \frac{k_{het}C_{0,NC}h}{V_{S,NC}} \quad D = \frac{V_{S,NC}}{h}$$

2.5 An Example of Changes to the Surface Composition of ENPs: Sulfidation of nAg

Silver nanoparticles released from consumer products are expected to undergo transformation upon entering the aquatic environment. Predictions indicate that majority of nAg are expected to end up in WWTPs (Gottschalk et al. 2009, Keller et al. 2013). The most common surface transformation process of nAg in natural and wastewater is interaction with bisulfides to produce Ag_2S (Levard et al. 2011). nAg and Ag^+ have been shown to form strong insoluble sulfide complexes (Collin et al. 2016). Ag_2S has a very low solubility constant (K_{sp}= 5.9 ×10^{-51}) (Collin

et al. 2016). Several studies have been done to determine mechanism of nAg sulfidation (Liu et al. 2011, Thalmann et al. 2016). Liu e*t al*. proposed two possible mechanisms for sulfidation of Ag ; oxidative dissolution of nAg followed by sulfide precipitation (indirect sulfidation) and direct conversion of nAg to nAg$_2$S via solid-fluid reaction (Liu et al. 2011). They demonstrated that sulfidation of nAg occurs primarily via direct conversion as indirect sulfidation is limited by available dissolved Ag concentration. However, they suggested indirect sulfidation would occur at lower sulfide concentrations. In the presence of oxygen and at near neutral pH systems, the following reactions were proposed for sulfidation of nAg.

$$4Ag + O_2 + 2H_2S \rightarrow 2Ag_2S + 2H_2O \tag{2.16}$$

$$4Ag + O_2 + 2HS^- \rightarrow 2Ag_2S + 2OH^- \tag{2.17}$$
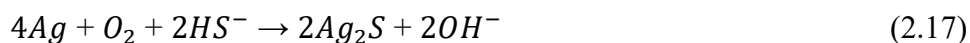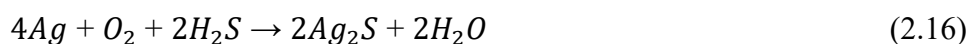
Levard *et al.*, showed that a low S/Ag ratio of 0.019 reduced dissolution by a factor of seven (Levard et al. 2011). However, recent studies have shown that sulfidated nAg may still be toxic due to incomplete sulfidation. For example, Kraas *et al*. reported that nAg (62 ± 47 nm, Tween 20) sulfidized in soil ecosystems were a source of Ag$^+$ to soil microorganisms after a 140 day incubation period(Kraas et al. 2017). Sulfidated PVP-nAg (S/Ag molar ratio of 2) had a decreased, but still measurable toxicity to *C. elegans* compared to pristine PVP-nAg with an approximate hydrodynamic diameter of 79.6 nm due to a decrease in release of free Ag ions (Starnes et al. 2016).

The presence of dissolved organic matter can influence the sulfidation nAg in different ways. For example, DOM enhances the colloidal stability of nanoparticles in aquatic systems due to steric stabilization (Fabrega et al. 2009, Baalousha et al. 2013, Philippe and Schaumann 2014, Sharma

et al. 2014). Studies investigating the effect of sulfides on nAg transformation have shown overall sulfidation rates increasing with a decrease in size and increase in HA concentrations (Thalmann et al. 2016). In another study, Suwanee river and Pahokee peat fulvic acid (PLFA) decreased release of dissolved Ag from sulfidized nAg, while, pony lake fulvic acid increased dissolution (Collin et al. 2016). Dissolved organic matter (DOM) is known to have a stabilizing effect on ENPs in aqueous media mainly through steric stabilization (Chen et al. 2006, Diegoli et al. 2008, Domingos et al. 2009, Zhou and Keller 2010, Bian et al. 2011). Decreased rates of dissolution and aggregation of ENPs in the presence of DOM have also been established previously (Pelley and Tufenkji 2008, Fabrega et al. 2009, Li et al. 2010, Fabrega et al. 2011). Baalousha *et al*., showed that Suwannee river fulvic acid (SRFA) diminished dissolution of Tween 20-coated nAg at low sulfide concentrations and reduced aggregation of citrate-coated nAg in the presence of sodium sulfide (Baalousha et al. 2015).

2.6 Analytical Techniques for Detection and Characterization of ENPs

2.6.1 AF4-MALS

The theory of Field Flow Fractionation (FFF) was first described by Giddings (Giddings et al. 1977, Giddings 1984, Giddings 1993, Giddings 1995). FFF is a hydrodynamic fractionation technique used to separate macromolecules, colloids, nano- and microparticles according to size. The FFF colloidal separation occurs under the effect of an applied field perpendicular to the main parabolic flow of the mobile phase/carrier fluid. FFF separation is not based on interaction between analytes and stationary phase but on the interaction of the analytes with the field in a non-uniform flow. In Asymmetrical Flow Field Flow Fractionation (AF4) the crossflow is applied through a semi-permeable channel covered by a membrane characterized by variable cut-offs and materials. The main difference between symmetrical and asymmetrical channel is that in AF4, the crossflow

is created by a difference in carrier in and outflow volumetric flow rate instead of a secondary pump directing the crossflow via a top-channel frit into the channel. Fractionated particles can be analysed on-line by coupling with UV/vis or differential refractive index (dRI) detectors as universal concentration source detectors for multi angle light scattering (MALS) which provides information about radius of gyration and molecular weights of the particles.
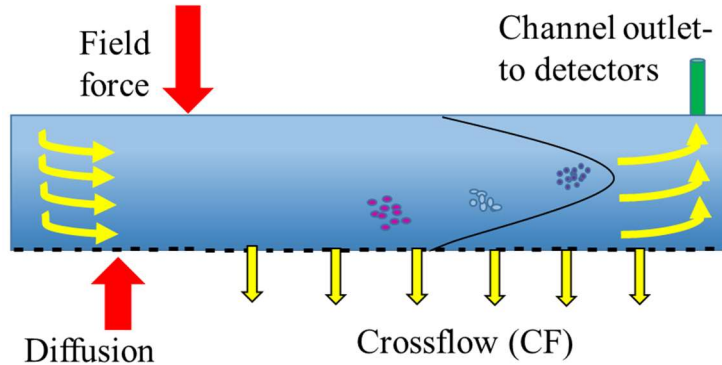
Figure 2.2: Schematic of AF4 with a semi-permeable membrane at the bottom of the channel and depiction of a parabolic flow profile with particles separated according to size

The particle hydrodynamic diameters can be calculated by using equations from the FFF theory given by equation (2.19):

$$t_r = \frac{\pi * d * w^2 * \eta}{2 * k * T} * \frac{V_{cross}}{V_{chann}} \tag{2.18}$$

d = stokes diameter, w = channel thickness, k = Boltzmann constant, η = Viscosity of solvent, T = Absolute temperature, V_{cross}= Cross flow, $V_{channel}$ = Channel flow, t_r = Retention time

The most important parameters that lead to effective fractionation is determined by the nature of membrane, crossflow rates, and composition of carrier fluid. These parameters influence particle-

membrane interaction which in turn has an effect on fractionation efficiency (Dubascoux et al. 2008). The quality of separation can be determined by sample recovery, minimal height of void peak, reproducibility of fractogram and the absence of overlap between the void peak and fractionated nanoparticle peak (retention ratio) (Baalousha et al. 2011). The most commonly used membranes for the separation of nanoparticles are Regenerated Cellulose (RC), Polyvinylidene di-Fluoride (PVDF), Polyethersulfone (PES) of either 5, 10 or 30-kDa cut-offs (Kammer et al. 2005, Kammer et al. 2011, Ulrich et al. 2012, Geiss et al. 2013). PES membranes are found to be relatively hydrophobic and have a high negative surface charge, while RC membranes are more hydrophilic and have lesser negative charge. The attraction caused between the particles and membrane can be accounted by DLVO theory (Gigault and Hackley 2013). van der waals and electrostatic forces are responsible for particle-membrane interactions in an AF4 channel. The model that is used for calculating the DLVO forces is the sphere-plate model which can be found elsewhere (Ulrich et al. 2012). The optimum crossflow rate is very important as this determines the extent of fractionation. The most common carrier fluids used are low concentrations of an anionic surfactant such as sodium dodecyl sulfate with a salt such as ammonium nitrate or FL-70 with an antibacterial agent such as sodium azide to avoid microbial growth on the membrane (Hagendorfer et al. 2012, Mitrano et al. 2012, Schachermeyer et al. 2012, Ulrich et al. 2012).

The hyphenation of AF4 with light scattering detectors like MALS and DLS provides information about the particle hydrodynamic size, root mean square, average weighted molecular weight, aggregation state, distribution and the conformation of the particle. MALS uses the first principle, in the sense that the measurements are absolute; purely dependent on the extent of scattered light. It is highly sensitive to changes in mass. Hence, it is an excellent method for detecting the extent of aggregation. The Quasi-elastic Light Scattering (QLES or DLS) determines the hydrodynamic

radius of the sample; inclusive of the hydration layer or any branching if present. Fractionation of heterogeneous samples by FFF helps overcome the disadvantage of polydispersity of samples when analysed with the DLS. This method has been used previously for the characterization of silver nanoparticles in aqueous media (Hagendorfer et al. 2012, Gigault and Hackley 2013).

In the flat channel, separation occurs due to two perpendicular hydrodynamic forces acting on the polydisperse sample which is fractionated based on the diffusion coefficient. The smaller particles are less influenced by the crossflow that leads to their higher position in the parabolic flow and hence elute out first. The combination of the two forces applied eventually results in the separation of the polydispere sample according to their respective diffusion coefficients (Stephan Elsenberg 2012).

For particles of sizes >1 μm (including bacterial cells), diffusion is not significant. Major forces acting are the hydrodynamic lift forces, which act to move larger particles further away from the accumulation wall, termed hyperlayer or steric mode. In the hyperlayer mode, larger particles elute out first followed by the smaller particles. The diameter at which this transition occurs can be as low as 500 nm (Reschiglian et al. 2002).

Many studies have characterized metallic nanoparticles on-line and off-line with AF4-ICPMS (Hassellöv et al. 1999, Amarasiriwardena et al. 2001, Bouby et al. 2008, Dubascoux et al. 2008, Dubascoux et al. 2010, Schmidt et al. 2011, Hoque et al. 2012). In a study by Poda *et al*., the lowest detectable signals for a silver nanoparticle mixture was found to be 6.7 μg/L (Poda et al. 2011). Environmental ultrafine colloids of sizes < 5nm were characterized by FFF-UV/vis-atomic force microscopy (Baalousha and Lead 2007). Humic acid of average size 3.2 nm and clay colloids in the size range of 30-200 nm were successfully characterized using AF4-ICPMS (Bouby et al. 2008). AF4-UV/vis-ICPMS has been used to study the effect of nAg and dissolved species of

silver in culture media and cells used in cytotoxicity tests (Bolea et al. 2014). AF4-UV/vis-MALS-ICPMS has been successfully used for the separation and analysis of various complex matrices samples containing natural colloids in aqueous samples, sub-surface water samples and even food matrices (Purawatt et al. 2007, Tiede et al. 2008, Loeschner et al. 2013, Grombe et al. 2014).

2.6.2 spICP-MS

The concept and methodology of single particle ICP-MS (spICP-MS) was first developed by Degueldre *et al*. for the analysis of colloids (Degueldre and Favarger 2003, Degueldre and Favarger 2004). Over the years, spICP-MS has been developed to analyse ENPs in complex aqueous matrices (Montano et al. 2014). Laborda *et al.* demonstrated the potential of spICP-MS to measure and characterize ENPs (Laborda et al. 2011). spICP-MS now has the ability to detect ENPs in the ng/L range depending on the element of interest and is capable of providing particle size distributions and concentrations while quantifying and differentiating between dissolved and particulate fractions (Lee et al. 2014, Montano et al. 2014). Liquid samples are first passed through the nebulizer where they are aerosolized into small droplets. These droplets reach the plasma, which is operated at a high temperature and are ionized here. Particle events occur as cluster of ions, which is represented as a transient peak or pulse signal, whereas, dissolved background ions appear as continuous baseline signals. Ionized samples reach the quadrupole ion deflector where only specified mass to charge ratios are allowed to pass through. The frequency of events directly translates to the number of particles or particle concentrations and the particle intensity (peak area) is the diameter of the particle. The quantification of ENP size and concentration is dependent on another parameter; nebulization or transport efficiency (TE) (Degueldre and Favarger 2004, Laborda et al. 2013). The importance of TE in spICP-MS arises from the difference in the transport of dissolved ions compared to particles. TE accounts for the volume loss during transport of the

aspirated samples through the spray chamber. Previous studies have used gold nanoparticles of 55-60 nm to determine the TE value (Hineman and Stephan 2014).

In the recent years, spICP-MS has been used for analysing ENPs in complex matrices. For example, Dan *et al*. develop a method to characterize TiO_2 nanoparticles used in different sunscreens (Dan et al. 2015). Detection of nAg in wastewater effluent using spICP-MS has been done by several studies (Mitrano et al. 2012, Azodi et al. 2016, Azimzada et al. 2017). Recent improvements in the spICP-MS technique have resulted in enabling dwell-times in the microsecond range (Hineman and Stephan 2014, Montano et al. 2014) enabling analysis of ENPs at lower concentrations, which are environmentally relevant. Typically, signal from a single nanoparticle (NP) event is in the microsecond range (Engelhard 2011). Therefore, working with the right dwell times is of high significance in ENP analysis, as using high dwell times (milli-second range) can cause signals of individual particles to overlap leading to larger instrument responses causing lower particle counting and, thereby affecting particle mass and number concentrations (Hineman and Stephan 2014).

Finally, in the present thesis, nAg, nAu, $nTiO_2$ are used for different purposes in the field of environmental nanotechnology. In order to understand the fate and transformation of ENPs such as nAg in aquatic systems, novel detection techniques such as spICP-MS are required to characterize the ENP samples at environmentally relevant concentrations. This thesis aims to understand the fate and transformation of nAg in the aquatic environment. This would include agglomeration processes, dissolution and sulfidation of nAg. To improve the detection of nanoparticles in the smaller size range, 30 nm sized nAu particles were used and compared with conventionally used 55 - 60 nm for particle sizing and counting efficiencies. Finally, the methods developed using AF4 and spICP-MS were used to improve detection of $nTiO_2$ which has

limitations in the spICP-MS, as the most abundant isotope ^{48}Ti (73.7%) has interferences with polyatomic compounds (PO, NO2, ArC, CCl, SO) and ^{48}Ca (0.19%).

2.7 References

1) Adam, V., et al. (2016). "Aggregation behaviour of TiO2 nanoparticles in natural river water." Journal of Nanoparticle Research **18**(1): 13.

2) Adegboyega, N. F., et al. (2013). "Interactions of Aqueous Ag+ with Fulvic Acids: Mechanisms of Silver Nanoparticle Formation and Investigation of Stability." Environmental Science & Technology **47**(2): 757-764.

3) Akaighe, N., et al. (2011). "Humic Acid-Induced Silver Nanoparticle Formation Under Environmentally Relevant Conditions." Environmental Science & Technology **45**(9): 3895-3901.

4) Alizadeh, S., et al. (2019). "Fate and inhibitory effect of silver nanoparticles in high rate moving bed biofilm reactors." Science of The Total Environment **647**: 1199-1210.

5) Amarasiriwardena, D., et al. (2001). "Trace elemental distribution in soil and compost-derived humic acid molecular fractions and colloidal organic matter in municipal wastewater by flow field-flow fractionation-inductively coupled plasma mass spectrometry (flow FFF-ICP-MS) Presented at the 2001 European Winter Conference on Plasma Spectrochemistry, Lillehammer, Norway, February 4–8, 2001." Journal of Analytical Atomic Spectrometry **16**(9): 978-986.

6) Azimzada, A., et al. (2017). "Transformations of silver nanoparticles in wastewater effluents: links to Ag bioavailability." Environmental Science: Nano **4**(6): 1339-1349.

7) Azodi, M., et al. (2016). "Dissolution Behavior of Silver Nanoparticles and Formation of Secondary Silver Nanoparticles in Municipal Wastewater by Single-Particle ICP-MS." Environmental Science & Technology **50**(24): 13318-13327.

8) Baalousha, M., et al. (2015). "Transformations of citrate and Tween coated silver nanoparticles reacted with Na2S." Science of the Total Environment **502**: 344-353.

9) Baalousha, M. and J. Lead (2007). "Characterization of natural aquatic colloids (< 5 nm) by flow-field flow fractionation and atomic force microscopy." Environmental science & technology **41**(4): 1111-1117.

10) Baalousha, M., et al. (2013). "Effect of monovalent and divalent cations, anions and fulvic acid on aggregation of citrate-coated silver nanoparticles." Science of the Total Environment **454-455**: 119-131.

11) Baalousha, M., et al. (2011). "Flow field-flow fractionation for the analysis and characterization of natural colloids and manufactured nanoparticles in environmental systems: a critical review." Journal of Chromatography A **1218**(27): 4078-4103.

12) Badawy, A. M. E., et al. (2010). "Impact of Environmental Conditions (pH, Ionic Strength, and Electrolyte Type) on the Surface Charge and Aggregation of Silver Nanoparticles Suspensions." Environmental Science & Technology **44**(4): 1260-1266.

13) Barton, L. E., et al. (2014). "Theory and methodology for determining nanoparticle affinity for heteroaggregation in environmental matrices using batch measurements." Environmental Engineering Science **31**(7): 421-427.

14) Benn, T. M. and P. Westerhoff (2008). "Nanoparticle Silver Released into Water from Commercially Available Sock Fabrics." Environmental science & technology **42**(11): 4133-4139.

15) Bian, S.-W., et al. (2011). "Aggregation and Dissolution of 4 nm ZnO Nanoparticles in Aqueous Environments: Influence of pH, Ionic Strength, Size, and Adsorption of Humic Acid." Langmuir **27**(10): 6059-6068.

16) Bolea, E., et al. (2014). "Detection and characterization of silver nanoparticles and dissolved species of silver in culture medium and cells by AsFlFFF-UV-Vis-ICPMS: application to nanotoxicity tests." Analyst **139**(5): 914-922.

17) Bouby, M., et al. (2008). "Application of asymmetric flow field-flow fractionation (AsFlFFF) coupled to inductively coupled plasma mass spectrometry (ICPMS) to the quantitative characterization of natural colloids and synthetic nanoparticles." Analytical and bioanalytical chemistry **392**(7-8): 1447-1457.

18) Brar, S. K., et al. (2010). "Engineered nanoparticles in wastewater and wastewater sludge – Evidence and impacts." Waste Management **30**(3): 504-520.

19) Brunelli, A., et al. (2013). "Agglomeration and sedimentation of titanium dioxide nanoparticles (n-TiO2) in synthetic and real waters." Journal of Nanoparticle Research **15**(6): 1684.

20) Chen, K. L. and M. Elimelech (2006). "Aggregation and Deposition Kinetics of Fullerene (C60) Nanoparticles." Langmuir **22**(26): 10994-11001.

21) Chen, K. L., et al. (2006). "Aggregation kinetics of alginate-coated hematite nanoparticles in monovalent and divalent electrolytes." Environmental science & technology **40**(5): 1516-1523.

22) Choi, O., et al. (2008). "The inhibitory effects of silver nanoparticles, silver ions, and silver chloride colloids on microbial growth." Water Research **42**(12): 3066-3074.

23) Chowdhury, I., et al. (2013). "Aggregate morphology of nano-TiO 2: role of primary particle size, solution chemistry, and organic matter." Environmental Science: Processes & Impacts **15**(1): 275-282.

24) Collin, B., et al. (2016). "Effect of natural organic matter on dissolution and toxicity of sulfidized silver nanoparticles to Caenorhabditis elegans." Environmental Science: Nano **3**(4): 728-736.

25) D'Mello, S. R., et al. (2017). "The evolving landscape of drug products containing nanomaterials in the United States." Nature Nanotechnology **12**: 523.

26) Dale, A. L., et al. (2015). "Much ado about α: reframing the debate over appropriate fate descriptors in nanoparticle environmental risk modeling." Environmental Science: Nano **2**(1): 27-32.

27) Dan, Y., et al. (2015). "Rapid analysis of titanium dioxide nanoparticles in sunscreens using single particle inductively coupled plasma–mass spectrometry." Microchemical Journal **122**(Supplement C): 119-126.

28) Degueldre, C. and P. Y. Favarger (2003). "Colloid analysis by single particle inductively coupled plasma-mass spectroscopy: a feasibility study." <u>Colloids and Surfaces A: Physicochemical and Engineering Aspects</u> **217**(1): 137-142.

29) Degueldre, C. and P. Y. Favarger (2004). "Thorium colloid analysis by single particle inductively coupled plasma-mass spectrometry." <u>Talanta</u> **62**(5): 1051-1054.

30) Delay, M., et al. (2011). "Interactions and stability of silver nanoparticles in the aqueous phase: Influence of natural organic matter (NOM) and ionic strength." <u>Journal of Chromatography A</u> **1218**(27): 4206-4212.

31) Diegoli, S., et al. (2008). "Interaction between manufactured gold nanoparticles and naturally occurring organic macromolecules." <u>Science of the Total Environment</u> **402**(1): 51-61.

32) Dobias, J. and R. Bernier-Latmani (2013). "Silver Release from Silver Nanoparticles in Natural Waters." <u>Environmental Science & Technology</u> **47**(9): 4140-4146.

33) Domingos, R. F., et al. (2009). "Characterizing manufactured nanoparticles in the environment: multimethod determination of particle sizes." <u>Environmental science & technology</u> **43**(19): 7277-7284.

34) Dubascoux, S., et al. (2008). "On-line and off-line quantification of trace elements associated to colloids by As-Fl-FFF and ICP-MS." <u>Talanta</u> **77**(1): 60-65.

35) Dubascoux, S., et al. (2010). "Field-flow fractionation and inductively coupled plasma mass spectrometer coupling: History, development and applications." <u>Journal of Analytical Atomic Spectrometry</u> **25**(5): 613-623.

36) Dubascoux, S., et al. (2008). "Optimisation of asymmetrical flow field flow fractionation for environmental nanoparticles separation." <u>Journal of Chromatography A</u> **1206**(2): 160-165.

37) Durán, N., et al. (2016). "Silver nanoparticles: A new view on mechanistic aspects on antimicrobial activity." <u>Nanomedicine: Nanotechnology, Biology and Medicine</u> **12**(3): 789-799.

38) Eckelman, M. J. and T. E. Graedel (2007). "Silver Emissions and their Environmental Impacts: A Multilevel Assessment." <u>Environmental Science & Technology</u> **41**(17): 6283-6289.

39) Ellis, L.-J. A., et al. (2018). "Seasonal variability of natural water chemistry affects the fate and behaviour of silver nanoparticles." <u>Chemosphere</u> **191**: 616-625.

40) Engelhard, C. (2011). "Inductively coupled plasma mass spectrometry: recent trends and developments." <u>Analytical and Bioanalytical Chemistry</u> **399**(1): 213-219.

41) Fabrega, J., et al. (2011). "Silver nanoparticles: behaviour and effects in the aquatic environment." <u>Environment international</u> **37**(2): 517-531.

42) Fabrega, J., et al. (2009). "Interactions of silver nanoparticles with Pseudomonas putida biofilms." <u>Environmental science & technology</u> **43**(23): 9004-9009.

43) Garner, K. L., et al. (2017). "Assessing the Risk of Engineered Nanomaterials in the Environment: Development and Application of the nanoFate Model." <u>Environmental Science & Technology</u> **51**(10): 5541-5551.

44) Geiss, O., et al. (2013). "Size and mass determination of silver nanoparticles in an aqueous matrix using asymmetric flow field flow fractionation coupled to inductively coupled plasma mass spectrometer and ultraviolet-visible detectors." Journal of Chromatography A **1321**: 100-108.

45) Giddings, J. C. (1984). "Field-flow fractionation." Separation Science and Technology **19**(11-12): 831-847.

46) Giddings, J. C. (1993). "Field-flow fractionation: analysis of macromolecular, colloidal, and particulate materials." Science **260**(5113): 1456-1465.

47) Giddings, J. C. (1995). "Measuring colloidal and macromolecular properties by FFF." Analytical Chemistry **67**(19): 592A-598A.

48) Giddings, J. C., et al. (1977). "Flow field-flow fractionation as a methodology for protein separation and characterization." Analytical Biochemistry **81**(2): 395-407.

49) Giese, B., et al. (2018). "Risks, Release and Concentrations of Engineered Nanomaterial in the Environment." Scientific Reports **8**(1): 1565.

50) Gigault, J. and V. A. Hackley (2013). "Differentiation and characterization of isotopically modified silver nanoparticles in aqueous media using asymmetric-flow field flow fractionation coupled to optical detection and mass spectrometry." Analytica Chimica Acta **763**: 57-66.

51) Gigault, J. and V. A. Hackley (2013). "Observation of size-independent effects in nanoparticle retention behavior during asymmetric-flow field-flow fractionation." Analytical and bioanalytical chemistry **405**(19): 6251-6258.

52) Gottschalk, F., et al. (2009). "Modeled environmental concentrations of engineered nanomaterials (TiO2, ZnO, Ag, CNT, fullerenes) for different regions." Environmental Science & Technology **43**(24): 9216-9222.

53) Grombe, R., et al. (2014). "Production of reference materials for the detection and size determination of silica nanoparticles in tomato soup." Analytical and bioanalytical chemistry: 1-13.

54) Gupta, B., et al. (2016). "TiO2 modification by gold (Au) for photocatalytic hydrogen (H2) production." Renewable and Sustainable Energy Reviews **58**: 1366-1375.

55) Gupta, S. M. and M. Tripathi (2011). "A review of TiO2 nanoparticles." Chinese Science Bulletin **56**(16): 1639.

56) Gurr, J.-R., et al. (2005). "Ultrafine titanium dioxide particles in the absence of photoactivation can induce oxidative damage to human bronchial epithelial cells." Toxicology **213**(1): 66-73.

57) Hagendorfer, H., et al. (2012). "Characterization of Silver Nanoparticle Products Using Asymmetric Flow Field Flow Fractionation with a Multidetector Approach–a Comparison to Transmission Electron Microscopy and Batch Dynamic Light Scattering." Analytical Chemistry **84**(6): 2678-2685.

58) Hassellöv, M., et al. (1999). "Determination of continuous size and trace element distribution of colloidal material in natural water by on-line coupling of flow field-flow fractionation with ICPMS." Analytical Chemistry **71**(16): 3497-3502.

59) Hineman, A. and C. Stephan (2014). "Effect of dwell time on single particle inductively coupled plasma mass spectrometry data acquisition quality." Journal of Analytical Atomic Spectrometry **29**(7): 1252-1257.

60) Hoque, M. E., et al. (2012). "Detection and characterization of silver nanoparticles in aqueous matrices using asymmetric-flow field flow fractionation with inductively coupled plasma mass spectrometry." Journal of Chromatography A **1233**: 109-115.

61) Hou, W.-C., et al. (2013). "Sunlight-driven reduction of silver ions by natural organic matter: formation and transformation of silver nanoparticles." Environmental Science & Technology **47**(14): 7713-7721.

62) Huynh, K. A. and K. L. Chen (2011). "Aggregation Kinetics of Citrate and Polyvinylpyrrolidone Coated Silver Nanoparticles in Monovalent and Divalent Electrolyte Solutions." Environmental Science & Technology **45**(13): 5564-5571.

63) Ilona, V., et al. (2014). "Rapid settling of nanoparticles due to heteroaggregation with suspended sediment." Environmental Toxicology and Chemistry **33**(8): 1766-1773.

64) Jiang, J., et al. (2009). "Characterization of size, surface charge, and agglomeration state of nanoparticle dispersions for toxicological studies." Journal of Nanoparticle Research **11**(1): 77-89.

65) Kaegi, R., et al. (2013). "Fate and transformation of silver nanoparticles in urban wastewater systems." Water Research **47**(12): 3866-3877.

66) Kaegi, R., et al. (2011). "Behavior of Metallic Silver Nanoparticles in a Pilot Wastewater Treatment Plant." Environmental Science & Technology **45**(9): 3902-3908.

67) Kammer, F. v. d., et al. (2005). "Field-flow fractionation coupled to multi-angle laser light scattering detectors: Applicability and analytical benefits for the analysis of environmental colloids." Analytica Chimica Acta **552**(1–2): 166-174.

68) Kammer, F. v. d., et al. (2011). "Separation and characterization of nanoparticles in complex food and environmental samples by field-flow fractionation." TrAC Trends in Analytical Chemistry **30**(3): 425-436.

69) Keller, A. A. and A. Lazareva (2013). "Predicted releases of engineered nanomaterials: from global to regional to local." Environmental Science & Technology Letters **1**(1): 65-70.

70) Keller, A. A., et al. (2013). "Global life cycle releases of engineered nanomaterials." Journal of Nanoparticle Research **15**(6): 1692.

71) Keller, A. A., et al. (2014). "Release of engineered nanomaterials from personal care products throughout their life cycle." Journal of Nanoparticle Research **16**(7): 1-10.

72) Keller, A. A., et al. (2010). "Stability and Aggregation of Metal Oxide Nanoparticles in Natural Aqueous Matrices." Environmental Science & Technology **44**(6): 1962-1967.

73) Kittler, S., et al. (2010). "Toxicity of Silver Nanoparticles Increases during Storage Because of Slow Dissolution under Release of Silver Ions." Chemistry of Materials **22**(16): 4548-4554.

74) Kraas, M., et al. (2017). "Long-term effects of sulfidized silver nanoparticles in sewage sludge on soil microflora." Environmental Toxicology and Chemistry **36**(12): 3305-3313.

75) Laborda, F., et al. (2011). "Selective identification, characterization and determination of dissolved silver(i) and silver nanoparticles based on single particle detection by inductively coupled plasma mass spectrometry." Journal of Analytical Atomic Spectrometry **26**(7): 1362-1371.

76) Lee, S., et al. (2014). "Nanoparticle Size Detection Limits by Single Particle ICP-MS for 40 Elements." Environmental Science & Technology **48**(17): 10291-10300.

77) Levard, C., et al. (2011). "Sulfidation Processes of PVP-Coated Silver Nanoparticles in Aqueous Solution: Impact on Dissolution Rate." Environmental Science & Technology **45**(12): 5260-5266.

78) Li, H., et al. (2009). "TiO2 Nanoparticle and ZnO Nanowire Composite for Solar Cell Application." Microscopy and Microanalysis **15**(S2): 1428-1429.

79) Li, Q., et al. (2008). "Antimicrobial nanomaterials for water disinfection and microbial control: Potential applications and implications." Water Research **42**(18): 4591-4602.

80) Li, X. and J. J. Lenhart (2012). "Aggregation and Dissolution of Silver Nanoparticles in Natural Surface Water." Environmental Science & Technology **46**(10): 5378-5386.

81) Li, X., et al. (2010). "Dissolution-Accompanied Aggregation Kinetics of Silver Nanoparticles." Langmuir **26**(22): 16690-16698.

82) Li, Z., et al. (2010). "Adsorbed polymer and NOM limits adhesion and toxicity of nano scale zerovalent iron to E. coli." Environmental science & technology **44**(9): 3462-3467.

83) Liu, J. and R. H. Hurt (2010). "Ion Release Kinetics and Particle Persistence in Aqueous Nano-Silver Colloids." Environmental Science & Technology **44**(6): 2169-2175.

84) Liu, J., et al. (2015). "Heteroaggregation of bare silver nanoparticles with clay minerals." Environmental Science: Nano **2**(5): 528-540.

85) Liu, J., et al. (2011). "Kinetics and Mechanisms of Nanosilver Oxysulfidation." Environmental Science & Technology **45**(17): 7345-7353.

86) Loeschner, K., et al. (2013). "Detection and characterization of silver nanoparticles in chicken meat by asymmetric flow field flow fractionation with detection by conventional or single particle ICP-MS." Analytical and bioanalytical chemistry **405**(25): 8185-8195.

87) Ma, R., et al. (2012). "Size-Controlled Dissolution of Organic-Coated Silver Nanoparticles." Environmental Science & Technology **46**(2): 752-759.

88) Markus, A., et al. (2015). "Modeling aggregation and sedimentation of nanoparticles in the aquatic environment." Science of the Total Environment **506**: 323-329.

89) Markus, A. A., et al. (2015). "Modeling aggregation and sedimentation of nanoparticles in the aquatic environment." Science of The Total Environment **506-507**: 323-329.

90) Meesters, J. A. J., et al. (2014). "Multimedia Modeling of Engineered Nanoparticles with SimpleBox4nano: Model Definition and Evaluation." Environmental Science & Technology **48**(10): 5726-5736.

91) Miller, R. J., et al. (2012). "TiO2 Nanoparticles Are Phototoxic to Marine Phytoplankton." PLOS ONE **7**(1): e30321.

92) Mitrano, D. M., et al. (2012). "Silver nanoparticle characterization using single particle ICP-MS (SP-ICP-MS) and asymmetrical flow field flow fractionation ICP-MS (AF4-ICP-MS)." Journal of Analytical Atomic Spectrometry **27**(7): 1131-1142.

93) Mitrano, D. M., et al. (2012). "Detecting nanoparticulate silver using single-particle inductively coupled plasma–mass spectrometry." Environmental Toxicology and Chemistry **31**(1): 115-121.

94) Mitrano, D. M., et al. (2014). "Tracking dissolution of silver nanoparticles at environmentally relevant concentrations in laboratory, natural, and processed waters using single particle ICP-MS (spICP-MS)." Environmental Science: Nano **1**(3): 248-259.

95) Montano, M. D., et al. (2014). "Improvements in the detection and characterization of engineered nanoparticles using spICP-MS with microsecond dwell times." Environmental Science: Nano **1**(4): 338-346.

96) Moore, M. N. (2006). "Do nanoparticles present ecotoxicological risks for the health of the aquatic environment?" Environment International **32**(8): 967-976.

97) Mueller, N. C. and B. Nowack (2008). "Exposure Modeling of Engineered Nanoparticles in the Environment." Environmental Science & Technology **42**(12): 4447-4453.

98) Navarro, E., et al. (2008). "Toxicity of Silver Nanoparticles to Chlamydomonas reinhardtii." Environmental Science & Technology **42**(23): 8959-8964.

99) Nowack, B., et al. (2015). "Progress towards the validation of modeled environmental concentrations of engineered nanomaterials by analytical measurements." Environmental Science: Nano **2**(5): 421-428.

100) Pelley, A. J. and N. Tufenkji (2008). "Effect of particle size and natural organic matter on the migration of nano- and microscale latex particles in saturated porous media." Journal of Colloid and Interface Science **321**(1): 74-83.

101) Petosa, A. R., et al. (2010). "Aggregation and Deposition of Engineered Nanomaterials in Aquatic Environments: Role of Physicochemical Interactions." Environmental Science & Technology **44**(17): 6532-6549.

102) Philippe, A. and G. E. Schaumann (2014). "Interactions of Dissolved Organic Matter with Natural and Engineered Inorganic Colloids: A Review." Environmental Science & Technology **48**(16): 8946-8962.

103) Poda, A. R., et al. (2011). "Characterization of silver nanoparticles using flow-field flow fractionation interfaced to inductively coupled plasma mass spectrometry." Journal of Chromatography A **1218**(27): 4219-4225.

104) Praetorius, A., et al. (2014). "Heteroaggregation of Titanium Dioxide Nanoparticles with Model Natural Colloids under Environmentally Relevant Conditions." Environmental Science & Technology **48**(18): 10690-10698.

105) Praetorius, A., et al. (2012). "Development of Environmental Fate Models for Engineered Nanoparticles—A Case Study of TiO2 Nanoparticles in the Rhine River." Environmental Science & Technology **46**(12): 6705-6713.

106) Purawatt, S., et al. (2007). "Flow field–flow fractionation–inductively coupled optical emission spectrometric investigation of the size-based distribution of iron complexed to phytic and tannic acids in a food suspension: implications for iron availability." Analytical and bioanalytical chemistry **389**(3): 733-742.

107) Quik, J. T., et al. (2012). "Natural colloids are the dominant factor in the sedimentation of nanoparticles." Environmental toxicology and chemistry **31**(5): 1019-1022.

108) Quik, J. T. K., et al. (2014). "Heteroaggregation and sedimentation rates for nanomaterials in natural waters." Water Research **48**: 269-279.

109) Reschiglian, P., et al. (2002). "High performance, disposable hollow fiber flow field-flow fractionation for bacteria and cells. First application to deactivated Vibrio cholerae." Journal of Separation Science **25**(8): 490-498.

110) Rezaei, B. and H. Mosaddeghi (2006). Applications of titanium dioxdie nanocoating. Nano-Technology in Environments Conference.

111) Schachermeyer, S., et al. (2012). "Impact of carrier fluid composition on recovery of nanoparticles and proteins in flow field flow fractionation." Journal of Chromatography A **1264**: 72-79.

112) Schmidt, B., et al. (2011). "Quantitative Characterization of Gold Nanoparticles by Field-Flow Fractionation Coupled Online with Light Scattering Detection and Inductively Coupled Plasma Mass Spectrometry." Analytical Chemistry **83**(7): 2461-2468.

113) Sharma, V. K., et al. (2014). "Organic-coated silver nanoparticles in biological and environmental conditions: Fate, stability and toxicity." Advances in Colloid and Interface Science **204**: 15-34.

114) Sotiriou, G. A. and S. E. Pratsinis (2010). "Antibacterial Activity of Nanosilver Ions and Particles." Environmental Science & Technology **44**(14): 5649-5654.

115) Starnes, D. L., et al. (2016). "Distinct transcriptomic responses of Caenorhabditis elegans to pristine and sulfidized silver nanoparticles." Environmental Pollution **213**: 314-321.

116) Stephan Elsenberg, T. J., Christoph Johann (2012). "Hollow Fibre Flow Field Flow Fractionation

117) (HF5) Increases Sensitivity and Efficiency in the

118) Separation of Proteins and Complex Protein Mixtures." Chromatography Today: 59-62.

119) Sun, T. Y., et al. (2017). "Envisioning Nano Release Dynamics in a Changing World: Using Dynamic Probabilistic Modeling to Assess Future Environmental Emissions of Engineered Nanomaterials." Environmental Science & Technology **51**(5): 2854-2863.

120) Thalmann, B., et al. (2016). "Effect of humic acid on the kinetics of silver nanoparticle sulfidation." Environmental Science: Nano **3**(1): 203-212.

121) Tiede, K., et al. (2008). "Detection and characterization of engineered nanoparticles in food and the environment." Food Additives and Contaminants **25**(7): 795-821.

122) Ulrich, A., et al. (2012). "Critical aspects of sample handling for direct nanoparticle analysis and analytical challenges using asymmetric field flow fractionation in a multi-detector approach." Journal of Analytical Atomic Spectrometry **27**(7): 1120-1130.

123) Velzeboer, I., et al. (2014). "Rapid settling of nanoparticles due to heteroaggregation with suspended sediment." Environmental toxicology and chemistry **33**(8): 1766-1773.

124) Wang, H., et al. (2015). "Heteroaggregation of engineered nanoparticles and kaolin clays in aqueous environments." Water research **80**: 130-138.

125) Warheit, D. B., et al. (2007). "Pulmonary toxicity study in rats with three forms of ultrafine-TiO2 particles: Differential responses related to surface properties." <u>Toxicology</u> **230**(1): 90-104.

126) Warheit, D. B., et al. (2006). "Pulmonary Instillation Studies with Nanoscale TiO2 Rods and Dots in Rats: Toxicity Is not Dependent upon Particle Size and Surface Area." <u>Toxicological Sciences</u> **91**(1): 227-236.

127) Wiesner, M. and J.-Y. Bottero (2007). <u>Environmental nanotechnology</u>, McGraw-Hill Professional Publishing New York.

128) Wimmer, A., et al. (2018). "New insights into the formation of silver-based nanoparticles under natural and semi-natural conditions." <u>Water Research</u> **141**: 227-234.

129) Zhang, Y., et al. (2008). "Stability of commercial metal oxide nanoparticles in water." <u>Water Research</u> **42**(8–9): 2204-2212.

130) Zhou, D., et al. (2013). "Influence of Material Properties on TiO2 Nanoparticle Agglomeration." <u>PLOS ONE</u> **8**(11): e81239.

131) Zhou, D. and A. A. Keller (2010). "Role of morphology in the aggregation kinetics of ZnO nanoparticles." <u>Water Research</u> **44**(9): 2948-2956.

132) Zhu, M., et al. (2014). "The effect of humic acid on the aggregation of titanium dioxide nanoparticles under different pH and ionic strengths." <u>Science of the Total Environment</u> **487**: 375-380.

133) Zhu, X., et al. (2010). "Toxicity and bioaccumulation of TiO2 nanoparticle aggregates in Daphnia magna." <u>Chemosphere</u> **78**(3): 209-215.

Chapter 3 . Characterization of the fate of primary and re-precipitated silver nanoparticles in lake water microcosms

---

Connecting Text: Extensive use of silver nanoparticles (nAg) in consumer products increases their potential to enter different environmental compartments including surface waters, where they may be bioavailable for uptake by various organisms. Particle size, agglomeration state, dissolved concentrations, surface transformation are important processes, which influence the bioavailability. Therefore, there is a need to study the fate of nAg in surface waters at environmentally relevant concentrations. This chapter evaluates the persistence of primary and re-precipitated nAg from primary silver nanoparticles in laboratory lake water microcosms in the absence and presence of colloids.

Findings from Chapter 3 are in preparation for submission to the following journal: Environmental Science: Nano. **Rao S**., Xiaoyu Gao., Ghoshal S., (2019) Characterization of the fate of primary and re-precipitated silver nanoparticles in lake water microcosms.

3.1 Introduction

Silver nanoparticles (nAg) are extensively used in consumer products due to their antimicrobial properties (Mueller and Nowack 2008, Geranio et al. 2009). The use of these products (e.g., cleaning and medical disinfection products, clothing) lead to releases of nAg to aquatic environments. In natural aquatic systems, nAg may undergo different physical/chemical transformation processes in natural aquatic systems influence the toxicity and bioavailability of nAg (Kvítek et al. 2008, Kittler et al. 2010, Kaegi et al. 2011, Park et al. 2011, Levard et al. 2012, Levard et al. 2013).

Physical transformations of nAg include homoagglomeration (agglomeration between nAg) and heteroagglomeration (the attachment of nAg to natural colloids) (Wang et al. 2015). Agglomeration rates are influenced by the size, surface charge, the surface chemistry and the concentration of the natural colloids and nAg, and the chemistry (e.g., ionic strength, pH) of natural waters. Dissolved organic matter (DOM) can colloidally stabilize nAg and natural colloids in aquatic systems through electrosteric forces (Fabrega et al. 2009, Baalousha et al. 2013, Philippe and Schaumann 2014, Sharma et al. 2014) and lower agglomeration rates (Quik et al. 2014). In natural water systems, natural colloids may be present at concentrations orders of magnitude higher than nAg (or other engineering nanoparticles, ENPs), leading to more heteroagglomeration than homoagglomeration of nAg (Praetorius et al. 2014, Quik et al. 2014).

Among chemical transformation process, oxidative dissolution of nAg under aerobic conditions in the presence and absence of UV light, has been widely studied (Li et al. 2010, Liu and Hurt 2010, Azodi et al. 2016). The oxidative dissolution of nAg releases Ag^+ and reactive oxygen species, particularly superoxide ($O_2^{\bullet -}$) which leads to formation of hydrogen peroxide (Jones et al. 2011, Rong et al. 2018). The H_2O_2 formed can contribute to dissolution of nAg^0 to Ag^+ (Rong et al. 2018). The superoxide also undergoes a series of reactions with nAg which involves electron transfers to form 'charged nAg' which reduces dissolved O_2 to $O_2^{\bullet -}$ and Ag^+ to nAg (He et al. 2012). The kinetics of the various reactions determine the net concentrations of Ag^+ and nAg at a given time. Re-precipitation of nAg from pristine nAg particles in wastewater effluents has been reported recently. The re-precipitation of nAg can be caused by sulfidation of Ag^+ dissolved from nAg, both by inorganic and organosulfur compounds, leading to formation of nAg_2S (Azodi et al. 2016) . The reduction of Ag^+ to nAg by different fractions of DOM (Akaighe et al. 2011, Adegboyega et al. 2013), particularly moieties contacting low- molecular-weight quinones

(Wimmer et al. 2018). Exposure of Ag^+ to light can accelerate the reduction of Ag^+ to nAg by DOM,(Yin et al. 2012, Hou et al. 2013) but is not essential for the precipitation reaction (Wimmer et al. 2018). Sulfidation of nAg in sulfidic natural waters can diminish rates of dissolution due to conversion of Ag^0 to insoluble Ag_2S (He et al. 2019).

Currently, there is no direct information available on the abundance, sizes, and persistence of r-nAg in natural waters after their formation, and on their role in agglomeration processes. The majority of the studies assessing nAg transformation in aquatic systems studies have employed high initial ENP concentrations owing to the limitations of the analytical techniques used for characterizing nAg concentrations, sizes and speciation, with the exception of a study done by Wimmer *et al.* (Wimmer et al. 2018). However, the use of high initial particle concentrations precludes the understanding of the nature and extent of dissolution, reformation and agglomeration behavior of nAg under environmentally relevant concentrations. Further, the studies generally focus on either physical or chemical transformations the interrelationships of the two have not been extensively studied (Li et al. 2010).

The objective of this study was to investigate the role of the physical and chemical transformation processes of dissolution, re-precipitation, and homo/heteroagglomeration on the concentrations and size distributions of nAg particles (pristine and transformed), in a model lake water microcosms. The microcosms were maintained under quiescent and mixed conditions (representing turbulence in natural waters) and the water column was characterized for nAg sizes and concentration over time, up to 44 days. Both filtered and unfiltered lake water microcosms were set up, to determine the effects of natural colloids on the physical and chemical transformation processes. PVP-nAg of 80 nm diameter was added to the microcosms at 6 μg/L or 56 nM, to balance the emphasis on environmentally relevant concentrations, as well as to enable

characterization of the size distributions, and mass and number concentrations of nAg added and any r-nAg formed. nAg size and concentrations, as well dissolved Ag concentrations were characterized primarily by single particle ICP-MS, a sensitive analytical technique for characterization of metal nanoparticles in complex aqueous matrices.

3.2 Materials and Methods

3.2.1 Lake water

Grab samples of lake water were collected approximately 1.5 m below the surface at Lac Hertel, at the Gault Nature Reserve (Mont-Saint-Hilaire, Quebec, Canada), McGill University, in pre-washed 2 L HDPE bottles and stored at 4 $^{\circ}$C until further use. Additional details of lake water analyses are presented in the Supplementary Information.

3.2.2 Lake water microcosms

The microcosms were comprised of 120 mL graduated cylindrical glass bottles (inner diameter: 4.5 cm; height: 10 cm; headspace: 2 cm) and were wrapped in aluminum foil to prevent exposure to light. Parallel systems were employed containing unfiltered lake water (UFLW), filtered lake water (FLW, 0.1 µm). On day 0, PVP-coated nAg (PVP-coated NanoXact nAg^0 (99.99% Ag purity, nanoComposix, nominal diameter of 80 nm) were added to yield a final concentration of 6 µg/L (56 nM), and mixed for 60 s to disperse the particles in each microcosm. Microcosms were maintained under quiescent conditions or were continuously mixed at 80 rpm on an orbital shaker. The microcosms were aerobic throughout the experiment due to the presence of a headspace. Sample dilutions were done immediately after sampling and the samples were analyzed promptly thereafter. The microcosms were sampled over a period of up to 45 days to determine changes in nAg size distributions and dissolved Ag concentrations. Aliquots (triplicates, 1 mL each) were

periodically sampled 3 cm above the base carefully using a pipet (Schematic representation, Figure S 3.1).

The final sampling time point for both quiescent and mixed UFLW systems corresponded to the time point when nAg concentrations were < 10 % of the initial spiked concentration which is 44 days for the quiescent condition and 21 days for the mixed condition. FLW experiments were sampled until then to maintain uniformity.

To independently study the rate of formation of nAg from dissolved Ag, Ag^+ was spiked (plasma cal, 1000 mg/L, SCP Science, Canada) at 10, 100 and 1000 µg/L into UFLW and FLW. All systems were set up in the dark under quiescent and mixed conditions in 50 mL polypropylene tubes (digiTubes, SCP Science, Canada). Control systems were set up in DI water. All samples were analysed for nAg using spICP-MS.

3.2.3 Analytical techniques

PerkinElmer NexION 300X ICP-MS supported by Syngistix software (ver1.1.) was used in single particle mode for nAg characterization. The limits of detection of size and concentration under these instrument conditions were 15 nm and 10 ng/L for 80 nm PVP-nAg in LW, respectively. The limit of detection of concentration decreased further for particles < 40 nm to 5 ng/L. The limit of detection of dissolved Ag concentration was 20 ng/L in lake water and 10 ng/L in DI water. Other instrumental parameters (Table S1) as well as total silver mass balances (Figure S 3.2) are reported as Supplementary Information. The dissolved silver measured by spICP-MS includes any free silver ions, soluble silver complexes, as well as small nAg <15 nm, which are not detectable and are counted as dissolved silver.

Philips CM200 200 kV TEM with AMT XR40B CCD Camera and EDAX Genesis EDS analysis systems were used to image nAg and analyze elemental composition. 20 μL of the concentrate was deposited on the Cu TEM substrates (Electron Microscopy Sciences, Carbon film 200 mesh Cu grids). The grids were kept in the dark and air-dried. The zeta potential and conductivity were determined using DLS (ZetaSizer Nano ZS, Malvern).

3.3 Results and Discussion

3.3.1 Lake water characterization

 The lake water had an electrical conductivity of 93.4 μS/cm and pH of 7.5. Total suspended solids (TSS) in UFLW was 2.7 mg/L and negligible in FLW. However, natural colloids < 100 nm may be present in FLW systems, which could not be measured by TSS analysis . The natural colloid number concentration in the 35 to 1000 nm size range was determined to be $1.2 \times 10^9 \pm 3.6 \times 10^8$ NP/mL (n = 4) with a mean diameter of 232.8 ± 57.8 nm using Nanoparticle Tracking Analysis (NTA NanoSight LM10, Malvern Panalytical). Because NTA is unable to detect particles greater than 1000 nm,(Filipe et al. 2010) the lake water was also characterized for colloids using laser diffraction (Horiba Laser Scattering Particle Size Analyzer). The average diameter detected by that technique was determined to be 7 μm (size distribution of 250 nm to 26 μm) (Figure S 3.3). The lake water was left undisturbed for ~ 6 months and the supernatant was analyzed using NTA to determine the non-settled fraction, which was determined to be $1.1 \times 10^8 \pm 2.5 \times 10^7$ NP/mL (n = 5) (Figure S 3.3) with a mean diameter of 296.8 ± 24 nm. DOC of UFLW and FLW was 3.5 mg/L and 2.4 mg/L, respectively. The inorganic carbon concentration was measured using a TOC analyzer (TOC-V, Shimadzu Corp.) and was determined to be 6.6 mg/L in both UFLW and FLW. nAg and dissolved Ag was not detected in unspiked UFLW and FLW by spICP-MS. Additional physicochemical and compositional characteristics of the lake water are shown in Table S2.

3.3.2 Characterization of silver nanoparticles

PVP-nAg added to the experimental systems had a mean diameter of 82 ± 14 nm ($n = 113$) as measured by TEM, and were primarily spherical (Figure S 3.4). spICP-MS analysis of the PVP-nAg in DI and UFLW yielded a mean diameter of 65.3 ± 6.9 nm and 64.4 ± 7 nm, respectively. The discrepancy between the TEM and spICP-MS measurements are attributable to the different particle population sizes measured by these techniques. PVP-nAg was negatively charged in a 1.5 mM NaCl solution (- 25.9 ± 2.8 mV).

3.3.3 Smaller nAg were formed after incubation of pristine nAg

FLW and UFLW systems were spiked with nAg$_{pristine}$ and the nAg concentrations measured by spICP-MS immediately thereafter were 6.1 ± 0.3 µg/L or $4 \times 10^6 \pm 1.8 \times 10^5$ NP/mL. Figure 3.1 (A) shows the particle size distributions of nAg in FLW and UFLW under quiescent conditions on day 0. The sizes were between 45 and 100 nm and thus this is designated as the primary nAg (p-nAg) population. All nAg particles measured in the >40 nm (pristine and homoagglomerated) range are hereafter referred to as p-nAg. It is important to note that we observed a few small signals corresponding to the <40 nm range in DI water, UFLW and FLW spiked with nAg, on day 0. These spikes are attributable to low concentrations of nAg that may have formed instantaneously (time scale of minutes) due to reformation of Ag$^+$ generated as observed by He *et al.* (He et al. 2012). Alternatively, these small concentrations of <40 nm nAg could have been present in the stock PVP-nAg solutions.

An increase in number concentrations in < 40 nm nAg range under mixed and quiescent conditions occurred on day 21 compared to day 0 (t-test, $p < 0.05$) in UFLW (Figure 3.1 (B)) and FLW (Figure 3.1 (C)) systems. As discussed later, sonication of all FLW and UFLW samples from day 21 and beyond indicated higher concentrations of r-nAg confirming that r-nAg was present in

significantly higher abundance. Sonication of day 0 samples did not enhance the particle concentrations (Figure S 3.5). The <40 nm nAg are referred to herein as re-precipitated (r-nAg) because they were formed by the DOM induced reduction/precipitation of dissolved Ag released by the primary nAg. A previous study attributed the low dissolved Ag from 11 nm citrate-nAg to re-precipitation in natural lake water (Ellis et al. 2018), however, the extent of re-precipitation was not quantified. Further, similar re-precipitation of nAg from $nAg_{pristine}$ was observed in the replicate fate experiments performed in UFLW systems (Figure S 3.14).
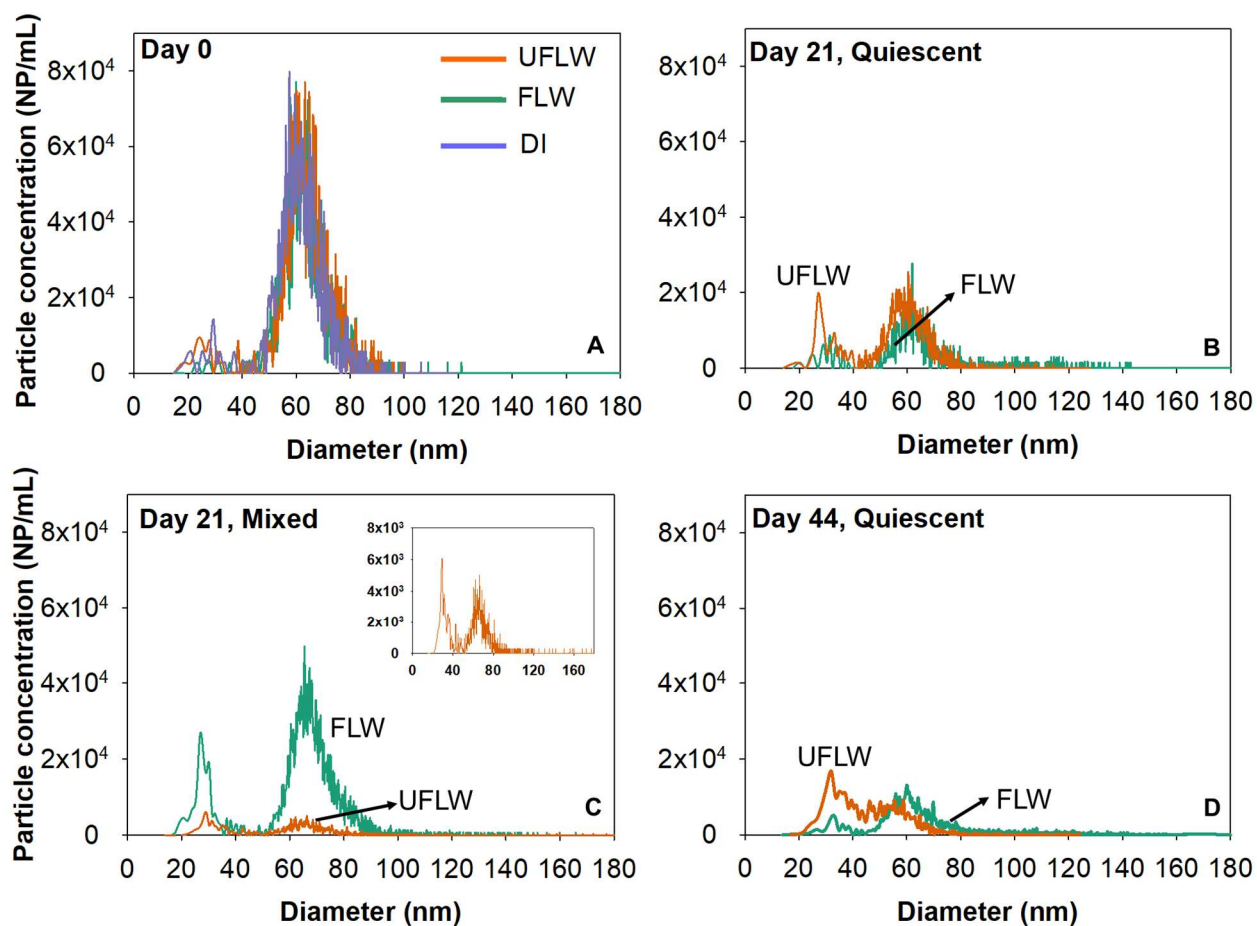
Figure 3.1: Particle size distribution of nAg on (A) Day 0 (B) quiescent conditions, Day 21 (C) mixed conditions, Day 21, Inset: Zoomed in particle size distribution of UFLW (D) Day 44 under quiescent conditions.

To verify if the r-nAg (<40 nm) particles in FLW and UFLW were derived from dissolution of nAg$_{pristine}$, the lake water samples were spiked with Ag$^+$ (1 and 10 µg/L) and incubated in the absence of light under quiescent and mixed conditions. In control systems, Ag$^+$ was spiked in DI water, which did not result in any formation of nAg at any time under those incubation conditions. Formation of nAg was immediately observed (Figure S 3.6) in UFLW systems (9.4 ×10^4 NP/mL or 4.7 ng/L at 1 h) but formation of nAg in FLW was slower (Figure 3.2 (A)). FLW had lower DOC (2.37 mg/L) than UFLW (3.48 mg/L), which likely contributed to the slower formation and fewer nAg. Similar effects of DOC concentrations on nAg formation have been reported elsewhere (Wimmer et al. 2018).

Figures 3.2 (B) and (C) represent particle size distributions of nAg formed in UFLW and FLW under quiescent conditions 7 days after being spiked with 1 µg/L and 10 µg/L of Ag$^+$. The estimated mean diameters of nAg in UFLW (Figure 2B) on day 7 using spICP-MS were determined to be 28.8 ± 3.9 nm and 44.3 ± 8.1 nm at spiked Ag$^+$ concentrations of 1 µg/L and 10 µg/L, respectively. In FLW systems (Figure 3.2 (C)), estimated mean diameters were slightly higher compared to UFLW systems, with 36.3 ± 3.8 nm at 1 µg/L Ag$^+$ and 60.3 ± 12.6 nm at 10 µg/L Ag$^+$ on day 7. There was no further increase in mean diameters over the incubation period of 30 days (Figure S6). Higher concentration of Ag$^+$ (1000 µg/L) was spiked for TEM analysis where, diameters of precipitated nAg in UFLW was 49 ± 17.9 (n = 93) (Figure 3.2 (D)) and 61.3 ± 16.8 nm (n = 71) in FLW (Figure 3.2 (F)). The higher initial Ag$^+$ concentration resulted in larger nAg formed. TEM images reveal precipitated nAg associated with organic matter (Figure 3.2 (D), S 3.6) which is confirmed with the high carbon signal observed in the EDS analysis of the precipitated nAg (Figure 3.2 (E)). The particle images in Figure 3.2 (F) are similar those in a recent study of asymmetric silver nanoparticle structures formed by spiking Ag$^+$ into a synthetic polymer

solution (Li et al. 2019). A high contrast silver nanoparticle was associated with a lower contrast region which comprised of low amounts of silver and polymer. Formation of nAg of similar diameter and concentrations in FLW and UFLW as above was also observed under mixed conditions (Figure S 3.7).

In the microcosms, the maximum dissolved Ag was 0.22 and 0.07 µg/L in FLW and UFLW, respectively, under mixed conditions and 0.28 µg/L in FLW and 0.16 µg/L in UFLW under quiescent conditions (Figure S 3.8), thus the size of r-nAg was close to nAg formed with 1 µg/L Ag^+. Previous studies on precipitation of nAg by DOM of Ag^+ were conducted with Ag^+ concentrations in the mg/L range (Yin et al. 2012, Hou et al. 2013). To date, only one study has demonstrated DOM-reduced formation of nAg with comparable Ag^+ concentrations (50 ng/L). (Wimmer et al. 2018)
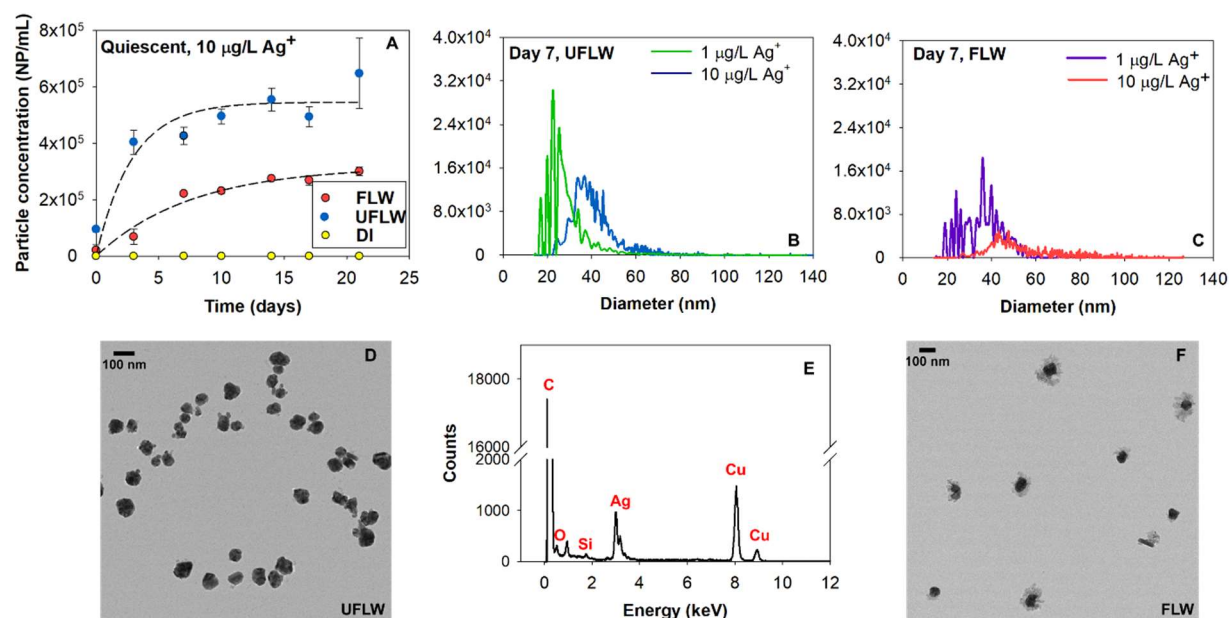
Figure 3.2: (A) Particle concentration in UFLW and FLW over time due to precipitation of nAg following addition of 10 g/L of Ag+ (Dashed line represent fit of first order kinetics with rate constants of UFLW: 0.35 day^{-1}, FLW: 0.13 day^{-1}). Size and numbers determined by spICP-MS

for precipitated nAg following spiking with Ag$^+$, Particle size distributions 7 days after spiking with 1 μg/L and 10 μg/L Ag$^+$ in (B) UFLW (C) FLW. TEM images of precipitated nAg from spiking with 1000 μg/L Ag$^+$ in (D) UFLW (E) EDS of precipitated nAg in UFLW (F) FLW.

3.3.4 In filtered lake water, homoagglomeration determines the sizes and concentrations of primary and re-precipitated nAg in the water column

In the absence of colloids (FLW) and under quiescent conditions, a shift to larger sizes with a statistically significant ~10 nm increase in particle diameters (paired t-test, $p < 0.05$) was observed after 21 days compared to day 0 (Figure 3.3 (A)), suggesting homoagglomeration. To determine the extent of homoagglomeration of nAg in FLW, samples taken at different time points from the test vials were immediately sonicated for 5 min, (37 kHz, Fisherbrand ultrasonic water bath) to thoroughly dis-agglomerate (Huynh and Chen 2014) and disperse r-nAg and nAg$_{pristine}$. Sonication yielded (i) smaller sizes of p-nAg, most frequent size measured decreased from 61.4 $\pm$ 0.3 nm to 25.3 $\pm$ 0.4 nm and (ii) a 29-fold increase (release of 1.07×10^6 NP/mL) in r-nAg number concentration upon sonication (Figure 3.3 (A)). Sonication also caused a 2.5 fold increase in number concentration of p-nAg, as a consequence of break up of larger homoagglomerates (80 - 140 nm). An increase in measured sizes due to agglomeration of citrate-nAg was also observed elsewhere in a filtered lake water sample (Ellis et al. 2018).

In mixed systems (Figure 3.3 (B)), sonication yielded 2.7×10^5 NP/mL of r-nAg after 21 days, which was 2.5 times higher than non-sonicated samples and approximately 6-times lower than r-nAg released from sonication of samples from the quiescent systems.
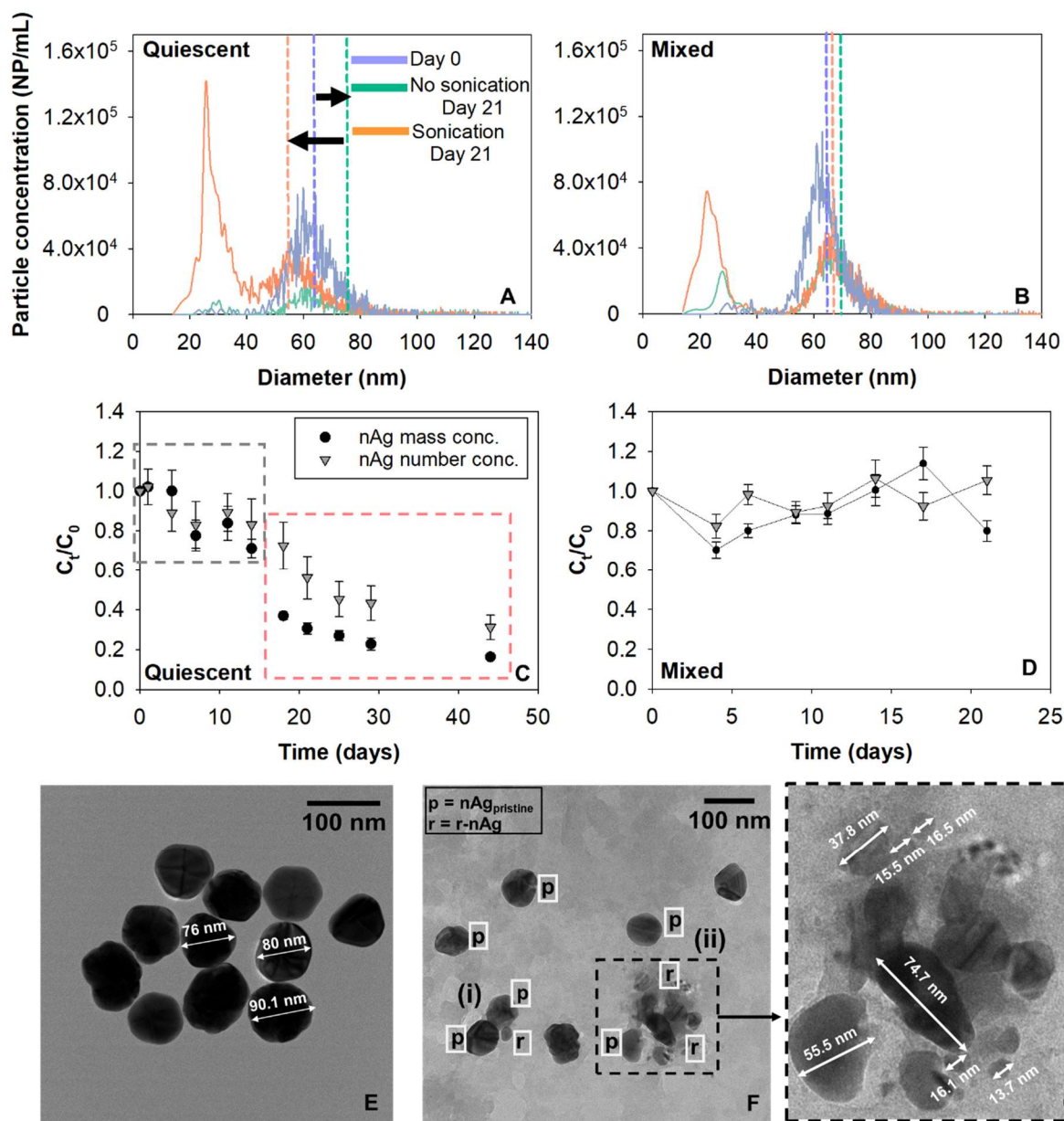
Figure 3.3: Effect of sonication on release of nAg in FLW (A) Quiescent conditions (B) Mixed conditions. Vertical dashed lines represent mass concentration-weighted mean diameters as calculated by spICP-MS. Normalized number and mass concentrations of total nAg (p-nAg and r-nAg) over time under (C) quiescent conditions (D) mixed conditions in FLW systems. TEM image of (E) pristine PVP-nAg and (F) nAg in FLW system under quiescent conditions, (i) and (ii) are

homoagglomerates consisting of $\text{nAg}_{\text{pristine}}$ and r-nAg (G) Section (ii) zoomed in from Figure 3.3 (F).

There was no significant change in nAg >40 nm particle concentrations in line with the lower extent of agglomeration in mixed systems. Higher dissolved Ag concentrations (0.22 µg/L) were measured in mixed systems on day 21 compared to quiescent systems where measured dissolved Ag concentrations were negligible (Figure S 3.8). This suggests that mixing resulted in unfavourable conditions for r-nAg formation from dissolved Ag.

In order to quantify homoagglomeration, particle number and mass concentrations in the suspension were evaluated over time. In quiescent systems (Figure 3.3 (C)), there was relatively limited change in particle mass and number concentrations over the first 14 days (C_t/C_0, number conc. decreased to 0.71) than in the subsequent 14-day period (C_t/C_0, number conc. = 0.23), suggesting an initial phase of low agglomeration and sedimentation rate, followed by an increase in both of these processes. These patterns are clearly reflected in the analyses of particle size distribution of non-sonicated samples of day 0, 14 and 18. (Figure S 3.9). Based on these results, the nAg concentration time profiles can be classified into two regimes: (i) decrease in nAg concentrations independent of homoagglomeration (black dashed box) (ii) homoagglomeration-induced sedimentation (red dashed box). In the absence of homoagglomeration and sedimentation, the number and mass concentration should remain unchanged over time. In the presence of homoagglomeration, the number concentration of NPs at a given time point would decrease while yielding the same mass concentration. Decreases in particle mass concentration is attributable solely to sedimentation. The change in mass concentration in the homoagglomeration regime was used to calculate a rate constant for sedimentation ($k_{\text{homo,sed}}$) of 0.036 day^{-1} (Figure S 3.10). In contrast, with the systems where Ag$^+$ was added to the FLW and maintained under quiescent

conditions there was no reduction in particle concentrations over time, suggesting that sedimentation occurs only in the nAg spiked FLW systems. In other studies, nAg formed in the presence of DOM (and indoor light) after addition of Ag^+ were found to be stable for upto 180 days, although the DOM concentrations were much higher than in this study.

In mixed systems, total particle number concentrations ($3.5\times10^6 \pm 7.3\times10^5$ NP/mL) remained effectively unchanged over the experimental period of 21 days (Figure 3.3 (D)). The mixing energy was likely sufficient to keep the r-nAg and p-nAg suspended, and may have increased interactions of $nAg_{pristine}$ and/or r-nAg with DOM leading to their higher steric stabilization, and limited homoagglomeration (Keller et al. 2010).

Figures 3E and 3F show TEM images of pristine nAg and nAg agglomerates formed in FLW. The agglomerate cluster in Figure 3.3 (C) has (i) two p-nAg (~ 70 nm) and one r-nAg (28 nm) and (ii) has 7 r-nAg and p-nAg particles ranging from 6 nm to 75 nm in diameter. Overall, the data suggests for nAg in FLW under quiescent conditions, homoagglomeration between p-nAg/r-nAg, r-nAg/r-nAg and p-nAg/p-nAg occurred, and led to sedimentation.

3.3.5 In unfiltered lake water natural colloids influence the concentration of primary and re-precipitated nAg in the water column

In the presence of colloids, the fate of nAg was more complex with potentially more heterogeneous interactions (p-nAg, r-nAg and natural colloids) occurring in the system. A decrease in total nAg particle number and mass concentrations over time was observed in quiescent and mixed systems in the presence of colloids (Figure 3.4 (A) and (B)), with a faster decrease in mixed systems. After 21 days under mixed conditions, only 3.1×10^5 NP/mL (7% of initial spiked particle number concentration) was detected in quiescent systems. This is different from the FLW mixed systems where there was no effective decrease in nAg concentrations. Sedimentation rate constants were

estimated to be 0.06 day^{-1} and 0.13 day^{-1} under quiescent and mixed conditions, respectively and were obtained by fitting the mass concentration over time in Figure 3.4 (A), (B) (Figure S 3.11).
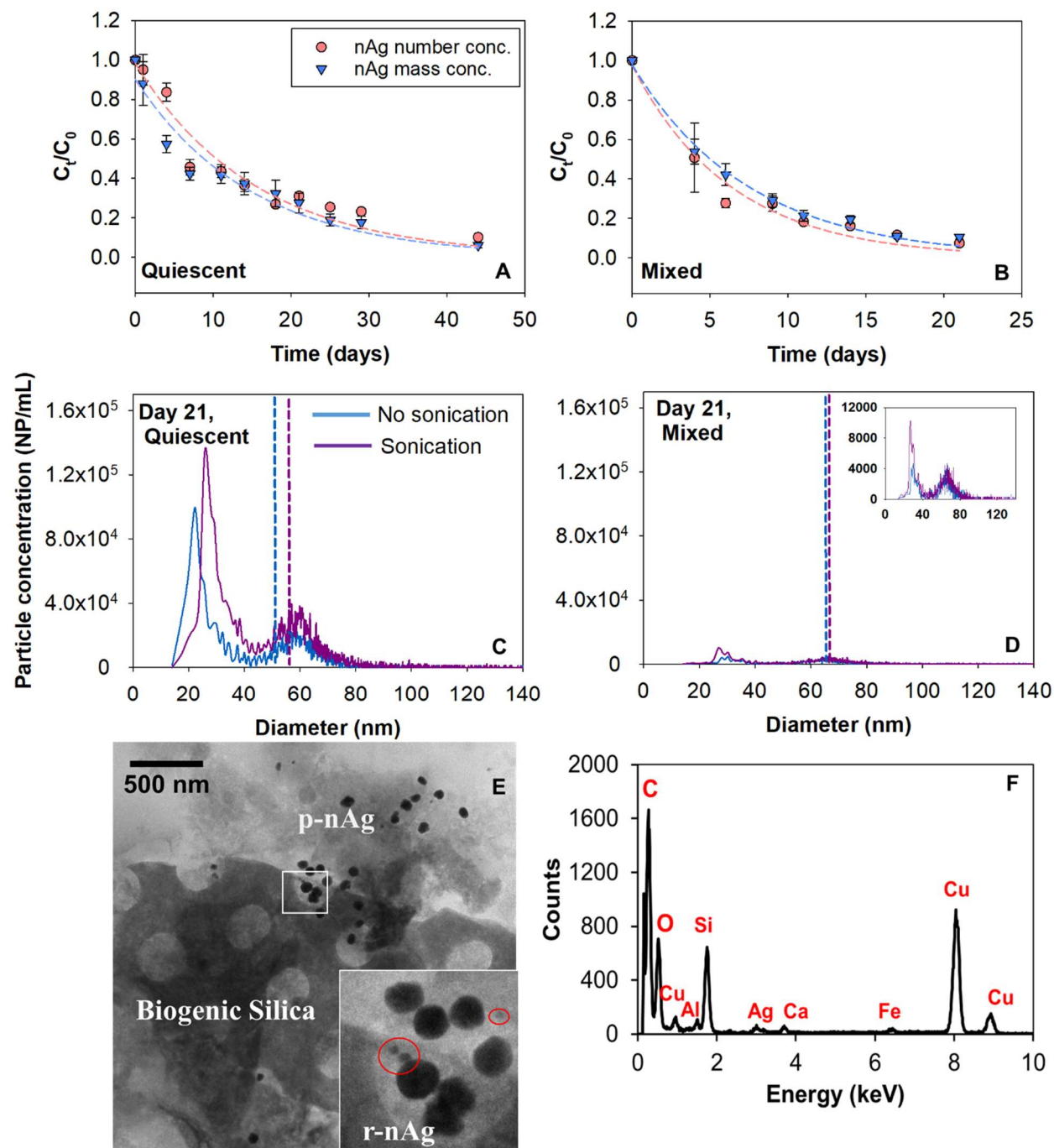
Figure 3.4: Normalized number and mass concentrations over time in UFLW (A) Quiescent (B) Mixed, dashed lines represents non-linear least square regression of experimental data. Effect of

sonication on release of nAg and change in particle size distributions in UFLW microcosms under (C) Quiescent conditions and (D) Mixed conditions. Vertical dashed lines represent mean diameters calculated by spICP-MS (E) TEM image of nAg in UFLW (F) EDS of sampled region.

A 2.5 fold increase in sedimentation rate constant in mixed system compared to the quiescent system can be attributed to increased collisions between nAg and natural colloids (heteroagglomeration) owing to the external mixing.(Walters et al. 2013, Ilona et al. 2014) These sedimentation results are consistent with the results obtained by Velzeboer *et al*., who showed that sedimentation rate constants were between one and two orders of magnitude higher in mixed systems compared to stagnant systems (Velzeboer et al. 2014).

Due to the complexity of the system, it is challenging to differentiate the impacts of sedimentation and agglomeration occurring in UFLW. Nevertheless, as explained in the previous section; if there is homoagglomeration, the following phenomena should occur; (a) shift in particle size distribution upon sonication (b) C_t/C_0 trends of number and mass concentrations should differ due to lower number concentrations compared to mass concentrations. Unlike the trends observed in FLW systems (Figure 3.3 (A)), there is no significant difference between mass and number normalized concentrations over time (Figure 3.4 (A), (B)) in UFLW systems. The number concentration of natural colloids was determined to be approximately 200 times greater than the spiked PVP-nAg suggesting heteroagglomeration between PVP-nAg and the natural colloids as the dominant process influencing nAg concentrations. TEM images of UFLW sampled near the bottom on the microcosm revealed presence of nAg with structures that resemble biogenic silica (MA 1986). EDS confirmed the presence of Ag^0 and Si (Figure 3.4 (E) and (F)). In FLW, no such natural colloid elements were detected using EDS (Figure S 3.12).

Sonication led to small increases in r-nAg number concentrations in UFLW samples (Figure 3.4 (C), (D)). Under quiescent conditions, a release of 1.1×10^6 NP/mL upon sonication (15.4% was <40 nm and 84.6% was >40 nm) after 21 days was observed. A release of 7.5×10^4 NP/mL (33.4% was <40 nm and 66.6% was >40 nm) was observed under mixed conditions. However, the absence of any significant shift in particle size distributions upon sonication in the presence of colloids (mixed and quiescent), along with the similar rates of change in particle and number and mass concentrations suggest that heteroagglomeration-induced sedimentation was the predominant phenomena in UFLW systems.

3.3.6 nAg are persistent in suspension over several weeks

A measureable fraction of p-nAg and r-nAg were present in suspension at the end of 21 days or 44 days in all systems (Figure 3.5 (A), (B)). In Table 3.1, Column 1 shows the mass and number fractions remaining in the water column and was quantified based on analysis of the non-sonicated samples (includes nAg$_{pristine}$ as well as agglomerates of p-nAg and r-nAg). The difference in sonicated and non-sonicated samples were calculated to determine the fraction of r-nAg (Table 3.1, Column 1A) and nAg$_{pristine}$ (Table 1, Column 1B) that was agglomerated. The settled fraction (Table 3.1, Column 4) was estimated as the difference between the initial spiked concentration and the suspended and dissolved concentrations.
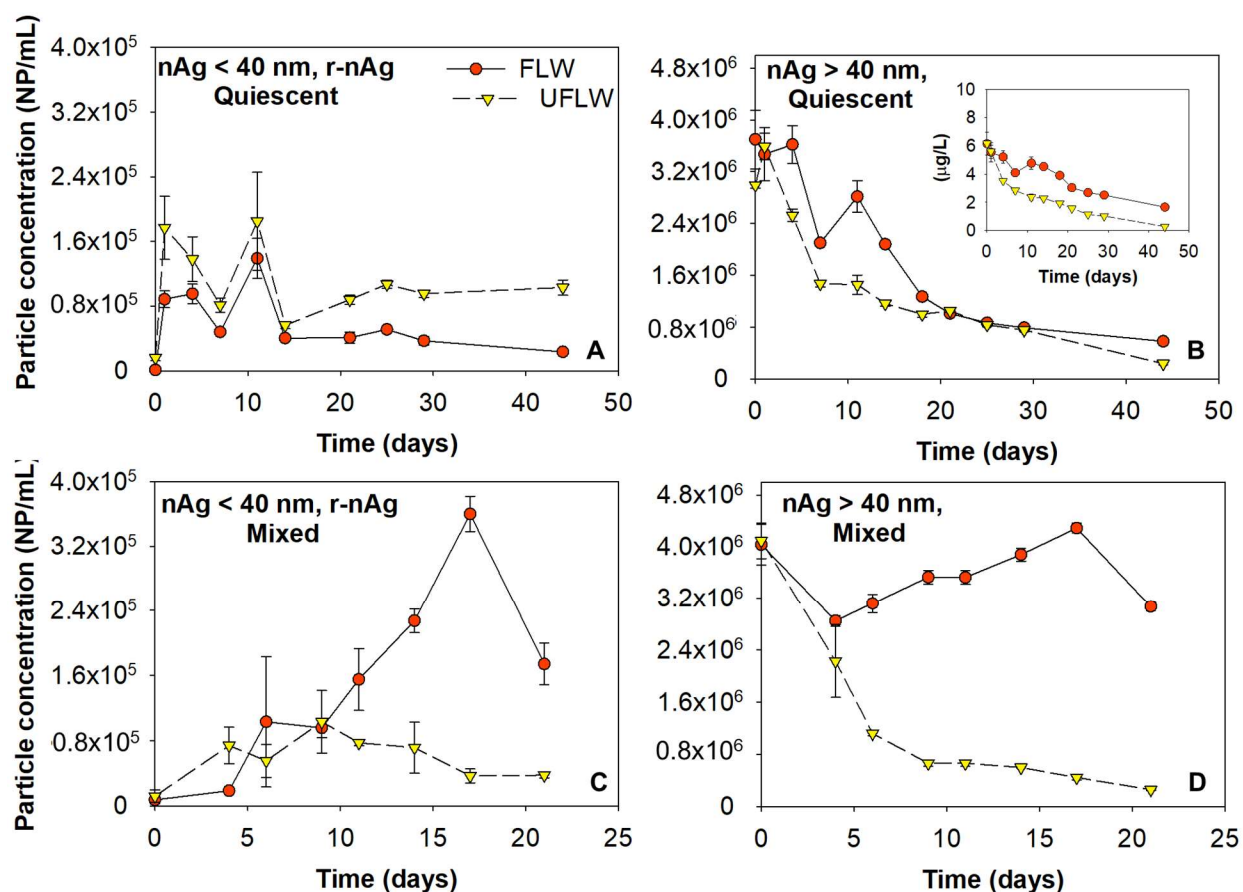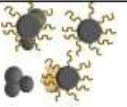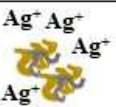
Figure 3.5: Suspended/free r-nAg and p-nAg concentrations in both FLW and UFLW under (A and B) Quiescent conditions (C and D) Mixed conditions, respectively. Inset in (B) is the mass concentration of nAg > 40 nm nAg.

Table 3.1 shows that for p-nAg, in both the quiescent condition and the mixed condition, at the end of the incubation period (21 days for mixed systems and 44 days for the quiescent systems), more particles remained in suspension in the FLW system (75.3% for mixed system and 15.7% for quiescent system) compared to the UFLW system (6.4% for the mixed system and 5.9% for the quiescent system). This can be attributed to more sedimentation induced by heteroagglomeration between nAg and natural colloids in UFLW. Similar trends were observed for r-nAg under mixed conditions with higher amounts of r-nAg present in the FLW (4.3%)

compared to UFLW (0.9%). Both heteroaggregation, and the lower amounts of r-nAg formed in UFLW (Figure 3.3 (B), 3.4 (D)) are underlying causes. However, under quiescent conditions, more r-nAg remained in the suspension in UFLW (2.6%) compared to FLW (0.6%), even though comparable numbers of r-nAg were formed in the two systems (Figures 3.3 (A), 3.4 (C)). The reason for this difference in unclear.

Table 3.1: Summary of the distribution of r-nAg and p-nAg in Mont St. Hilaire lake water in the presence and absence of colloids on day 21 and day 44, respectively. The values reported in Percentages reported are concentrations of nAg or dissolved Ag present relative to the initial dosed nAg$_{pristine}$ concentration.

System	Suspended nAg > 40 nm	After Sonication		Suspended nAg < 40 nm (r-nAg)	Dissolved Ag	Settled fraction, All nAg sizes
		Released r-nAg from agglomerates	Released nAg$_{pristine}$ from agglomerates		Ag$^+$ Ag$^+$ Ag$^+$ Ag$^+$	
	(1)	(1A)	(1B)	(2)	(3)	(4) = Initial − (1) − (2) − (3)
			Mass concentration			
FLW$_{mixed, 21d}$	105.0%	0.02 µg/L	-	0.4%	3.5%	-
UFLW$_{mixed, 21d}$	9.8%	0.004 µg/L	0.2 µg/L	0.1%	1.1%	89.4%
FLW$_{quiescent, 21d}$	0.1%	0.15 µg/L	1.9 µg/L	54.9%	0.0%	52.7%
UFLW$_{quiescent, 21d}$	0.3%	0.06 µg/L	2.2 µg/L	25.1%	2.5%	73.0%
FLW$_{quiescent, 44d}$	28.9%	0.05 µg/L	-	0.1%	2.8%	67.0%
UFLW$_{quiescent, 44d}$	4.5%	-	0.3 µg/L	0.3%	4.6%	89.6%
			Number concentration			
FLW$_{mixed, 21d}$	75.3%	$2.7 * 10^5$ NP/mL	-	4.3%	-	20.5%
UFLW$_{mixed, 21d}$	6.4%	$2.5 *10^4$ NP/mL	$6 * 10^4$ NP/mL	0.9%	-	92.7%
FLW$_{quiescent, 21d}$	27.3%	$1.1 * 10^6$ NP/mL	$1.5 * 10^6$ NP/mL	1.1%	-	69.5%
UFLW$_{quiescent, 21d}$	28.4%	$1.6 *10^5$ NP/mL	$1.1 * 10^6$ NP/mL	2.5%	-	69.0%
FLW$_{quiescent, 44d}$	15.7%	$5.6 * 10^5$ NP/mL	$1.8 * 10^6$ NP/mL	0.6%	-	83.8%
UFLW$_{quiescent, 44d}$	5.9%	-	$4.2 *10^4$ NP/mL	2.6%	-	89.9%

The extended presence of both p-nAg and r-nAg in the water column in UFLW systems is likely because (i) heteroagglomeration between nAg and natural colloids was much slower than the

sedimentation of the natural colloids, making heteroagglomeration the rate-limiting step, and (ii) the natural colloids in suspension at the end of the experiment were very colloidally stable with negligible settling velocity. Even after 6-months of quiescent incubation the natural colloid concentrations was ~10% of the initial number count, as obtained using NTA (35 to 400 nm diameter), confirming the presence of a stable fraction of natural colloids.

Persistence of nAg in the water column has also been reported elsewhere with 3.8 % of 500 µg/L PVP-nAg suspension in river water remaining at the end of 14 days under mixed conditions (Velzeboer et al. 2014). In the absence of mixing, 23.2 % of the spiked 500 µg/L PVP-nAg was still in suspension in fresh water at the end of 14 days (Quik et al. 2014). In another study, PVP-nAg (~ 11 nm, dosed at 100 µg/L) in a lake water microcosm was reported to be persistent in the water column for up to 28 days (Ellis et al. 2018). Although persistence of nAg in the water column was investigated before, no characterization on the speciation and particle number concentration of nAg was performed. Furthermore, those previous studies have evaluated colloidal stability of nAg in natural waters by dosed at concentrations at least 10-times higher than this study. By using sp-ICP-MS, this study demonstrated that a fraction of both nAg$_{pristine}$ and r-nAg remain colloidally stable, while the remained settles after homo and heteroagglomeration, even when nAg$_{pristine}$ is added at a low, close to environmentally relevant concentration for surface waters of 6 µg/L. This study also highlights the importance of investigating both the particle mass and particle number concentrations when investigating the behavior of NPs in the water system. Under mixed conditions, the r-nAg mass concentration remaining in the FLW and UFLW water column was only 0.4% and 0.1 %, respectively. of the initial nAg$_{pristine}$ mass concentration. However, this represents 4.3% and 0.9% of the initial particle concentration. Particle sizes and concentrations provide data on particle surface areas, which may provide an alternative basis for

toxicity and risk potential. Only reporting mass concentration of NPs in the water system might thus resulted in biased understanding of their potential risks.

3.4 Conclusions

Ag^+ released by dissolution from 80 nm PVP-coated $nAg_{pristine}$ was precipitated as $r\text{-}nAg^0$ with a mean diameter of ~ 26 nm, thus dramatically changing the particle size distributions over time. The reaction occurred under dark conditions in both FLW and UFLW and mixed and quiescent systems. Fewer r-nAg were formed in mixed systems compared to quiescent systems for both FLW and UFLW. Homoagglomeration of r-nAg and $nAg_{pristine}$ was the dominant fate process in the absence of natural colloids (FLW), whereas heteroagglomeration of both r-nAg and p-nAg with natural colloids dominated in UFLW. The sedimentation rates of total nAg mass was higher in UFLW than in FLW, and heteroaggregation was a more dominant process for removal of nAg from the aqueous phase. At the end of the experiments (21 days for mixed systems and 44 days for quiescent systems), varying amounts of r-nAg and p-nAg remained in the water column depending on the system conditions.

Current ENP fate and transport models and risk assessments do not account for formation of re-precipitated particles and their fate in aquatic ecosystems. The detailed size distribution data from sp ICP-MS analysis presented herein will be used to support modeling of the re-precipitation and their agglomeration behavior in future studies, towards providing a more robust analysis of Ag fate in aquatic systems. Detailed characterization of nAg speciation using sensitive techniques, as reported in this study, is important for through quantitative assessments of fate processes, and characterization based on mean diameters and total Ag concentrations would not have captured the re-precipitated particles and their fate.

3.5 Acknowledgements

3.6 Supplementary Information
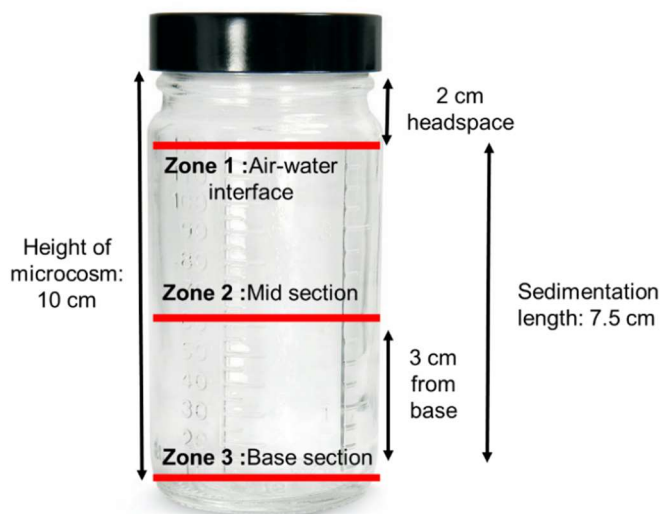
Figure S 3.1: Fate experiment microcosm set-up

spICP-MS Conditions

The integration dwell time of 100 μs was used throughout all experiments. Sampling time was set to 100 s and a wash time of 90 s between samples. Duplicate samples were collected at every time point, and each sample was measured three times. Transport efficiency was calculated using 57.1 nm ultra-uniform nAu stabilized with PEG-COOH (nanoComposix) with a mass concentration of

170 ng/L. Transport efficiency values were between 6 and 8% for all time points measured. Silver calibration curve was made using dissolved silver standards (SCP Science) between 10 ng/L and 1000 ng/L in 1% ICP grade nitric acid.

Table S 3.1: Instrument operating parameters of NexION 300X spICP-MS

spICP-MS	
Sample Uptake Rate (ml/min)	0.28-0.34
Nebulizer and Spray Chamber	Glass Concentric
RF Power (w)	1600
Analysis time (s)	90- 120
Dwell time (μs)	100

Mass balances of Silver

Mass balances of nAg were done using a method previously established in our lab(Azodi et al. 2016). The total mass measured using spICP-MS (sum of dissolved and particle mass) should compare with total acid digested silver in the same sample at the same time point. A method was developed by spiking nAg in LW, FLW and DI water and measured total mass in single particle mode as well as total metals analysis by digesting nAg with 67% ICP grade nitric acid on a hot-block for 60 minutes at 90^0C. Samples from mixed filtered LW systems at different time points were also analysed for mass balances.
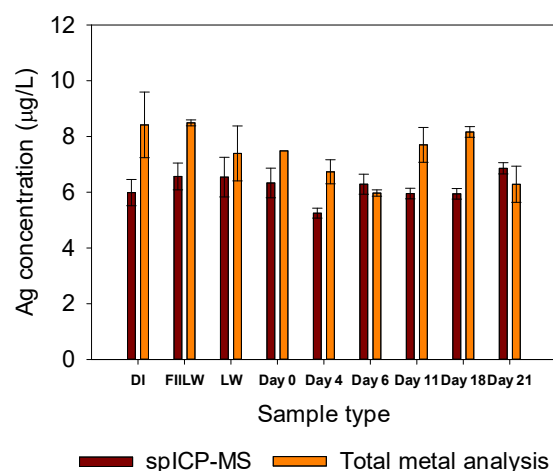
Figure S 3.2: Silver mass balance (Time: mixed systems in FLW) digested versus spICP-MS

We observed lower masses in spICP-MS, this may be because of adsorption of nAg particles to centrifuge tubes or tubing in the instrument. All samples were vortexed between measurements.

Lake water Analysis:

Lac Hertel has an area of 0.3 km^2 with maximum depth of 9 m. The lake is fed by at least three permanent streams and drained by only one. All anthropogenic activities like bathing, fishing, and swimming are forbidden and there is no agricultural or urban runoff that enters the lake. We determined the elemental composition of the filtrate of ultrafiltered (3 kDa, Millipore) lake water (which should only consist of dissolved ions that pass through the filter). Our results indicated the presence of Cu, Zn, Al, Si in the dissolved form. The exact elemental composition is reported in Table S 3.2.

Table S 3.2: Characteristics of lake water used in study

Characteristics of lake water from Mont-Saint-Hilaire					
pH	7.5	Calcium, mg/L	9.4	Iron, mg/L	0.0015
Conductivity , μs/cm	93.4	Magnesium, mg/L	1.2	Fluoride, mg/L	0.2
TSS, mg/L	2.7	Potassium, mg/L	0.1	Chloride, mg/L	1.0
DOC, mg/L	3.5	Zinc, mg/L	0.0	Nitrate, mg/L	1.1
Zeta potential of LW colloids, mV	-17.7	Sodium, mg/L	1.9	Sulfate, mg/L	5.5
DO, mg/L	10.4	Silica, mg/L	1.5	Total Sulfur, mg/L	2.7

Colloidal size analysis of lake water was performed by concentrating lake water colloids by centrifugation at 4500g for 30 minutes and measured using Horiba Laser Scattering Particle Size Analyzer, all samples were sonicated before analysis (Figure S2).
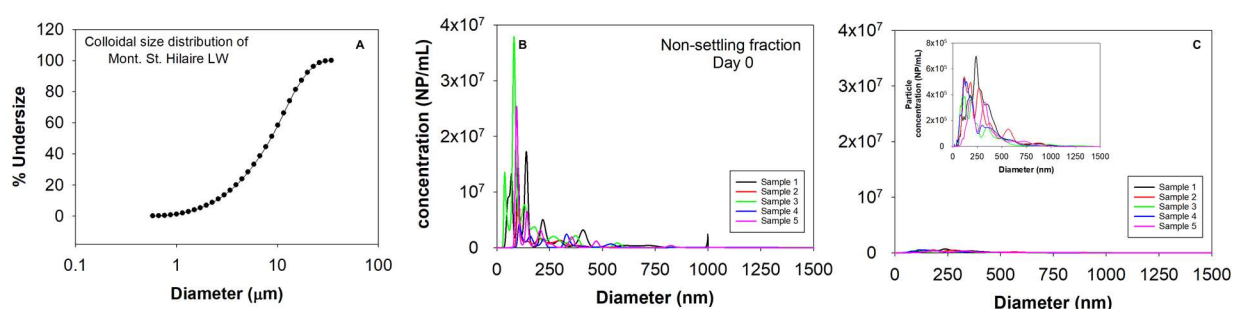
Figure S 3.3: (A) Colloidal size distribution of lake water measured using laser light scattering. Size distribution of natural colloids obtained using NTA on (B) Day 0 (C) ~ 6 months

The lake water was also characterized for pH, conductivity, zeta potential, total suspended solids, total ions (anion and cation analysis), dissolved organic carbon and size distribution of colloids. For FLW, lake water was centrifuged at 4500g for 30 min and the supernatant was collected. The supernatant was filtered through 0.1 μm (cellulose acetate membrane) filter and stored at 4 °C until further use.

Zeta Potential: The zeta potential and conductivity were determined using DLS (ZetaSizer Nano ZS, Malvern). PVP-nAg in UFLW had a negative zeta potential of (- 14.3 ± 0.6 mV). There was a decrease in the negative zeta potential of nAg in FLW (-11.5 ± 0.9 mV).

Total suspended solids: Whatman™ 934-AH™ Glass Microfiber filters were carefully placed in aluminum weigh boats and dried overnight in an over at 105^0C. Total weight of filter plus boat were noted before filtering 100 mL of lake water through vaccum filtration. Filters with solids were dried for 24 hours at 105^0C and weighed. TSS was calculated as follows:

$$\frac{\text{Final weight} - \text{Initial weight (mg)}}{\text{Volume (L)}}$$

Dissolved organic carbon: Lake water samples were filtered through 0.45 micron PTFE syringe filters and analysed for DOC using TOC analyser.

Elemental analysis: Total metal ions were determined using ICP-OES (Perkin Elmer Optima 8300) by digesting lake water in aqua regia (HNO_3:HCl, 1:3) on a hot block (Perkin Elmer) at 90^0 C for 45 min. Water was added to these samples to reduce the acid content to <5% and measured using ICP-OES. IC analysis (ICS-5000 ThermoFisher) was done with a Dionex IonPac AS18-4 μm, 2×150 mm , mobile phase 32 mM KOH and flow rate: 0.25 mL/min. The suppressor was Dionex ERS 500 Suppressor (2 mm) and a conductivity detector was used.

Colloidal size analysis of lake water was performed by concentrating natural lake water colloids by centrifugation at 4500g for 30 minutes and measured using Horiba Laser Scattering Particle Size Analyzer.
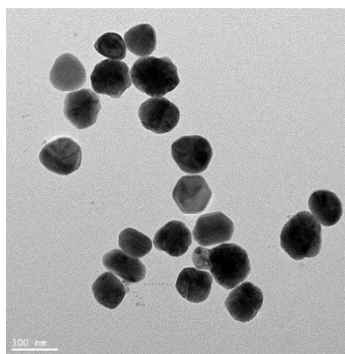
Figure S 3.4: TEM image of pristine nAg-PVP 80 nm `
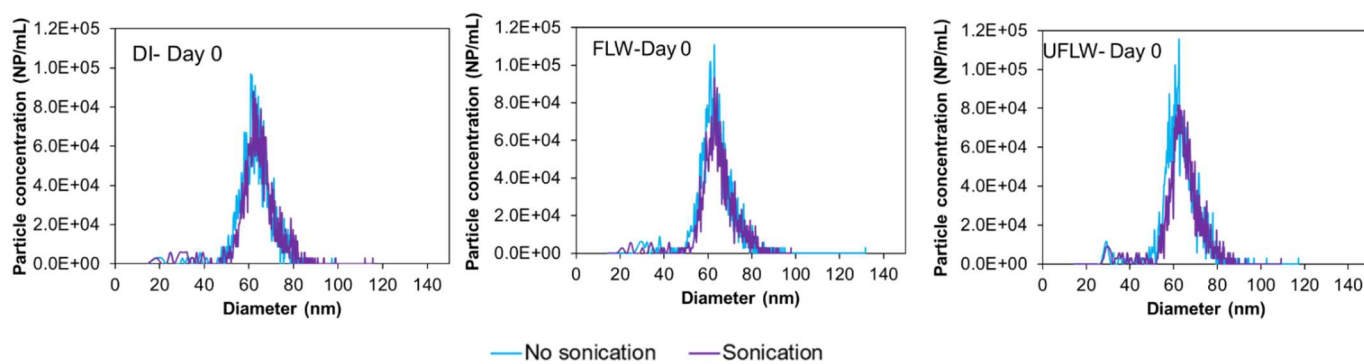
Figure S 3.5: Effect of sonication on spiked nAg in DI, FLW and UFLW systems
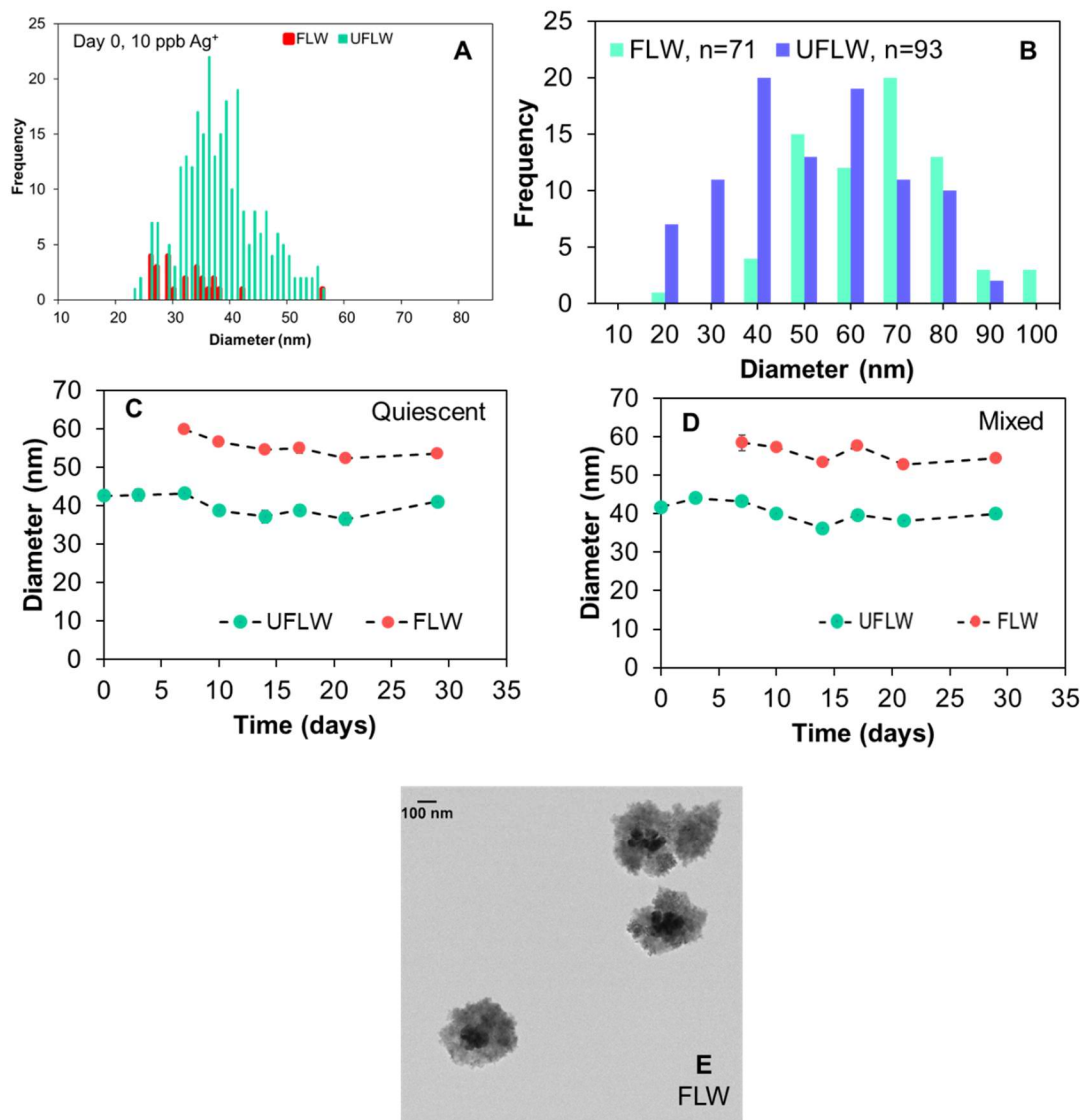
Figure S 3.6: (A) Frequency of precipitated nAg on Day 0 spiked with 10 µg/L Ag⁺. TEM size distribution of precipitated nAg from spiked Ag⁺ ions in (B) UFLW and FLW. Diameter of naturally formed nAg in (C) Quiescent (D) Mixed. TEM image of nAg cluster in DOM in FLW (E).
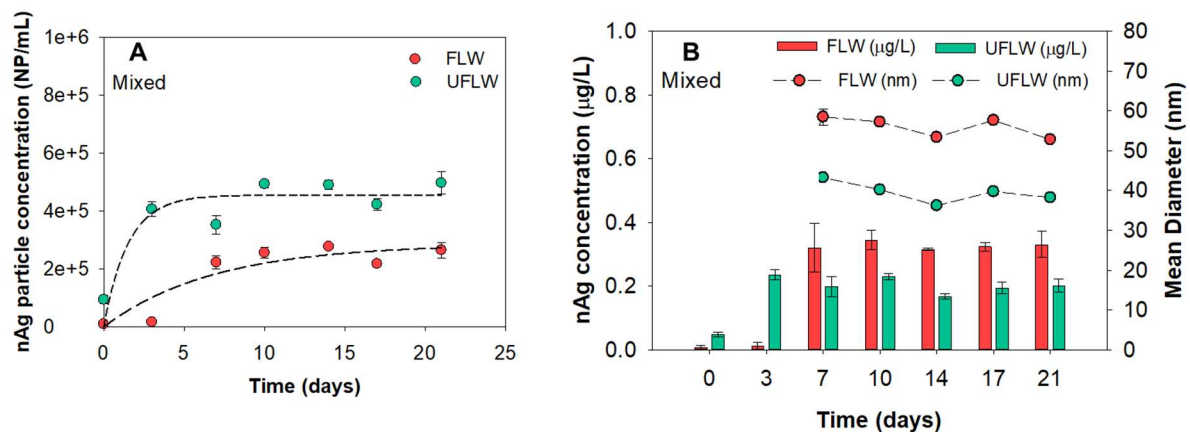
Figure S 3.7: (A) Change in nAg particle concentration due to reformation from 10 µg/L spiked Ag$^+$. Dashed line represents non-linear regression of experimental data (UFLW: 0.66 day^{-1}, FLW: 0.15 day^{-1}) (B) Change in mean diameters and mass concentration of re-precipitated nAg over time.
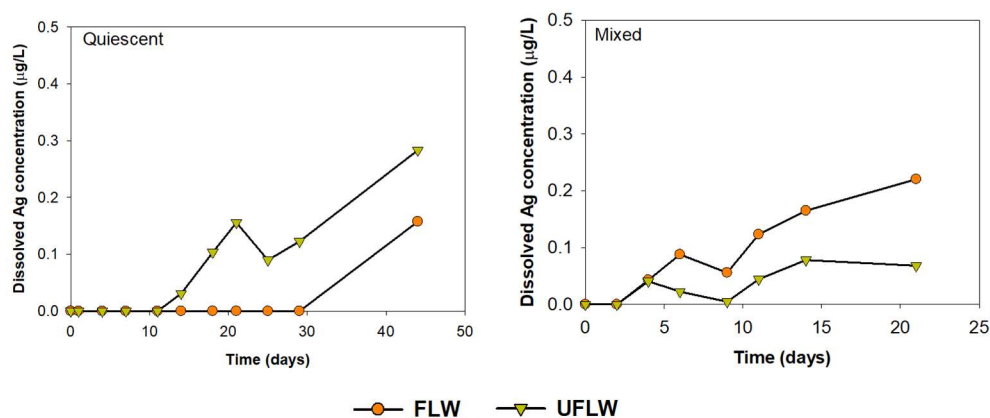
Figure S 3.8: Dissolved silver concentrations in filtered LW and LW systems over time under both quiescent and mixed conditions.
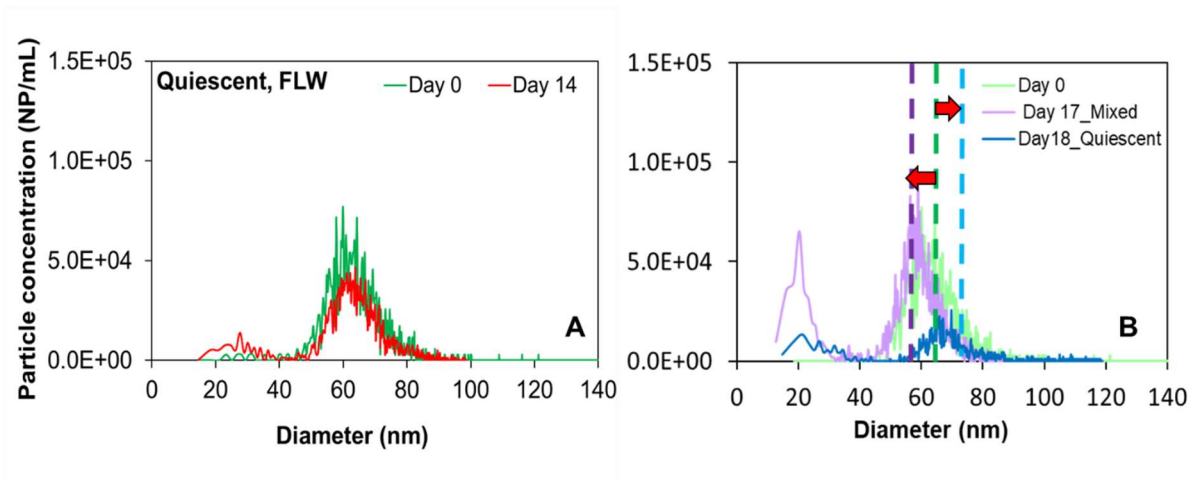
Figure S 3.9: (A) Particle size distribution of nAg at the mid-section on day 0 and day 14 (B) Particle size distributions of nAg at the mid-sections in FLW under mixed and quiescent conditions.
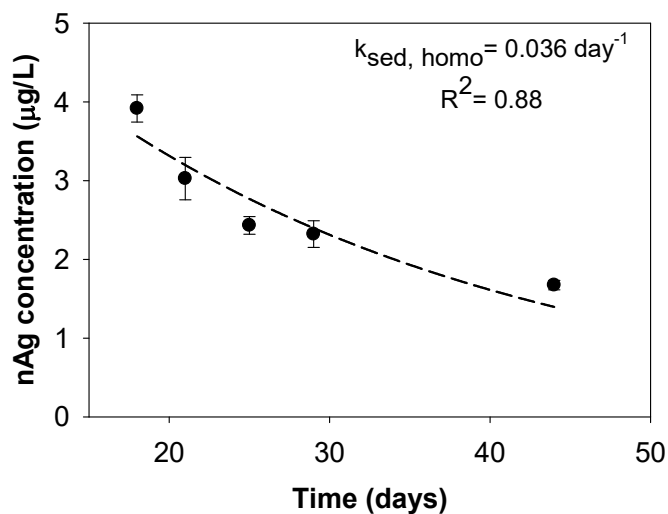
Figure S 3.10: Homoagglomeration induced sedimentation of nAg in FLW under quiescent conditions using mass concentration of nAg over time.
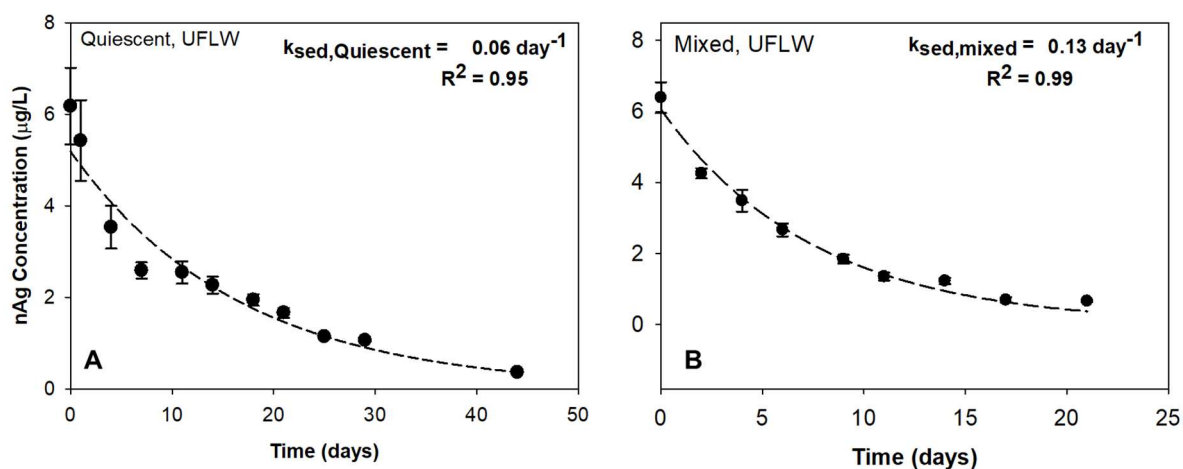
Figure S 3.11: Sedimentation data: decrease in nAg mass concentration over time in UFLW systems
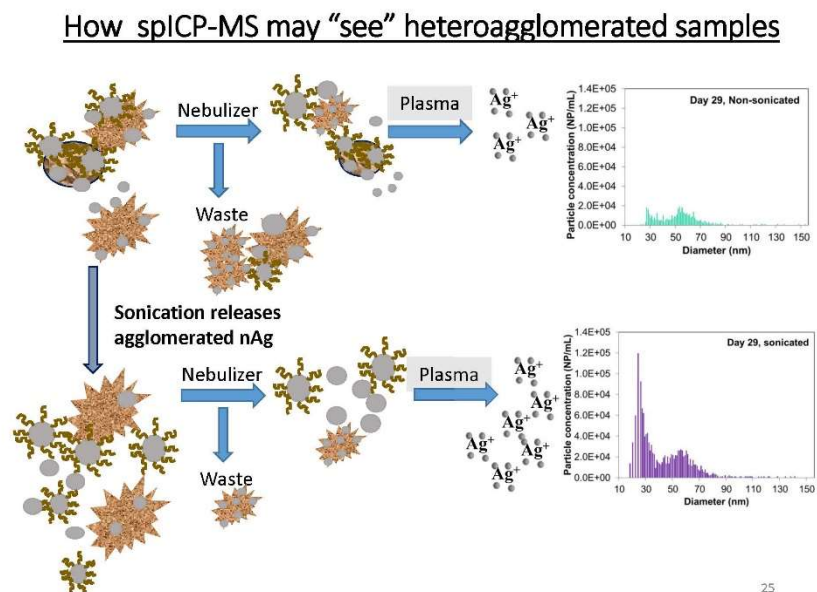
Figure S 3.12: Depiction of heteroagglomerates (nAg and colloids) upon entering spICP-MS
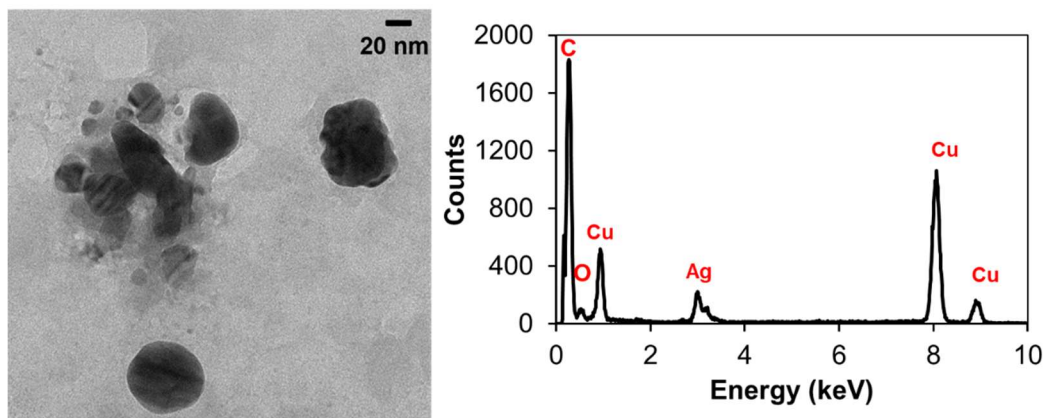
Figure S 3.13: TEM image of nAg in FLW and EDS of the imaged area
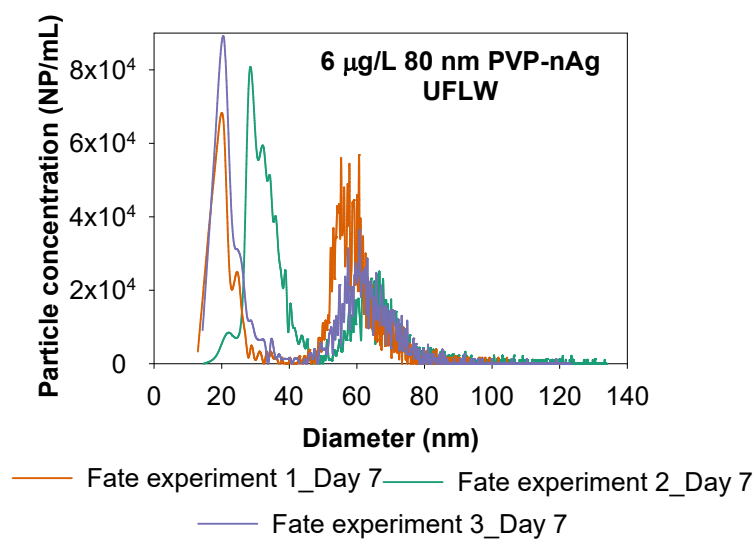
Figure S 3.14: Experimental replicates of 80 nm PVP-nAg spiked in UFLW at 6 µg/L
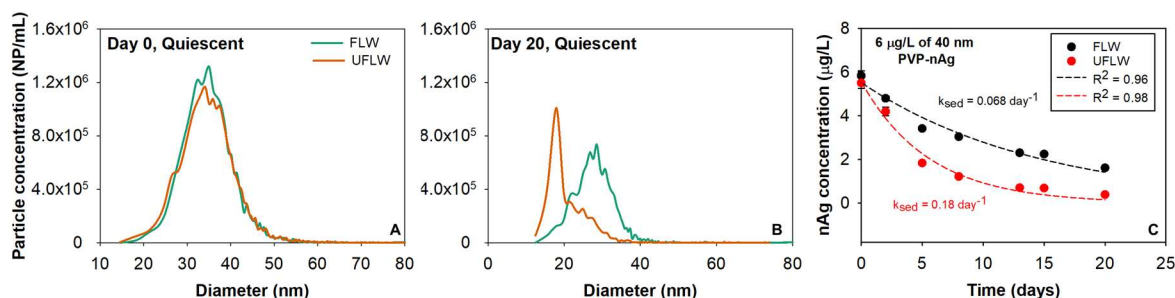
Figure S 3.15: Fate experiment of 40 nm PVP-nAg spiked in UFLW and FLW at 6 µg/L. Particle size distribution of 40 nm PVP-nAg in FLW and UFLW on (A) day 0 (B) day 20 (C) sedimentation data and calculated sedimentation rates of 40 nm PVP-nAg over time.

3.7 References

1) Adam, V., et al. (2016). "Aggregation behaviour of TiO2 nanoparticles in natural river water." Journal of Nanoparticle Research **18**(1): 13.

2) Adegboyega, N. F., et al. (2013). "Interactions of Aqueous Ag+ with Fulvic Acids: Mechanisms of Silver Nanoparticle Formation and Investigation of Stability." Environmental Science & Technology **47**(2): 757-764.

3) Akaighe, N., et al. (2011). "Humic Acid-Induced Silver Nanoparticle Formation Under Environmentally Relevant Conditions." Environmental Science & Technology **45**(9): 3895-3901.

4) Azodi, M., et al. (2016). "Dissolution Behavior of Silver Nanoparticles and Formation of Secondary Silver Nanoparticles in Municipal Wastewater by Single-Particle ICP-MS." Environmental Science & Technology **50**(24): 13318-13327.

5) Baalousha, M., et al. (2013). "Effect of monovalent and divalent cations, anions and fulvic acid on aggregation of citrate-coated silver nanoparticles." Science of The Total Environment **454-455**: 119-131.

6) Badawy, A. M. E., et al. (2010). "Impact of Environmental Conditions (pH, Ionic Strength, and Electrolyte Type) on the Surface Charge and Aggregation of Silver Nanoparticles Suspensions." Environmental Science & Technology **44**(4): 1260-1266.

7) Ellis, L.-J. A., et al. (2018). "Seasonal variability of natural water chemistry affects the fate and behaviour of silver nanoparticles." Chemosphere **191**: 616-625.

8) Fabrega, J., et al. (2009). "Interactions of Silver Nanoparticles with Pseudomonas putida Biofilms." Environmental Science & Technology **43**(23): 9004-9009.

9) Filipe, V., et al. (2010). "Critical Evaluation of Nanoparticle Tracking Analysis (NTA) by NanoSight for the Measurement of Nanoparticles and Protein Aggregates." Pharmaceutical Research **27**(5): 796-810.

10) Geranio, L., et al. (2009). "The Behavior of Silver Nanotextiles during Washing." Environmental Science & Technology **43**(21): 8113-8118.

11) He, D., et al. (2012). "H2O2-Mediated Oxidation of Zero-Valent Silver and Resultant Interactions among Silver Nanoparticles, Silver Ions, and Reactive Oxygen Species." Langmuir **28**(27): 10266-10275.

12) He, D., et al. (2019). "Silver sulfide nanoparticles in aqueous environments: formation, transformation and toxicity." Environmental Science: Nano.

13) Hou, W.-C., et al. (2013). "Sunlight-driven reduction of silver ions by natural organic matter: formation and transformation of silver nanoparticles." Environmental Science & Technology **47**(14): 7713-7721.

14) Huynh, K. A. and K. L. Chen (2014). "Disaggregation of heteroaggregates composed of multiwalled carbon nanotubes and hematite nanoparticles." Environmental Science: Processes & Impacts **16**(6): 1371-1378.

15) Ilona, V., et al. (2014). "Rapid settling of nanoparticles due to heteroaggregation with suspended sediment." Environmental Toxicology and Chemistry **33**(8): 1766-1773.

16) Jones, A. M., et al. (2011). "Superoxide-Mediated Formation and Charging of Silver Nanoparticles." Environmental Science & Technology **45**(4): 1428-1434.

17) Kaegi, R., et al. (2013). "Fate and transformation of silver nanoparticles in urban wastewater systems." Water Research **47**(12): 3866-3877.

18) Kaegi, R., et al. (2011). "Behavior of Metallic Silver Nanoparticles in a Pilot Wastewater Treatment Plant." Environmental Science & Technology **45**(9): 3902-3908.

19) Keller, A. A., et al. (2010). "Stability and Aggregation of Metal Oxide Nanoparticles in Natural Aqueous Matrices." Environmental Science & Technology **44**(6): 1962-1967.

20) Kittler, S., et al. (2010). "Toxicity of Silver Nanoparticles Increases during Storage Because of Slow Dissolution under Release of Silver Ions." Chemistry of Materials **22**(16): 4548-4554.

21) Kvítek, L., et al. (2008). "Effect of Surfactants and Polymers on Stability and Antibacterial Activity of Silver Nanoparticles (NPs)." The Journal of Physical Chemistry C **112**(15): 5825-5834.

22) Levard, C., et al. (2012). "Environmental Transformations of Silver Nanoparticles: Impact on Stability and Toxicity." Environmental Science & Technology **46**(13): 6900-6914.

23) Levard, C., et al. (2013). "Effect of Chloride on the Dissolution Rate of Silver Nanoparticles and Toxicity to E. coli." Environmental Science & Technology **47**(11): 5738-5745.

24) Li, R., et al. (2019). "In Situ Production of Ag/Polymer Asymmetric Nanoparticles via a Powerful Light-Driven Technique." Journal of the American Chemical Society.

25) Li, X. and J. J. Lenhart (2012). "Aggregation and Dissolution of Silver Nanoparticles in Natural Surface Water." Environmental Science & Technology **46**(10): 5378-5386.

26) Li, X., et al. (2010). "Dissolution-Accompanied Aggregation Kinetics of Silver Nanoparticles." Langmuir **26**(22): 16690-16698.

27) Liu, J. and R. H. Hurt (2010). "Ion Release Kinetics and Particle Persistence in Aqueous Nano-Silver Colloids." Environmental Science & Technology **44**(6): 2169-2175.

28) MA, S. (1986). "Structural aspects of biogenic silica." Silicon biochemistry: 40.

29) Markus, A., et al. (2015). "Modeling aggregation and sedimentation of nanoparticles in the aquatic environment." Science of the Total Environment **506**: 323-329.

30) Mueller, N. C. and B. Nowack (2008). "Exposure Modeling of Engineered Nanoparticles in the Environment." Environmental Science & Technology **42**(12): 4447-4453.

31) Park, M. V. D. Z., et al. (2011). "The effect of particle size on the cytotoxicity, inflammation, developmental toxicity and genotoxicity of silver nanoparticles." Biomaterials **32**(36): 9810-9817.

32) Philippe, A. and G. E. Schaumann (2014). "Interactions of Dissolved Organic Matter with Natural and Engineered Inorganic Colloids: A Review." Environmental Science & Technology **48**(16): 8946-8962.

33) Praetorius, A., et al. (2014). "Heteroaggregation of Titanium Dioxide Nanoparticles with Model Natural Colloids under Environmentally Relevant Conditions." Environmental Science & Technology **48**(18): 10690-10698.

34) Quik, J. T. K., et al. (2014). "Simplifying modeling of nanoparticle aggregation–sedimentation behavior in environmental systems: A theoretical analysis." Water Research **62**: 193-201.

35) Quik, J. T. K., et al. (2014). "Heteroaggregation and sedimentation rates for nanomaterials in natural waters." Water Research **48**: 269-279.

36) Rong, H., et al. (2018). "In vitro characterization of reactive oxygen species (ROS) generation by the commercially available Mesosilver™ dietary supplement." Environmental Science: Nano **5**(11): 2686-2698.

37) Sharma, V. K., et al. (2014). "Organic-coated silver nanoparticles in biological and environmental conditions: Fate, stability and toxicity." Advances in Colloid and Interface Science **204**: 15-34.

38) Velzeboer, I., et al. (2014). "Rapid settling of nanoparticles due to heteroaggregation with suspended sediment." Environmental Toxicology and Chemistry **33**(8): 1766-1773.

39) Walters, C., et al. (2013). "Aggregation and dissolution of silver nanoparticles in a laboratory-based freshwater microcosm under simulated environmental conditions." Toxicological & Environmental Chemistry **95**(10): 1690-1701.

40) Wang, H., et al. (2015). "Heteroaggregation of nanoparticles with biocolloids and geocolloids." Advances in Colloid and Interface Science **226**: 24-36.

41) Wimmer, A., et al. (2018). "New insights into the formation of silver-based nanoparticles under natural and semi-natural conditions." Water Research **141**: 227-234.

42) Yin, Y., et al. (2012). "Sunlight-induced reduction of ionic Ag and Au to metallic nanoparticles by dissolved organic matter." ACS nano **6**(9): 7910-7919.

43) Zhou, D., et al. (2012). "Clay Particles Destabilize Engineered Nanoparticles in Aqueous Environments." Environmental Science & Technology **46**(14): 7520-7526.

44) Zhu, M., et al. (2014). "The effect of humic acid on the aggregation of titanium dioxide nanoparticles under different pH and ionic strengths." Science of The Total Environment **487**: 375-380.

Chapter 4 . Extent of silver nanoparticle sulfidation in a polydisperse population is independent of particle size

Connecting Text: Chapter 3 studied the fate of nAg in lake water. However, in other aquatic environmental compartments such as wastewater treatment plants, other fate processes may be more dominant. For example, the presence of sulfides leads to sulfidation of nAg in aquatic systems, which has shown to reduce toxicity of nAg particles. However, recent studies showing persistent toxicity of sulfidated nAg which necessitates the need to examine the sulfidation mechanism in a more comprehensive manner. This chapter evaluates the influence of particle size and S/Ag dose available on extent of sulfidation.

The results from this study will be submitted to the following journal Environmental Pollution:

Rao S., Hofmann T., Kammer F., Ghoshal S., (2020) Extent of silver nanoparticle sulfidation in a polydisperse population is independent of particle size.

4.1 Introduction

Silver nanoparticles (nAg) are one of the most widely used engineered nanoparticles (nAg) in consumer products (Sharma et al. 2014). The increasing use of nAg (Gottschalk et al. 2009, Keller and Lazareva 2013, Keller et al. 2013, Garner and Keller 2014, Garner et al. 2017) leads to their inevitable release into the environment. Upon entering the aquatic environment, they may undergo transformation processes such as, aggregation (Fabrega et al. 2009, Kaegi et al. 2013) , dissolution (Brar et al. 2010, Kaegi et al. 2013) or surface transformation. The physical and chemical transformations of nAg following its release determines their fate, transport and bioavailability in the environment (Diegoli et al. 2008, Lin et al. 2011). A significant fraction of nAg particles are

expected to end up in the wastewater treatment plants (WWTP) (Gottschalk et al. 2009, Keller and Lazareva 2014), where they can accumulate in the sewage sludge or (Kim et al. 2010) or biosolids (Gardea-Torresdey et al. 2014, Ma et al. 2014)over time.

The presence of sulfidated nAg in sludge and pilot-scale WWTPs (Kim et al. 2010, Kaegi et al. 2011, Kent et al. 2014) suggests that sulfidation of nAg is a common transformation process which occurs during its transport through the wastewater system, prior to its release into receiving water bodies (Kim et al. 2010, Kaegi et al. 2013). Studies have shown that nAg (Levard et al. 2011) and Ag^+ (Liu et al. 2011) readily transform into Ag_2S ($K_{sp} = 6.2 \times 10^{-52}$) (Goates et al. 1951) in presence of inorganic and organic sulfur ligands (Azodi et al. 2016) leading to decreased bioavailability and therefore toxicity, as Ag^+ release from nAg is the primary mechanism for nAg toxicity (Levard et al. 2011, Collin et al. 2016). Two possible sulfidation mechanisms have been proposed for the sulfidation of nAg ; oxidative dissolution of nAg followed by sulfide precipitation (indirect sulfidation) and direct conversion of nAg to nAg_2S through the oxysulfidation reaction (Liu et al. 2011). That study demonstrated that sulfidation of nAg primarily occurs via direct conversion, as indirect sulfidation is limited by the available dissolved Ag concentration in the system. Further, nAg reacts with sulfides significantly faster than it dissolves. Factors such as dissolved oxygen levels, dissolved organic matter (DOM), pH, aqueous chemistry, initial size and coating of nAg also influence the extent of sulfidation (Levard et al. 2011, Baalousha et al. 2015, Thalmann et al. 2016, Zhu et al. 2016).

The presence of dissolved organic matter can influence the sulfidation nAg in different ways. For example, DOM enhances the colloidal stability of nanoparticles in aquatic systems due to steric stabilization (Fabrega et al. 2009, Baalousha et al. 2013, Philippe and Schaumann 2014, Sharma et al. 2014) leading to higher sulfidation rates (Liu et al. 2011, Thalmann et al. 2016). The

complexation of free HS⁻ with humic acids (HA) or organo-metal present in HA or sorption to the non-polar groups of HA decreases the availability of sulfides for sulfidation (Bhattacharjee and Ghoshal 2018). Adsorption of HA on the nanoparticle surface can influence the extent of sulfidation by either facilitating the access of HS⁻ to the surface (Thalmann et al. 2016) or by blocking the nanoparticle sulfidation reaction site by to adsorption of HA (Bhattacharjee and Ghoshal 2018). Overall, the impact of DOM on sulfidation varies between studies depending on the aquatic conditions, nature of DOM and nanoparticles (He et al. 2019).

Recent studies have shown that sulfidated nAg may still be toxic due to incomplete sulfidation. For example, Kraas *et al.* reported that nAg (average hydrodynamic diameter or d_{avg} 62 nm, Tween 20) sulfidized in soil ecosystems were a source of Ag^+ to soil microorganisms after a 140 day incubation period (Kraas et al. 2017). Sulfidated PVP-nAg ($[S/Ag]_{dose}$ molar ratio of 2) had a decreased, but still measurable toxicity to *C. elegans* compared to pristine PVP-nAg with an approximate hydrodynamic diameter of 79.6 nm due to a decrease in release of Ag^+ (Starnes et al. 2016).

The effect of nAg size distribution and aggregation state on extent of sulfidation of nAg has been previously reported. For example, in a study by Reinsch *et al.*, difference in extents of sulfidation of a monodisperse and a polydisperse suspension of PVP- nAg at a concentration of 800 mg/L was observed (Reinsch et al. 2012). Over 48 h, at an S/Ag_{dose} of 2.02, a lower sulfidation extent ($\sim[S/Ag]_{particle} = 0.36$) was observed for the polydisperse PVP-nAg particles (d_{avg} of 256 nm) compared to smaller monodisperse PVP- nAg which ($d_{avg} = 83$ nm) reached complete sulfidation ($\sim[S/Ag]_{particle} = 0.47$) (Reinsch et al. 2012). Similar reduced sulfidation reaction rates with increasing sizes were observed by Liu *et al.*, in experiments with three sizes of nAg (5 nm, 30 nm and 1- 3 μm) (Liu et al. 2011). In a study by Kaegi *et al.*, 10 nm citrate-nAg particles were

completely sulfidated ($[S/Ag]_{particle} = 0.5$) compared to only 10% of 100 nm citrate nAg within 24 hours. However, an increase in sulfidation of 100 nm particles over time indicated that, in addition to the effect of size, the depth dependence of sulfidation, the nAg structure (polycrystallinity of the nAg, which may provide additional surfaces for sulfidation) can influence the kinetics of sulfidation (Kaegi et al. 2013). The heterogeneity of sulfidation is influenced by the degree of polycrystallinity of the different nAg particles (Reinsch et al. 2012, Kaegi et al. 2013, Thalmann et al. 2014). Higher energy surfaces may get converted to Ag_2S preferentially compared to lower energy surfaces and unreacted metallic edges may be a source of Ag^+ (Baalousha et al. 2015).

Determining the actual extent of sulfidation or $[S/Ag]_{particle}$ is an important parameter in determining the fate, behaviour and bioavailability of the transformed nAg in aquatic environments, as incomplete sulfidation of nAg can continue to act as a source of Ag^+, thus retaining its toxic potential. Incomplete sulfidation may be caused due to the available sulfide dose relative to Ag mass present, and over shorter periods, due to size of nAg, which in turn can influence the sulfidation kinetics. Previous studies have shown that the extent ($[S/Ag]_{particle}$) (Reinsch et al. 2012, Kaegi et al. 2013) and rates (Liu et al. 2011, Thalmann et al. 2014, Thalmann et al. 2016) of sulfidation are dependent on particle size , however, these have only been evaluated on the whole particle population basis. If indeed size influenced the extent of sulfidation in a polydisperse population, some sizes would be less sulfidated than other sizes. The present study was designed to verify this hypothesis. Although the current methods (X-ray absorption spectroscopy (Levard et al. 2011, Reinsch et al. 2012, Collin et al. 2016, Thalmann et al. 2016), microscopy techniques; transmission electron microscope (TEM) and scanning electron microscope (SEM)) (Liu et al. 2011, Baalousha et al. 2015), X-ray diffraction (Levard et al. 2011,

Liu et al. 2011)) used for detection and characterization of sulfidated nAg provide information about the extent of sulfidation (Ag_2S formed), they are not capable of distinguishing size dependent effects of sulfidation in a polydisperse sample.

A number of particle sizing techniques, such as electron microscopy (Ma et al. 2012), UV-vis spectrophotometry (Baalousha et al. 2015), dynamic light scattering (Huynh and Chen 2011, Li and Lenhart 2012) and single particle ICP-MS (Mitrano et al. 2012, Azodi et al. 2016) have been used to characterize nAg in complex matrices. However, these techniques are not easily amenable for coupling to analytical techniques for sulfur and Ag mass measurements to obtain information on effective extents of sulfidation with size in a polydisperse particle suspension. The use of asymmetric flow field flow fraction (AF4) coupled to a downstream detector such as inductively coupled plasma mass spectrometer (ICP-MS) is a promising technique for the characterization of nanoparticles in aqueous matrices to retrieve information about particle size related properties and elemental composition (Baalousha et al. 2011, Mitrano et al. 2012, Montaño et al. 2019). Both AF4 and ICP-MS have many complementary advantages in detecting and characterizing size, particle mass and dissolved concentrations in environmental matrices (Poda et al. 2011, Hoque et al. 2012, Mitrano et al. 2012, Azodi et al. 2016). Fractionation of sulfidated nAg according to size using AF4 prior to ICP-MS analysis facilitated enhanced understanding of the effect of particle size on the extent of sulfidation of PVP-nAg.

The objective of this study was to investigate if the mass of sulfur associated with nAg particles ($S_{particle}$) vary within a size range due to higher specific surface areas of smaller particles compared to larger nAg particles. This was done by characterizing the effect of sulfide dose on the effective extent of sulfidation of a relatively polydisperse PVP-nAg suspension (20 – 120 nm). For this purpose, longer sulfidation experiments (7 days) were performed (in comparison to previous

sulfidation studies (Liu et al. 2011, Reinsch et al. 2012, Levard et al. 2013, Thalmann et al. 2016)) using PVP-nAg using three S/Ag_{dose} (0.5, 1 and 5), at stoichiometrically exact and excess doses and the extents of sulfidation were determined. The effect of natural organic matter (NOM) on extent of sulfidation was investigated by analysing the [S/Ag] system with added Suwannee River NOM, and systems without additional NOM.

4.2 Materials and Methods

4.2.1 Chemicals

Commercially available PVP-coated Econix nAg (nanoComposix, San Diego, CA, USA) at a stock concentration of 5 mg/mL was used in all experiments. spICP-MS measurements yielded a mean diameter of 67.9 ± 7.1 nm. Ultrapure water (18.2 MΩ.cm, ELGA System, Purelab, Chorus, ELGA UK) was used for preparing AF4 carrier solutions as well all samples. Sodium sulfide (407410-10G) was purchased from Sigma-Aldrich and FL-70[TM] concentrate from Thermo Fisher Scientific (New Jersey, USA). Sulfur (1000 mg/L S) and silver (1000 mg/L) traceable to SRM from NIST centripur ICP standards were used as calibration standards for ICP-MS analysis. In order to study the effect of natural organic matter on sulfidation of nAg, Suwannee River natural organic matter (SRNOM) was purchased from the International Humic Substance Society (St. Paul, MN, USA). NIST polystyrene standards with diameters 30, 60, 90 and 150 nm were purchased from Duke Scientific (Palo Alto, CA, USA) for calibration of the AF4 channel.

4.2.2 Sulfidation Experiments

Silver nanoparticles were sulfidated using a 5 mM solution of sodium sulfide (Na_2S). Ultrapure water purged with N_2 gas was used for preparation of all samples in order to prevent oxidation of sulfides in solution by dissolved oxygen (Fletcher et al. 2019) and reduce losses of the sulfide as volatile H_2S (Baalousha et al. 2015). nAg concentration was fixed at 0.25 mM and Na_2S

concentration was varied to attain ratios of 0.5, 1 and 5 with 1 mM $NaNO_3$ as the background electrolyte. The pH of the three systems at the initial time point was between 10.1 and 11.2 and decreased to values between 9.1 and 10.5 at the end of the experiment. Samples were vortexed for 20 seconds immediately after sulfidation and placed on a reciprocal shaker (GFL 3018 set to 125/min) to ensure the saturation of solution with oxygen. All samples were enclosed in foil to minimize the effect of light (vial was 8.5 cm in height with 3 cm headspace, diameter of vial was 2 cm). After the addition of sulfides, the measured dissolved oxygen (Dissolved oxygen - DO meter YSI 5000) concentration after vortexing and mixing was 7.2 mg/L and the DO of non-purged water was 8.1 mg/L. The DO concentration plateaued at 8.4 mg/L after an hour and remained consistent for the remaining experimental period. Only the lowest $[S/Ag]_{dose}$ (0.5) was chosen to study the effect of natural organic matter on sulfidation of nAg, as higher doses were likely to result in complete sulfidation of nAg. In these systems nAg was first exposed to 10 mg of C/L for 24 hours after which, calculated amount of Na_2S was added to the systems. All systems were prepared in duplicates; one replicate was used to monitor the effect of $[S/Ag]_{dose}$ as well as exposure time on extent on sulfidation and consequently AF4-ICP-MS analysis. The other replicate was used for batch d_{avg} and zeta potential measurements, which were performed using Zetasizer Nano ZS instrument, Malvern Instruments, UK.

4.2.3 AF4-UV-MALS-ICPMS

Wyatt Eclipse Dualtec (Wyatt Technology Europe, Dernbach, Germany) was used for fractionation of the nAg samples. A short channel (SC 145 mm) with a 10 kDa regenerated cellulose membrane (NADIR, Wies-baden, Germany) and 350 μm spacer thickness was used for separation. A 0.025% FL-70 solution was used as carrier fluid and was delivered with a quaternary HPLC pump (Agilent Technologies, 1260 Infinity series). The detectors used for sample analysis

were all downstream to fractionation; UV/vis diode array detector (Agilent Technologies, 1260 Infinity series) with absorption wavelengths ranging from 390 to 500 nm, multi angle light scattering (MALS DAWN HELOS II Wyatt Technologies) and finally through a triple quadrupole ICP-MS (8800 series ICP-MS; Agilent Technologies, Santa Clara, CA, USA). Outlet flow from AF4-UV/vis-MALS was split using a three-way union with one path to waste and the other to the nebulizer using a white-black tubing (I.D 0.95 mm, ESI, Elemental Scientific) through a truflow meter to main a constant flowrate. The limit of quantification of sulfur (2.2 µg/L) and silver (0.096 µg/L) was calculated by determining the 10σ of the blank intensities. All the other details of the AF4 -ICP-QQQ run conditions and details of TEM analyses are listed in the SI and Table S 4.1.

4.2.4 AF4 recoveries and performance

The AF4 channel recoveries were determined by dividing the peak areas of runs in the presence and absence of cross flows using the MALS 90^0 detector. The channel recovery in the presence of SRNOM was 93.4 % compared to pristine PVP-nAg, which was determined to be 81 %. SRNOM improves colloidal stability of nanoparticles due to steric stabilization, which may be the reason for higher recoveries of nAg in the AF4 channel. For all the sulfidated nAg samples, recoveries ranged between 77 % and 100 %, with an average recovery of 89 %. Lower recoveries may be attributed to particle-membrane interactions occurring in the channel during the run (Dubascoux et al. 2008, Dubascoux et al. 2010). The MALS detector was not used for determining the radius of gyration values as it is not suitable for detection of metallic ENPs because of their unusual scattering behavior (due to their surface plasmon resonance effect) (Hagendorfer et al. 2011, Loeschner et al. 2013, Meisterjahn et al. 2014). Linear size separation of polystyrene nanoparticles (30, 60, 90, 150 nm) (Figure S 4.1) was achieved using AF4 under the same flow conditions as sulfidated nAg. Polystyrene standards for calibration of the AF4 channel is well established, as

long as the elution patterns of the particles is determined by their diffusion behavior (Wagner et al. 2015). The effectiveness of separation was further confirmed by separating a mixture of two citrate coated - nAg particles (20 nm and 40 nm in diameter). Converting the retention times of the eluent peaks to hydrodynamic size using the polystyrene calibration curve yielded in accurate d_{avg} (24.1 and 46.6 nm) (Figure S 4.1). Additionally, converting the retention time of sulfidated nAg peaks to d_{avg} yields similar values to individual DLS d_{avg} estimations (Figure S 4.1).

4.2.5 Data Analysis

In order to obtain a size distribution of fractionated sulfidated nAg, retention time of NIST polystyrene standards were converted to d_{avg} by subtracting the void peak from the retention time of the polystyrene standard to create size versus time calibration curve. AF4 channel recoveries were determined by injecting samples without applying a cross flow. Area under the curve obtained from UV/vis signal and MALS 90^0 were used to calculate recoveries. Lastly, mass concentrations obtained from ICP-MS were converted to molar concentrations to determine $[S/Ag]_{particle}$.

4.3 Results and Discussions

4.3.1 Complete sulfidation of nAg occurs at a sulfide dose 10 times higher than the stoichiometric dose in 24 hours

Sulfidated nAg at different $[S/Ag]_{doses}$ systems had minimal impact on PVP-nAg hydrodynamic diameters immediately after the addition of sulfides as similar AF4 retention times of the sulfidated and un-sulfidated PVP-nAg (Figure S 4.1) were obtained. The similarity in diameters was also confirmed with batch DLS measurements (Figure S 4.1). TEM images of pristine PVP-nAg showed nearly spherical nAg particles with a broad size range from 8 nm to 108 nm (excluding the PVP coating) and a mean diameter of 64.7 ± 21.9 nm (n = 300) (Figure S4.2). The Z-average

diameter obtained from DLS was determined to be 126.2 ± 56.9 nm with a PDI of 0.16 ± 0.03. The zeta potential of sulfidated nAg particles remained similar to that of the pristine PVP-nAg in 1mM NaNO$_3$ (pH ~ 7) which was determined to be -36.6 ± 0.5 mV (Table S 4.2). TEM analysis of sulfidated nAg showed formation of a silver sulfide shell on the nAg particle core immediately after sulfidation. This is discussed in more detail in the following sections (Figure 4.4). The average hydrodynamic diameters of all three [S/Ag]$_{dose}$ systems on day 0 was determined to be 114.3 ± 4.9 nm.

The change in Ag and S concentration profiles with particle diameter as determined by AF4 - ICP-MS is shown in Figure 4.1 (A – F). The amount of S associated with nAg increases with increasing [S/Ag]$_{dose}$. Any dissolved S or Ag is not included in these plots, as these would have passed through the 10 kDa RC membrane during the AF4 fractionation step. The total mass represented by the entire Ag particle size distributions remained consistent with only 8 % variation between all [S/Ag]$_{dose}$ systems over time (Figure 4.1 (A – C)), indicating a colloidally stable suspension over the incubation period.

Assuming complete sulfidation occurs with Ag$_2$S being the only sulfidation product, theoretical amount of sulfides associated with dosed nAg was determined be 270 µM of S (based on the concentration of nAg eluted). Immediately after the addition of sulfides, 34.5 % of the expected theoretical S was detected, indicating that only a fraction of the available sulfides had reacted with nAg. This increased to 62.9 % and 67.9 % after 1 and 7 days of incubation, respectively. Stoichiometrically excess doses ([S/Ag]$_{dose}$ 1 and 5) resulted in similar values (27.7 % and 34.7 %, respectively) immediately after addition of sulfides. Higher extents of sulfidation occurred at [S/Ag]$_{dose}$ of 1 (87.8 %) and complete sulfidation of all nAg mass was achieved only at [S/Ag]$_{dose}$ of 5 (109 %) at the end of 7 days. For a given particle population, the amount of available sulfides

plays an important role in determining the extent of sulfidation. In a study by Levard *et al*. approximately 60% and 90 % of nAg mass was converted to Ag_2S at an S/Ag_{dose} of 0.5 and 1, respectively using Extended X-ray Absorption Fine Structure spectroscopy (EXAFS)(Levard et al. 2011), which measures all Ag bearing phases. In another study, 79.7 % of PVP- nAg (aggregated) was converted to Ag_2S compared to monodisperse nAg (96.6 %) at an S/Ag_{dose} of 2.02 within 2 days (Reinsch et al. 2012). The difference in sulfidation extent was attributed to the polydispersity of nAg particles.
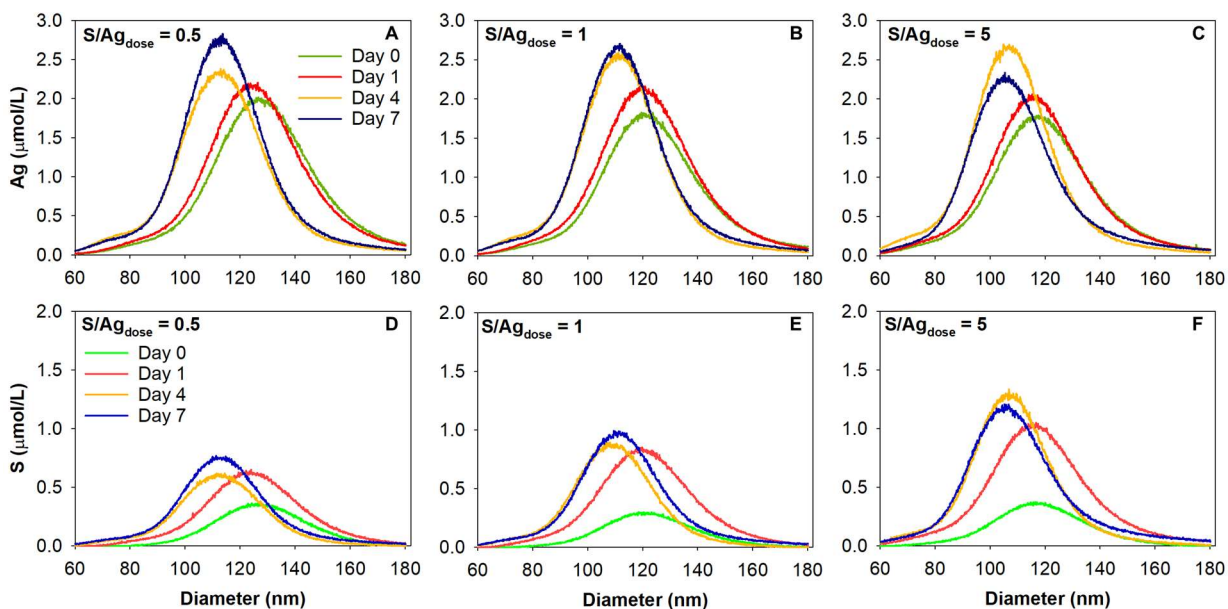
Figure 4.1: AF4 – ICPMS concentration profiles and particle size distributions of nAg (A – C) and S associated with nAg (D – F) over 7 days.

A slight shift in particle size distributions towards smaller sizes was observed over time in all three $[S/Ag]_{dose}$ systems (Figure 4.1 (A – C)). Diameters calculated using AF4 retention times revealed decreasing mean diameters over time at each dose. AF4 provides the d_{avg}, which includes the size of the metallic particle, hydration layer and surface coating, if present. The PVP coating used in the present study can contribute towards a maximum of 17 nm in size (PVP coating mean thickness

was 8.6 ± 2.3 nm, Figure S 4.3). This is in the same range of the calculated decrease in diameters observed between day 0 and day 7 at $[S/Ag]_{dose}$ values of 0.5, 1 and 5 (8.9 nm, 7.8 nm and 11.1 nm, respectively) (Figure S 4.4). Therefore, the shift in particle size distributions towards smaller sizes can be attributed to the loss of PVP coating over time, which has also been observed previously (Zhang et al. 2016, Zhu et al. 2016).

4.3.2 Extent of sulfidation is independent of nAg size within a particle population

The effect of particle size related parameters such as specific surface area (SSA) and surface area available for each particle diameter bin or SA (d) on the extent of sulfidation is discussed herein. For the particle size range (65 nm – 160 nm) considered in this study, there was a two-fold variation in SSA (7 m^2/g to 3.5 m^2/g) (Figure 4.2 (B)), and if sulfidation was dependent on SSA, there would have been higher $[S/Ag]_{particle}$ at smaller diameters. However, $[S/Ag]_{particle}$ was constant over the size range (Figure 4.2). A previous study showed a faster rate of sulfidation for 5 nm nAg (~ 109 m^2/g) compared to 30 nm nAg (~ 19 m^2/g) (Liu et al. 2011) , with the sulfidation reaction monitored by measuring the residual sulfide in solution using an ion-selective electrode. The sulfide concentration in solution decreased in 2 days for all sizes. However, the same mass of nAg was used (2mM) for both size classes, implying that the number of nAg particles available for sulfidation for the 5 nm system had more particles and therefore a 6-fold higher surface area (SA) available for sulfidation than the 30 nm system. Depending on the concentration of the available sulfides in solution, the sulfidation reaction of the nAg present will either be completed (All nAg is converted to Ag_2S) or will not be completed (partial or incomplete sulfidation).

The effective extent of sulfidation or $[S/Ag]_{particle}$ immediately after the addition of Na_2S, was 0.15 ± 0.05, 0.15 ± 0.02 and 0.19 ± 0.01 at $[S/Ag]_{dose}$ of 0.5, 1 and 5, respectively, across the entire size range (Figure 4.2 (A)). After 1 day, the $[S/Ag]_{particle}$ ratios increased in all systems ($[S/Ag]$ 0.5 , 1

and 5) to 0.27 ± 0.04, 0.37 ± 0.04 and 0.51 ± 0.02, respectively, and remained constant thereafter. As the [S/Ag]particle reaches a plateau over the incubation period, the sulfidation reaction attained its maximum reaction potential for that given [S/Ag]dose . A previous study reported no change in sulfidation extents beyond 24 hours with citrate-nAg dosed at an [S/Ag]dose of 0.53 (Baalousha et al. 2015). However, the extent of sulfidation in the study was determined by monitoring the change in normalized absorbance at the λ_{max} (392 and 412 nm), which related to the decrease in surface plasmon resonance and the concentration of non-sulfidated nAg. Those measurements are indirect assessments of [S/Ag]particle ratios (Baalousha et al. 2015).
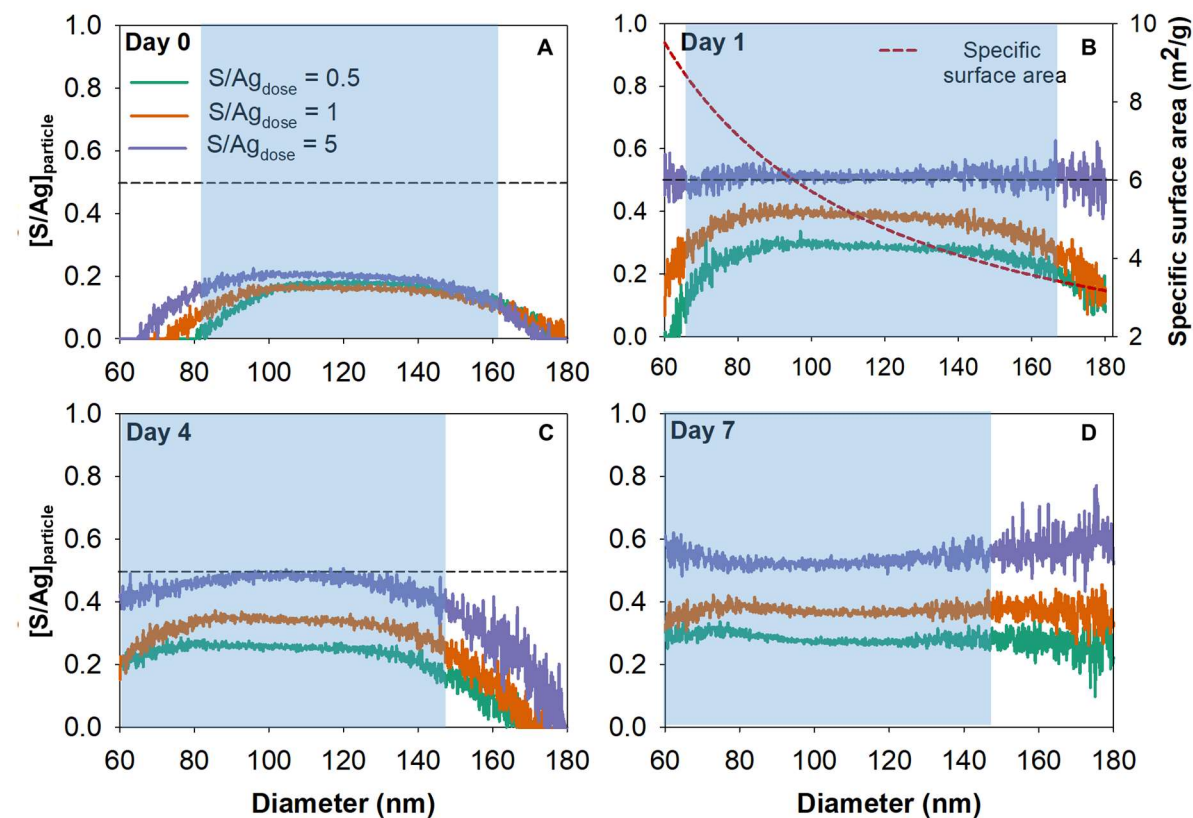
Figure 4.2: [S/Ag]particle ratios estimated using AF4-ICPMS at [S/Ag]dose = 0.5 , 1 and 5 on (A) Day 0 (B) Day 1, secondary y-axis is the profile of specific surface area over size (C) Day 4 (D) Day 7. Blue shaded area is above the limit of quantification of S using ICP-MS.

The [S/Ag]$_{particle}$ values shows a gradual increase in [S/Ag]$_{particle}$ in the lower diameter range (80 - 100 nm) and plateaus over the remaining size distribution (Figure 4.2 (A, B)). To determine the cause for lower [S/Ag]$_{particle}$, the average S and Ag concentrations were compared in the lower (80 – 100 nm) and higher (120 -140 nm) range. The lower [S/Ag]$_{particle}$ on day 0 can be attributed to the 7-fold lower nAg mass present in the lower range (28 ± 11 µg/L) compared to the higher range (200 ± 16 µg/L) at an [S/Ag]$_{dose}$ of 0.5 (Figure 4.2 (A)). This leads to a 12-fold lower average S concentration associated with nAg in the lower range (0.84 ± 0.69 µg/L) compared to the higher range (10 ± 0.95 µg/L). Similar trends of nAg mass in the 80 – 100 nm range can be attributed to the lower [S/Ag]$_{particle}$ measured at [S/Ag]$_{dose}$ of 1 and 5. The [S/Ag]$_{particle}$ at all three doses are consistent over the entire size distribution on day 7.   This is due to the overall shift in particle size distribution towards smaller sizes (as seen in Figure 4.1 (A)), which leads to increased nAg concentrations in that range. This effect was confirmed with a 3-fold increase in nAg mass in the 80 – 100 nm range (81 ± 47 µg/L) which is now available for sulfidation compared to day 0 ([S/Ag]$_{dose}$ of 0.5).

4.3.3 Sulfur loading is independent of specific surface area and dependent on surface area available per size bin

The cause for overall invariance in [S/Ag]$_{particle}$ was examined further by investigating different parameters which could have influenced the sulfur loading on nAg particles; nAg mass, particle number concentration as well as surface area of any given size bin. The surface area available per size bin or SA (d) was calculated by determining the surface area of the particle of that size bin times the number of particles present in that size bin. The influence of particle size and nAg mass on sulfur loading (S$_{particle}$, g/L) was determined by holding the SA (d) available for sulfidation (Figure S 4.5) constant for two size classes (Table 4.1, (1)).   For example, at an [S/Ag]$_{dose}$ of 0.5,

two diameters (98.1 nm and 148.1 nm) with the same SA (d) values were chosen (3.4 ×10^{-4} m^2/L). Higher mass of Ag was available (1.5 fold) with the larger size bin (148.1 nm) compared to the smaller bin (98.1 nm) leading to higher sulfur loading in the larger bin (~1.5-fold higher) compared to the smaller bin, despite the larger bin having a lower particle concentration (2-fold lower). The invariance in $[S/Ag]_{particle}$ at both diameters is due to a 2-fold lower particle surface area for the smaller bin (3×10^{-14} m^2) compared to the larger bin (6.9×10^{-14} m^2), therefore requiring lower amounts of S to reach an $[S/Ag]_{particle}$ of 0.28. These results demonstrate that larger particles are associated with higher amounts of S for a given SA (d).

In a situation where the Ag mass is constant (~7 ×10^{-5} g/L) for two particle sizes bins (smaller and larger) (Table 4.1, (2)), the SA (d) values are higher for the smaller nAg diameters, due to the presence of higher particle number concentrations which influence the total surface area available for sulfidation for all S/Ag doses. However, the $S_{particle}$ associated with each of these size bins (smaller and larger) is similar which can be attributed to the similar mass of nAg available for sulfidation. The smaller sizes at each $[S/Ag]_{dose}$ has a slightly higher $[S/Ag]_{particle}$, which is attributed to the ~ 3 fold higher particle concentrations present in the smaller size bin. These results indicate that the extent of sulfidation is dependent on both nAg mass as well as surface area in a polydisperse particle population. These results are different from previous studies that have used multiple individual size populations to derive a relationship between size and extent of sulfidation (Liu et al. 2011, Reinsch et al. 2012, Kaegi et al. 2013).

Table 4.1: Effect of nAg mass and total surface area of nAg available for sulfidation on extent of sulfidation on Day 1.

	$[S/Ag]_{dose}$	Diameter (nm)	Particle SA (m^2)	Particle concentration (NP/L)	Mass of Ag (g/L)	SA (d) (m^2/L)	Mass of S or $S_{particle}$ (g/L)	$[S/Ag]_{particle}$
SA (d) held constant (1)	0.5	98.1	$3.0*10^{-14}$	$1.1*10^{10}$	$5.9*10^{-5}$	**$3.4*10^{-4}$**	$5.0*10^{-6}$	0.28
		148.1	$6.9*10^{-14}$	$5.0*10^{9}$	$8.9*10^{-5}$	**$3.4*10^{-4}$**	$7.1*10^{-6}$	0.26
	1	94.2	$2.8*10^{-14}$	$1.2*10^{10}$	$5.7*10^{-5}$	**$3.4*10^{-4}$**	$6.8*10^{-6}$	0.39
		144.6	$6.6*10^{-14}$	$5.1*10^{9}$	$8.5*10^{-5}$	**$3.4*10^{-4}$**	$9.4*10^{-6}$	0.36
	5	90.1	$2.5*10^{-14}$	$1.3*10^{10}$	$5.3*10^{-5}$	**$3.4*10^{-4}$**	$8.2*10^{-6}$	0.51
		139.1	$6.1*10^{-14}$	$5.6*10^{9}$	$8.3*10^{-5}$	**$3.4*10^{-4}$**	$1.3*10^{-5}$	0.51
Ag mass held constant (2)	0.5	100.3	$3.2*10^{-14}$	$1.3*10^{10}$	**$7.0*10^{-5}$**	$4.0*10^{-4}$	$6.2*10^{-6}$	0.29
		151.7	$7.2*10^{-14}$	$3.7*10^{9}$	**$7.0*10^{-5}$**	$2.7*10^{-4}$	$5.5*10^{-6}$	0.26
	1	96.8	$2.9*10^{-14}$	$1.4*10^{10}$	**$6.9*10^{-5}$**	$4.1*10^{-4}$	$8.4*10^{-6}$	0.40
		147.1	$6.8*10^{-14}$	$4.1*10^{9}$	**$7.1*10^{-5}$**	$2.8*10^{-4}$	$8.3*10^{-6}$	0.38
	5	93.5	$2.7*10^{-14}$	$1.6*10^{10}$	**$7.0*10^{-5}$**	$4.3*10^{-4}$	$1.1*10^{-5}$	0.51
		141.3	$6.3*10^{-14}$	$4.6*10^{9}$	**$7.1*10^{-5}$**	$2.9*10^{-4}$	$1.1*10^{-5}$	0.50

Finally, the dependence of sulfur loading ($S_{particle}$) per size bin on surface area over the entire size distribution was determined by normalizing $S_{particle}$ with SA (d), g/m^2 (Figure 4.3 (A, B)). An increase in $S_{particle}$/SA (d) was observed with $[S/Ag]_{dose}$, over time, as well as with size. For example, after 7 days, a 2-fold increase in $S_{particle}$/SA (d) occurred at $[S/Ag]_{dose}$ = 0.5 and 3-fold increase for $[S/Ag]_{dose}$ = 5 with size. The mass of Ag per surface area in a given size bin (Figure 4.3 (B), secondary y-axis) or Ag/SA (d) also had an increasing trend with size, showing that there was higher mass associated with larger particles and has a positive correlation with $S_{particle}$/SA(d) (0.97, $p < 0.05$, Pearson's correlation coefficient). These results indicate that fewer large nAg particles have the ability to react with a higher mass of sulfides owing to their higher mass. Similar trends were observed for $[S/Ag]_{dose}$ = 1 systems (Figure S 4.6).
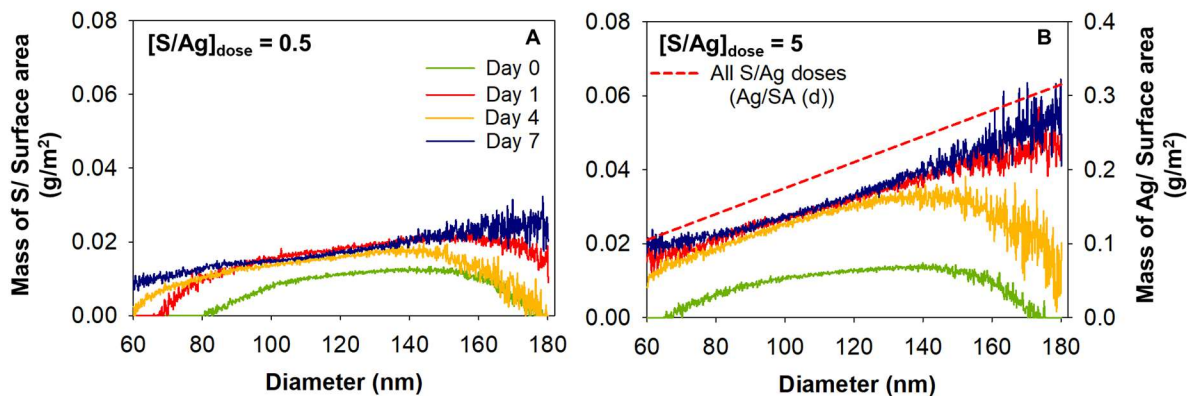
Figure 4.3: Sulfur loading normalized with total surface area available for sulfidation per size bin at S/Ag$_{dose}$ (A) 0.5, (B) 5; secondary axis is the mass of nAg normalized with surface area of the size bin

4.3.4 Sulfidation of silver nanoparticles is diffusion driven

Based on the results obtained from AF4 -ICPMS, the following mechanism for sulfidation of nAg is proposed. When the solid surface of the reactant is non-porous and impervious to the fluid surrounding the solid surface, the reaction occurs at the surface of the solid or between the interface of the solid and product layer (Wen 1968). Furthermore, formation of Ag$_2$S upon contact of Na$_2$S with spiked Ag$^+$ in solution is instantaneous (Figure S 4.7). This suggests that the sulfidation reaction is very rapid, but the diffusion of Ag$^+$ from nAg to the bulk solution is much slower in comparison to the sulfidation reaction itself. Therefore, the zone of reaction is confined between the interface of the unreacted solid reactant and the product (Wen 1968). The mechanism of sulfidation of each PVP-nAg particle in the present study appears to be a shrinking core model (Figure 4.4 (A-C)). The absence of increase in diameters obtained from AF4 (Figure 4.1, S 4.4) indicate that "r" or the radius of the particle does not grow over time. However, the value of "r$_c$", which is the radius of the Ag(0) core decreases upon sulfidation as observed from TEM measurements, with a higher decrease for [S/Ag]$_{dose}$ 5 compared to 0.5 (Figure S 4.8). In order to

convert the entire nAg particle to Ag_2S, the sulfides in the solution will have to move through various layers of resistance; the fluid film, the porous ash layer and the reaction at the unreacted surface of the nAg particle (Wen 1968). Complete conversion of nAg to Ag_2S was observed only at a10-fold stoichiometric excess $[S/Ag]_{dose}$ of 5 as seen in Figure 4.3. In the $[S/Ag]_{dose}$ 0.5 system, one of the above resistances was the rate-limiting step. We propose the following: after the first layer of sulfide ions react with the silver ions at an $[S/Ag]_{dose}$ of 0.5, the concentration of sulfide ions in solution goes further down. Therefore, there is a decreased driving force (concentration gradient) through the Ag_2S layer (internal diffusion), which is not a limiting factor in the presence of excess sulfides, which enables complete coverage due to a higher concentration of sulfides in solution. A higher concentration gradient is formed at $[S/Ag]_{dose}$ 5 due to the higher concentration of sulfides in solution and therefore creates a stronger driving force towards the surface of PVP-nAg, which results in higher coverage of nAg core with Ag_2S. At an $[S/Ag]_{dose}$ ratio of 0.5, a concentration gradient still exists, but there is uneven coverage due to lower sulfide concentration in solution.

ImageJ (version 1.50i) was used to obtain the diameters (d_c) of the shrinking nAg core which were estimated to be 77.3 ± 7.9 nm and 66.5 ± 13.6 nm at $[S/Ag]_{dose}$ of 0.5 and 5, respectively (Figure S 4.8). The EDAX analysis of the core and shell of Figure 4.4 (A) is reported in Figure S 4.9. Analysis of TEM images revealed distinct changes in morphology of PVP-nAg upon sulfidation. For example, the lattice spacing varied between pristine nAg (Figure 4.4 (D)), spiked Ag^+ in Na_2S (Figure 4.4 (E)) solution and Ag_2S formed as a part of the core-shell structure (Figure 4.4 (F)). Different types of crystal structure influences the lattice spacing of the particle. The lattice spacing of pristine nAg and Ag_2S (from spiked Ag^+ and core-shell) are in the similar range as observed previously in literature (Chen et al. 2008, Reinsch et al. 2012). Further, the population of sulfidated

nAg particles were either present as individual nAg-Ag$_2$S particles or bridged sulfidated nAg particles. The primary mechanism occurring in all our systems is the direct route or oxysulfidation of PVP-nAg through solid-fluid reaction at all three [S/Ag]$_{dose}$ values.
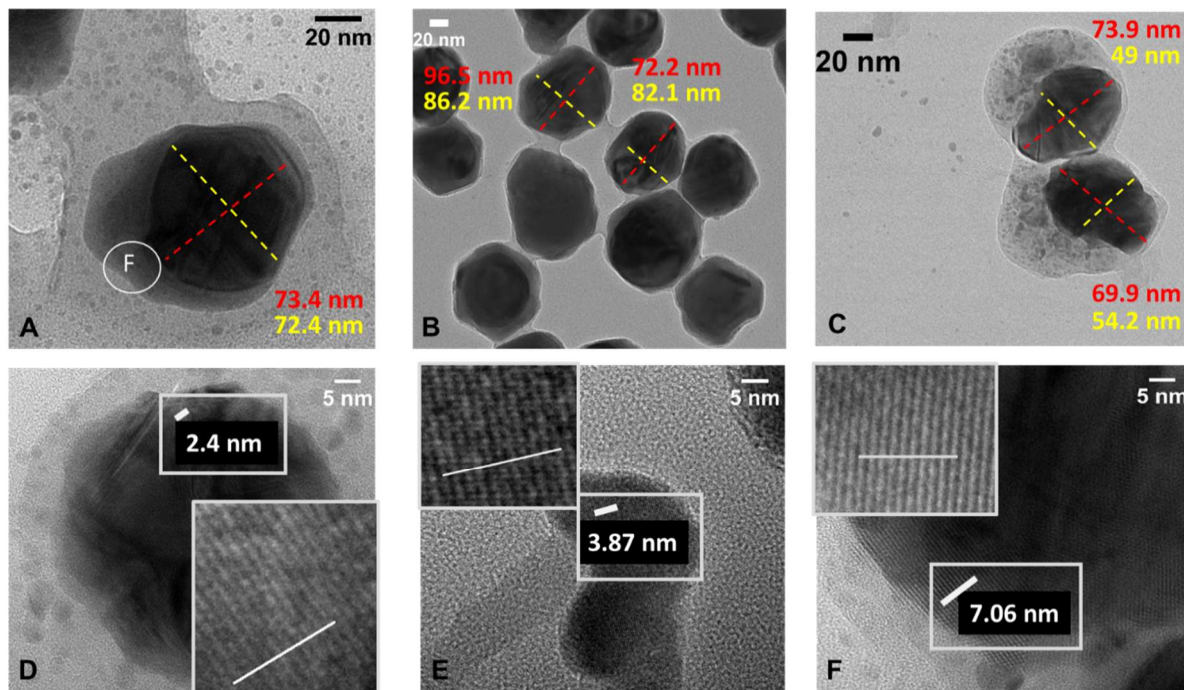
Figure 4.4: TEM images of nAg immediately after the addition of sulfides at [S/Ag]$_{dose}$ = 0.5 (A,B) [S/Ag]$_{dose}$ = 5 (C) Lattice spacing of 10 lattices in (D) PVP-nAg in MilliQ (E) Ag$_2$S formed from adding Na$_2$S to Ag$^+$ ions in solution (F) Ag$_2$S formed on the outer layer of [S/Ag]$_{dose}$ = 0.5 in (A). Insets (D-F) are zoomed in areas to show lattice spacing.

4.3.5 SRNOM does not influence extent of sulfidation

The effect of NOM on sulfidation of PVP-nAg was tested under the stoichiometrically sufficient [S/Ag]$_{dose}$ of 0.5 by exposing the PVP-nAg to NOM for 24 hours prior to adding Na$_2$S. The calculated contribution of S from SRNOM was determined to be ~ 1.25×10^{-8} mol/L per sample injection (calculated from the weight fraction information provided by IHSS), which is lower than the limit of quantification of ICP-MS (2.03×10^{-8} mol/L). Therefore, it is assumed that any S

measured primarily arises from sulfidated nAg. Concentration profiles of Ag and S obtained from [S/Ag] systems with NOM are similar to those without NOM ([S/Ag]$_{dose}$ 0.5) (Figure S 4.10). Immediately after the addition of Na$_2$S at an [S/Ag]$_{dose}$ of 0.5, the average [[S/Ag]]$_{particle}$ in the presence of NOM was lower (0.085 ± 0.021) compared to the system in the absence of NOM (0.14 ± 0.05) (Figure S 4.11). This discrepancy probably arises due to the replacement of PVP with NOM (Lau et al. 2013) leading to lower interactions between nAg surface and sulfides (Zhang et al. 2016). Previous studies have indicated contradicting results for effect of NOM on sulfidation, depending on the aquatic chemistry(He et al. 2019). An increase in sulfidation rate was observed in NOM system due to the increased colloidal stability (Liu et al. 2011, Thalmann et al. 2016). In the present study, no significant increase in colloidal stability of nAg was observed over time (Table S 4.2). However, after 7 days, the [S/Ag]$_{particle}$ in the presence and absence of NOM was 0.28 ± 0.023 and 0.28 ± 0.024, respectively. The mass of nAg sulfidated in the absence and presence of NOM ([S/Ag]$_{dose}$ = 0.5) was 59.6 % and 66.4 % on day 1 and 64.3 % and 56.3 % on day 7, respectively. After the initial time point, all the samples were on a shaker, which created enhanced mixed conditions causing increased contact between the sulfides and nAg surface leading to uniform sulfidation over the remaining experimental period. Therefore, a decrease in initial sulfidation rate can be designated to the possible electrostatic repulsions between bisulfides and NOM (Zhang et al. 2016). Overall, the presence of SRNOM did not influence the [S/Ag]$_{particle}$ over the full exposure period. It is important to note that different types of NOM possess different properties (Leenheer and Croué 2003) which can lead to different types of interactions between nAg and NOM substances (Levard et al. 2011, Liu et al. 2011) especially in heterogeneous systems.

4.4 Conclusions

The results from this study demonstrate that the extent of sulfidation of nAg within a given population is dependent on nAg mass, total surface area available for sulfidation and is independent of size of particle. Previous studies have established an inverse correlation between nAg size and completeness of sulfidation for different sets of nAg size distributions on a whole population basis (Reinsch et al. 2012, Thalmann et al. 2016). However, in a given nAg population of different size fractions, larger nAg particles can provide a source of Ag^+ for the heterogeneous sulfidation reaction due to its larger particle surface area per unit volume of sample in the presence of sufficient sulfides. Smaller particles present in higher number concentrations within a given size bin, can continuously undergo sulfidation until one of the reactants of the heterogeneous reaction (Ag surface for Ag ions or sulfides in solution) is exhausted.

The completeness of nAg sulfidation $[S/Ag]_{particle}$ is influenced by $[S/Ag]_{dose}$, which in turn can affect the fate, bioavailability and toxicity of nAg. In natural aquatic systems, sulfides are present in the low ng/L range (Luther and Tsamakis 1989, Tang and Santschi 2000), creating $[S/Ag]_{particle}$ ratios below 0.5, which can lead to incomplete sulfidation. Preliminary environmental fate results performed using spICP-MS in this study show that environmental implications of incomplete sulfidation leads to a continued release of Ag^+ over time (Figure S 4.12). However, the presence of sulfides in the aqueous phase enables re-precipitation of Ag_2S from Ag^+. Re-precipitated Ag_2S particles are significantly smaller than the primary nAg particle size. The presence of NOM can further influence the fate of sulfidated nAg and re-precipitated nAg in the following ways. NOM can increases the colloidal stability of nAg by enhancing their surface charge or by electrosteric repulsion (Huynh and Chen 2011, Sharma et al. 2014). The presence of NOM of can influence the re-precipitation of dissolved Ag to form secondary nAg particles (Azodi et al. 2016, Wimmer et

al. 2018). There may be complexation between NOM and dissolved Ag leading lower free concentrations of Ag^+ for the direct sulfidation reaction to form Ag_2S particles causing the slow appearance of secondary Ag_2S particles. Although Ag_2S particles are known to be extremely stable, recent studies have shown oxidation of Ag_2S particles with disinfectants such as chlorine (Li et al. 2017) and ozone treatment (Thalmann et al. 2015), thereby increasing the toxic potential of Ag_2S (He et al. 2019) . This phenomenon is significant for smaller Ag_2S particles, as they may be more susceptible to faster oxidation and be more reactive due to their high specific surface area. A comprehensive study of sulfidated nAg under environmentally relevant conditions is required to completely recognize the long-term environmental implications of sulfidated nAg.

Knowing the state in which ENPs are initially released into the environment is still a challenge (Nowack et al. 2015). AF4-ICPMS can be a promising technique for distinguishing between transformed nAg (Ag_2S, AgCl) and pristine nAg and their characterization in environmental matrices. spICP-MS is a robust technique which can determine extents of dissolution and colloidally stable concentrations over long-term exposure periods. The use of AF4-ICPMS and spICP-MS together should be able to provide sufficient information about long-term environmental implications of sulfidated nAg.

4.5 Acknowledgements

4.6 Supplementary Information

TEM Details

Philips CM200 200 kV TEM with AMT XR40B CCD Camera and EDAX Genesis EDS analysis system was used to measure PVP-nAg and sulfidated nAg sizes. 20 μL of the concentrate was deposited on the Cu TEM substrates (Electron Microscopy Sciences, Carbon film 200 mesh Cu grids). The grids were kept in dark and air-dried.

Table S 4.1: AF4-ICPMS and spICP-MS operational conditions

AF4 -MALS		ICP-QQQ		spICP-MS	
Channel length (mm)	145	RF- power (W)	1550	Sample Uptake Rate (ml/min)	0.28-0.34
Spacer height (μm)	350	Carrier gas flow (L/min)	(Argon) 0.8	Nebulizer and Spray Chamber	Glass Concentric
Membrane	RC 10 kDa	Make up gas flow (L/min)	(Oxygen 30%) 0.45	RF Power (w)	1600
Focus flow rate (ml/min)	0.5	Torch Material	Quartz	Analysis time (s)	90- 120
Focussing time (min)	8	Spray Chamber	Quartz	Dwell time (μs)	100
Cross flow rate (ml/min)	0.5	Nebulizer	Micromist		
Detector flow rate (ml/min)	1	Sample and Skimmer cone	Platinum		
Carrier fluid	0.025 % FL-70	Sample depth (mm)	10		

Table S 4.2: Zeta potential of sulfidated nAg at initial and final time point

	S:Ag= 0.5		S:AgNOM=0.5		S:Ag=1		S:Ag=5	
	Average (mV)	Stdev	Average (mV)	Stdev	Average (mV)	Stdev	Average (mV)	Stdev
Day 0	-30.3	0.4	-38.0	0.8	-27.4	0.4	-23.1	0.5
Day 7	-27.5	0.3	-33.7	0.5	-28.8	0.7	-26.1	0.5
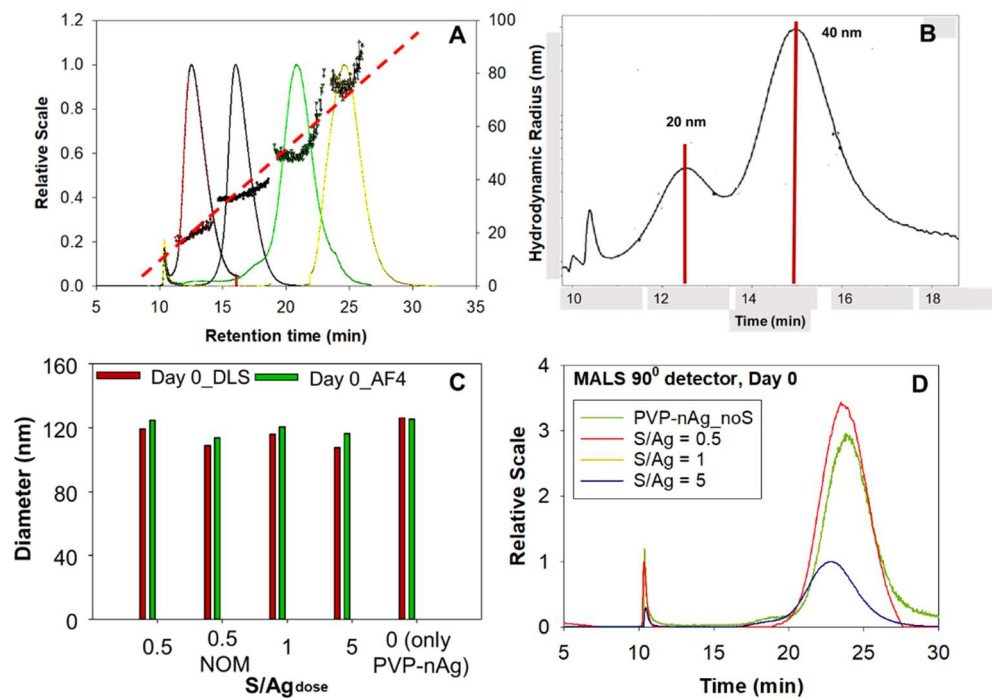
Figure S 4.1: (A) Retention time of polystyrene particles of 30 nm, 60 nm, 90 nm and 150 nm (B) Elution of 20 nm and 40 nm nAg particles (C) Comparison between DLS and AF4 hydrodynamic diameters (D) Retention times of sulfidated and non-sulfidated nAg.
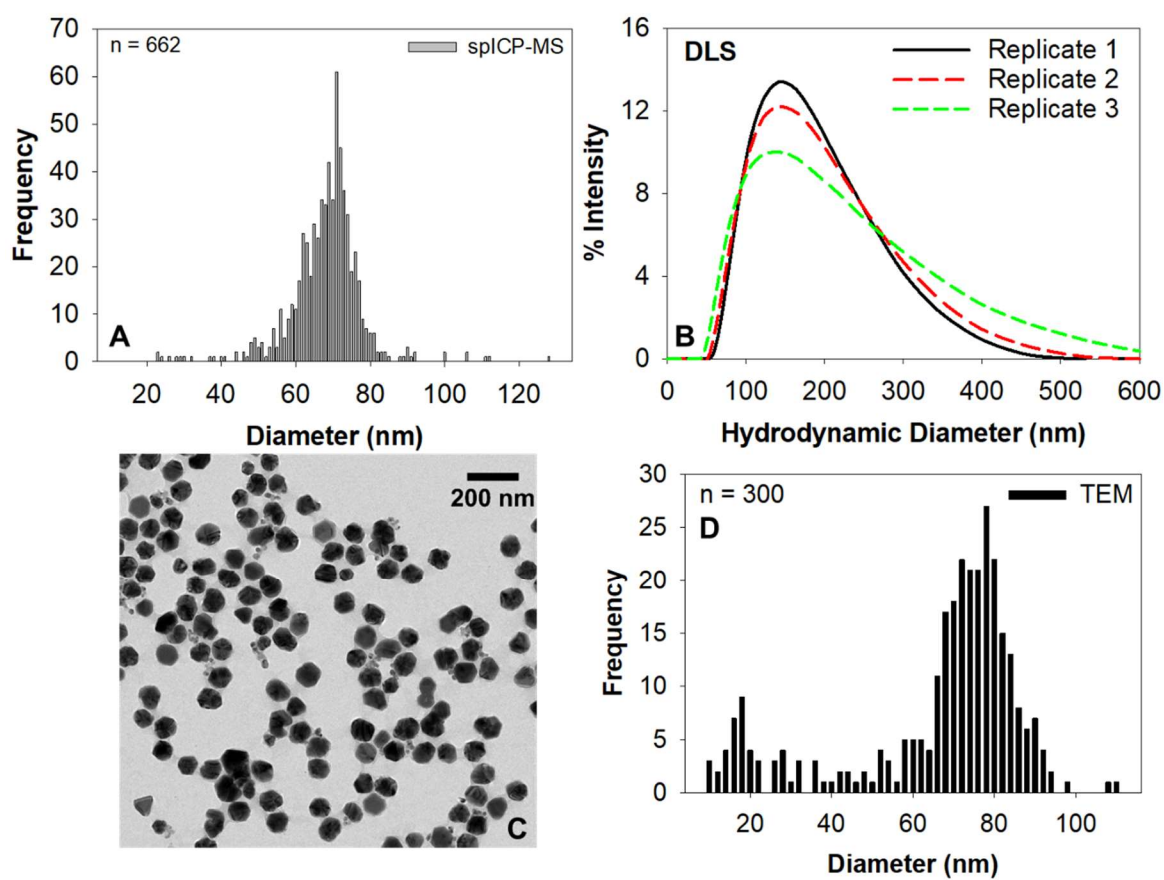
Figure S 4.2: Particle size distribution of 75 nm PVP-nAg using (A) spICP-MS (B) DLS. (C) TEM image of PVP-nAg (D) Particle size distribution using TEM
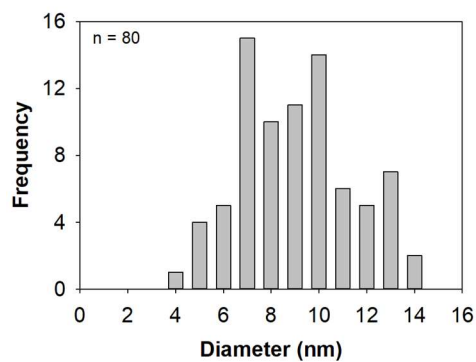
Figure S 4.3: TEM size distribution of PVP coating on nAg
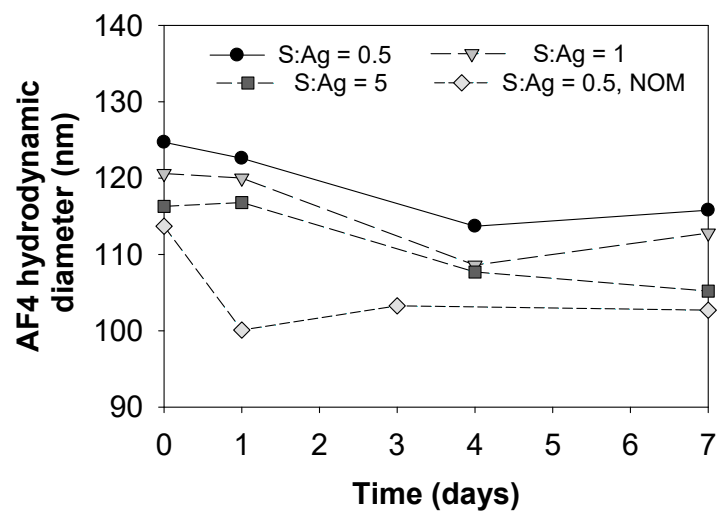
Figure S 4.4: Diameters of sulfidated nAg over time measures using AF4-ICPMS
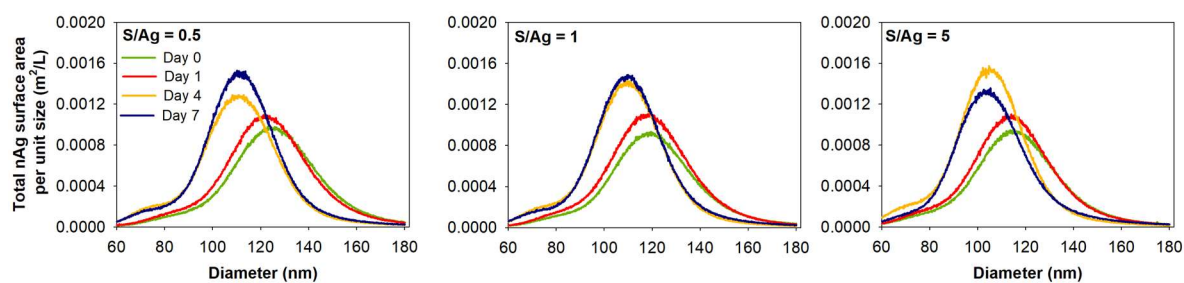
Figure S 4.5: Particle size distributions of total nAg surface area available for sulfidation at S/Ag (A) 0.5 (B) 1 and (C) 5
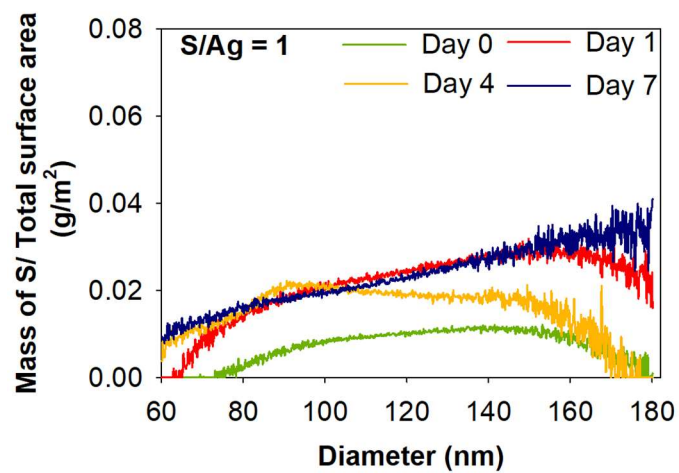
Figure S 4.6: Mass of S normalized with total surface area of silver nanoparticles per size bin

available for sulfidation
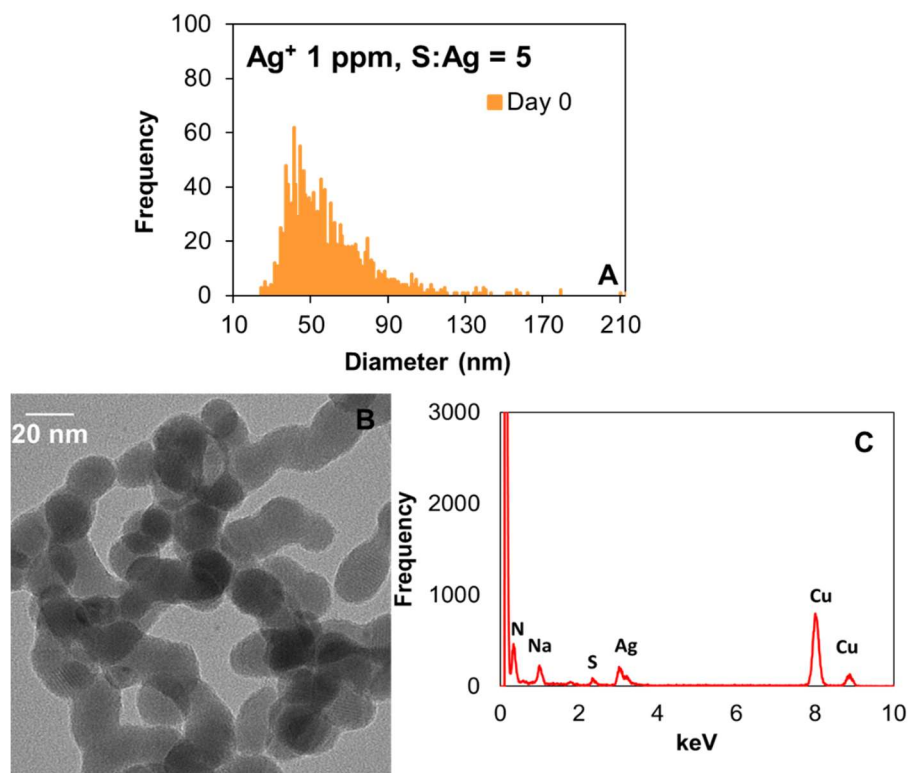
Figure S 4.7: (A) Particle size distribution of Ag_2S from spiked Ag^+ and Na_2S (S/Ag = 5) determined using spICP-MS immediately after spiking (B) TEM image of Ag_2S formed by spiking Na_2S in Ag+ (C) EDS of a sampled area
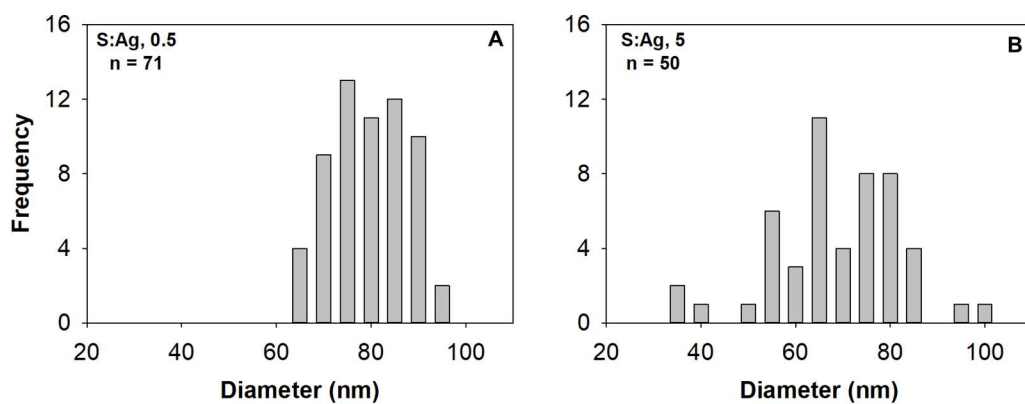
Figure S 4.8: TEM size distributions of nAg core of Ag - Ag$_2$S (core-shell) particles at (A) S:Ag = 0.5 (B) S:Ag = 5
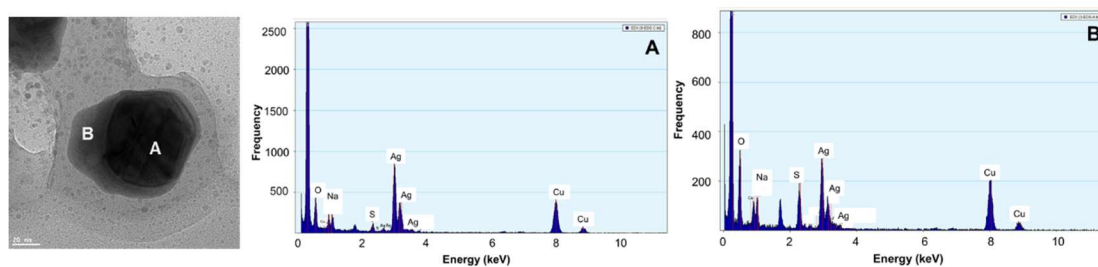
Figure S 4.9: TEM image of sulfidated nAg at S:Ag = 0.5. (A) and (B) are areas sampled for EDAX analysis
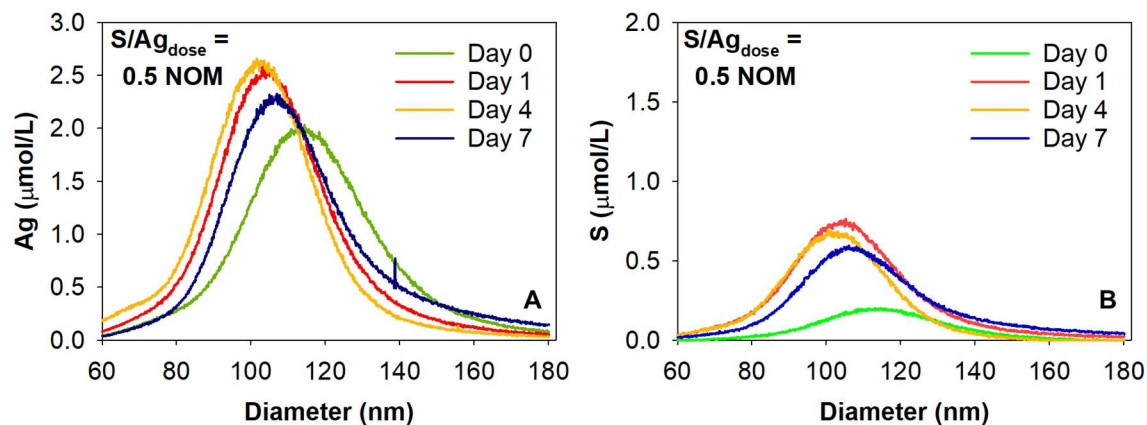
Figure S 4.10: Concentration profiles and particle size distributions of nAg and S associated with

nAg obtained from AF4 – ICPMS over 7 days.
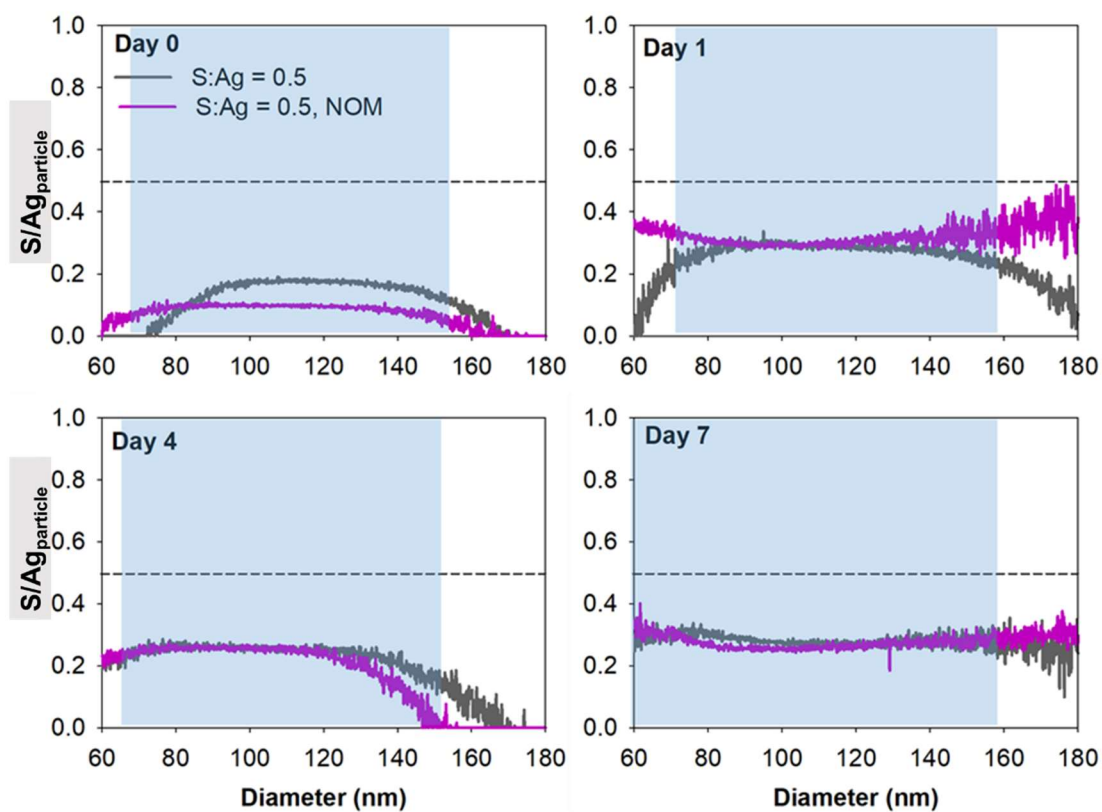
Figure S 4.11*: [S/Ag]particle ratios estimated using AF4-ICPMS measurements over time at S/Ag*

= 0.5 with and without NOM. Blue shaded area represents the section of data where sulfur

concentrations were greater than 10σ of the sulfur calibration blanks (> 2.02×10⁻⁸ mol/L or 2.2 µg/L).

Incomplete sulfidation has environmental implications

The results obtained from AF4-ICPMS show that complete sulfidation occurs at an S/Ag dose 10-times higher than the stoichiometrically required dose. In order to examine the implications of incomplete sulfidation by determining the fate and behavior of sulfidated nAg at environmentally relevant concentrations, the particle concentration, mass concentration and dissolved Ag concentrations of 50 µg/L PVP-nAg were investigated at S/Ag doses of 0.5, 1 and 5 using spICP-MS for 7 days. Results from these experiments suggested that only a fraction of nAg are in suspension after 7 days (Figures S 4.12-A and S 4.12-B). Previous studies have suggested that sulfidation of PVP-nAg causes the formation of aggregates connected with Ag_2S bridges(Levard et al. 2011, Reinsch et al. 2012). Formation and loss of aggregates due to sedimentation explains the decreasing concentrations of detected nAg over time as seen in Figure 4.4A and 4.4B. The formation of Ag_2S bridges and aggregates upon sulfidation were observed on TEM (Figure S 4.12).

Beyond 4 days, a secondary particle size distribution at S/Ag ratio of 0.5 ("i" in Figure S 4.11 A) was observed, with elevated dissolved Ag concentrations (4 % of initial nAg mass concentration on day 4 and 3 % on day 7). No such dissolved Ag concentrations were detected at S/Ag ratios of 1 and 5 implying that the presence of excess sulfides prevent dissolution of nAg. In a previous study, a small fraction (1- 1.5 % of initial mass concentration ~ 10 µg/L) of dissolved Ag^+ was observed in both de-ionized (DI) and effluent waste water by sulfidated PVP-nAg (S/Ag = 0.5) with a mean diameter of 80 nm after 7 days (Azodi et al. 2016). Several studies have reported the bioavailability of metallic Ag(0) even after sulfidation and possibly acting as a source of ionic Ag (Lowry et al. 2012, Kaegi et al. 2013, Baalousha et al. 2015). We suspect the formation of Ag_2S

particles in S/Ag = 0.5 systems is due to the dissolution of PVP-nAg causing a release of Ag^+ ions which then react with the sulfide species in solution. This hypothesis was tested by adding sulfides to a solution with Ag^+ and measuring these particles using spICP-MS. As spICP-MS does not have the ability to differentiate between different forms of nAg (Nowack et al. 2015), Ag_2S particles appear as peaks of nAg (Figure S 4.7). Further, the absence of any such secondary peaks in the PVP-nAg system in MilliQ water (Figures S 4.12-D) during the experimental period confirms that the secondary peaks observed in Figures S 4.12-A are indeed Ag_2S particles, as the aquatic composition (1mM $NaNO_3$, absence of Na_2S) of the PVP-nAg MilliQ system is identical to the S/Ag at 0.5. The estimated mean diameters of colloidally stable sulfidated PVP-nAg using spICP-MS on day 0 were determined to be 72 ± 0.3 nm, 72 ± 0.1 nm and 71.8 ± 0.19 nm at S/Ag = 0.5, 1 and 5, respectively and these values remained consistent for S/Ag doses of 1 and 5 for the remaining incubation period (Figure S 4.13). The mean diameter of the S/Ag 0.5 system decreased to 41 ± 2.9 nm due to the dissolution of 75 nm PVP-nAg and the increased formation of re-precipitated Ag_2S.
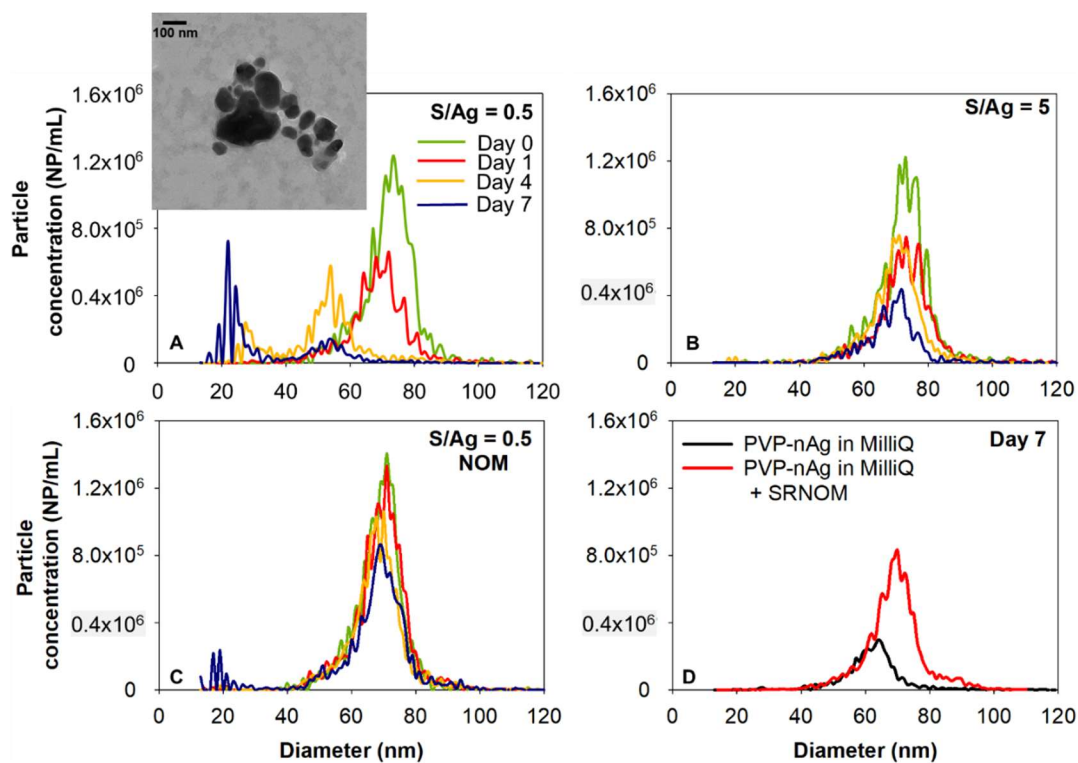
Figure S 4.12: Single particle ICP-MS particle size distributions of PVP-nAg at S/Ag ratios of (A) 0.5, inset is a TEM image of sulfidated nAg at 0.5 (B) 5 (C) 0.5 with SRNOM (D) PVP-nAg in MilliQ water on day 7
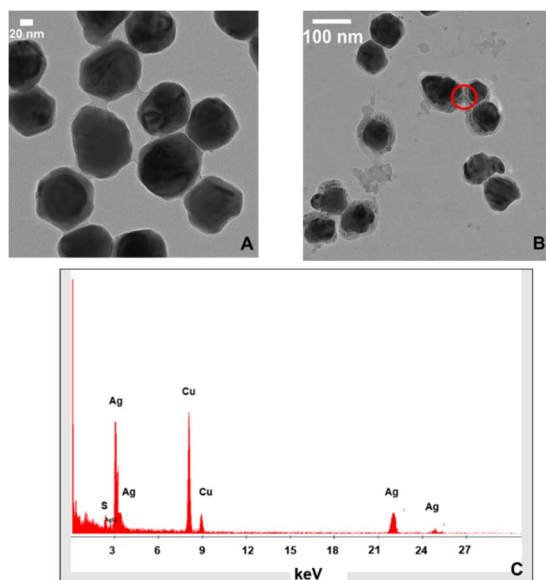
Figure S 4.13: TEM images of sulfidated nAg with bridges of Ag$_2$S in S:Ag (A) 0. 5 (B) 5 (C) EDAX of Ag$_2$S bridge
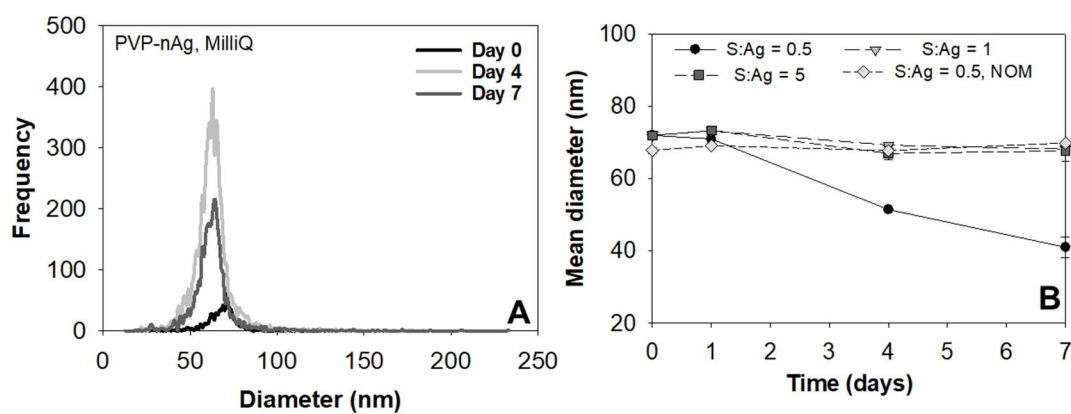
Figure S 4.14: *(A) Particle size distribution of PVP-nAg in MilliQ water over time (B) Mean diameters of sulfidated nAg over time using spICP-MS*

NOM delays re-precipitation of Ag$_2$S

The free or detectable concentration of nAg in the presence of NOM after 7 days was 10-fold higher with 67.2 % of nAg mass concentration remaining in suspension compared to the system

without NOM (Figure S 4.12-C). In a previous study, lower aggregation of 55 nm PVP-nAg (S/Ag = 1.08) was observed in the presence of SRHA (10 mg/L) compared to systems without SRHA(Zhu et al. 2016). Natural organic matter increases the colloidal stability of nAg by enhancing their surface charge or by electrosteric repulsion (Huynh and Chen 2011, Sharma et al. 2014). In this study, higher particle number concentrations of PVP-nAg in MilliQ water were observed in the presence of NOM (Figure S 4.12-C) Similar extents of dissolution were determined in the absence and presence of NOM at the S/Ag ratio of 0.5 (3.8 % on day 4 and 3.6 % on day 7 of the initial spiked nAg mass concentration). Since similar dissolution extents observed in the absence and presence of NOM at an S/Ag ratio of 0.5, there should be similar extents of Ag_2S particle formation in systems with NOM as well. However, unlike sulfidated systems without SRNOM, a secondary particle size distribution was not observed until day 7. There may be complexation between NOM and dissolved Ag leading lower free concentrations of Ag^+ for the direct sulfidation reaction to form Ag_2S particles causing the slow appearance of secondary Ag_2S particles. The persistence of the secondary peak (with a mean diameter ~ 30 nm) was observed on day 14 as well (an extra data point was measured on day 14) indicating that the spikes were indeed arising from a secondary peak and were not a measurement artifact (Figure S 4.15). Previous studies have reported the natural formation of nAg from Ag^+ in natural waters is associated with the reduction of Ag^+ to nAg by different fractions of natural organic matter (Akaighe et al. 2011, Adegboyega et al. 2013). Both humic and fulvic acid from different sources (river, sediment) can reduce Ag^+ to nAg at ambient temperatures. After 14 days, no nAg peaks were observed in control systems with spiked 1 mg/L of Ag^+ ions in 10 mg/L of NOM, indicating the absence of natural formation of nAg (Figure S 4.16) in this NOM system. This may be due to the different compositions of natural organic matter used in studies. Additionally, the absence of

any such secondary size distributions in MilliQ systems (Figure S 4.12-D) after 7 days, confirms

the appearance of a secondary peak is due to the formation of Ag_2S particles over time. Overall,

the presence of NOM increases the colloidal stability and persistence of sulfidated nAg over the

incubation period of this study at environmentally relevant concentrations.
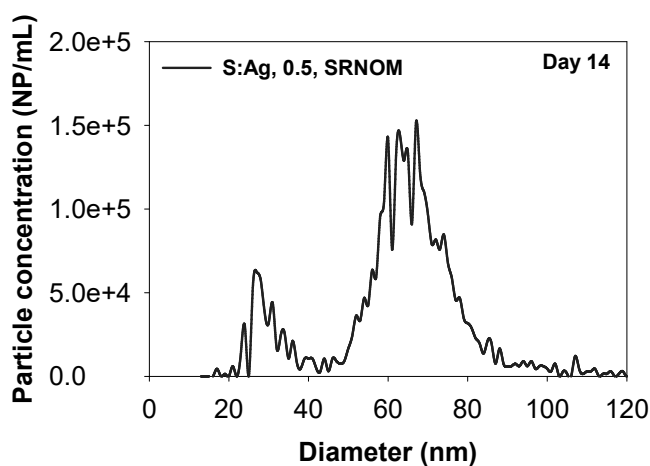
Figure S 4.15: Particle size distribution of S:Ag = 0.5 with SRNOM on day 14 using spICP-MS
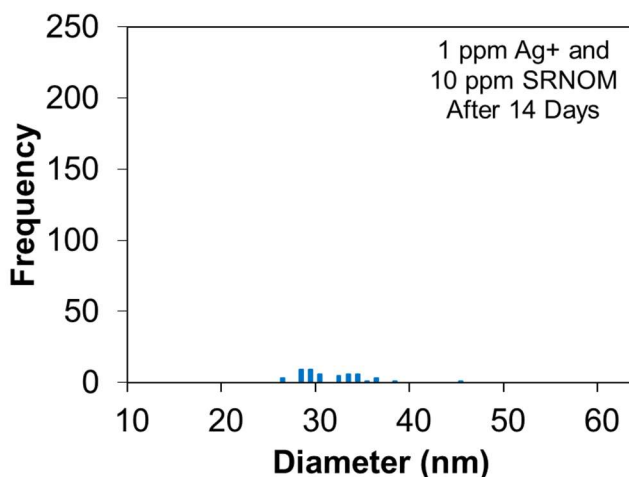
Figure S 4.16: No natural formation of nAg from Ag+ in the presence of SRNOM measured using

spICP-MS

4.7 References

1) Adegboyega, N. F., et al. (2013). "Interactions of Aqueous Ag+ with Fulvic Acids: Mechanisms of Silver Nanoparticle Formation and Investigation of Stability." Environmental Science & Technology **47**(2): 757-764.

2) Akaighe, N., et al. (2011). "Humic Acid-Induced Silver Nanoparticle Formation Under Environmentally Relevant Conditions." Environmental Science & Technology **45**(9): 3895-3901.

3) Azodi, M., et al. (2016). "Dissolution Behavior of Silver Nanoparticles and Formation of Secondary Silver Nanoparticles in Municipal Wastewater by Single-Particle ICP-MS." Environmental Science & Technology **50**(24): 13318-13327.

4) Baalousha, M., et al. (2015). "Transformations of citrate and Tween coated silver nanoparticles reacted with Na2S." Science of the Total Environment **502**: 344-353.

5) Baalousha, M., et al. (2013). "Effect of monovalent and divalent cations, anions and fulvic acid on aggregation of citrate-coated silver nanoparticles." Science of the Total Environment **454-455**: 119-131.

6) Baalousha, M., et al. (2011). "Flow field-flow fractionation for the analysis and characterization of natural colloids and manufactured nanoparticles in environmental systems: A critical review." Journal of Chromatography A **1218**(27): 4078-4103.

7) Bhattacharjee, S. and S. Ghoshal (2018). "Sulfidation of nanoscale zerovalent iron in the presence of two organic macromolecules and its effects on trichloroethene degradation." Environmental Science: Nano **5**(3): 782-791.

8) Brar, S. K., et al. (2010). "Engineered nanoparticles in wastewater and wastewater sludge – Evidence and impacts." Waste Management **30**(3): 504-520.

9) Chen, R., et al. (2008). "Silver sulfide nanoparticle assembly obtained by reacting an assembled silver nanoparticle template with hydrogen sulfide gas." Nanotechnology **19**(45): 455604.

10) Collin, B., et al. (2016). "Effect of natural organic matter on dissolution and toxicity of sulfidized silver nanoparticles to Caenorhabditis elegans." Environmental Science: Nano **3**(4): 728-736.

11) Diegoli, S., et al. (2008). "Interaction between manufactured gold nanoparticles and naturally occurring organic macromolecules." Science of the Total Environment **402**(1): 51-61.

12) Dubascoux, S., et al. (2010). "Field-flow fractionation and inductively coupled plasma mass spectrometer coupling: History, development and applications." Journal of Analytical Atomic Spectrometry **25**(5): 613-623.

13) Dubascoux, S., et al. (2008). "Optimisation of asymmetrical flow field flow fractionation for environmental nanoparticles separation." Journal of Chromatography A **1206**(2): 160-165.

14) Fabrega, J., et al. (2009). "Interactions of silver nanoparticles with Pseudomonas putida biofilms." Environmental science & technology **43**(23): 9004-9009.

15) Fletcher, N. D., et al. (2019). "Stability of silver nanoparticle sulfidation products." Science of the Total Environment **648**: 854-860.

16) Gardea-Torresdey, J. L., et al. (2014). "Trophic Transfer, Transformation, and Impact of Engineered Nanomaterials in Terrestrial Environments." Environmental Science & Technology **48**(5): 2526-2540.

17) Garner, K. L. and A. A. Keller (2014). "Emerging patterns for engineered nanomaterials in the environment: a review of fate and toxicity studies." Journal of Nanoparticle Research **16**(8): 2503.

18) Garner, K. L., et al. (2017). "Assessing the Risk of Engineered Nanomaterials in the Environment: Development and Application of the nanoFate Model." Environmental Science & Technology **51**(10): 5541-5551.

19) Goates, J. R., et al. (1951). "Thermodynamic Properties of Silver Sulfide1." Journal of the American Chemical Society **73**(2): 707-708.

20) Gottschalk, F., et al. (2009). "Modeled environmental concentrations of engineered nanomaterials (TiO2, ZnO, Ag, CNT, fullerenes) for different regions." Environmental Science & Technology **43**(24): 9216-9222.

21) Hagendorfer, H., et al. (2011). "Application of an asymmetric flow field flow fractionation multi-detector approach for metallic engineered nanoparticle characterization – Prospects and limitations demonstrated on Au nanoparticles." Analytica Chimica Acta **706**(2): 367-378.

22) He, D., et al. (2019). "Silver sulfide nanoparticles in aqueous environments: formation, transformation and toxicity." Environmental Science: Nano.

23) Hoque, M. E., et al. (2012). "Detection and characterization of silver nanoparticles in aqueous matrices using asymmetric-flow field flow fractionation with inductively coupled plasma mass spectrometry." Journal of Chromatography A **1233**: 109-115.

24) Huynh, K. A. and K. L. Chen (2011). "Aggregation Kinetics of Citrate and Polyvinylpyrrolidone Coated Silver Nanoparticles in Monovalent and Divalent Electrolyte Solutions." Environmental Science & Technology **45**(13): 5564-5571.

25) Kaegi, R., et al. (2013). "Fate and transformation of silver nanoparticles in urban wastewater systems." Water Research **47**(12): 3866-3877.

26) Kaegi, R., et al. (2011). "Behavior of Metallic Silver Nanoparticles in a Pilot Wastewater Treatment Plant." Environmental Science & Technology **45**(9): 3902-3908.

27) Keller, A. A. and A. Lazareva (2013). "Predicted releases of engineered nanomaterials: from global to regional to local." Environmental Science & Technology Letters **1**(1): 65-70.

28) Keller, A. A. and A. Lazareva (2014). "Predicted Releases of Engineered Nanomaterials: From Global to Regional to Local." Environmental Science & Technology Letters **1**(1): 65-70.

29) Keller, A. A., et al. (2013). "Global life cycle releases of engineered nanomaterials." Journal of Nanoparticle Research **15**(6): 1692.

30) Kent, R. D., et al. (2014). "Controlled Evaluation of Silver Nanoparticle Sulfidation in a Full-Scale Wastewater Treatment Plant." Environmental Science & Technology **48**(15): 8564-8572.

31) Kim, B., et al. (2010). "Discovery and Characterization of Silver Sulfide Nanoparticles in Final Sewage Sludge Products." Environmental Science & Technology **44**(19): 7509-7514.

32) Kraas, M., et al. (2017). "Long-term effects of sulfidized silver nanoparticles in sewage sludge on soil microflora." Environmental Toxicology and Chemistry **36**(12): 3305-3313.

33) Lau, B. L. T., et al. (2013). "A preliminary assessment of the interactions between the capping agents of silver nanoparticles and environmental organics." Colloids and Surfaces A: Physicochemical and Engineering Aspects **435**: 22-27.

34) Leenheer, J. A. and J.-P. Croué (2003). Peer reviewed: characterizing aquatic dissolved organic matter, ACS Publications.

35) Levard, C., et al. (2013). "Sulfidation of Silver Nanoparticles: Natural Antidote to Their Toxicity." Environmental Science & Technology **47**(23): 13440-13448.

36) Levard, C., et al. (2011). "Sulfidation Processes of PVP-Coated Silver Nanoparticles in Aqueous Solution: Impact on Dissolution Rate." Environmental Science & Technology **45**(12): 5260-5266.

37) Li, L., et al. (2017). "New Insights into the Stability of Silver Sulfide Nanoparticles in Surface Water: Dissolution through Hypochlorite Oxidation." Environmental Science & Technology **51**(14): 7920-7927.

38) Li, X. and J. J. Lenhart (2012). "Aggregation and Dissolution of Silver Nanoparticles in Natural Surface Water." Environmental Science & Technology **46**(10): 5378-5386.

39) Lin, S., et al. (2011). "Deposition of silver nanoparticles in geochemically heterogeneous porous media: predicting affinity from surface composition analysis." Environmental science & technology **45**(12): 5209-5215.

40) Liu, J., et al. (2011). "Kinetics and Mechanisms of Nanosilver Oxysulfidation." Environmental Science & Technology **45**(17): 7345-7353.

41) Loeschner, K., et al. (2013). "Optimization and evaluation of asymmetric flow field-flow fractionation of silver nanoparticles." Journal of Chromatography A **1272**: 116-125.

42) Lowry, G. V., et al. (2012). "Long-Term Transformation and Fate of Manufactured Ag Nanoparticles in a Simulated Large Scale Freshwater Emergent Wetland." Environmental Science & Technology **46**(13): 7027-7036.

43) Luther, G. W. and E. Tsamakis (1989). "Concentration and form of dissolved sulfide in the oxic water column of the ocean." Marine Chemistry **27**(3): 165-177.

44) Ma, R., et al. (2014). "Fate of Zinc Oxide and Silver Nanoparticles in a Pilot Wastewater Treatment Plant and in Processed Biosolids." Environmental Science & Technology **48**(1): 104-112.

45) Ma, R., et al. (2012). "Size-Controlled Dissolution of Organic-Coated Silver Nanoparticles." Environmental Science & Technology **46**(2): 752-759.

46) Meisterjahn, B., et al. (2014). "Asymmetrical Flow-Field-Flow Fractionation coupled with inductively coupled plasma mass spectrometry for the analysis of gold nanoparticles in the presence of natural nanoparticles." Journal of chromatography. A **1372C**: 204-211.

47) Mitrano, D., et al. (2012). "Field-flow fractionation coupled with ICP-MS for the analysis of engineered nanoparticles in environmental samples." Spectroscopy-Eugene **27**(9): 36.

48) Mitrano, D. M., et al. (2012). "Silver nanoparticle characterization using single particle ICP-MS (SP-ICP-MS) and asymmetrical flow field flow fractionation ICP-MS (AF4-ICP-MS)." Journal of Analytical Atomic Spectrometry **27**(7): 1131-1142.

49) Montaño, M. D., et al. (2019). "Opportunities for examining the natural nanogeochemical environment using recent advances in nanoparticle analysis." Journal of Analytical Atomic Spectrometry **34**(9): 1768-1772.

50) Nowack, B., et al. (2015). "Progress towards the validation of modeled environmental concentrations of engineered nanomaterials by analytical measurements." Environmental Science: Nano **2**(5): 421-428.

51) Philippe, A. and G. E. Schaumann (2014). "Interactions of Dissolved Organic Matter with Natural and Engineered Inorganic Colloids: A Review." Environmental Science & Technology **48**(16): 8946-8962.

52) Poda, A. R., et al. (2011). "Characterization of silver nanoparticles using flow-field flow fractionation interfaced to inductively coupled plasma mass spectrometry." Journal of Chromatography A **1218**(27): 4219-4225.

53) Reinsch, B. C., et al. (2012). "Sulfidation of Silver Nanoparticles Decreases Escherichia coli Growth Inhibition." Environmental Science & Technology **46**(13): 6992-7000.

54) Sharma, V. K., et al. (2014). "Organic-coated silver nanoparticles in biological and environmental conditions: Fate, stability and toxicity." Advances in Colloid and Interface Science **204**: 15-34.

55) Starnes, D. L., et al. (2016). "Distinct transcriptomic responses of Caenorhabditis elegans to pristine and sulfidized silver nanoparticles." Environmental Pollution **213**: 314-321.

56) Tang, D. and P. H. Santschi (2000). "Sensitive determination of dissolved sulfide in estuarine water by solid-phase extraction and high-performance liquid chromatography of methylene blue." Journal of Chromatography A **883**(1): 305-309.

57) Thalmann, B., et al. (2016). "Effect of humic acid on the kinetics of silver nanoparticle sulfidation." Environmental Science: Nano **3**(1): 203-212.

58) Thalmann, B., et al. (2014). "Sulfidation Kinetics of Silver Nanoparticles Reacted with Metal Sulfides." Environmental Science & Technology **48**(9): 4885-4892.

59) Thalmann, B., et al. (2015). "Effect of Ozone Treatment on Nano-Sized Silver Sulfide in Wastewater Effluent." Environmental Science & Technology **49**(18): 10911-10919.

60) Wagner, S., et al. (2015). "First steps towards a generic sample preparation scheme for inorganic engineered nanoparticles in a complex matrix for detection, characterization, and quantification by asymmetric flow-field flow fractionation coupled to multi-angle light scattering and ICP-MS." Journal of Analytical Atomic Spectrometry **30**(6): 1286-1296.

61) Wen, C. (1968). "Noncatalytic heterogeneous solid-fluid reaction models." Industrial & Engineering Chemistry **60**(9): 34-54.

62) Wimmer, A., et al. (2018). "New insights into the formation of silver-based nanoparticles under natural and semi-natural conditions." Water Research **141**: 227-234.

63) Zhang, Y., et al. (2016). "Impacts of morphology, natural organic matter, cations, and ionic strength on sulfidation of silver nanowires." Environmental Science & Technology **50**(24): 13283-13290.

64) Zhu, T., et al. (2016). "Effects of natural organic matter and sulfidation on the flocculation and filtration of silver nanoparticles." Environmental Science: Nano **3**(6): 1436-1446.

Chapter 5 . Reference nanoparticle size used for transport efficiency estimation influences particle counting and sizing in single particle ICP-MS

Connecting Text: The previous chapters have shown that spICP-MS is a robust technique to measure ENP concentrations, sizes under environmentally relevant conditions. The re-precipitation of nAg from Ag^+ leading to the formation of smaller nAg particles (~ 26 nm) creates a need to increase detection and sensitivity of spICP-MS closer to the detection limit. This is of higher environmental significance as smaller NPs are more bioavailable than larger NPs. Therefore, this chapter delves into a key aspect of spICP-MS analysis; the effect of NP size used for transport efficiency, which is used in the particle concentration and size estimation calculations.

Findings from Chapter 3 are in preparation for submission to the following journal: Environmental Science: Nano. **Rao S.**, Rahim A., Bechu A., Ghoshal S., (2020) Reference nanoparticle size used for transport efficiency estimation influences particle counting and sizing in single particle ICP-MS.

5.1 Introduction

The use of engineered nanoparticles (ENPs) in commercial and consumer products is increasing rapidly, to enable functions and properties that are not easily achievable with bulk materials.(Giese et al. 2018) Release of ENPs into the environment has raised questions about their transport, fate, bioavailability and toxicity. Currently, several studies have predicted ENP release and exposure based on modeling methodologies (Sun et al. 2016, Giese et al. 2018, Parker and Keller 2019). Models have predicted environmental concentrations of different ENPs in aquatic compartments such as surface water to be in the µg/L to ng/L range (Sun et al. 2016). However, these models have to be validated using experimental data to ensure that the model is capturing all possible

aspects of ENP fate in the environmental system (Nowack et al. 2015). Analytical measurements of ENPs at environmentally relevant concentrations may be challenging due high abundance of background particles (Montano et al. 2014) and interferences caused due to naturally occurring polyatomic species (Tuoriniemi et al. 2012). Developing and optimizing analytical techniques to overcome these challenges and improve detection is a priority (Hassellöv et al. 2008).

Single particle ICP-MS (spICP-MS) has the ability to detect ENPs in the low to high ng/L range (depending on the element of interest) and is capable of providing particle size distributions and concentrations (Lee et al. 2014, Montano et al. 2014). An important parameter required for the detection of metal ions generated from an ENP at a given mass to charge ratio is the user-specified interval of time or dwell time (units of millisecond per reading). The intensity readings in this time window is correlated to the amount of metal present in the sample (Pace et al. 2011). Recent improvements in the spICP-MS instrumentation have resulted in enabling dwell-times or data acquisition rates in the microsecond range (Hineman and Stephan 2014, Montano et al. 2014), which has significantly improved detection compared to past studies that have used dwell times in the millisecond range (Pace et al. 2011, Pace et al. 2012, Tuoriniemi et al. 2012, Lee et al. 2014). Because the signal from a single nanoparticle (NP) event is in the microsecond range (Engelhard 2011), measuring at dwell times at a similar order of magnitude enables the detection of ENPs at environmentally relevant concentrations. Recent studies using microsecond dwell times have shown improved sensitivity and data quality, reduced coincidences leading to better particle counting and sizing and reduced background interferences (Hineman and Stephan 2014, Montano et al. 2014) . The quantification of ENP size and concentration is also dependent on another parameter; nebulization or transport efficiency (TE) (Degueldre and Favarger 2004, Laborda et al. 2013) .The importance of TE in spICP-MS arises from the difference in the transport of dissolved

ions compared to particles. TE represents the fraction of aqueous sample that reaches the plasma (Montano et al. 2014) and therefore accounts for the volume loss of particles during transport of the aspirated samples through the spray chamber (Pace et al. 2011). Pace *et al.* suggested three different methodologies to determine transport efficiency: (i) waste collection method which determines TE indirectly by collecting the waste stream exiting the spray chamber and determining the total analyte reaching the plasma by comparing the volume that was lost in the spray chamber to the sample uptake volume. The other two methods are more direct methods and they measure the fraction of analyte that actually reaches the plasma; (ii) particle size and (iii) particle frequency methods. The waste collection method led to overestimation of TE, which underestimated particle number concentrations and overestimated sizes(Pace et al. 2011). The particle size and frequency methods produced more realistic particle size and number concentrations. The particle frequency method has been adopted by various studies to calculate η_n or TE (Pace et al. 2012, Hadioui et al. 2015, Azodi et al. 2016) is calculated using eq (5.1) (Pace et al. 2011).

$$\eta_\eta = \frac{f(I_p)}{q_{liq} \cdot N_p} \tag{5.1}$$

Where, $f(I_p)$ is the number of pulses (peaks)/min and the term I_p represents the individual pulse intensities (counts), N_p is the particle number concentration (NP/mL) and q_{liq} is the inlet flow rate (mL/min). Typically, 60 nm nAu is used for determination TE. However, the influence of nAu size on TE estimation and therefore, on the accuracy of size and particle number concentration has not yet been clearly demonstrated. Theoretically, TE is used to convert concentration (C, μg/mL) of ions to mass flux (W, μg/event) using the following equation (Pace et al. 2011):

$$W = \eta_n \cdot q_{liq} \cdot t_{dt} \cdot C \tag{5.2}$$

Where, W= mass observed per event (µg/event), η_n or TE = transport efficiency, q_{liq} = flow rate (mL/ms), t_{dt} = dwell time (ms/event). In short, mass flux calibrates the detected cluster of ions in an event to a particle mass.

When measuring samples, these mass flux calibrations are used to determine particle mass and size. In this study, we demonstrate that it is important to determine the TE value representative of the particular size range being measured, as this TE value influences particle diameter and number concentration calculations. Use of improper TE values may influence the particle sizing and counting efficiencies.

While this study addresses a systematic error to improve detection of ENPs by spICP-MS, other recent studies have demonstrated improved particle detection by improving data and signal processing methods (Laborda et al. 2013, Cornelis and Hassellöv 2014). By hyphenating spICP-MS with ion-exchange resin columns background interferences from dissolved ions were reduced, and desolvating nebulizers (Hadioui et al. 2015) allow reduction of interferences from oxygen and hydrogen to analyte signals. For example, hyphenating an ion-exchange column with a highly sensitive sector - field ICP-MS (ICP-SF-MS) improved the size detection limit of ZnO from the previously reported 45 nm(Lee et al. 2014) to 8.2 nm in deionized water (Fréchette-Viens et al. 2019) and attained a ZnO particle detection limit of 1000 NP/mL in river water. The use of a desolvating nebulizer (which removes the water vapor phase in aerosols to create a dry aerosol) with both spICP-MS as well as ICP-SF-MS led to increased sensitivity due to higher transport efficiencies and higher efficiencies of ion extraction from the plasma (Hadioui et al. 2019). However, these adaptations require additional set-ups or unique instrumentation to achieve improved detection. In this study, we identify methods, which can make detection more accurate using only regular ICP-MS systems. The objectives of this study was to determine the effect of

nAu$_{TE}$ size and dwell times (in the μs range) on particle size and concentration measurements. The impact of nAu$_{TE}$ size as a proof-of-concept on particle sizing and counting efficiencies was demonstrated by comparing the particle concentration recoveries and estimated particle size of 30 nm nAu using two nAu$_{TE}$ sizes (30 nm and 55.5 nm). The estimated particle sizes using spICP-MS were compared with sizes obtained from transmission electron microscopy (TEM).

5.2 Materials and Methods

5.2.1 spICP-MS analysis

PerkinElmer NexION 300X ICP-MS supported by Syngistix software (ver1.1) was used in the single particle mode for nAu characterization. The integration dwell time for experiments was varied between 10 μs to 500 μs. Sampling time was set to 60 s and a wash time of 90 s between samples. Daily flowrate was calculated by measuring the initial and final weight of a tube with 2% nitric acid (PlasmaPure Plus 67 – 70%, SCP Science, Quebec, Canada) for a given period. Dissolved calibrations (10 ng/L to 1000 ng/L) were prepared from dissolved Au (PlasmaCal, Quebec, Canada) 1000 μg/mL. All samples were measured three times.

5.2.2 Transport efficiency determination

Transport efficiencies were determined using a stock suspension of 55.5 nm (ultra-uniform nAu stabilized with PEG-COOH, nanoComposix, California, USA) supplied at a concentration of 54 mg/L. A stock suspension of 30 nm nAu (ultra-uniform with PEG-carboxyl in 2 mM sodium citrate, nanoComposix) supplied at 53 mg/L, and 20 nm nAu (PELCO nanoxact, capped with tannic acid TED PELLA, California, USA) supplied at 50 mg/L were also used for TE estimation. At the time these experiments were conducted, NIST SRM 8013 (60 nm) and 8012 (30 nm) particles were out of stock and not available. Therefore, ultra-uniform nAu particles from nanoComposix were used in all the experiments. The uniformity and monodispersity of size was

confirmed using TEM. The primary particle sizes of 20, 30 and 55.5 nm nAu measured by TEM were determined to be 19 ± 3 nm (n = 135), 27 ± 3 nm (n = 124) and 54 ± 3 nm (n = 143), respectively (Figure S 5.1). All nAu particles were uniform in appearance and spherical in morphology. TE values may differ depending on the day between different experiments (8% variation). TE varies based on sample flow rate, viscosity and gas flowrate on any given day (Pace et al. 2011) and needs to be measured on a day-to-day basis to obtain reliable results. Therefore, all experiments studying the effect of nAu_{TE} size, number concentration and dwell time on TE were performed on the same day. Mass based TE estimation was used in this study by inputting a known mass of nAu_{TE} standard and the flowrate for that particular day and obtaining corresponding TE values.

To determine the effect of nAu_{TE} size on transport efficiency values used for particle sizing and concentration estimation, a particle number concentration of ~ 100,000 NP/mL was used for all TE value estimations (20 nm = 9.89×10^4 NP/mL or 8 ng/L , 30 nm = 9.52×10^4 NP/mL or 26 ng/L and 55.5 nm = 9.84×10^4 NP/mL or 170 ng/L). Fresh suspensions were prepared from the stock every day of the analysis. All particle suspensions for the spICP-MS study were prepared immediately before the analysis to avoid settling.

5.2.3 ENP samples in environmental matrices

TiO$_2$ anatase 35-50 nm (US Research Nanomaterials, Inc) and 30 nm polyvinyl-pyrrolidone (PVP) nAg from nanoComposix were used to determine particle sizing and counting efficiencies. A mass concentration of 50 ng/L of $nTiO_2$ was spiked in DI water and 10 ng/L of nAg was spiked in diluted WW Sludge (100x) obtained from a municipal wastewater treatment plant in Calgary, Canada.

5.2.4 Transmission electron microscopy (TEM)

Philips CM200 200 kV TEM with AMT XR40B CCD Camera was used to measure sizes. 20 μL of the concentrate was deposited on the Cu TEM substrates (Electron Microscopy Sciences, Carbon film 200 mesh Cu grids). The grids were kept in the dark and air-dried.

5.3 Results and Discussions

5.3.1 Theoretical dependence of particle size and recovery on TE and dwell time

The effect of nAu$_{TE}$ size on particle sizing and counting calculations was first tested by determining the relationship between diameter and transport efficiency. The steps influencing particle size and particle number calculations and the relevance of TE estimation in those are shown in Figure 5.1 and are discussed below.

The dissolved concentration of the analyte (C, μg/mL) is related to the intensity (I_p) through a linear calibration curve (Figure 5.1, Box (2)) described as $I_p = S \cdot C + I_{p,intercept}$, where S is the slope, and $I_{p,intercept}$ is the intercept representing the intensities generated from 0 μg/L Au$^+$ or the blank sample. $I_{p,intercept}$ was found to be 0 in the analyses performed. It is important to note that for both 30 nm and 55.5 nm nAu$_{TE}$ calibrations were performed using the same dissolved Au standards (0, 10, 50, 100, 500, 1000 ng/L Au$^+$).

$$C = \frac{I_p - I_{p,intercept}}{S} \tag{5.3}$$

The slopes ($S1$ and $S2$) of the calibration curve of intensity vs. concentration (Figure 5.1, Box (2)) are independent of nAu$_{TE}$. The very slight difference in slopes S1 (0.297) and S2 (0.28) likely arises from the difference in instrument conditions as the calibration curves were generated on two different days.

Eq (5.3) is substituted into the mass per event (W, eq (5.2)) calculation for particle analysis, resulting in the following:

$$W = \eta_n \cdot q_{liq} \cdot t_{dt} \cdot C = \eta_n \cdot q_{liq} \cdot t_{dt} \cdot \left(\frac{I_p - I_{p,intercept}}{S} \right) \qquad (5.4)$$

After processing all the data points of Box (2), Figure 5.1 using eq (5.4), a calibration curve of intensity vs mass per event (Figure 5.1, Box (3)) is generated with a slope L. Because the dissolved Au concentrations, dwell times, and flow rates of both 55 nm Au and 30 nm Au calibrations are the same, the difference in the slopes of the curves arises solely from transport efficiency.

The mathematical expression for slope L can be calculated as from $I_p = L \cdot W + I_{p,intercept}$ and eq (5.4) as the following:

$$L = \frac{S}{\eta_n \cdot q_{liq} \cdot t_{dt}} \qquad (5.5)$$

Next, the mass of the particle (m_p) is calculated using the following equation (Pace et al. 2011):

$$m_p = f_a^{-1} \left| \frac{((I_p - I_{Bgd})/\eta_i)}{L} \right| \qquad (5.6)$$

In this example, we assume that both the mass fraction of the element of interest (f_a^{-1}) and the ionization efficiency (η_i) is 100% (Degueldre et al. 2006). The ionization efficiency is defined as the ratio of the ionization extent of the particle to the ionization extent of the corresponding dissolved metal solution (Pace et al. 2011). Usually, gold and silver have ~ 100 % ionization efficiencies (Pace et al. 2011) (Sugiyama 2013). I_{Bgd} is the average background intensity. Eq (5.6) is simplified to form the following equation:

$$m_p = \frac{(I_p - I_{Bgd})}{L} \qquad (5.7)$$

Substituting the value of L from eq (5.5) to (5.7) results in the following:

$$m_p = \frac{(I_p - I_{Bgd}) \cdot \eta_n \cdot q_{liq} \cdot t_{dt}}{S} \qquad (5.8)$$

Then, the diameter of the particle is calculated (assuming spherical shape) using eq (5.9) (Pace et al. 2011) with the mass of the particle equation (5.8) substituted, proving that the diameter of the particles is a function of the cube root of the transport efficiency and dwell time.

$$d = \sqrt[3]{\frac{6 \cdot m_p}{\rho \cdot \pi}} = \sqrt[3]{\frac{6 \cdot (I_p - I_{Bgd}) \cdot \eta_n \cdot q_{liq} \cdot t_{dt}}{\rho \cdot \pi \cdot S}} \qquad (5.9)$$

Particle concentration recoveries have an inverse relationship with TE as shown in eq (5.10),

$$N_p = \frac{f(I_p)}{q_{liq} \cdot \eta_n} \qquad (5.10)$$

The results shown in Box (5) and the effects of nAu$_{TE}$ size on transport efficiency calculations are discussed in more detail in Section 5.3.2 and Section 5.3.3, respectively.
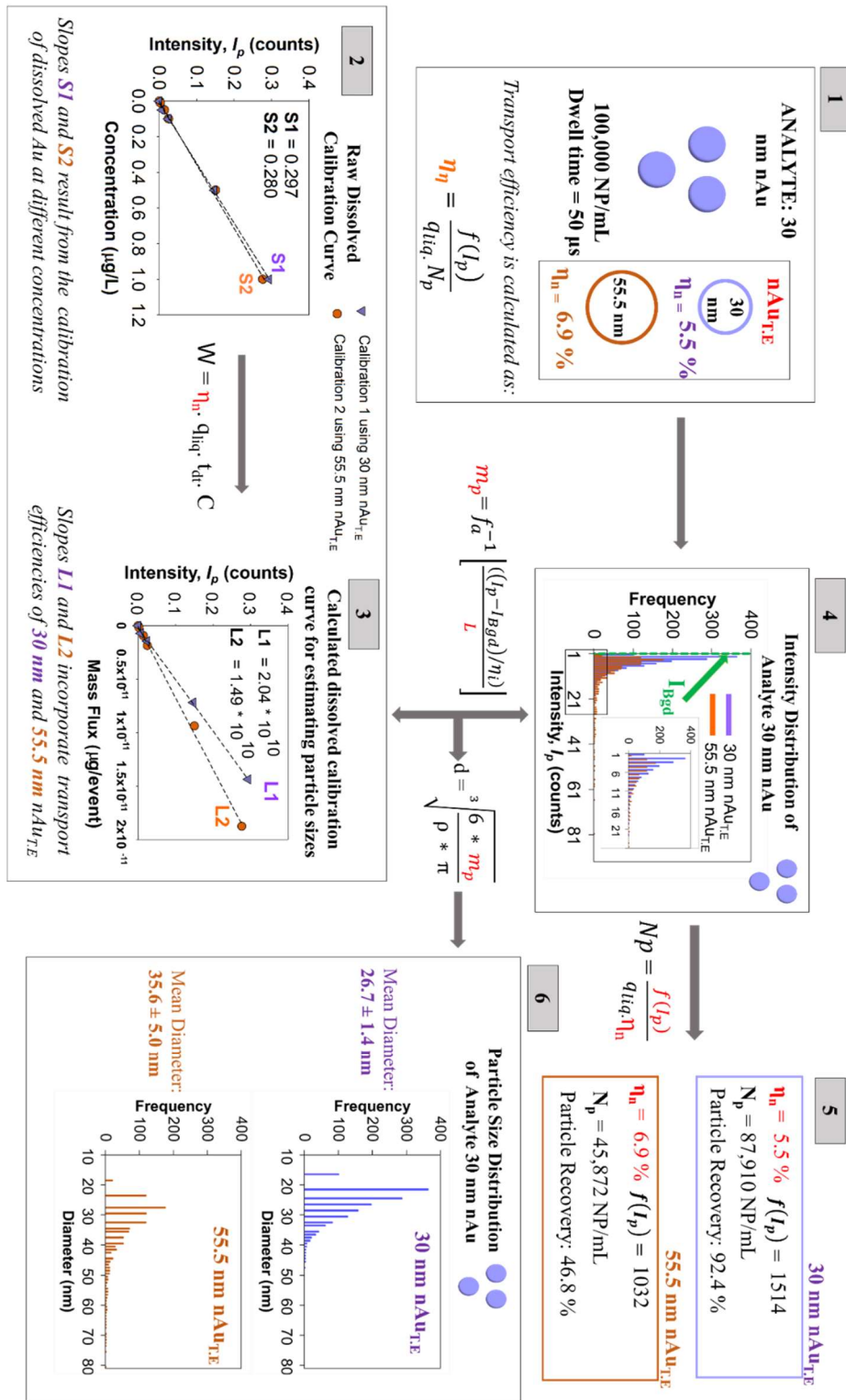
Figure 5.1: This figure has been adapted and modified from Pace *et al.* (Pace et al. 2011) Influence of nAu$_{TE}$ size on subsequent particle size and particle concentration estimations. Box (1) η$_n$ is the

transport efficiency calculated by inputting a known concentration of nAu (2) Dissolved calibration curve which relates known concentration to intensity (3) Calibration curve where concentration is converted to mass per event (4) Intensity distribution required to calculate particle concentration as well as the input parameter to convert intensity to particle size. Boxes (5) and (6) are the converted values to obtain particle concentrations as well as particle sizes and distributions. Terms highlighted in red are the parameters likely influencing the calculations in that particular step.

5.3.2 Transport efficiency values are dependent on dwell time and reference gold nanoparticle sizes

This section describes how experimentally derived TE (stated in Box (1) of Figure 5.1) was influenced by three nAu (20 nm, 30 nm and 55.5 nm) reference sizes and the choice of the dwell time. Figure 5.2 shows the $f(Ip)$ and estimated TE at different nAu$_{TE}$. According to eq (5.1), for a given flowrate and particle number concentration, $f(Ip)$ values should be identical and not be influenced by the NP size. However, the $f(Ip)$ values are different at dwell times between 10 μs and 100 μs with different nAu$_{TE}$ sizes (30 and 55.5 nm). This suggests that changes in TE are due to inconsistent measurements of $f(Ip)$.

A direct comparison of TE values generated from 20 and 30 nm nAu at different dwell times provides insight on the extent of deviation from the commonly used 55.5 nm nAu$_{TE}$. For 20 nm nAu$_{TE}$, $f(Ip)$ and TE values decreased between 50 and 500 μs (Figure 5.2 (A) and (B), respectively). This decrease is attributed to the increase in coincidences of NPs due to a large dwell time window. This phenomenon occurs when the particle event itself is much smaller than the dwell time interval.(Montano et al. 2014) The average mean particle intensities of 20 nm at dwell times of 10

μs and 30 μs (Figure S 5.2) were close to the mean intensities of the DI water blank (1.02 ± 0.005 counts), due to which TE values at 10 and 30 μs could not be determined. Examining TE values for higher dwell times such as 50 μs and 100 μs (Inset, Figure 5.2 (B)), shows a difference in the values (rank-sum test, $p > 0.05$) for different nAu_{TE} sizes (~ 1.2 times higher estimated TE for 55.5 nm compared to 30 nm nAu_{TE}). The discrepancies in *f(Ip)* values and therefore TE are the reason for observing lower estimations of recoveries and sizes in Figure 5.1, Box (5) and (6).

Different nAu_{TE} sizes possess different mean particle intensities, which may be the reason for determining different TE values at different dwell times. We confirmed that the differences in estimated TE was not due to the slight differences in spiked nAu concentrations at different sizes. As there was no significant difference (rank-sum test, $p < 0.05$) in estimated TE values at different dwell times (Figure S 5.3) between 50,000 NP/mL and 100,000 NP/mL. Therefore, these discrepancies may indeed be caused due to the differences in the instrument's ability to measure certain Au mass per particle, leading to different mean particle intensities. The mean particle intensity generated from a particle is proportional to the mass of the particle and therefore the volume. Therefore, analyte NPs with similar sizes (or masses) will produce similar intensities.
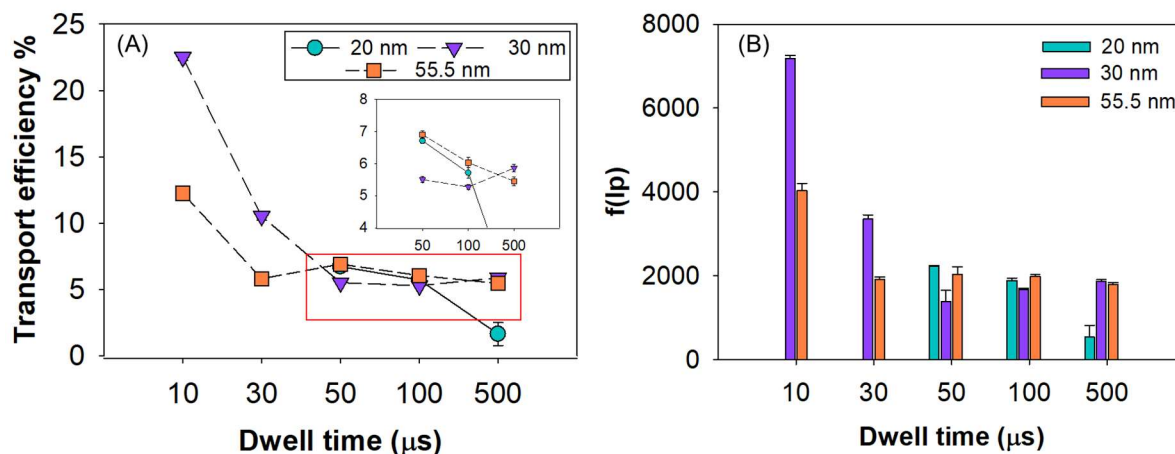
Figure 5.2: Effect of dwell time on (A) Transport efficiency using nAu$_{TE}$ 20, 30 and 55.5 nm at a particle concentration of 100,000 NP/mL and (B) f(Ip). Inset in (A) is the zoomed TE values at dwell times of 50 and 100 μs.

It is noteworthy that for 30 nAu$_{TE}$ at 10 μs, TE reaches 22.5 % which is significantly higher than the values observed for higher dwell times. The sharp increase in TE can be attributed to a combination of the short dwell time window (10 μs) as well as the small particle size (i.e. 30 nm) resulting in overestimated pulses counted per unit time. The low mean particle intensity of 30 nm at 10 μs (1.29 ± 0.002) was determined to be close to the DI water blank background intensity (1.02 ± 0.005) resulting in poor resolution and differentiation between background ions and NP events. As the mean intensities of 20 nm nAu at all dwell times in the scope of this study ($10 -$ 100 μs) is very close to the background intensities.

The TE of 55.5 nm nAu$_{TE}$ at 10 and 100 μs at a flow rate of 0.29 mL/min were 11.1 and 5.5 % respectively. Figure 5.3 (A) demonstrates the change in particle size distribution of 55.5 nm nAu as analyte (spiked concentration of 100,000 NP/mL) at two dwell times. The mean diameters using dwell times of 10 μs and 100 μs were estimated to be 42.1 ± 4.7 nm and 58.8 ± 3 nm, respectively.

The mean size obtained by TEM was 54 ± 3 nm (n = 143) which is comparable to the mean diameter obtained by spICP-MS at 100 μs. At a dwell time of 100 μs, the dissolved concentrations of 55.5 nm nAu estimated by spICP-MS were negligible (Figure 5.3 (B)). However, at a dwell time of 10 μs, there was a 7-fold increase in background-dissolved concentration at 10 μs compared to 100 μs. It appears as if a single particle event is being sliced multiple times leading to an increase in $f(I_p)$ (2984 ± 301 peaks at 10 μs and 1458 ± 51 peaks at 100 μs). This results in only a part of the particle event being counted as "particle" and the remaining counted as dissolved which leads to underestimated mean diameters and increased dissolved concentration (as a fraction of smaller NPs are counted as "dissolved Au"). Similar $f(I_p)$ values are obtained for all dwell times except for 10 μs (30 μs: 1498 ± 141 peaks and 50 μs: 1686 ± 90 peaks. This phenomenon provides insight on why higher TE values are obtained at lower dwell times such as 10 μs compared to other dwell times (30 – 500 μs).
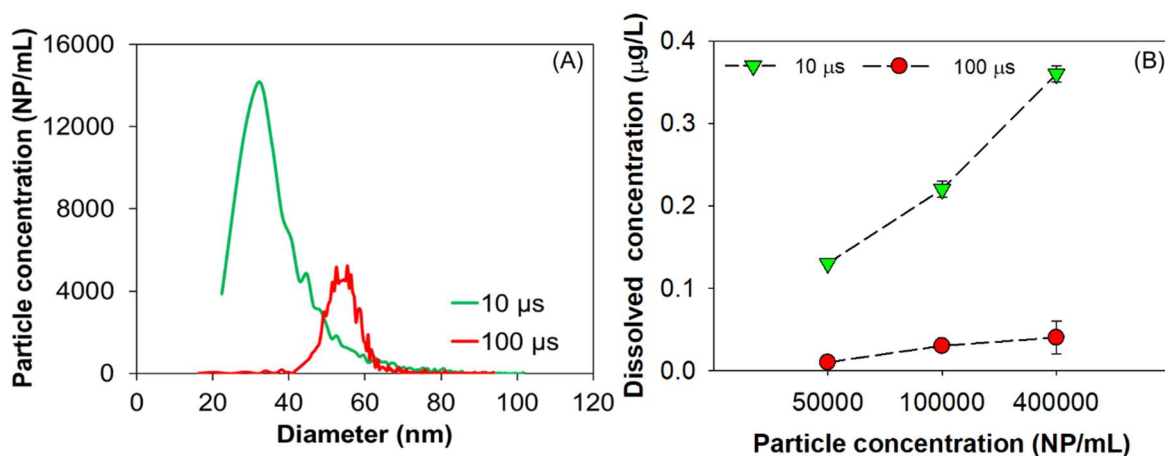
Figure 5.3: Effect of 10 μs dwell time on (A) particle concentration and size distribution of 55.5 nm nAu using 100,000 NP/mL (B) measured dissolved Au concentrations of 55.5 nm nAu at 10 and 100 μs.

For a given set of conditions such as constant flowrate, nAu_{TE} and concentration, dwell time does not have an effect on estimated particle number concentrations (8.2×10^4 NP/mL $\pm 8.3 \times 10^3$ NP/mL at 10 μs and 9.2×10^4 NP/mL $\pm 3.2 \times 10^3$ NP/mL at 100 μs). . Results from this study indicate that using a dwell time as low as 10 μs results in mean intensities close to the background signal and increased $f(I_p)$ leading to inaccurate integration of NP signals as dissolved signals. Therefore, using a low dwell time such as 10 μs is not recommended based on the results obtained from this study.

5.3.3 Particle sizing and counting efficiencies improve with suitable dwell time and reference gold nanoparticle sizes

The dependence of particle size and recovery on TE and dwell time was verified experimentally by comparing the particle concentrations and sizes of spiked 30 nm nAu (100,000 NP/mL) in deionized water using 30 nm and 55.5 nm nAu_{TE} (Figure 5.4 (A)). The particle concentration recoveries were excessively high for a dwell time of 10 μs for both 30 nm and 55.5 nm nAu_{TE} (130.6 ± 2.1 % and 129.7 ± 3.2 % respectively). The particle size distribution trends of 30 nm nAu at 10 μs and 100 μs (Figure S 5.5) is similar to the trends observed in Figure 5.3 (A) for 55 nm nAu. Further, similar to Figure 5.3 (B), at a low dwell time such as 10 μs, elevated dissolved Au concentrations are observed at both TE's (30 nm and 55.5 nm nAu_{TE}) due to the poor resolution between NP events and dissolved concentrations (Figure 5.4 (B), Figure S 5.4). As we approach closer to the limit of size detection of the instrument (16 nm for nAu in this study), data obtained from the spICP-MS needs to be carefully interpreted (Mozhayeva and Engelhard 2019). Examining the mean particle intensities sheds light on the discrepancies in measured data close to the limit of detection as seen in the previous section. For example, the mean intensities of 30 nm nAu at 10 μs was estimated to be 1.3 ± 0.004 counts and 1.8 ± 0.02 counts using 30 nm and 55.5 nm nAu_{TE} (Figure S 5.6), respectively. These values are in the similar range of the background

mean intensities of DI water (1.02 ± 0.005 counts for 30 nm and 1.04 ± 0.45 counts for 55.5 nm nAu_{TE}). These results highlight the importance of carefully interpreting results close to the detection limit, especially for smaller particles.

Particle number recoveries for the 30 nm analyte using 55.5 nm nAu_{TE} at higher dwell times of 50 µs and 100 µs were determined to be 46.8 ± 1.4 % and 59 ± 4.5 %, respectively. These recoveries increased to 92.4 ± 6.4 % and 91.7 ± 7.3 % when 30 nm nAu_{TE} was used for TE estimation. The discrepancy in recoveries between different nAu_{TE} at 50 µs and 100 µs arise from the difference in estimated TE values. For example, at a dwell time of 50 µs, transport efficiency using nAu_{TE} of 30 and 55.5 nm were determined to be 5.5 and 6.9 %, respectively. The actual percentage of particles sized 30 nm reaching the detector are 5.5%, however, using 55.5 nm nAu_{TE} overestimates the number of particles reaching the detector leading to lower recoveries. There are fewer particles of that size fraction reaching the detector.
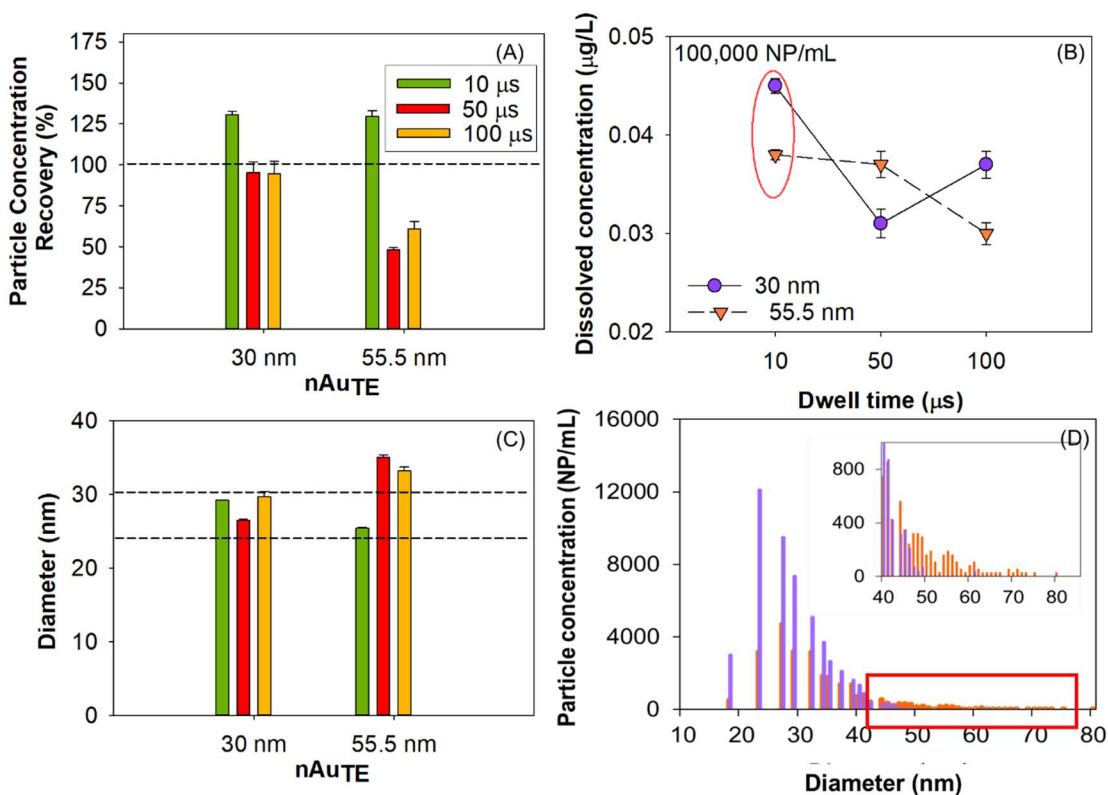
Figure 5.4: Effect of nAu$_{TE}$ size on (A) particle concentration recoveries of 30 nm nAu (analyte), dashed line represents 100% recovery (B) dissolved Au concentrations measured using spICP-MS at different dwell times and (C) on mean diameters. Dashed lines represent upper (30 nm) and lower (24 nm) TEM measured diameter of 30 nm nAu (27 ± 3 nm, n = 124)) (D) Comparison of particle size distributions of 30 nm nAu at 50 μs dwell time measured using 30 nm and 55.5 nm nAu$_{TE}$ spiked at a concentration of 100,000 NP/mL. Inset: zoomed in image of the tailing size distribution.

Figure 5.4 (C) shows the effect of nAu$_{TE}$ size on estimating mean diameters using spICP-MS. The accuracy of measured mean diameters was tested by comparing the diameters with the upper and lower limit of TEM mean diameters (27 ± 3 nm, n = 124). For 30 nm nAu$_{TE}$, diameters at all

measured dwell times were in good agreement with the TEM measurements. However, for 55.5 nm nAu_{TE}, mean diameters are over the TEM range at 50 µs and 100 µs. At a dwell time of 50 µs, the mean diameters of 30 nm nAu at 30 nm and 55.5 nm nAu_{TE} were 26.7 ± 1.4 nm and 35.6 ± 5 nm, respectively. The reason for larger estimated mean diameters for 55.5 nm nAu_{TE} was investigated by examining the particle size distribution of spiked 30 nm nAu (Figure 5.4 (D)). The size distribution obtained using nAu_{TE} of 55.5 nm shows a tailing effect of the particle size distribution in the > 40 nm range. A similar tailing effect was observed when higher dwell times (millisecond range) were used to detect 100 nm nAu particles leading to coincidences between particles at higher dwell times (3 ms and 10 ms) compared to 100 µs.(Montano et al. 2014) Because the dwell times used in this study are in the lower range (10 - 100 µs), the effect of nAu_{TE} on other parameters estimated from spICP-MS measurements such as mass concentrations, particle size distributions, mean diameters were further examined. Comparing the mass concentration and particle concentration recoveries of 30 and 55.5 nm nAu_{TE} sheds light on the tailing effect seen in Figure 5.4 (D). At 50 µs, the mass recovery using 30 nm nAu_{TE} was estimated to be 74.7 % (19.4 ± 1.02 ng/L), while the mass recovery increased to 97.3 % (25.3 ± 1.4 ng/L) using 55.5 nm nAu_{TE}. The mass concentration in the > 40 nm range was 15 - times higher (13.6 ng/L) for 55.5 nm nAu_{TE} compared to the mass concentration detected using 30 nm nAu_{TE} (0.9 ng/L). This indicates that approximately 54 % of the mass detected (of the spiked 26 ng/L) of 30 nm nAu was encompassed in the > 40 nm range for 55.5 nm nAu_{TE}. The absence of larger particles (> 40 nm) in the TEM analysis (Figure S 5.1) confirms that the tailing effect likely arises (Inset, Figure 5.4 (D)) due to the difference in estimated slopes of the calibration curve as seen in eq (5.4), Figure 1, Box 3. For example, at an intensity of 0.2 (eq (5.4)), the mass flux estimated using 55.5 nm nAu_{TE} (1.3×10^{-11} µg/event) is 1.34 times higher than 30 nm nAu_{TE} (9.7×10^{-12} µg/event). By using 30 nm nAu_{TE}

instead of 55.5 nm nAu$_{TE}$ at a dwell time of 50 µs and a spiked nAu (30 nm) particle concentration of ~ 100,000 NP/mL, the particle number coincidences reduced from 22.9 % to 1.4 % > 40 nm range (Figure 5.4 (D)). Similar tailing effects were also observed at a dwell time of 100 µs (Figure S 5.7). In a previous study, attempts to improve measured mean diameter of 10 nm nAg using spICP-MS was shown using 20 nm nAu$_{TE}$ (9.5 ± 0.7 nm) instead of 60 nm nAu$_{T.E}$ (19.6 ± 0.2 nm) at a dwell time of 100 µs (Azodi 2017). However, in the study, the same mass concentration of nAu$_{TE}$ was aspirated for both sizes (207 ng/L). A TE of 1.1 % was obtained for 20 nm nAu$_{TE}$ compared to 60 nm nAu$_{TE}$, which was 9.9 %. Lower (and more realistic) diameters obtained using 20 nm nAu$_{TE}$ was attributed to the lower TE values estimated (1.1 %) using spICP-MS.

The applicability of the developed method was also employed to characterize silver nanoparticles (nAg) in diluted wastewater sludge (WW sludge) and titanium dioxide nanoparticles (nTiO$_2$) in DI water. For this purpose, the particle size distributions and mass recoveries of nTiO$_2$ obtained using 55.5 nm and 30 nm nAu$_{TE}$ were monitored using ^{47}Ti isotope on spICP-MS (Figure 5.5 (A)).
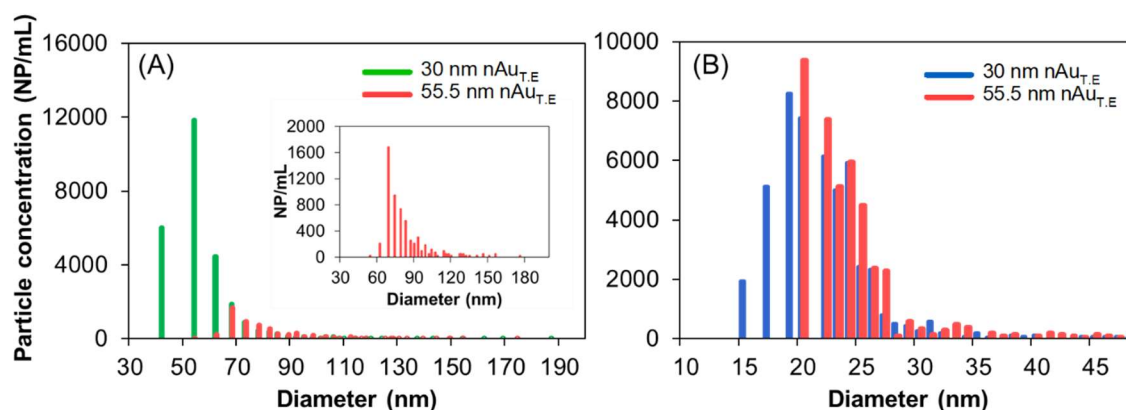
Figure 5.5: Particle size distribution measured using 30 and 55.5 nm nAu_{TE} (A) 50 ng/L of $nTiO_2$ at 50 μs. The zoomed in size distribution obtained using 55.5 nm nAu_{TE} is the inset (B) 10 ng/L of 30 nm PVP-nAg in 100x diluted WW Sludge matrix at 100 μs.

The exact spiked particle number concentration was unknown due to the polydispersity of the $nTiO_2$ sample; therefore, the particle number recoveries were not estimated. The overall particle size distribution shifts towards smaller sizes with a mean diameter of 57 ± 13.2 nm using 30 nm nAu_{TE} compared to 55.5 nm nAu_{TE} (91.9 ± 28.9 nm), which is closer to the size distribution as determined by TEM (51 ± 46 nm) (Figure S 5.8). Further, there was a 5-fold increase in detection of $nTiO_2$ particle number concentration (Figure 5.5 (A)) between 30 nm (41,206 ± 984 NP/mL) and 55.5 nm (5,741 ± 346 NP/mL) reference nAu_{TE}, respectively.

The monodispersity of the 30 nm PVP-nAg enabled accurate estimation of particle concentration recoveries in the WW sludge matrix (Figure 5.5 (B)). The expected number concentration for 10 ng/L of nAg with a mean diameter of 30 nm is 6.7×10^4 NP/mL. The particle number concentration recoveries improved by a factor of 1.5 when 30 nm nAu_{TE} (74.3 %) was used instead of 55.5 nm nAu_{TE} (48.4 %). The lower particle number concentration recoveries of nAg with 30 nm nAu_{TE} is attributed to the complexity of the background matrix. Measuring the same 30 nm PVP-nAg in DI

water (Figure S 5.8) yielded in higher particle number recoveries (93.6 % for nAu_{TE} of 30 nm and 82.2 % for nAu_{TE} of 55.5 nm). The estimated diameters were 24.3 ± 5.2 nm and 26.3 ± 6.1 nm using 30 nm nAu_{TE} and 55.5 nm nAu_{TE}, respectively. The lower estimated mean diameters in diluted WW sludge matrix (20.9 ± 5.2 nm and 24.5 ± 4.1 nm using 30 nm nAu_{TE} and 55.5 nm nAu_{TE} is likely a result of the matrix. Similar decrease in mean diameters of 80 nm PVP-nAg were observed in WW effluent and WW mixed liquor systems [15]. Further, it is important to note that WW sludge contributes a continuous background signal and makes ENP analysis more challenging and less sensitive closer to the detection limit on spICP-MS (Montaño et al. 2016).

The results obtained from the present study highlight the importance of using the appropriate nAu_{TE} sizes and concentrations for spICP-MS analysis as it leads to better resolution between particles, improves peak deconvolution and reduces any artifacts of data processing, which enhances the overall quality of the data. We also demonstrate that using the right nAu_{TE} size can improve detection of ENPs, independent of the element and matrix.

5.4 Conclusions

Single Particle ICP-MS has proven to be a powerful technique in its ability to reach dwell times in the microsecond range while distinguishing between particulate and dissolved concentrations at environmentally relevant concentrations. This study is the first to delve into the impact of an aspect of spICP-MS, transport efficiency, on appropriate calibration and subsequent ENP measurements. The accuracy and sensitivity of spICP-MS was enhanced by exploring the effect of nAu reference size on transport efficiency; consequently, its effects on nanoparticle counting and sizing efficiencies. The results obtained from this study indicate that detection, particle counting and

sizing efficiencies of smaller size NPs (< 30 nm) are influenced if an improper nAu$_{TE}$ is used due to the direct relationship between diameter and TE (diameter $\propto \sqrt[3]{T.E}$).

Previous studies have shown improved sensitivity, particle sizing and counting with lowering dwell times to the µs range compared to the ms range (Hineman and Stephan 2014, Montano et al. 2014). However, results from this study show that, using very low dwell times such as 10 µs can lead to erroneous results for all particle sizes. Particularly poorer for smaller sizes (closer to the limit of detection) due to their low mean particle intensities making particle sizing and counting more challenging. Further, dissolved and particulate data obtained by changing dwell times, should be cautiously interpreted. While using microsecond dwell times and reference nAu size for TE calculations tailored to the target ENP has improved spICP-MS sensitivity, challenges with complex environmental ENP analysis still exist. For example, the preliminary results obtained from performing spICP-MS analysis with 1 µg/L of nTiO$_2$ using a lake water matrix indicated that both, the dwell time as well as the background matrix influenced the measured mean intensities. For example, at lower dwell times (30 µs), sample matrix contributes towards measuring higher mean intensities (approximately 1.3 times higher) compared to the mean intensities measured at higher dwell times (100 µs) (Figure S 5.9), this in turn increases the overall limit of detection. Lowering dwell times to improve detection of smaller NPs will lead to lower intensities making detection challenging; as NP size approaches LOD$_{size}$, mean particle intensity approaches the intensity of the continuous background signal. Choosing the right dwell times to improve detection needs to be done carefully, working with a range of dwell times, which do not drastically influence estimated TE values is a good starting point for optimizing methods.

Improving the resolution and overall data quality obtained from spICP-MS increases the range of applicability of this technique. Using spICP-MS for acquisition of size and concentration data for

environmental samples containing ENPs needs to be done more meticulously. The following methodical approach is suggested based on the results obtained from this study. Scanning the environmental samples for overall size distributions using standard nAu (50-60 nm); if preliminary results indicate presence of smaller NPs or a tailing effect, choose another nAu reference standard closer to the sample constitution to obtain more accurate particle counting and sizing results. Further work needs to be done to improve sensitivity towards smaller NPs as well as NPs in complex environmental systems.

5.5 Acknowledgements

5.6 Supplementary information

Table S 5.1: Transport efficiency values at different dwell time measured for nAu 20, 30 and 55.5 nm

Dwell time	T.E, 100,000 NP/mL			
	10 µs	30 µs	50 µs	100 µs
20 nm			8.0	4.8
30 nm	24.3	9.3	5.5	6
55.5 nm	11.1	5.5	6.9	5.5
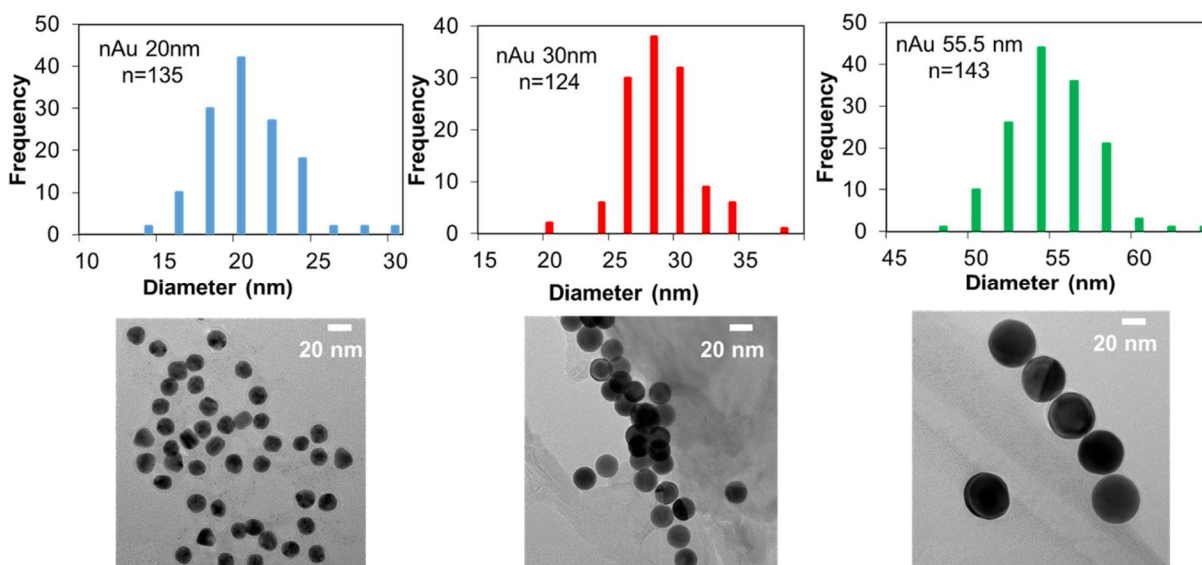
Figure S 5.1: TEM size distributions and images of 20, 30 and 55.5 nm nAu
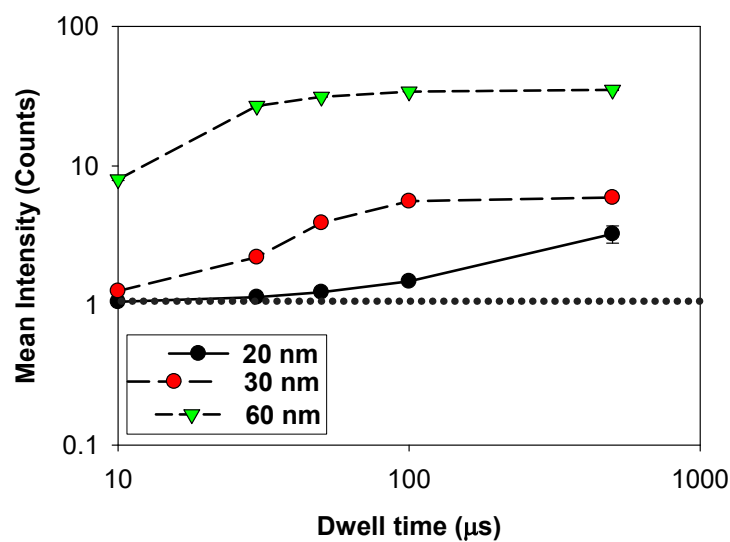
Figure S 5.2: Effect of dwell time and nAu size for T.E on mean particle intensity at 100,000 NP/mL. Dotted line is the background mean intensity of DI water
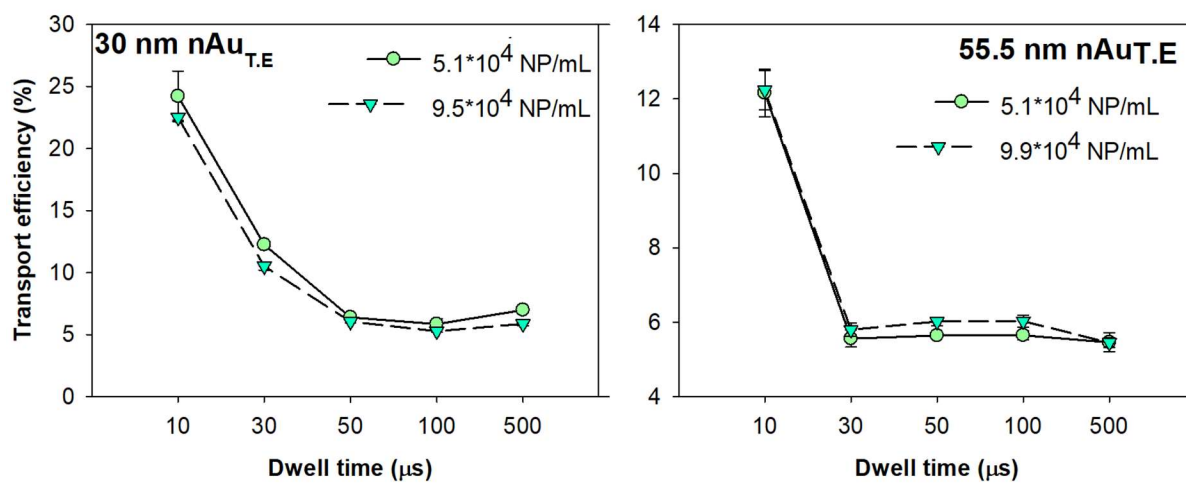
Figure S 5.3: Transport efficiencies estimated using 30 nm and 55.5 nm nAuT.E at ~ 50,000 NP/mL and 100,000 NP/mL
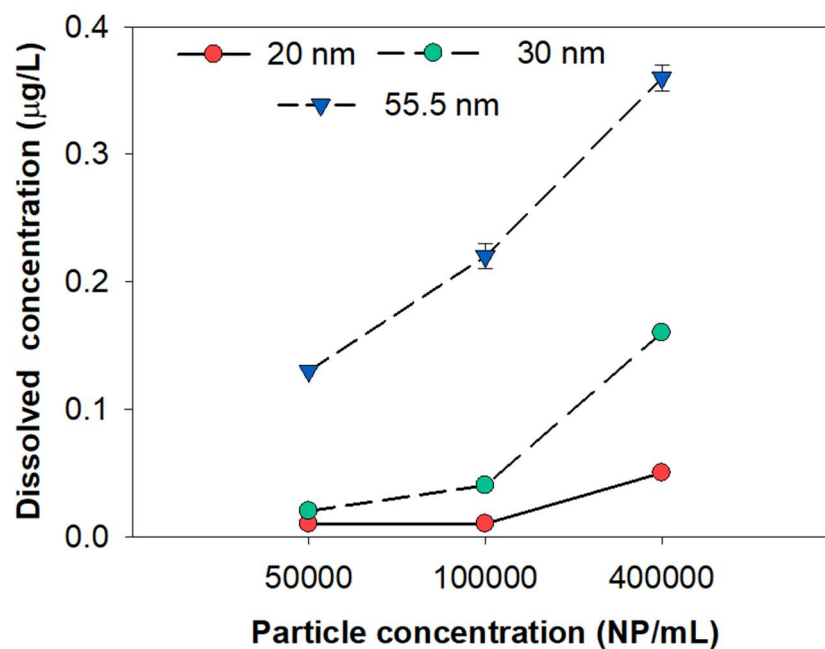
Figure S 5.4 : Dissolved concentrations of 20, 30 and 55.5 nm nAu at 10 µs
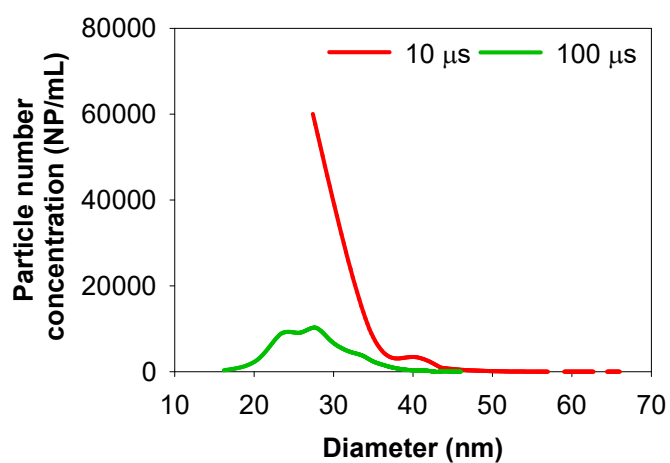
Figure S 5.5: Effect of dwell time on particle size distribution of 30 nm nAu using 30 nm nAu$_{T.E}$
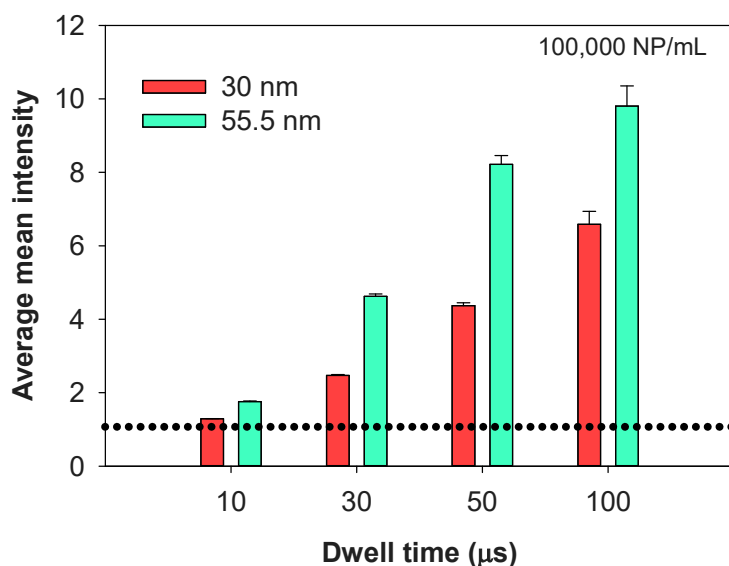
Figure S 5.6: Comparison of mean intensities of 30 nm nAu measured using 30 and 55.5 nm nAu as reference for T.E at different spiked number concentrations. Black dotted line is the background intensity for DI water
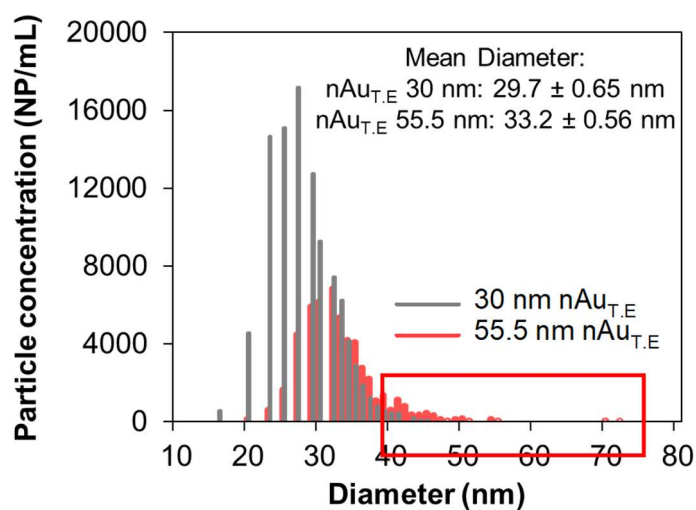
Figure S 5.7: Comparison of particle size distributions of 30 nm nAu at 100 μs dwell time and spiked concentration of 100,000 NP/mL. Inset: zoomed in image of the tailing particle size

distribution. Coincidences in the > 40 nm range reduce from 11.2 % for 55.5 nm nAu$_{T.E}$ to 1.3 %

for 30 nm nAu$_{T.E}$
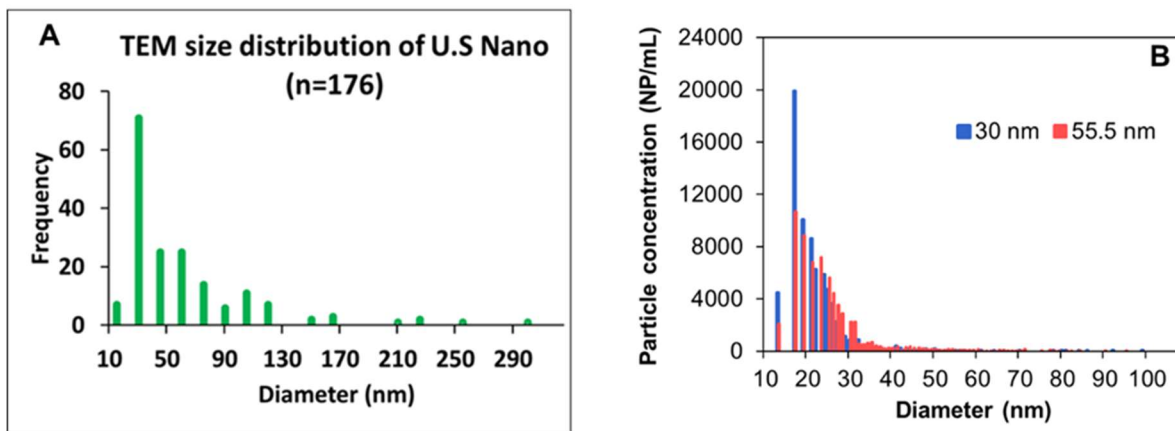
Figure S 5.8: (A) TEM size distribution for nTiO2 U.S Nanomaterials Research (B) 30 nm PVP-nAg in DI water
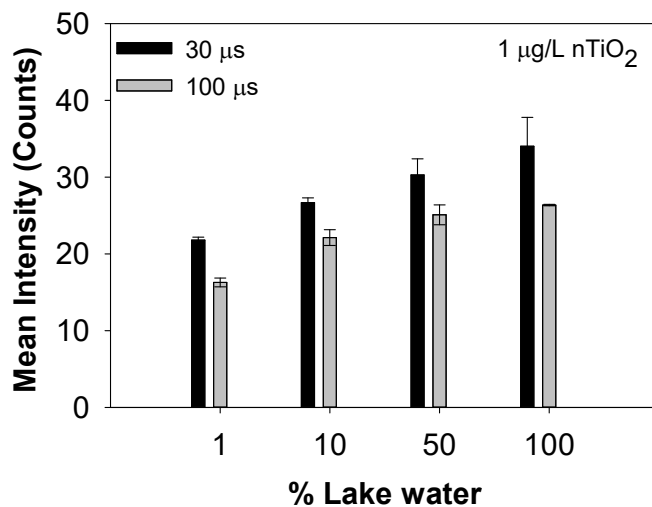
Figure S 5.9: Effect of background matrix on detection of 1 µg/L of nTiO$_2$ P25 using ^{47}Ti at two

different dwell times

5.7 References

1) Azodi, M. (2017). Dissolution Behavior of Silver Nanoparticles in Environmental Samples Using Single Particle Inductively Coupled Plasma Mass Spectrometry, McGill University Libraries.

2) Azodi, M., et al. (2016). "Dissolution Behavior of Silver Nanoparticles and Formation of Secondary Silver Nanoparticles in Municipal Wastewater by Single-Particle ICP-MS." Environmental Science & Technology **50**(24): 13318-13327.

3) Cornelis, G. and M. Hassellöv (2014). "A signal deconvolution method to discriminate smaller nanoparticles in single particle ICP-MS." Journal of Analytical Atomic Spectrometry **29**(1): 134-144.

4) Degueldre, C. and P. Y. Favarger (2004). "Thorium colloid analysis by single particle inductively coupled plasma-mass spectrometry." Talanta **62**(5): 1051-1054.

5) Engelhard, C. (2011). "Inductively coupled plasma mass spectrometry: recent trends and developments." Analytical and bioanalytical chemistry **399**(1): 213-219.

6) Fréchette-Viens, L., et al. (2019). "Quantification of ZnO nanoparticles and other Zn containing colloids in natural waters using a high sensitivity single particle ICP-MS." Talanta **200**: 156-162.

7) Giese, B., et al. (2018). "Risks, Release and Concentrations of Engineered Nanomaterial in the Environment." Scientific Reports **8**(1): 1565.

8) Hadioui, M., et al. (2019). "Lowering the Size Detection Limits of Ag and TiO2 Nanoparticles by Single Particle ICP-MS." Analytical Chemistry **91**(20): 13275-13284.

9) Hadioui, M., et al. (2015). "Detection and Characterization of ZnO Nanoparticles in Surface and Waste Waters Using Single Particle ICPMS." Environmental Science & Technology **49**(10): 6141-6148.

10) Hassellöv, M., et al. (2008). "Nanoparticle analysis and characterization methodologies in environmental risk assessment of engineered nanoparticles." Ecotoxicology **17**(5): 344-361.

11) Hineman, A. and C. Stephan (2014). "Effect of dwell time on single particle inductively coupled plasma mass spectrometry data acquisition quality." Journal of Analytical Atomic Spectrometry **29**(7): 1252-1257.

12) Laborda, F., et al. (2013). "Critical considerations for the determination of nanoparticle number concentrations, size and number size distributions by single particle ICP-MS." Journal of Analytical Atomic Spectrometry **28**(8): 1220-1232.

13) Lee, S., et al. (2014). "Nanoparticle Size Detection Limits by Single Particle ICP-MS for 40 Elements." Environmental Science & Technology **48**(17): 10291-10300.

14) Montano, M. D., et al. (2014). "Improvements in the detection and characterization of engineered nanoparticles using spICP-MS with microsecond dwell times." Environmental Science: Nano **1**(4): 338-346.

15) Montaño, M. D., et al. (2016). "Single Particle ICP-MS: Advances toward routine analysis of nanomaterials." Analytical and Bioanalytical Chemistry **408**(19): 5053-5074.

16) Mozhayeva, D. and C. Engelhard (2019). "A quantitative nanoparticle extraction method for microsecond time resolved single-particle ICP-MS data in the presence of a high background." Journal of Analytical Atomic Spectrometry.

17) Nowack, B., et al. (2015). "Progress towards the validation of modeled environmental concentrations of engineered nanomaterials by analytical measurements." Environmental Science: Nano **2**(5): 421-428.

18) Pace, H. E., et al. (2012). "Single Particle Inductively Coupled Plasma-Mass Spectrometry: A Performance Evaluation and Method Comparison in the Determination of Nanoparticle Size." Environmental Science & Technology **46**(22): 12272-12280.

19) Pace, H. E., et al. (2011). "Determining Transport Efficiency for the Purpose of Counting and Sizing Nanoparticles via Single Particle Inductively Coupled Plasma Mass Spectrometry." <u>Analytical Chemistry</u> **83**(24): 9361-9369.

20) Parker, N. and A. A. Keller (2019). "Variation in Regional Risk of Engineered Nanoparticles: nanoTiO2 as a Case Study." <u>Environmental Science: Nano</u>.

21) Sun, T. Y., et al. (2016). "Dynamic Probabilistic Modeling of Environmental Emissions of Engineered Nanomaterials." <u>Environmental Science & Technology</u> **50**(9): 4701-4711.

22) Tuoriniemi, J., et al. (2012). "Size Discrimination and Detection Capabilities of Single-Particle ICPMS for Environmental Analysis of Silver Nanoparticles." <u>Analytical Chemistry</u> **84**(9): 3965-3972.

Chapter 6 . Improving Detection and Characterization of Engineered Nanoparticles using AF4-MALS and spICP-MS in complex matrices

Connecting Text: The previous chapters have shown the advantages of both AF4 and spICP-MS for nAg detection and characterization. Titanium dioxide ($nTiO_2$) is another commonly used ENP in consumer products, however, $nTiO_2$ detection has remained challenging over the years due to its polydispersity. AF4 can be a promising method for detection and characterization of $nTiO_2$. Further, using AF4 as a sample clean-up technique prior to spICP-MS analysis can significantly improve ENP detection. This chapters discusses AF4 optimization methods for different $nTiO_2$ and the optimized method is used to fractionate $nTiO_2$ from released paint samples and characterize it for size and concentration using offline spICP-MS measurements.

6.1 Introduction

In the recent years, use of engineered nanoparticles (ENPs) in commercial products has increased (Boxall et al. 2007, Gottschalk et al. 2009, Keller et al. 2014). nano-TiO_2 ($nTiO_2$) is one of the most widely consumed nanoparticles (Chowdhury et al. 2012) in consumer products such as sunscreen, paints and coatings. Studies have shown that metal nanoparticles (e.g. Ag, TiO_2, ZnO, and Fe_2O_3) can enter human cells and exhibit cytotoxicity, and cause cell membrane leakage and inflammatory response (Zhang et al. 2008). Recently, estimates have been provided from model predictions based on approximate worldwide production volumes, and materials flow analyses from the products to different environmental compartments (Mueller and Nowack 2008, Gottschalk et al. 2009). Estimates by Mueller *et al.,*(Mueller and Nowack 2008) indicate that

current environmental levels of several metal ENPs, particularly nTiO$_2$, may pose a threat to aquatic organisms.

Detection and characterization of ENPs in complex media is a challenge due to the presence of large amounts of natural colloids (e.g. colloids of clays, mineral oxides, silica as well as biocolloids) and natural organic matter. Microscopy techniques like scanning electron microscopy (SEM), transmission electron microscopy (TEM) require extensive sample preparation and do not provide reliable quantitative information about the concentration (Hassellöv et al. 1999, Tiede et al. 2008). Although conventional techniques (light scattering, microscopy) provide some information about particle sizes, they are biased towards the larger aggregates present in the sample. In theory, larger aggregates will settle down faster due to sedimentation, which only leaves the smaller particles in suspension. The smaller particles and aggregates are an environmental concern as they are more bioavailable (Sharma 2009, Andersson et al. 2011). Asymmetric flow field flow fractionation (AF4) is a hydrodynamic elution technique that allows separation of particles according to their sizes. The retention times of nanoparticles or colloids is obtained by separating the sample according to size by applying a field force on the parabolic channel flow. Hyphenating AF4 with static; multi angle light scattering (MALS) and dynamic light scattering (DLS), ultraviolet-visible (UV-vis), and inductively coupled plasma mass spectrometer (ICP-MS) detectors will enable gathering a varied suite of information about size and concentration. This configuration has the potential to provide information about confirmation (aspect ratio; defined as ratio between radius of gyration and hydrodynamic radius), particle size distribution. Recent studies have successfully used these techniques for the characterization of metallic ENPs (Au, Ag, and Fe) at environmentally relevant concentrations. However, the sample matrices in these studies

have been relatively clean (Kammer et al. 2005, Baalousha et al. 2006, Bouby et al. 2008, Plathe et al. 2010, Kammer et al. 2011, Poda et al. 2011, Hagendorfer et al. 2012).

Single particle inductively coupled plasma mass spectrometry (spICP-MS) is a powerful technique for characterizing metallic ENPs for sizes and concentrations in complex environmental samples, but is limited in terms of detecting ENP sizes smaller than 20 nm (Mitrano et al. 2012). However, spICP-MS has its own limitation with titanium detection. The most abundant isotope ^{48}Ti (73.7%) has interferences with polyatomic compounds (PO, NO$_2$, ArC, CCl, SO) and ^{48}Ca (0.19%). Most natural waters samples are abundant in calcium, which makes using ^{48}Ti for detection extremely challenging leading to higher detected background concentrations. Other sources of background concentrations arise from instrument noise (i.e. flicker and shot noises) or signal emerging from the dissolved part of the measured isotope (Cornelis and Hasellöv 2014) which leads to a decrease in instrument sensitivity. When particle signal intensities are smaller compared to the continuous background signal, particle size distribution (PSD) determination becomes inaccurate, because a significant fraction of the particle signals may be recognized as dissolved signals or vice versa by the subjectively set threshold limit. In order to overcome this, ^{47}Ti is often used to measure TiO$_2$. However, due to lower abundance (7.44%), the quality of detection is further reduced. The limit of detection of size is high as TiO$_2$ has only 60% mass of Ti. This influences the ionization potential of Ti (the number of ions that can be generated from each particle in the plasma) as only a small fraction of the atoms in the particle are ionised in the plasma and arrive at the detector (Cornelis and Hasellöv 2014, Tharaud et al. 2017). The contribution of lower abundances (^{47}Ti) along with lower ionization leads to higher size and concentration detection limits. Therefore, employing any sample pre-treatment steps to reduce any additional interferences posed by complex environmental sample matrix should enable improved detection of nTiO$_2$ in spICP-MS.

We hypothesize that analysing polydisperse $nTiO_2$ samples through AF4 prior to spICP-MS analysis will help improve data quality and sensitivity of spICP-MS, especially in the smaller size range.

The characterization of ENPs is an important step for any upstream applications of nanotechnology or for the fate, behavior and risk assessments studies performed at the end of their life cycle downstream. The properties ENPs possess is primarily due to their morphology, shape and small size. Therefore, any advancements in nanometrology is a step closer to improving detection and characterization for any inadvertent consequences they may pose upon release. The present study demonstrates the capabilities of novel NP detection techniques such as AF4 and spICP-MS in improving sensitivity and selectivity to characterize inorganic ENPs. This was done by measuring pristine as well as transformed ENPs by developing methods for AF4 and spICP-MS. Key parameters required for robust fractionation of ENPs such as carrier fluid composition, cross flow rate, focus flow rate and focussing times were investigated. NIST polystyrene standards of different sizes were used to create a calibration curve to convert retention time to mean size on the AF4 channel. AF4 methods were developed for three types of commercial pristine $nTiO_2$ particles; one with surface treatment and two without treatment. The developed AF4 method was used as a sample pre-treatment step to test if spICP-MS detection of $nTiO_2$ improved. Finally, the applicability of the optimized methods was used to evaluate the size and concentration data quality of $nTiO_2$ particles released from painted surfaces. There are few studies, which focus on improving detection techniques for different types of $nTiO_2$.

6.2 Materials and Methods

6.2.1 Chemicals

NIST™ traceable polystyrene size standard of different sizes (40, 80, 200 nm) were purchased from Thermo Fisher Scientific, California, USA. Three types of pristine titanium dioxide nanoparticles were used; TiO_2 anatase (35-50 nm) from US Research Nanomaterials, Inc, (Texas, USA) and Degussa p25 TiO_2 nanopowder (Delaware, USA) and CristalACTiV™ PC105 TiO_2 nanopowder (Maryland, USA). TiO_2 anatase from U.S research nanomaterials is used for many applications such as coatings, paints, cosmetics and wastewater purification (US Research Nanomaterials). TiO_2 P25 (mixture of rutile and anatase) is known to be a good photocatalyst (Contado and Pagnoni 2008) and is often used for exposure and toxicity testing (Long et al. 2006). PC105 TiO_2 anatase is commercially used for its photocatalytic properties (Cristal). ASTM Type 1 de-ionized water was used for preparing carrier fluid as well as NP suspensions. Ammonium carbonate (ACS certified) and FL-70™ concentrate detergent were purchased from Fisher Scientific. Technical grade humic acid (HA) was purchased from Sigma Aldrich

6.2.2 Instrumentation

Particle sizing. Dynamic light scattering (ZetaSizer Nano ZS, Malvern) and nanoparticle tracking analysis (LM10, Malvern) were used to screen nanoparticle suspensions for size. Horiba Laser Scattering Particle Size Analyzer was used for laser diffraction measurements.

AF4-UV-MALS. Wyatt Eclipse Dualtec (Wyatt Technology) was used for fractionation of all ENP samples. A short channel (SC 145 mm) with a 10 kDa regenerated cellulose membrane and 350 μm spacer thickness for separation. Carrier solutions were varied for different NP suspensions and was delivered with an isocratic HPLC pump (Agilent Technologies, 1260 Infinity series). The detectors used for sample analysis were all downstream to fractionation; UV/vis diode array detector (Agilent Technologies, 1260 Infinity series) with different absorption wavelengths

dependent on the NP used , multi angle light scattering (MALS DAWN HELOS II Wyatt Technology).

spICPMS. Perkin Elmer NexION 300X ICP-MS supported by Syngistix software (ver1.1.) was used in single particle mode for all ENP characterization. The integration dwell time of either 50 or 100 μs was used throughout all experiments. Sampling time was set to 100 s and a wash time of 90 s between samples. Transport efficiency was calculated using 60 nm nAu (NIST, Maryland, USA) with a mass concentration of 207 ng/L. Transport efficiency values were between 6 and 8% for all time points measured. Silver and titanium calibration curve was made using dissolved silver standards (SCP Science, Quebec, Canada) between 50 ng/L and 1000 ng/L in 1% ICP grade Nitric Acid (SCP Science, Quebec, Canada).

AF4-spICP-MS. For all experiments where NPs were fractionated using AF4 prior to spICP-MS analysis, samples were collected manually at different time fractions. Samples were diluted using DI water to obtain optimum concentrations to measure using spICP-MS.

TEM. Philips CM200 200 kV TEM with AMT XR40B CCD Camera and EDAX Genesis EDS analysis system was used to measure sizes. 20 μL of the concentrate was deposited on the Cu TEM substrates (Electron Microscopy Sciences, Carbon film 200 mesh Cu grids). The grids were kept in dark and air-dried. FEI Inspect F50 FE-SEM with EDAX Octane Super 60 mm^2 SDD and TEAM EDS analysis system was used for nAg sizing and detection.

6.2.3 Data Analysis

NIST polystyrene standards were converted to hydrodynamic diameter by subtracting the retention time of the void peak from the retention time of the polystyrene standard to create size versus time calibration curve. AF4 channel recoveries were determined by injecting samples without applying

a cross flow. Area under the curve obtained from UV/vis signal and MALS 90^0 were used to calculate recoveries. Data collected from MALS can also be used for particle sizing; angular variation of scattered light is directly related to the size of the particle. Zimm, Debye and Berry fitting assume arbitrary shapes (Kammer et al. 2005). Zimm 1st order can be reliably used for irregular shaped particles < 100nm (Kammer et al. 2005, Dubascoux et al. 2008), sphere model was used for NIST polystyrene standards.

6.3 Results and discussions

6.3.1 Characterization of nTiO2 used in AF4 separation

Primary particle sizes of all three $nTiO_2$ particles were between 20 - 30 nm (Table S 6.1). Shape and morphology of $nTiO_2$ determined using TEM showed irregularly shaped particles for all samples (Figure 6.1 (a), (b) and (c)). Particle size analysis was performed using different light scattering techniques. Figure 6.1 (d) compares the particle sizes obtained using different techniques. Intensity weighted mean diameters of three replicate measurements using DLS was 120 ± 1.55 nm for U.S nano and 187.7 ± 3.61 and 1007.13 ± 27.73 nm for P25 and PC105, respectively. $nTiO_2$ often appear to be polydisperse in aqueous suspensions with primary particles as well as agglomerates (Qi et al. 2013, Loosli et al. 2014). DLS often poses problems because the scattering intensity is proportional to the sixth power of particle size, even the presence of a small amount of larger particles will lead to biased higher estimates of size (Baalousha et al. 2011, Mitrano et al. 2012).

 The TEM diameters in Figure 6.1 (d) are derived from aggregate sizes (Table S 6.3) and they correspond closer to those values calculate using NTA. Samples measured on NTA are not as heavily influenced by the presence of a few large particles compared to DLS, as the displacement

caused due to Brownian motion of particle movement, is tracked individually. U.S Nano was the least polydisperse with a polydispersity index (PDI) of 0.24 ± 0.01 while PC105 and P25 had higher polydispersity indices (0.98 ± 0.02 and 0.3 ± 0.1, respectively).
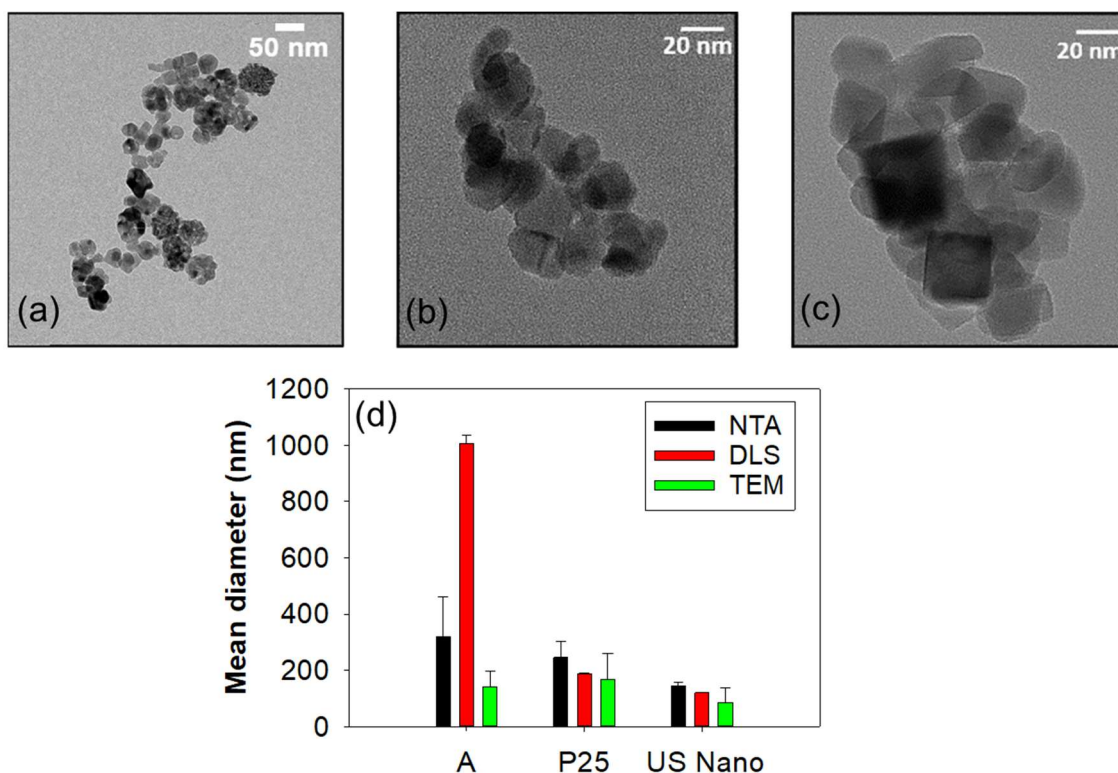
Figure 6.1: TEM images of nTiO2 (a) US Nano (b) P25 (c) PC105/A (d) mean diameters of nTiO$_2$ measured using different techniques.

6.3.2 AF4 method development

AF4 method development requires optimization of flow parameters such as cross flow rate, focus flow rate, focussing time and carrier fluid composition (Schachermeyer et al. 2012). In principle, smaller particles need a higher cross flow rate and larger particles need a lower cross flow rate for better separation and high recoveries. Further, if the channel is operated with constant cross flow, the maximum size range that can be analysed is about 10-fold the smallest particle size which is

resolved from the void peak in a given run (Kammer et al. 2005). For a polydisperse sample, using a high constant cross flow rate for smaller particles may result in higher particle-membrane interactions of the larger particles (Hagendorfer et al. 2011).

In this study, an AF4 method was first developed using polystyrene standards of different diameters. The effect of carrier fluid composition, focus time and cross flow rate on effective polystyrene separation was tested. Focus time is an important parameter as it determines the overall resolution of the fractionation. Too low focus times lead to improper focussing which cause a loss of particles in the void peak (Figure S 6.1). After attaining the optimum focus time, any further increase in focussing time does not lead to improved recoveries (Table S 6.2).

Different carrier fluid compositions were tested to obtain optimum separation and high recoveries; filtered DI water (0.1 μm , Nalgene® Rapid-Flow™ PES membrane), 4 mM NaCl and 0.025% FL-70, DI water adjusted to pH 6, 8, 10 and ammonium carbonate solutions adjusted to different molar concentrations (0.1, 0.25, 0.5 mM). Ions present in the carrier fluid influence the membrane charge as well as particle charge (Schachermeyer et al. 2012). In DI water (Figure S 6.2), polystyrene NPs pre-elute due to electrostatic repulsion between the negatively charged 10 kDa RC membrane and the polystyrene NPs, this force pushes the particles away from the membrane leading to early elution (Loeschner et al. 2013). Similar trends with early elution were observed when carrier fluids different pH (6, 8, 10) conditions were used. Delayed elution was observed (Figure S 6.2) with carrier fluid made up of 0.025% FL-70 and 4 mM NaCl. This is attributed to the decreased electrical double layer thickness which causes increased adsorption of NPs on the RC membrane (Loeschner et al. 2013). Good separation is said to be achieved when different sizes of polystyrene standards elute out linearly (Kammer et al. 2005) over time, or in other words follow the following equation:

$$t_{r} = \frac{\pi * d * w^{2} * \eta}{2 * k * T} * \frac{V_{cross}}{V_{chann}}$$ (6.1)

d = stokes diameter (m), w = channel thickness (m), k = Boltzmann constant (m^2 kg s^{-2} K^{-1}), η = Viscosity of solvent (kg $m^{-1} \cdot s^{-1}$), T = absolute temperature (K), V_{cross} = cross flow (ml/min), $V_{channel}$ = channel flow rate (ml/min), t_r = retention time (s)

Linear separation of polystyrene standards was achieved (Figure 6.2 (a)) using a carrier fluid composition of 0.25 mM ammonium carbonate with a cross and focus flow rate of 0.5 ml/min with a 2 min focus step followed by a 3 min focus and injection step. Figure 6.2 (b) presents the linear calibration curve plotted with void volume peak subtracted from retention time versus mean diameter of polystyrene particles. Data obtained from MALS is fitted to a spherical model on ASTRA, which assumes a spherical shape to calculate the geometric radius of the polystyrene standards.
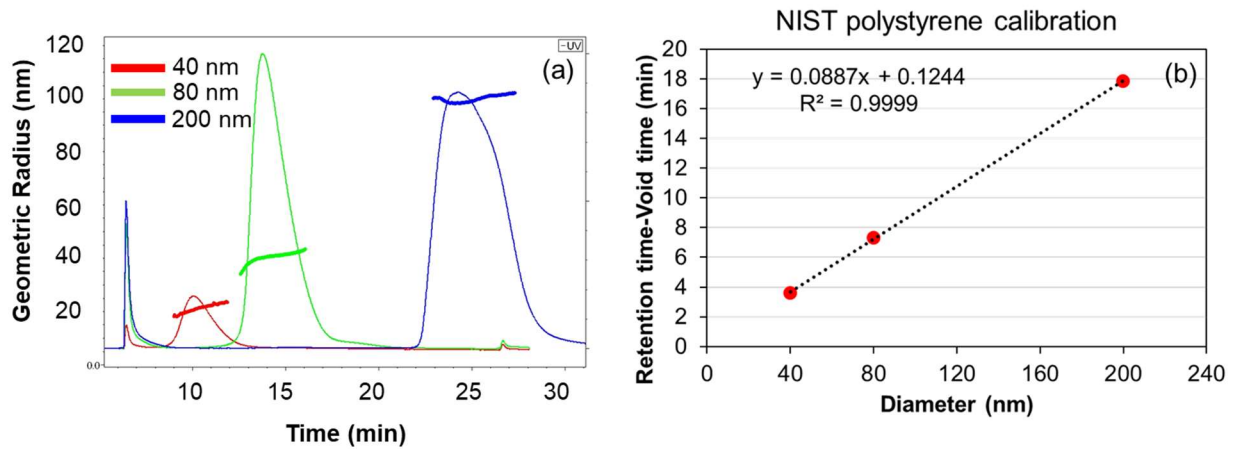
Figure 6.2: (a) UV signal @ 280 nm of polystyrene standards fitted in the sphere model, horizontal lines on the peak represent particle size distribution calculated using spherical model on ASTRA (b) Calibration curve of retention time versus size of polystyrene standards.

6.3.3 AF4 optimization of nTiO₂

Preliminary screening experiments revealed, U.S nano TiO_2 was most stable in suspension, therefore the AF4 method for TiO_2 was first developed using U.S nano particles. Optimized flow conditions and carrier fluid compositions for all tested pristine $nTiO_2$ is reported in Table 6.1. Figure 6.3 (a) shows fractionated NPs over time and the root mean square (RMS) data from 90^0 MALS is almost linear. Smaller sized particles close to the void peak are influenced by the larger un-retained particles during the focusing step due to which a V-shaped fraction is observed close to void peak (Figure 6.3 (a)). The light scattering data is fitted using Debye 3rd order function on ASTRA, which fits data over a wider size range. Figure 6.3 (b) reveals information about the possible conformation of the TiO_2 NPs. Smaller sized particles have a higher aspect ratio (RMS/ hydrodynamic radius) and large particles have a lower aspect ratio. This indicates heterogeneity between different sizes of the U.S nano NPs. A spherical particle has an aspect ratio 0f 0.775 (Kammer et al. 2005). The results obtained from the present study indicate that a certain fraction of NPs in the mid size range are spherical whereas the smaller and larger NPs deviate from the sphere.
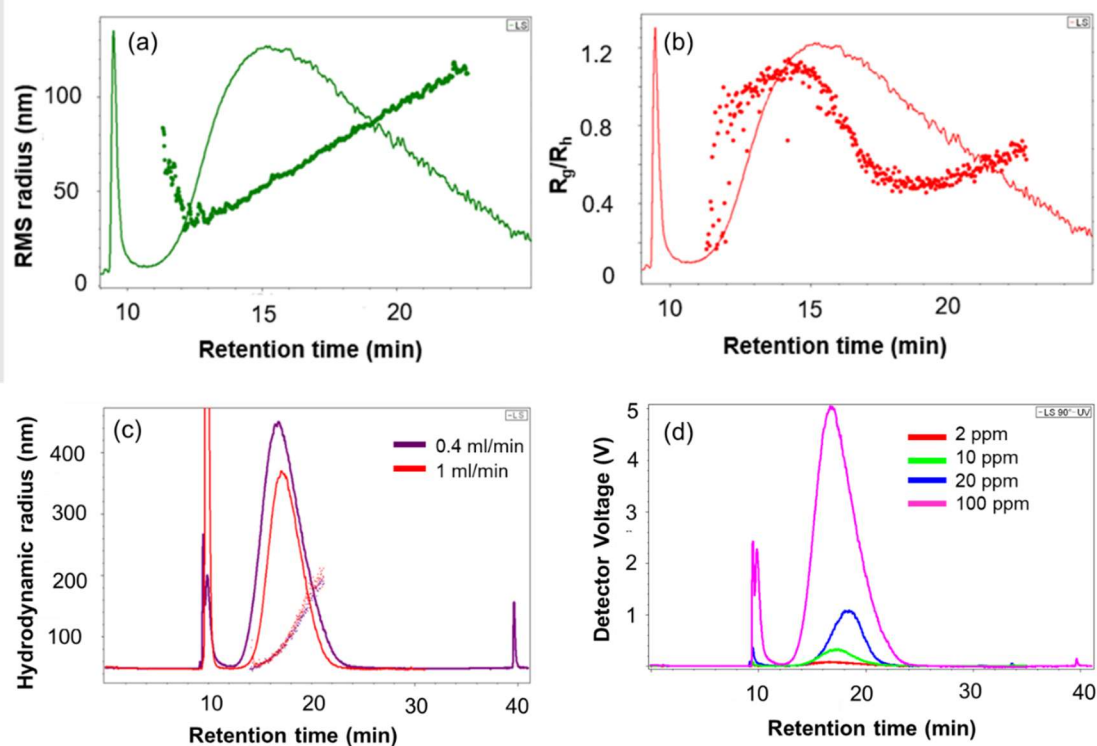
Figure 6.3: (a) nTiO$_2$ U.S nano fitted with Debye 3rd order model (b) Aspect ratio of U.S nano (c) Effect of focus flow rate on nTiO2 P25 fractionation (d) Effect of nTiO$_2$ concentration on MALS 90^0 detector signal.

Improved recoveries of nTiO$_2$ P25 were obtained by stabilizing them with humic acid (HA). Figure 6.3 (c) shows linear fractionation of P25 and the effect of focus flow rate on fractionation. An increase in focus flow rate decreases the area under the eluted peak leading to lower recoveries. This phenomenon occurs when there is a higher adsorption of NPs to the membrane during the focussing step, due to the increased focus flow rate. Using accurate focus flow rates is of significance at lower particle concentrations, as losses of NP occur on the membrane due to the increased force, which lead to lower detector signals making detection and characterization challenging. The mass or the concentration of particles injected into the AF4 system is another important parameter in method optimization. The effect of particle concentration on 90^0 MALS

signal is clearly seen in Figure 6.3 (d). Higher particle concentrations have higher detector voltage signals on the MALS detector. Using ICP-MS as a downstream detector enables measuring lower concentrations, which is more environmentally relevant (Mitrano et al. 2012).

Table 6.1: Optimized AF4 conditions for different types of pristine $nTiO_2$

$nTiO_2$	Carrier Fluid	Cross flow (ml/min)	Recovery % MALS 90 detector
A	DI water	constant 0.3 ml/min	90.90%
US Nano	0.1 mM Sodium pyrophosphate decahydrate + 0.025% FL-70	gradient 0.3 ml/min with focus flow of 0.5 ml/min	74.00%
P25	DI water	constant of 0.4 ml/min	94.40%

Different types of $nTiO_2$ NPs require different optimization conditions based on their inherent surface charge, morphology and size range. AF4 is a robust method to fractionate and characterize $nTiO_2$ sizes. A study by Zhou et al showed that $nTiO_2$ of the same chemical composition have different material properties, stability and mobility (Zhou et al. 2013). The variety of tunable parameters such as carrier fluid compositions, flow rates and membrane type provides an opportunity to carefully tailor flow conditions to each sample (Montaño et al. 2019).

6.3.4 Application of AF4: improving data quality of spICP-MS

Determining particle number concentrations of ENP fractions post AF4 separation requires a downstream detector capable of estimating number concentrations. spICP-MS is a good choice as it has low concentration detection limits (ng/L) (Lee et al. 2014) and detection is not impacted by the dilution that occurs during the AF4 fractionation step. Therefore, the hypothesis of pre-fractionation of $nTiO_2$ using AF4 prior to spICP-MS analysis was tested by first running U.S nano $nTiO_2$ only through spICP-MS. Subsequently, this was compared to the sample that was

fractionated using AF4, which enables collection of different fractions offline. Fractions in the lower size range (45-90 nm) were collected and run through spICP-MS. The difference in data quality with nTiO$_2$ run through AF4 and without AF4 is demonstrated in Figure 6.4. The tailing effect caused due to the polydispersity of the particle size distribution improves which is seen in with the decrease in standard deviation of the estimated mean diameters (62.7± 31.6 nm for no AF4 and 62.8 ± 4.8 nm after AF4 separation). This technique can be used for samples that require precise characterization in a certain size range as it improves data quality by removing larger particles.
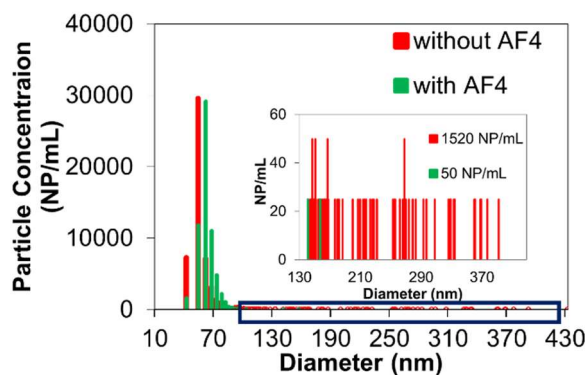
Figure 6.4: nTiO$_2$ U.S Nano fraction separated in AF4 and analysed using optimized spICP-MS conditions @ ^{47}Ti and dwell time of 50 μs

The above developed method was used to characterize nTiO$_2$ released from paint. Different fractions were collected from the AF4 and analysed using spICP-MS. Polystyrene weighing dishes were painted with custom-made paint (base paint and PC105/TiO$_2$ A) allowed to dry before exposing them to simulated "harsh conditions" by using mild sonication. Released nTiO$_2$ particles were diluted with DI water before further analysis. Figure 6.5 shows released nTiO$_2$ from paint on spICP-MS with and without fractionation on AF4. Released nTiO$_2$ was run through AF4 and collected as two fractions: between 12 -15 min and 15-20 min. Figure 6.5 (a) shows the shift in

particle size distributions of different fractions and without fractionation. Released nTiO2 concentration in the 12-15 min fraction was determined to be 4 µg/L or 6.05×10^6 NP/mL and the 15-20 min fraction was 99.8 µg/L or 2.06×10^7 NP/mL. The mean diameters of the size distributions significantly improve Figure 6.5 (b-d). Without prior fractionation, the mean diameter of the release $nTiO_2$ from paint was determined to be 86.1± 40 nm. The smaller fraction (12 – 15 min) had a mean diameter of 56.5 ± 15.2 nm and the 15-20 min fraction had a mean diameter of 104.1 ± 38.5 nm.

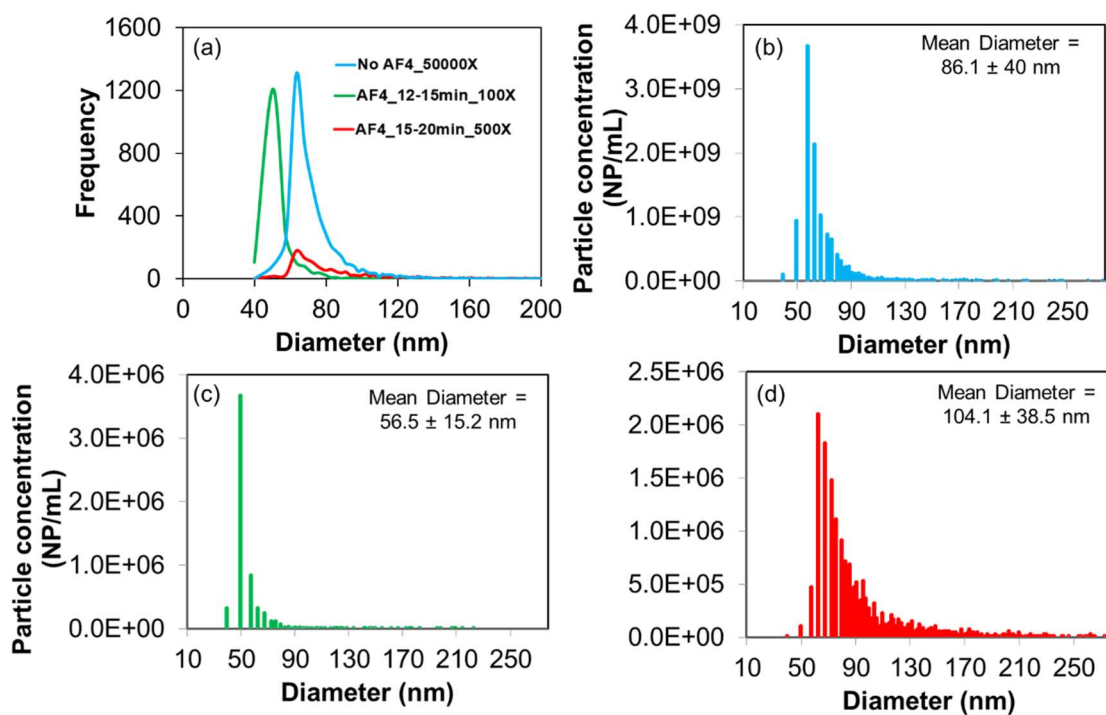**Figure 6.5:** (a) Comparison of spICP-MS size distribution of fractionated and un-fractionated nTiO2. Particle size distributions of (b) No AF4 fractionation (c) Fraction collected between 12 and 15 min (d) Fraction collected between 15 and 20 min.

6.3.5 Application of AF4: method development for complex matrices

Iron based nanoparticles are widely used in a variety of applications such as drug delivery (Ma et al. 2003), remediation (Zhang 2003), wastewater treatment (Ali et al. 2016). However, conventional light scattering techniques pose challenges in characterization of these nanoparticles due to their polydispersity (Ali et al. 2016). spICP-MS techniques have advanced with the inclusion of reaction/collision cell before entering the quadrupole to reduce polyatomic interferences with iron (Lee et al. 2014). However, detection can still be challenging when these iron based NPs when they are present in complex matrices. In the present study, AF4-MALS was used to characterize pristine magnetite as well as magnetite spiked in custom-made base paint to study the effect of the paint matrix on the stability of these NPs.

Figure 6.6 (a) shows a fractogram of pristine magnetite NPs. Light scattering data was best fitted using ZIMM 1st order, which assumes irregularly shaped particles, as sphere model did not fit the data well. Linear separation is observed with 0.6 ml/min cross flow as well as focus flow rate with a 7 min focussing step. Custom-made paint consisting of magnetite NPs showed a shift in fractogram indicating longer retention times due to increased sizes. Paint matrix seems to induce aggregation leading to an increase in sizes approximately two-fold (Figure 6.6 (b)). This information sheds light on possible fate processes that may occur upon release of NPs from the paint matrix.
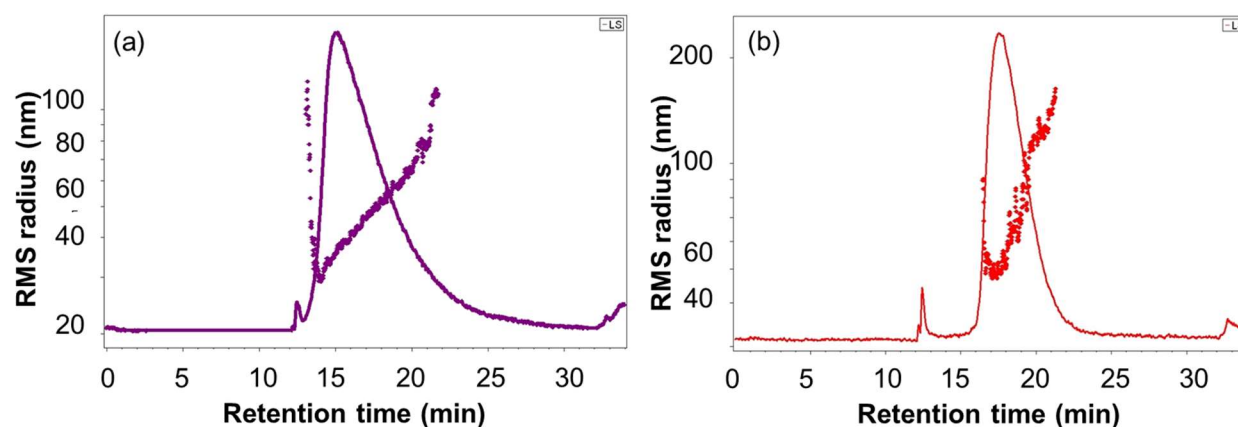
Figure 6.6: (a) Pristine nano Magnetite diluted 1000X from 35% solids suspension (b) Custom-made paint spiked with nano Magnetite diluted 5000X. AF4 conditions: 0.6 ml/min cross and focus flow with a 7 min focussing step with DI water as carrier fluid.

6.3.6 Proposed method for analysis of ENPs in environmental matrices

In the recent years, numerous studies have established methods to characterize and determine the fate of pristine ENPs in complex aquatic systems such as wastewater (Fabrega et al. 2009, Jarvie et al. 2009, Kaegi et al. 2013), surface water (Li and Lenhart 2012, Quik et al. 2014, Ellis et al. 2018). However, distinguishing and characterizing transformed ENPs in complex aquatic systems remains a challenge due to the heterogeneity of the matrix. Many studies have characterized inorganic ENPs in complex aquatic systems using ICP-MS techniques (Furtado et al. 2014, Quik et al. 2014, Velzeboer et al. 2014, Ellis et al. 2018). However, standard ICP-MS does not provide any information about particle size, particle concentrations and is unable to distinguish between dissolved and particulate fractions. spICP-MS has the ability determine the size and number concentrations of ENPs (Stephan et al. 2014) which overcomes the challenges posed by standard ICP-MS. The coupling of AF4 and spICP-MS can be used to improve detection of ENPs in

complex matrices in multiple ways: detection of ENPs at lower concentration due to low concentration detection limits of spICP-MS unlike other spectrometry or light scattering techniques that require higher concentrations. Information on number concentration and composition of heteroaggregated ENPs (Nowack et al. 2015) can be obtained by first running samples through AF4 prior to spICP-MS.
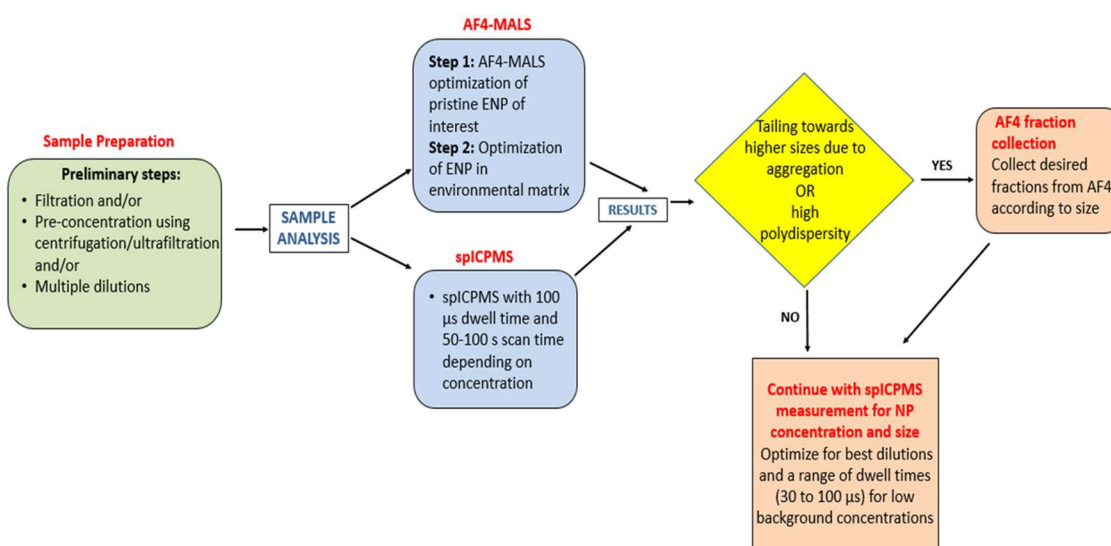
Figure 6.7: Schematic for detection and characterization of ENP in environmental matrices

In order to improve detection and characterization of ENPs in complex aquatic matrices, we propose the following procedure (Figure 6.7) based on our experimental findings. Depending on the source of the environmental sample containing ENPs, pre-treatment of the sample is required by one of the following techniques. (i) Filtration to remove large flocs and particulate matter (ii) pre-concentrate sample by centrifugation or ultrafiltration to increase ENP concentrations to ensure that it is above limit of detection of the instrument. (iii) Diluting with DI water if the sample has very high ENP concentrations.

It is important to note that both AF4 and spICP-MS are not required for all environmental ENP samples. As AF4 method development can be repetitive, therefore, spICP-MS analysis of the desired sample should be the first step of analysis. Transport efficiency can be estimated using nAu 55-60 nm at a dwell time of 100 μs. This dwell time is used for preliminary screening analysis, as we are still unaware of the nature of the ENPs in the environmental sample. Initial sampling time of 90-100 s is chosen to ensure enough NPs reaching the detector. The next step of analysis depends on the data obtained from spICP-MS. If presence of large aggregates or polydispersity is not observed, spICP-MS conditions can be modified to obtain better data quality. For example, decrease dwell times to 50 or 30 μs if preliminary data reveals presence of smaller NPs. However, it is important to note that decreasing dwell time may increase the background concentrations. If preliminary results indicate high polydispersity, AF4 fractionation prior to spICP-MS analysis will improve data quality.

For AF4 fractionation, a method has to be developed for the ENP of interest preferably using pristine NPs to make the method development process simpler. Upon determining the basic flow conditions for pristine NPs, it will be easier to modify flow conditions for ENPs in complex samples. Samples fractionated from AF4 can be collected manually or automatically using a fraction collector. If collected manually, the first separation should be done to gather data from the fractogram to determine time collection intervals. After collection of fractions, they can be diluted if necessary, before analysing using spICP-MS.

6.4 Conclusion

The present study optimized AF4 for characterizing different types of pristine polydisperse $nTiO_2$. The chemical composition of the carrier fluid and flow conditions varied for different types of

pristine $nTiO_2$ tested showing that despite having the same chemical composition, other properties like surface coating, morphology, size range influence flow conditions. A method was developed to improve sizing and concentration for lower size fraction data obtained by spICP-MS by pre-fractionating $nTiO_2$ with AF4.

AF4 has many applications for environmental samples as it has the potential to be coupled with a variety of detectors, which can provide a wide suite of information on particle size distributions, chemical compositions of different sizes and concentrations. We now have a procedure developed to analyse ENPs in complex environmental samples using two robust techniques; AF4 and spICP-MS.

6.5 Acknowledgements

6.6 Supplementary Information

Table S 6.1: Primary particle diameters estimated using TEM

nTiO$_2$ Type-Primary	n	Diameter (nm)
CristalActiv TiO$_2$	100	26.71 ± 5.94
TiO$_2$ P25	60	26.18 ± 8.1
U.S Nano TiO$_2$	105	24.64 ± 7.37

Table S 6.2: Recovery of 80 nm polystyrene with different focussing times

Focus time (min)	Peak Recovery	Peak with void volume recovery
3	59	81.76
5	100	100
8	100	100
12	100	100

Table S 6.3: Aggregate sizes estimated using TEM

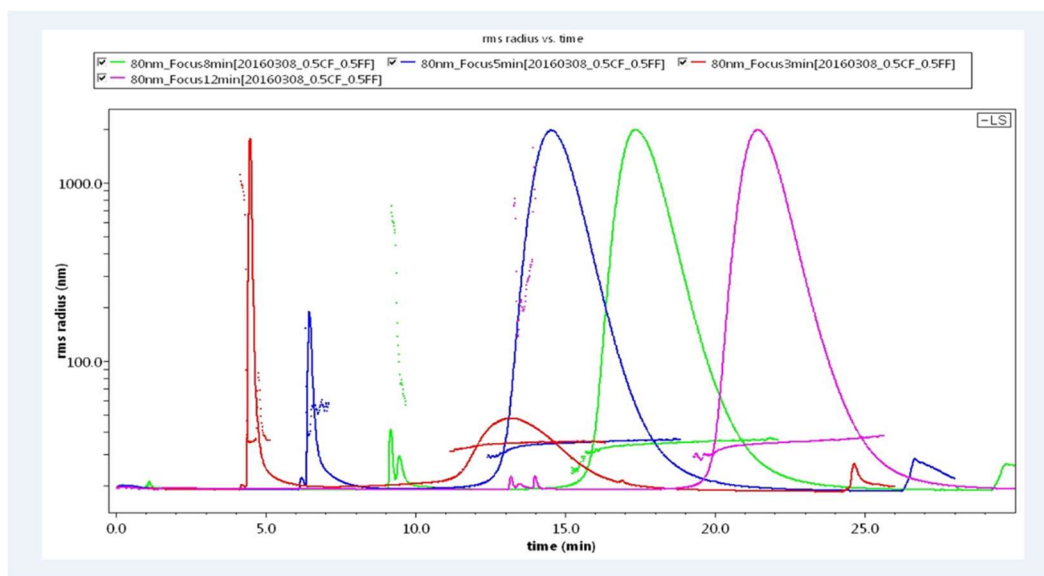| nTiO$_2$ Type-Aggregate	n	Diameter (nm)
CristalActiv TiO$_2$	16	140.06 ± 55.76
TiO$_2$ P25	38	168.94 ± 91.85
U.S Nano TiO$_2$	76	86.58 ± 50.73

Figure S 6.1: Effect of focussing time on fractionation of 80 nm polystyrene. Flow conditions: 0.5ml/min cross flow, 0.5 ml/min focus flow with 2 min initial focus followed by 3 min of injection and focussing. Carrier fluid: 0.25mM Ammonium Carbonate and Injection Mass: 10 μg.
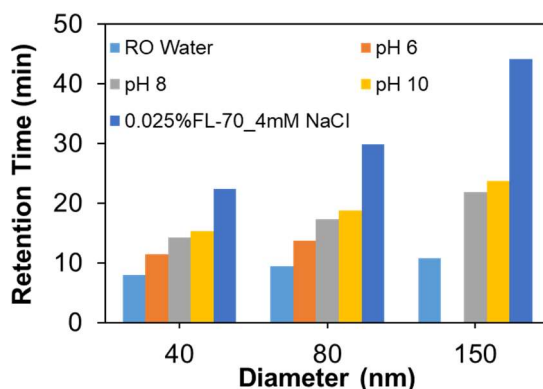
Figure S 6.2: Effect of carrier fluid composition on retention time of polystyrene standards

6.7 References

1) Ali, A., et al. (2016). "Synthesis, characterization, applications, and challenges of iron oxide nanoparticles." Nanotechnology, science and applications **9**: 49-67.

2) Andersson, P. O., et al. (2011). "Polymorph- and Size-Dependent Uptake and Toxicity of TiO2 Nanoparticles in Living Lung Epithelial Cells." Small **7**(4): 514-523.

3) Baalousha, M., et al. (2006). "Size fractionation and characterization of natural colloids by flow-field flow fractionation coupled to multi-angle laser light scattering." Journal of Chromatography A **1104**(1): 272-281.

4) Baalousha, M., et al. (2011). "Flow field-flow fractionation for the analysis and characterization of natural colloids and manufactured nanoparticles in environmental systems: a critical review." Journal of Chromatography A **1218**(27): 4078-4103.

5) Bouby, M., et al. (2008). "Application of asymmetric flow field-flow fractionation (AsFlFFF) coupled to inductively coupled plasma mass spectrometry (ICPMS) to the quantitative characterization of natural colloids and synthetic nanoparticles." Analytical and bioanalytical chemistry **392**(7-8): 1447-1457.

6) Boxall, A. B., et al. (2007). "Current and future predicted environmental exposure to engineered nanoparticles." Central Science Laboratory, Department of the Environment and Rural Affairs, London, UK: 89.

7) Chowdhury, I., et al. (2012). "Combined Factors Influencing the Aggregation and Deposition of nano-TiO2 in the Presence of Humic Acid and Bacteria." Environmental Science & Technology **46**(13): 6968-6976.

8) Contado, C. and A. Pagnoni (2008). "TiO2 in Commercial Sunscreen Lotion: Flow Field-Flow Fractionation and ICP-AES Together for Size Analysis." Analytical Chemistry **80**(19): 7594-7608.

9) Cornelis, G. and M. Hassellöv (2014). "A signal deconvolution method to discriminate smaller nanoparticles in single particle ICP-MS." Journal of Analytical Atomic Spectrometry **29**(1): 134-144.

10) Cristal. "CristalACTiV™ PC105." from http://www.cristal.com/products-and-services/ultrafine-and-specialty-tio2/ultrafine-and-specialty-tio2-products/Pages/PC105.aspx.

11) Dubascoux, S., et al. (2008). "Optimisation of asymmetrical flow field flow fractionation for environmental nanoparticles separation." Journal of Chromatography A **1206**(2): 160-165.

12) Ellis, L.-J. A., et al. (2018). "Seasonal variability of natural water chemistry affects the fate and behaviour of silver nanoparticles." Chemosphere **191**: 616-625.

13) Fabrega, J., et al. (2009). "Interactions of Silver Nanoparticles with Pseudomonas putida Biofilms." Environmental Science & Technology **43**(23): 9004-9009.

14) Furtado, L. M., et al. (2014). "The persistence and transformation of silver nanoparticles in littoral lake mesocosms monitored using various analytical techniques." Environmental Chemistry **11**(4): 419-430.

15) Gottschalk, F., et al. (2009). "Modeled environmental concentrations of engineered nanomaterials (TiO2, ZnO, Ag, CNT, fullerenes) for different regions." Environmental Science & Technology **43**(24): 9216-9222.

16) Hagendorfer, H., et al. (2012). "Characterization of Silver Nanoparticle Products Using Asymmetric Flow Field Flow Fractionation with a Multidetector Approach—a Comparison to Transmission Electron Microscopy and Batch Dynamic Light Scattering." Analytical Chemistry **84**(6): 2678-2685.

17) Hagendorfer, H., et al. (2011). "Application of an asymmetric flow field flow fractionation multi-detector approach for metallic engineered nanoparticle characterization – Prospects and limitations demonstrated on Au nanoparticles." Analytica Chimica Acta **706**(2): 367-378.

18) Hassellöv, M., et al. (1999). "Determination of continuous size and trace element distribution of colloidal material in natural water by on-line coupling of flow field-flow fractionation with ICPMS." Analytical Chemistry **71**(16): 3497-3502.

19) Jarvie, H. P., et al. (2009). "Fate of Silica Nanoparticles in Simulated Primary Wastewater Treatment." Environmental Science & Technology **43**(22): 8622-8628.

20) Kaegi, R., et al. (2013). "Fate and transformation of silver nanoparticles in urban wastewater systems." Water Research **47**(12): 3866-3877.

21) Kammer, F. v. d., et al. (2005). "Field-flow fractionation coupled to multi-angle laser light scattering detectors: Applicability and analytical benefits for the analysis of environmental colloids." Analytica Chimica Acta **552**(1): 166-174.

22) Kammer, F. v. d., et al. (2011). "Separation and characterization of nanoparticles in complex food and environmental samples by field-flow fractionation." TrAC Trends in Analytical Chemistry **30**(3): 425-436.

23) Keller, A. A., et al. (2014). "Release of engineered nanomaterials from personal care products throughout their life cycle." Journal of Nanoparticle Research **16**(7): 1-10.

24) Lee, S., et al. (2014). "Nanoparticle Size Detection Limits by Single Particle ICP-MS for 40 Elements." Environmental Science & Technology **48**(17): 10291-10300.

25) Li, X. and J. J. Lenhart (2012). "Aggregation and Dissolution of Silver Nanoparticles in Natural Surface Water." Environmental Science & Technology **46**(10): 5378-5386.

26) Loeschner, K., et al. (2013). "Optimization and evaluation of asymmetric flow field-flow fractionation of silver nanoparticles." Journal of Chromatography A **1272**: 116-125.

27) Long, T. C., et al. (2006). "Titanium Dioxide (P25) Produces Reactive Oxygen Species in Immortalized Brain Microglia (BV2): Implications for Nanoparticle Neurotoxicity." Environmental Science & Technology **40**(14): 4346-4352.

28) Loosli, F., et al. (2014). "Effect of natural organic matter on the disagglomeration of manufactured TiO 2 nanoparticles." Environmental Science: Nano **1**(2): 154-160.

29) Ma, M., et al. (2003). "Preparation and characterization of magnetite nanoparticles coated by amino silane." Colloids and Surfaces A: Physicochemical and Engineering Aspects **212**(2): 219-226.

30) Mitrano, D., et al. (2012). "Field-flow-fractionation coupled with ICP-MS for the analysis of engineered nanoparticles in environmental samples."

31) Mitrano, D. M., et al. (2012). "Silver nanoparticle characterization using single particle ICP-MS (SP-ICP-MS) and asymmetrical flow field flow fractionation ICP-MS (AF4-ICP-MS)." Journal of Analytical Atomic Spectrometry **27**(7): 1131-1142.

32) Montaño, M. D., et al. (2019). "Opportunities for examining the natural nanogeochemical environment using recent advances in nanoparticle analysis." Journal of Analytical Atomic Spectrometry **34**(9): 1768-1772.

33) Mueller, N. C. and B. Nowack (2008). "Exposure modeling of engineered nanoparticles in the environment." Environmental Science & Technology **42**(12): 4447-4453.

34) Nowack, B., et al. (2015). "Progress towards the validation of modeled environmental concentrations of engineered nanomaterials by analytical measurements." Environmental Science: Nano **2**(5): 421-428.

35) Plathe, K. L., et al. (2010). "Using FlFFF and aTEM to determine trace metal–nanoparticle associations in riverbed sediment." Environmental Chemistry **7**(1): 82-93.

36) Poda, A. R., et al. (2011). "Characterization of silver nanoparticles using flow-field flow fractionation interfaced to inductively coupled plasma mass spectrometry." Journal of Chromatography A **1218**(27): 4219-4225.

37) Qi, J., et al. (2013). "Dispersion and stability of titanium dioxide nanoparticles in aqueous suspension: effects of ultrasonication and concentration." Water Science and Technology **67**(1): 147-151.

38) Quik, J. T. K., et al. (2014). "Heteroaggregation and sedimentation rates for nanomaterials in natural waters." Water Research **48**: 269-279.

39) Schachermeyer, S., et al. (2012). "Impact of carrier fluid composition on recovery of nanoparticles and proteins in flow field flow fractionation." Journal of Chromatography A **1264**: 72-79.

40) Sharma, V. K. (2009). "Aggregation and toxicity of titanium dioxide nanoparticles in aquatic environment—A Review." Journal of Environmental Science and Health, Part A **44**(14): 1485-1495.

41) Stephan, C., et al. (2014). "Single Particle Inductively Coupled Plasma Mass Spectrometry: Understanding How and Why." PerkinElmer white paper.

42) Tharaud, M., et al. (2017). "TiO2 nanomaterial detection in calcium rich matrices by spICPMS. A matter of resolution and treatment." Journal of Analytical Atomic Spectrometry **32**(7): 1400-1411.

43) Tiede, K., et al. (2008). "Detection and characterization of engineered nanoparticles in food and the environment." Food Additives and Contaminants **25**(7): 795-821.

44) US Research Nanomaterials, I. (29/12/2017). "Titanium Oxide (TiO2) Nanopowder / Nanoparticles Water Dispersion." from https://www.us-nano.com/inc/sdetail/1056.

45) Velzeboer, I., et al. (2014). "Rapid settling of nanoparticles due to heteroaggregation with suspended sediment." Environmental Toxicology and Chemistry **33**(8): 1766-1773.

46) Zhang, W.-x. (2003). "Nanoscale Iron Particles for Environmental Remediation: An Overview." Journal of Nanoparticle Research **5**(3): 323-332.

47) Zhang, Y., et al. (2008). "Stability of commercial metal oxide nanoparticles in water." Water Research **42**(8–9): 2204-2212.

48) Zhou, D., et al. (2013). "Influence of Material Properties on TiO2 Nanoparticle Agglomeration." PLOS ONE **8**(11): e81239.

Chapter 7 . Conclusions and Future Work

7.1 Conclusions

Increasing use of engineered nanoparticles (ENPs) has led to their inevitable release into different environmental compartments, natural waters being one of them. The goal of this thesis was to examine the transformation processes ENPs undergo in aquatic environments, in order to provide better understanding of their overall fate, behavior and possible implications on the aquatic ecosystem.

In **Chapter 3**, the fate of 80 nm PVP-nAg in the presence (unfiltered lake water or UFLW) and absence (filtered lake water or FLW) of natural colloids was determined in lake water sampled from Lac Hertel in Mont. St. Hilaire. Re-precipitation of nAg (r-nAg) from primary nAg (p-nAg) was an important transformation process which was observed in all our systems (~26 nm) using single particle ICP-MS (spICP-MS). Environmental fate of p-nAg and r-nAg was evaluated and contrasted under both favorable (quiescent) and unfavorable (mixed) settling conditions. Absence of natural colloids led to increased homoagglomeration of r-nAg (with other r-nAg or p-nAg) which translated into increased Ag mass per particle ($Ag_{\text{mass per particle, day 21}} = 1.5 \times Ag_{\text{mass per particle, day 0}}$) under quiescent conditions. An increased persistence of r-nAg was observed (r-nAg-mixed $_{\text{day 21, NP/mL}} = 4.25 \times$ r-nAg-quiescent $_{\text{day 21, NP/mL}}$) under mixed conditions in FLW. In the presence of natural colloids, heteroagglomeration-induced sedimentation was determined to be the dominant fate process of r-nAg and p-nAg under both mixed and quiescent conditions. Unfavorable settling conditions revealed counterintuitive behavior of r-nAg, with lower persistence (r-nAg-mixed $_{\text{day 21, NP/mL}} = 0.4\times$ r-nAg-quiescent $_{\text{day 21, NP/mL}}$) and faster sedimentation in the presence of colloids. The results from this chapter suggest that fate and behavior of re-precipitated nAg is less predictable from that of primary nAg in natural lake waters.

Chapter 4 investigated sulfidation of PVP-nAg, which is another important transformation process in aquatic systems as sulfidation of nAg has been shown to reduce toxicity of nAg by blocking the release of Ag^+ due to oxidative dissolution. However, recent studies indicating continued toxicity of nAg despite sulfidation requires further understanding of the sulfidation process. In this study, the effective extents of sulfidation of nAg in the presence of excess sulfides was determined. At a stoichiometric molar S/Ag ratio of 0.5, the effective sulfidation ratio was only 0.25 after 7 days. These phenomena contribute to dissolution of Ag from the sulfidated nAg, which can contribute to adverse effects. The [S/Ag] dose available for sulfidation controls the extent of sulfidation as higher extents of sulfidation. Particle sizes within the nAg particle distribution did not show any size dependence on the extent of sulfidation ([S/Ag]$_{particle}$) achieved. This implies that extent of sulfidation is more dependent on total surface area available for sulfidation and less dependent on specific surface area. The presence of natural organic matter (NOM), at an S/Ag ratio of 0.5, did not have any impact on the extent of sulfidation.

The ability of spICP-MS to characterize particle concentrations in the ng/L range while distinguishing dissolved from particulate material makes it a promising technique for routine ENP analysis. **Chapter 5** describes a method developed to improve detection and characterization of ENPs by exploring the transport efficiency parameter. The influence of size of gold nanoparticles (nAu$_{TE}$) used as a reference for determining transport efficiencies is currently unknown. The relationship between transport efficiency and mean diameters was derived theoretically using spICP-MS equations leading to the following; (diameter $\propto \sqrt[3]{TE}$). The effect of nAu$_{TE}$ size (20, 30 and 55.5 nm) on particle sizing and counting efficiencies of nAu was first investigated, followed by validating the newly developed method by spiking nAg and nTiO$_2$ in wastewater sludge and DI water, respectively. Improved particle counting efficiencies were observed especially in the

lower size range (20 - 40 nm), by employing smaller reference nAu_{TE} 30 nm). The particle number concentration recoveries improved by a factor of 1.5 when 30 nm nAu_{TE} (74.3 %) was used instead of 55.5 nm nAu_{TE} (48.4 %) of 30 nm PVP-nAg spiked in diluted (100X) wastewater sludge matrix. Improving the resolution and overall data quality obtained from spICP-MS increases the range of applicability of this technique.

AF4 has many applications for environmental samples as it has the potential to be coupled with a variety of detectors, which can provide a wide suite of information on particle size distributions, chemical compositions of different sizes and concentrations. In **Chapter 6,** methods were developed to analyse different ENPs such as nAg, $nTiO_2$, $nSiO_2$, nZnO, magnetite in complex environmental samples using AF4. Further, detection of $nTiO_2$ was improved by first size fractionating the polydisperse sample using AF4 followed by employing 30 nm nAu for TE estimation. This optimized method improved detection of $nTiO_2$ in the 45 – 90 nm range from 25.4 % to 99.4 % without and with AF4 prior fractionation, respectively.

7.2 Future Work

Determining the fate of nAg (free, agglomerated, re-precipitated, and dissolved) enables inputting realistic and accurate parameters into environmental fate models or in environmental risk assessment studies. In this study, different transformation processes of nAg in natural lake water were quantified at environmentally relevant concentrations using spICP-MS. All the experiments in this study were performed in lab-scale microcosms. Results obtained from this study are representative of one set of aquatic conditions (colloidal concentration, ionic strength, natural organic matter, and pH). However, it is expensive and challenging to perform these experiments under a variety of aquatic conditions. Incorporating realistic values (or fractions undergoing

different fate processes) obtained from laboratory experiments into environmental fate models may emerge to be a promising method for risk assessment studies.

Re-precipitation of nAg (r-nAg) from primary nAg is a definitive fate process of nAg that occurs in natural waters in the presence of natural organic matter. Current environmental fate models do not incorporate re-precipitation in their prediction studies. Re-precipitated nAg is different (transformed) from pristine nAg with smaller mean diameters. This stipulates the possibility for higher bioavailability of newly formed nAg and therefore should be incorporated in toxicity studies and risk assessment studies. In this study, size of nAg was used as a "discriminating factor" to distinguish between r-nAg and p-nAg. If larger r-nAg particles or agglomerates are formed naturally via re-precipitation, size discrimination is not optimal to distinguish between naturally formed nAg and commercial or anthropogenic nAg. Analytical techniques to fully understand and quantitatively predict the behavior of r-nAg in natural waters need to be developed.

Developing a method to detect and characterize transformation processes nAg such as sulfidation using AF4-ICP-MS opens the possibility to closely understand the mechanisms of these reactions at the nanoscale level. Further, the multi-element detection capability of ICP-MS using the mass-shift mode enables the detection of challenging elements such as sulfur associated with silver. In this study, all experiments were performed under controlled aquatic chemistries. Applying this method to ENPs in real environmental samples (wastewater, biosolids extract, surface waters) can provide more information about transformation and behavior of ENPs in the environment. This optimized method is a step closer to discriminating between pristine nAg and transformed nAg (Ag_2S). Determining the effect of size (across a wide range 10 – 200 nm) on sulfidation extents using the ability of AF4 to fractionate according to size will provide important information from a toxicity standpoint. Further, incomplete sulfidation has environmental implications such as

dissolution and re-precipitation of Ag_2S particles of smaller sizes. The fate and behavior of these transformed particles under environmentally relevant conditions needs to be determined to understand their environmental implications.

Data quality obtained from spICP-MS in this study was improved using different techniques; improving particle sizing and counting efficiencies using different sizes for determining transport efficiencies, and using AF4 as a sample clean-up step to improve the detection of polydisperse TiO_2 NP samples. This technique can be employed to distinguish free NPs from homo and heteroagglomerated particles. spICP-MS has the ability to provide information about mass and particle number concentrations of each of these fractions. In the current study, nAg, $nTiO_2$ and nAu are the only ENPs tested using these optimized techniques. Further studies need to be performed to test the effectiveness of the optimized techniques on other commonly used ENPs such as nZnO, $nSiO_2$, nCu for measuring particle diameter and mass concentrations and particle number concentrations.